UNIVERSITY OF OKLAHOMA

GRADUATE COLLEGE

THE RESPONSE OF A LONG-LIVED MESOSCALE CONVECTIVE SYSTEM TO CHANGES IN LOWER-TROPOSPHERIC CONDITIONS

A THESIS

SUBMITTED TO THE GRADUATE FACULTY

in partial fulfillment of the requirements for the

Degree of

MASTER OF SCIENCE IN METEOROLOGY

By

MANDA BETH CHASTEEN
Norman, Oklahoma
2017

THE RESPONSE OF A LONG-LIVED MESOSCALE CONVECTIVE SYSTEM TO CHANGES IN LOWER-TROPOSPHERIC CONDITIONS

A THESIS APPROVED FOR THE
SCHOOL OF METEOROLOGY

BY

Dr. David Parsons, Chair

Dr. Howard Bluestein

Dr. Alan Shapiro

Acknowledgments

Many thanks to my adviser, David Parsons, for his guidance and the opportunity to perform this research. I am also grateful for my committee members, Alan Shapiro and Howie Bluestein. I am thankful for the discussions had with Kevin Haghi, Steven Koch, Dylan Reif, Evgeni Fedorovich, Elizabeth Smith, and Josh Gebauer about this research. I am especially thankful for the resources and plotting scripts I received from Ben Blake and Larissa Reames. I am grateful to Kelton Halbert for his help with installing and utilizing SHARPpy. I would like thank Monica Deming from the Oklahoma Climatological Survey for access to the Oklahoma Mesonet data. The simulations performed for this study were made possible because of the computing resources provided by the Oklahoma Supercomputing Center for Education and Research and the National Center for Atmospheric Research Computational Information Systems Laboratory. I am also grateful for my friends, especially Daniel Phoenix, Ethan Collins, Lauren Carter, and Zachary Wienhoff, for their support throughout the roller coaster that is graduate school. I also want to thank my oldest brother, Dave, who always pushed me as a kid and told me, "Bs make honey, As make money". This work was funded by National Science Foundation grant AGS-1237404.

Table of Contents

List of Tables

List of Figures

Abstract

Most continental regions experience an afternoon or evening maximum of convective activity, which is dominated by convection driven by surface heating. However, the Great Plains of North America experiences a nocturnal maximum in convective precipitation during the warm season, which is associated with the frequent occurrence of elevated mesoscale convective systems (MCSs). These elevated convective systems are sustained by inflow above a near-surface stable layer, and their existence is often attributed to the presence of a nocturnal low-level jet (LLJ), which transports warm, moist air poleward during the nighttime. While the presence of a strong LLJ and a stable layer are well known to exist in nocturnal convective environments, there is a lack of understanding on what environmental factors control the longevity of these nocturnal systems. While the majority of nocturnal MCSs tend to weaken or dissipate by late morning, many continue into the afternoon. Additionally, few studies have examined how convection evolves as it encounters environments with changing boundary layer characteristics throughout the diurnal cycle.

Herein we present observations and WRF-ARW simulations of a poorly forecast, long-lived MCS that initiated at approximately 0300 UTC (2100 LST) in a nocturnal environment thought to be unsupportive of convection. This MCS produced numerous severe reports, including a nocturnal tornado. Surface observations suggested that two mesoscale boundaries originating from a weak cold front were responsible for triggering this initially-elevated convection. WRF simulations

depicted a rapidly evolving environment owing to a nocturnal LLJ, which was critical for the initiation and persistence of this MCS. Additionally, the structure of the LLJ led to considerable spatial variability in the low-level convective instability field owing to moisture advection, downwelling radiation, and turbulence.

The simulated system was initially elevated and maintained by a bore-like disturbance, but the development of a strong cold pool resulted in the transition to a cold-pool-driven system despite that the highest instability existed aloft. As the system moved farther south into an increasingly unstable air mass, the system eventually became surface-based and persisted until moving off the Gulf Coast. The evolution of the convective structure and lifting mechanism during the system's lifetime was examined in terms of vorticity balance (i.e., RKW theory) and wave analysis frameworks with similar results to past studies. The ability for the system to become maintained by a strong cold pool without the presence of a bore allowed the system to persist into a destabilizing environment, which is unfavorable for the maintenance of bores. After the system cold pool became the dominant forcing for ascent, the system behaved in a similar manner to that expected from RKW theory.

This study was one of the first to examine this persistence and transition in terms of both wave dynamics and vorticity balance frameworks. Because elevated, nocturnal systems are commonly maintained by bores, the ability for the primary convective region of the system to reduce its dependence on a bore for maintenance suggests that it was able to persist through a changing environment. Future studies, especially those utilizing high-resolution observations, are needed to determine whether or not this process is found in other long-lived, persistent MCSs.

Chapter 1

Introduction and Background

The nocturnal precipitation maximum over the Great Plains region of the United States during the warm season is well documented (e.g., Means, 1952; Wallace, 1975) and is associated with mesoscale convective systems (MCSs) (Fritsch et al., 1986). These systems are often thought to be elevated in that they are maintained by instability located above the stable boundary layer or near-surface inversion (e.g., Maddox, 1980, 1983; Corfidi, 2003; Moore et al., 2003). Less studied, however, is how convection transitions from being elevated to surface-based (or vice versa) as it persists throughout the diurnal cycle and encounters environments with different wind shear and stability profiles. To our knowledge, only two prior studies (Marsham et al., 2011; Trier et al., 2011) have examined long-lived convection that underwent this transition.

These transitioning systems can persist for several hours while traversing hundreds of kilometers and pose a significant challenge for both short-term and long-range forecasting (e.g., Corfidi et al., 2008). Several previous studies have found that numerical weather prediction (NWP) models poorly represent the diurnal cycle of precipitation (e.g., Davis et al., 2003; Clark et al., 2007; Surcel et al., 2010). Nocturnal convective initiation is especially problematic, and NWP models often have significant errors in the timing and location of initiation and poorly represent the longevity of these systems (Davis et al., 2003; Kain et al., 2013; Pinto et al.,

2015). Moreover, poor representation of these large MCSs in NWP can result in downstream forecast busts (Rodwell and Coauthors, 2013). Additionally, during the warm season, convective weather is the largest source of disruption to the aviation industry, and the persistence of these MCSs into the morning and afternoon is likely one large contributing factor to this statistic[1].

The MCS discussed herein formed after 0200 UTC on 6 October 2014 in an environment thought to be characterized by minimal convective instability. This particular case was poorly forecast by operational NWP models, but persisted for more than 18 h, producing numerous severe wind and hail reports and a tornado at 0600 UTC[2] (0000 LST). While it has long been assumed that many of the nocturnal MCSs are elevated in that they are largely fed from air originating above the nocturnal boundary layer or a near-surface frontal inversion (e.g., Colman, 1990a,b; Moore et al., 2003; Wilson and Roberts, 2006), several recent studies (e.g., Parker, 2008; Billings and Parker, 2012; Schumacher, 2015) have shown that is not necessarily true. In this case, the presence of a nocturnal tornado would imply that the system was at least locally able to ingest near-surface air, suggesting that a likely elevated system at initiation was able to transition to being partially surface-based well before sunrise (e.g., Billings and Parker, 2012). This study aims to advance the understanding of why some nocturnal convective systems regenerate and persist into the following day through the employment of a case study which utilizes both observations and numerical simulations. We hope to better understand the environments supportive of persistent, transitioning MCSs and how their convective structure evolves throughout the diurnal cycle.

[1] `https://www.faa.gov/nextgen/programs/weather/faq/`

[2] UTC = LST + 6

1.1 Climatology of Great Plains Nocturnal Convection

The occurrence of a nocturnal maximum in precipitation over the Great Plains region of the United States has long been known (e.g., Kincer, 1916; Means, 1952; Wallace, 1975). An early study by Kincer (1916) examined the distribution of warm-season (April through September) rainfall occurrence periods for different regions of the United States and found that 65% or more of the total rainfall occurs at night (between the hours of 1900 and 0700 LST) in the central Great Plains. This nocturnal maximum is attributed to a high frequency of nocturnal thunderstorms.

Several subsequent studies have attributed this nocturnal maximum in warm season precipitation to a phenomenon called the nocturnal low-level jet (LLJ; Means, 1952). Means (1944) proposed that strong low-level warm air advection from this LLJ acts to destabilize the atmosphere and is important for the formation of nocturnal thunderstorms. Curtis and Panofsky (1958) also examined the nocturnal maximum over the Midwestern United States and attributed its existence to the presence of a southerly LLJ.

Pitchford and London (1962) investigated how the LLJ relates to the occurrence of nocturnal thunderstorms over the Midwest, finding consistency between the mean axis of the LLJ and the maximum in nocturnal thunderstorm occurrence. Additionally, Augustine and Caracena (1994) examined afternoon precursors to nocturnal MCS development over the central U.S. and found that long-lived MCSs are likely to exist downwind of the surface geostrophic wind maximum, assuming that area is collocated with 850-hPa frontogenesis. The role of a synoptic front in these environments is to provide a focus for low-level ascent through convergence associated with the LLJ. Arritt et al. (1997) examined the LLJ frequency during

the 1993 warm season, which was characterized by a high frequency of MCSs and historic flooding in the Midwest. This study also attributed these MCSs to frequent and strong LLJs. An additional study by Tuttle and Davis (2006) found similar results in relating the LLJ to the nocturnal maximum in precipitation over the Great Plains.

Because this convection commonly forms at night in the presence of a near-surface inversion, the parcels feeding these updrafts are thought to be "elevated" (Corfidi et al., 2008), or originate above the stable boundary layer. Additionally, Colman (1990a,b) noted that elevated thunderstorms are commonly observed atop frontal surfaces, which are also isolated from surface diabatic heating effects often considered to be crucial to the development of thunderstorms. Colman (1990a) used the criterion that a thunderstorm must lie on the cold side of a surface boundary and, based on that criterion, he found that the greatest frequency of elevated thunderstorms in the warm season occurred over the Great Plains. Colman also noted the northward shift of the frequency of elevated convection throughout the summer, which was attributed to the northward advance of surface warm fronts and the presence of nocturnal LLJs. While nocturnal MCSs frequently owe their existence to convergence as the nose of the LLJ (and associated advection of warm, moist air) intercepts a frontal boundary aloft (e.g., Maddox, 1983), these elevated convective systems also occur in the absence of a surface frontal boundary atop a nocturnal stable layer (e.g., Wilson and Roberts, 2006; Reif, 2015).

Several climatological studies have examined additional aspects of the nocturnal precipitation maximum over the Great Plains (e.g., Means, 1952; Wallace, 1975; Easterling and Robinson, 1985; Riley et al., 1987; Heideman and Fritsch, 1988). Easterling and Robinson (1985) noted that the time corresponding to the most frequent nocturnal precipitation tends to become later with eastward distance from the Rocky Mountains, which is consistent with the findings of Wallace (1975) (Fig.

1). Easterling and Robinson (1985) attributed this later frequency of precipitation toward the east to lines of convection that initiated near the Rocky Mountains and then propagated eastward across the Great Plains. However, Riley et al. (1987) noticed a similar trend in timing, but concluded that the nocturnal maximum in precipitation over the eastern Great Plains could not be solely explained by these eastward propagating systems as the nocturnal maximum is also impacted by convection that forms at night over this region.

Other precipitation climatologies, such as Tripoli and Cotton (1989), found that an afternoon maximum exists along the eastern Rocky Mountains, which is

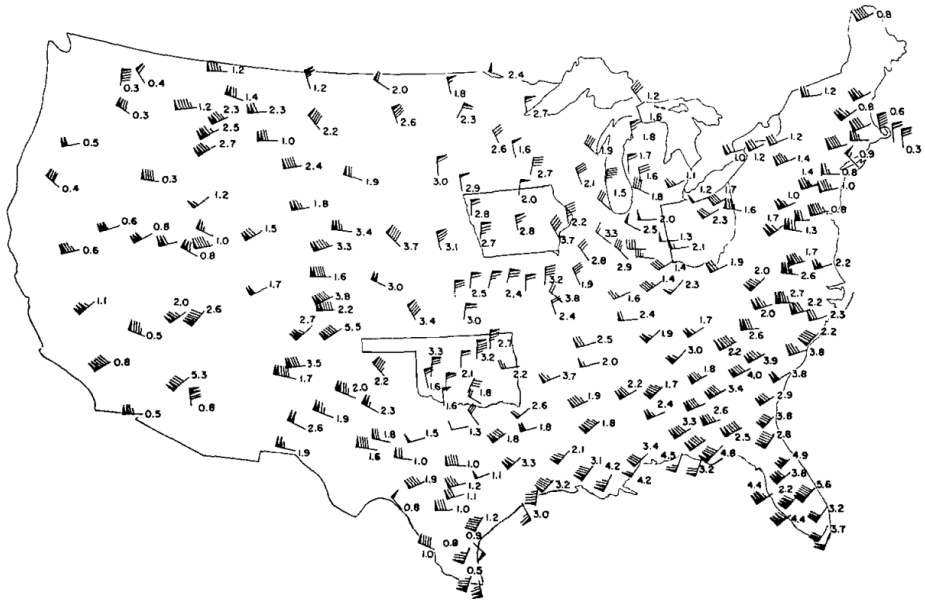

Figure 1: The diurnal cycle of summertime (June-August) thunderstorm frequency over the United States. Each barb represents a normalized amplitude, as described in Wallace (1975). Half barbs, full barbs, and flags represents 5%, 10%, and 50%, respectively. The direction of the barbs represent the time, with an arrow from the north representing a 0000 LST maximum, and an arrow from the east represents a 0600 LST maximum. The numbers plotted next to the barbs are the 24-hour mean frequencies from Wallace (1975). Adapted from Wallace (1975).

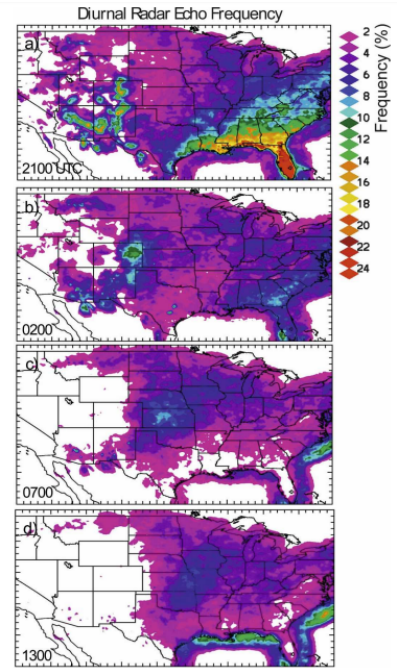

Figure 2: Diurnal radar echo frequency of occurrence for 12 summers (June-August). The expressed frequency is the percent of days within a given hour that a precipitation echo is present for (a) 2100, (b) 0200, (c) 0700, and (d) 1300 UTC. Adapted from Fig. 2 of Carbone and Tuttle (2008).

attributed to sensible heating over an elevated heat source, and a subsequent generation of nocturnal convection over the Plains. Carbone and Tuttle (2008) conducted a 12-year climatology of the diurnal cycle of rainfall occurrence during the summer months (June-August) and found that ascent and precipitation propagates eastward off the Rockies into the central United States throughout the night (Fig. 2). Carbone and Tuttle suggest that three mechanisms may be responsible for this eastward progression over time: 1) eastward propagation of convective systems off the Rockies owing to prevailing westerly flow; 2) a reversal of the mountain-plains solenoid[3] (Wolyn and McKee, 1994) which results in ascent over the mountains

[3]The mountain-plains solenoid acts on a horizontal scale of several hundred (i.e., ~500-800) kilometers.

during the day and ascent over the Plains at night; 3) momentum and moisture transport via the Great Plains LLJ (e.g., Bonner, 1968).

1.2 Mechanisms for the Low-Level Jet

Since the LLJ has been linked to nocturnal convection, this section discusses several of the theoretical studies investigating the phenomenon. Blackadar (1957) published a pioneering study on the causes and structure of the LLJ, which noted that the LLJ frequently occurs in dry, clear conditions conducive to strong radiative cooling and the subsequent formation of a near-surface nocturnal inversion. According to Blackadar's study, a rapid stabilization of the boundary layer occurs after sunset in relatively dry, cloud-free environments, which decreases turbulent mixing and results in an initial acceleration of the low-level wind - an inertial oscillation. Blackadar further proposed that the LLJ is located near the top of the inversion (usually 1 km AGL or lower) with peak intensity during the early morning hours. The study found that the jet tends to veer with time and proposed that the veering was a result of the inertial oscillation before dissipating with the onset of daytime turbulent mixing. This LLJ enhances low-level temperature and moisture advection during the nighttime, which Blackadar (1957) hypothesized, is a significant factor leading to the high frequency of nocturnal thunderstorms in the Great Plains region.

While the Blackadar (1957) theory does well at qualitatively explaining the presence of a low-level wind maximum, the theory fails explain spatial variations resulting in a LLJ and does not result in substantially supergeostrophic wind speeds, such as those commonly observed. Additionally, the theory cannot explain the spatial variations in wind that result in a jet nor why LLJs are frequently observed over the sloping terrain of the Great Plains and not over other areas of the country (e.g., Holton, 1967; Bonner and Paegle, 1970; Shapiro and Fedorovich, 2009, 2010).

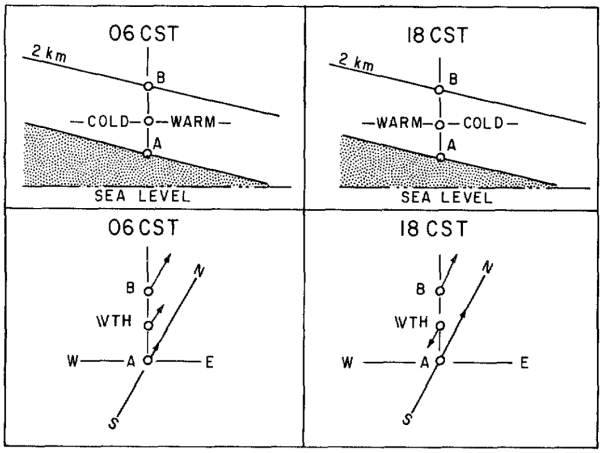

Figure 3: The diurnal variation of the low-level thermal wind over sloping terrain, such as the Great Plains of the United States. Figure adapted from Bonner and Paegle (1970).

To explain these discrepancies, Holton (1967) and Bonner and Paegle (1970) examined the baroclinicity associated with the cooling of sloping terrain at night and resultant reversal of the low-level thermal wind from day to night (Fig. 3). Holton (1967) proposed that contributions from the sloping terrain were attributed to the formation and favored location of the LLJ.

Recent studies (e.g., Shapiro and Fedorovich, 2009, 2010; Shapiro et al., 2016) have attempted to combine the inertial oscillation theory of Blackadar (1957) with the contributions of baroclinicity proposed by Holton (1967). The most recent study, Shapiro et al. (2016), has proposed a unified theory that results in LLJ structures and evolution consistent with observations and climatology. The LLJs produced in Shapiro et al. (2016) veered in direction with both height and time (from the inertial oscillation proposed by the Blackadar theory) and had realistic structure and magnitude owing to the included effects of baroclinicity (from the Holton theory). The evolution proposed by Shapiro et al. (2016) will be compared with the LLJ in this case study in section 4.2.

LLJs can also occur due to synoptic-scale forcing mechanisms. For example, Browning and Harrold (1969) noted that LLJs commonly occur in proximity to surface cold fronts. In addition, Uccellini and Johnson (1979) examined the role that upper-level jets have in the formation of LLJs. Their study found that upper-level jets can be coupled with low-level flow through the transverse ageostrophic circulation found with unbalanced jet streaks. More specifically, a thermally-indirect circulation is present in the exit region of upper-level jet streaks, with low-level flow oriented orthogonal to the jet axis and toward the poleward side of the jet (Uccellini and Johnson, 1979; Bluestein, 1993). This low-level flow branch can result in a LLJ which has different characteristics than those formed by an inertial oscillation. Additionally, previous studies (e.g., Uccellini, 1980) have found that isallobaric effects associated with lee troughing or lee cyclogenesis east of the Rocky Mountains can also promote the formation of LLJs over the Great Plains.

1.3 Structure of Mesoscale Convective Systems

The convection in this study grew upscale into an organized MCS. These convective systems are typically made up of an organized line or collection of convection with a much greater area of stratiform precipitation (e.g., Houze et al., 1990). MCSs are typically maintained by ascent along a surface cold pool or a bore, which act to regenerate new convection, allowing the systems to be self-sustaining (e.g., Bluestein and Jain, 1985). One primary designation of MCSs is a squall line, which is linear in nature and often the result of forcing along a surface boundary. Zipser (1977) described squall lines as "cumulonimbus clouds, organized in linear fashion, associated with a pseudo-cold front (squall front) at the surface, propagating with considerable speed with respect to the ambient low-level air, in the general direction

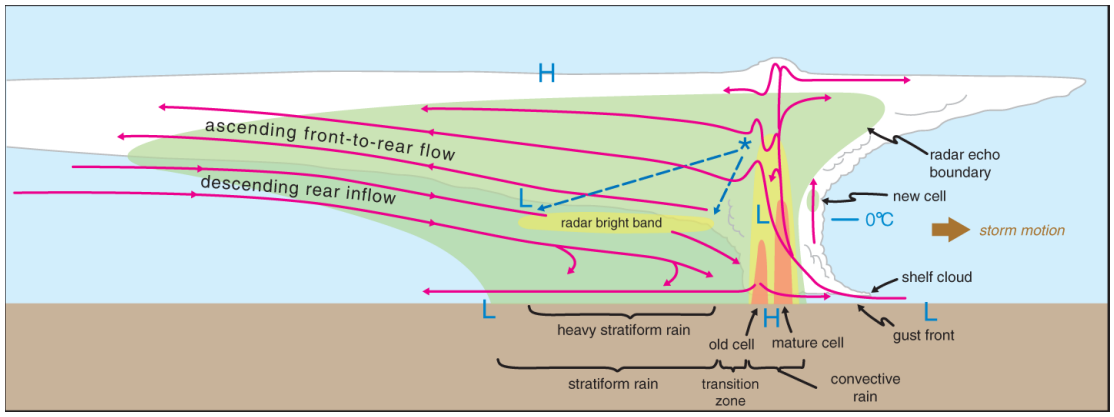

Figure 4: Conceptual model of a leading-line, trailing-stratiform MCS viewed along a cross section perpendicular to the convective line. The orange shading represents greater radar echoes associated with convective cells. Pressure minima and maxima and the melting level height (just above the radar bright band) are also indicated (Markowski and Richardson (2011) adaptation of Fig. 1 of Houze et al. (1989)).

of the squall wind in the cold air behind the squall front". The leading-line, trailing-stratiform squall line (Fig. 4; Houze et al., 1989, 1990) configuration is the most similar to the convective system in this case.

The largest types of MCSs in terms of lateral extent are mesoscale convective complexes (MCCs), which were first defined by Maddox (1980). These systems tend to form in weakly-forced environments common during the nighttime in the Great Plains warm season, so Maddox hypothesized that convectively-driven, mesoscale circulations dominate in the MCC. Many of the features noted by Maddox (1980) in MCCs are also observed in leading-line, trailing-stratiform MCSs and squall lines. Houze et al. (1989, 1990) found that the vertical structure of heating and cooling was important in forming the induced circulations found within these systems. More specifically, Houze et al. noted that MCSs are characterized by a leading convective line, which forms along the surface outflow boundary.

Parcels lifted over the outflow boundary often maintain their front-to-rear momentum through the convective line and continue ascending in the mesoscale updraft to the rear of the convective line, forming a stratiform area of precipitation.

In these systems, evaporationally-driven convective downdrafts result in hydrostatic mesohigh pressure centers near the surface. Above the cold pool, midtropospheric latent heating results in the formation of a warm-core low pressure center. In a system-relative framework, the flow within the system is often initially front-to-rear at all levels. However, the formation of horizontal buoyancy gradients within the anvil region results in the formation of a rear-inflow jet (RIJ; Weisman, 1992). This RIJ gradually descends as part of a mesoscale downdraft region of rear-to-front flow until it approaches the leading convective line. This region of subsaturated descent can enhance evaporation and sublimation beneath the anvil, strengthening diabatic effects in the cold pool. Additionally, the downward momentum transport from the RIJ can cause severe surface winds and the formation of bowing segments (e.g., Mahoney et al., 2009).

If the system persists over sufficiently long timescales, effects of the Coriolis force acting upon these mesoscale circulations (e.g., Skamarock et al., 1994; Knievel and Johnson, 2003) can result in the formation of a mesoscale convective vortex (MCV; e.g., Maddox, 1983; Smull and Houze, 1985; Bartels and Maddox, 1991). These mature MCVs can range greatly in horizontal diameter from less than 50 km to greater than 300 km (e.g., Johnston, 1981; Bartels and Maddox, 1991). The residual convectively-induced circulations often outlast the convection from which they developed, acting to initiate downstream convection (Johnston, 1981). At upper levels, a large-scale mesoscale area of high pressure exists above the mesoscale updraft and region of maximum latent heating, which can result in significant upper-level height and wind perturbations (e.g., Fritsch and Maddox, 1981; Maddox et al., 1981). If these circulations are incorrectly represented by

numerical models, they may result in medium-range forecast busts downstream owing to the generation of downstream-propagating Rossby waves (Rodwell and Coauthors, 2013; Lillo and Parsons, 2016).

1.4 Dynamics of Surface-Based and Elevated Convection

As stated earlier, the MCS presented herein transitioned from being an elevated system to being surface-based, allowing active convection to persist into the following afternoon. This section describes the differences between the maintenance of elevated and surface-based systems and the transition between the two modes of convection. As previously discussed, nocturnal convective systems are often assumed to be elevated in that they are maintained by inflow located above a near-surface inversion. However, this assumption is not always valid, and previous studies have shown that these systems can often ingest near-surface parcels provided that they possess CAPE (e.g., Parker, 2008; Nowotarski et al., 2011; Billings and Parker, 2012). Additionally, idealized studies (e.g., Parker, 2008; French and Parker, 2010) have shown how initially surface-based systems may transition to being elevated as the boundary layer stabilizes. However, systems can also initiate as elevated convection (e.g., Bluestein, 1985) and transition to surface-based (e.g., Trier et al., 2011; Marsham et al., 2011), which has been less documented in the literature.

In order to understand the maintenance, propagation, and evolution of nocturnal squall lines, Parker (2008) conducted idealized, 2- and 3-D simulations with a convective permitting cloud model and horizontally homogeneous initial conditions. In these simulations, Parker (2008) allowed surface-based convection to develop and mature prior to imposing artificial low-level cooling to represent the

formation of a nocturnal boundary layer. The design of these experiments allowed insight into nocturnal convection and how systems might transition from being surface-based to elevated. Parker (2008) examined the evolution of the squall line in terms of RKW theory (Rotunno et al., 1988). This theory (which will be elaborated on further in section 5.2) hypothesizes that new updraft regeneration along an outflow boundary will be maximized if an "optimal state" exists, resulting in a vertically-oriented updraft. This "optimal state" is described as a balance between horizontal vorticity associated with the environmental vertical wind shear and the baroclinically-generated horizontal vorticity associated with the system's cold pool (convective outflow). If an "optimal state" exists, these two vorticity contributions are of equal and opposite signs.

While the system was surface-based, Parker (2008) argued on the basis of RKW theory that the low-level vertical shear is critical to explaining the dynamics of the squall line (Fig. 5a). As the cooling commenced, the temperature gradient across the gust front decreased, resulting in a decrease in the forward speed of the squall line. Parker (2008) termed this stage the stalling phase. In this phase, the system was characterized by a weakening cold pool with a disturbance above, which had net upward displacements characteristic of a bore (Fig. 5b). In this stage, the vertical shear above the stable boundary layer became increasingly important in describing the system dynamics as the effective inflow layer shifted upward; moreover, an "optimal state" can occur with the appropriate deep vertical shear resulting in a secondary peak in system intensity. Continued cooling resulted in the eventual transition of the system to being fully elevated (Fig. 5c), whereby the system was maintained by a gravity-wave-like-bore, which lifted elevated parcels to their LFCs. This resulted in an increase in the system forward propagation speed as the gravity wave propagation speed exceeded that of the former density

current. Parker (2008) argued that the critical vertical shear for this phase is the shear that interacts with the bore (Fig. 5c).

Additionally, Parker (2008) found that substantial cooling of 10 K was necessary to disrupt the flow of surface-based parcels into a mature squall line. Parker found that as long as surface-based CAPE existed for these near-surface parcels, a mature cold pool is often capable of lifting them to their LFCs despite that the most-unstable air existed aloft. This finding suggests that mature systems are capable of remaining partially surface-based despite that the inflow environment is characterized by strong low-level static stability. This knowledge is important for the forecasting and nowcasting these events owing to an increased potential for severe winds or even a tornado (e.g., Horgan et al., 2007; Corfidi et al., 2008).

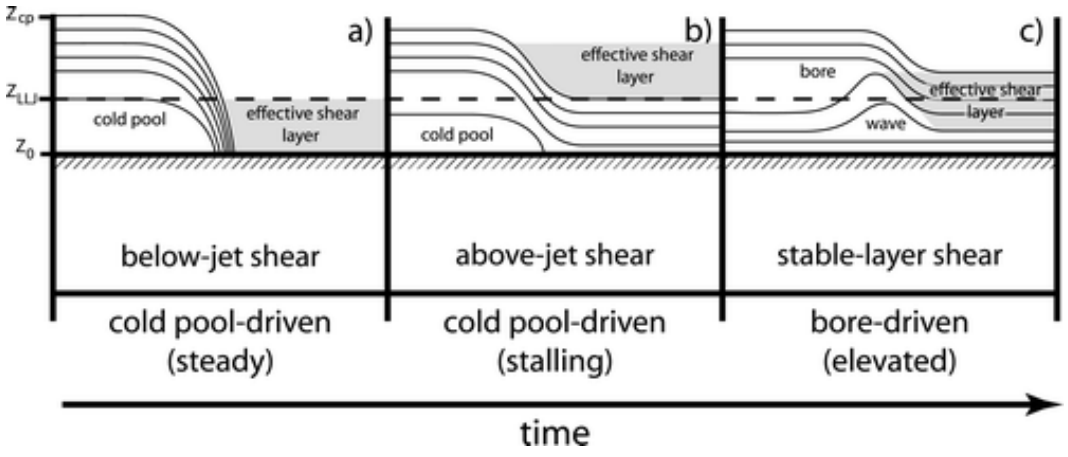

Figure 5: Depiction of a mature squall line transitioning between being surface-based to elevated. In (a), the system is maintained by a cold pool, but as the boundary layer cools, the system becomes maintained by a density-current-like-bore (b), and eventually, a gravity-wave-like-bore (c). The layers of vertical wind shear important for a cold pool-shear balance are denoted by the shaded region. The dashed line (Z_{LLJ}) indicates the level of maximum LLJ winds. Solid lines are the representative isentropes that define the cold pool or bore (from Fig. 18 of French and Parker (2010)).

In a subsequent study, French and Parker (2010) investigated conditions more relevant to nocturnal convection over the Great Plains through exploring impacts of a low-level jet. They found that incorporating the LLJ into the simulations had two important effects. First, the addition of a LLJ impacted the vertical wind shear profile, which resulted in altering the updraft intensity from an RKW perspective (e.g., Rotunno et al., 1988). Second, the LLJ affected the magnitude of the system-relative inflow within that layer, which tended to impact the total upward mass flux in the updrafts. However, differing orientations of the LLJ with respect to the convective line were the most favorable for convective maintenance during different phases of the system. For the density current phases, this orientation was determined in terms of an RKW framework. Moreover, as the near-surface air began to cool, the effective shear layer shifted upward in response to the greatest θ_e air being located above the surface. However, as the system transitioned to being elevated, the lifting mechanism evolved from a cold pool to a bore. At this time, the vertical wind shear became crucial for modulating the amplitude of the wave response (e.g., Schmidt and Cotton, 1990).

Another study which examined how convection evolves as the boundary layer stabilizes was Billings and Parker (2012). Billings and Parker found that, despite the presence of a stable boundary layer, sufficient dynamical forcing from the system can still lift parcels to their LFCs so long as surface-based CAPE is present. In their case, previously surface-based convection persisted into the night and was able to maintain itself through the forced ascent from deep cold pool lifting (squall line). Moreover, nocturnal supercells and their associated upward-directed perturbation pressure gradient force (Nowotarski et al., 2011) was able to draw in stable near-surface air, resulting in nocturnal tornadoes (i.e., after 0600 UTC). This result was supported by the previous finding that tornadoes require stretching of vorticity at the surface to exist (e.g., Davies-Jones et al., 2001). Therefore, while

systems are generally assumed to either be exclusively elevated or surface-based, mature supercells or MCSs often lie in a continuum between the two (Corfidi et al., 2008), where portions of the system are still able to ingest near-surface parcels despite being partially elevated. This result was also found in Schumacher (2015), in which a mature MCS was cold-pool-driven in proximity to the strongest convection but maintained by a gravity wave farther to the west. The MCS presented in this study found similar results as these aforementioned studies, which will be discussed in section 4.1.

In contrary to the studies done on the evening surface-based to elevated transition, fewer studies have examined the transition of nocturnal systems as they persist into the morning. However, Bryan and Weisman (2006) documented observed cases that began as elevated convection and produced severe surface winds despite the presence of a low-level stable layer in proximity soundings. In these cases, an elevated mixed layer was found above the stable layer, which has been shown in previous studies (e.g., Bryan et al., 2005) to aid in the production of deep cold pools through considerable latent cooling aloft. These cases were examined using idealized simulations which were characterized by a stable, nearly saturated low-level profile with an elevated mixed layer above. Early in the simulations, despite the presence of precipitation, no surface cold pool was present. However, a cold pool was found aloft in the near-neutral layer, acting as an elevated density current which promoted new cell development. Eventually, dry midlevel air via the RIJ descended to the surface, enhancing evaporative cooling potential, which eventually resulted in the cold pool extending downward over time. As this occurred, severe winds extended to the surface. However, this study does not discuss whether or not the system is able to ingest near-surface air as the cold pool descends, but illustrates the importance in understanding whether or not convective downdrafts are able to penetrate the stable boundary layer.

The first clear documentation of this elevated to surface-based transition was completed in a two-part study using both observations (Marsham et al., 2011) and numerical modeling (Trier et al., 2011). In Marsham et al. (2011), the boundary layer had stabilized owing to prior convection and radiative cooling, and elevated convective initiation occurred near the terminus of the LLJ. Additionally, gravity waves and bores generated from convective outflow proceeded to initiate further convection. During the morning, the convective system evolved into surface-based squall line.

Trier et al. (2011) also simulated the convective system presented by Marsham et al. (2011) using the Weather Research and Forecasting model with the Advanced Research Core (WRF-ARW). In the simulations, the convective system lacked a well-defined cold pool until mid-morning, indicating that it had maintained itself as an elevated system through the duration of the night. Moreover, this study found that solar heating of the environment did not have significant impacts on the strength of the convection until the system had become primarily surface-based. As the cold pool developed, the system acquired an upshear-tilt, which is consistent with a vorticity imbalance explained by RKW theory (Rotunno et al., 1988).

The ability for previously elevated nocturnal convection to transition to being surface-based is important for the regeneration of convection during the morning, leading to systems that persist into the afternoon. Hane et al. (2003) and later Hane et al. (2008) conducted a climatology of morning MCSs over a portion of the southern Great Plains (Fig. 6). While the areas focused on in this study are undoubtedly not the only areas which see the occurrence of morning convection, this region is relevant to the case study presented herein. Specifically, Hane et al. (2008) examined 145 MCSs during the summer months (June-August) of the 5-year period of 1996-2000. Of these 145 systems, 12% were found to dissipate

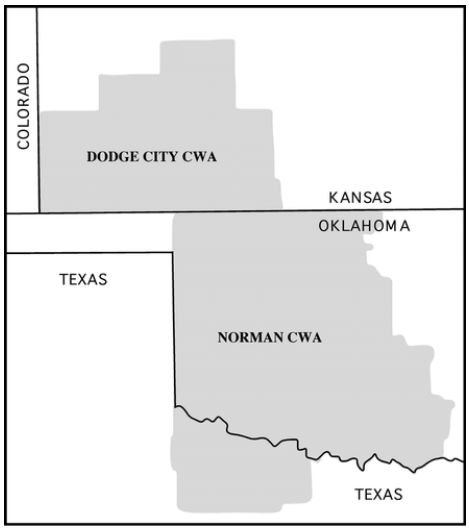

Figure 6: Map of the Norman, OK, and Dodge City, KS, National Weather Service County Warning Areas. Adapted from Fig. 1 of Hane et al. (2008).

between 0900 and 1300 UTC, and 60% weakened or dissipated between 1300 and 1700 UTC. Thus, while 72% of systems weakened or dissipated by late morning, 28% remained steady or strengthened and persisted into the afternoon. Hane et al. (2008) also sought to find whether or not certain environmental factors increased the longevity of these MCSs. They concluded that the movement with an upper-level feature (i.e., a midlevel shortwave trough, synoptic front, etc.) does not increase the likelihood of MCS persistence despite that these features played a role in initiation. Moreover, Hane et al. (2008) could not determine what environmental factors result in the persistence of some nocturnal MCSs while the majority either weaken or dissipate by late morning.

In summary, this area of research on the morning persistence and elevated-to-surface-based transition is still growing, and the case-study presented herein is just one of few studies that have examined this process. Therefore, we hope to expand on the few previous studies of regenerating systems by examining both the available observations and numerical simulations of this event in order to develop insight into the factors leading to this morning persistence.

1.5 Bow Echoes and Mesovortices

Organized convective systems, such as the one in this case, are oftentimes not comprised of a continuous convective line, but rather contain three-dimensional structures, such as line segments and embedded circulations. These systems are known as quasi-linear convective systems (QLCSs; e.g., Weisman and Davis, 1998). One such structure is a bowing segment, or "bow echo", which was first described by Fujita (1978). The nocturnal convective system presented in this case study produced multiple bowing segments, one of which was associated with the formation of a mesoscale vortex and EF-1 tornado (will be described in section 2.2.2).

Bowing segments are typically on the order of 40-100 km and are often associated with strong surface winds. Bow echoes often result in the formation of mesoscale vortices of opposing signs, commonly referred to as "bookend vortices" (e.g., Fujita, 1978; Weisman, 1993; Weisman and Davis, 1998). These opposing vortices have been shown to be of comparable strength early in their lifetime, but the Coriolis force results in the domination of the cyclonic circulation over time and the transition from a "symmetric" to "asymmetric" MCS structure (e.g., Houze et al., 1990; Skamarock et al., 1994; Weisman and Davis, 1998, Fig. 7).

Weisman (1993) used an idealized cloud model to investigate the dynamics of bow echoes. The environment in his simulations was characterized by high values of CAPE (i.e., ~2000 J kg^{-1}) and strong low-level vertical wind shear (>20 m s^{-1} over lowest 2.5 km). In this environment, the system evolved into a bow echo with cyclonic and anticyclonic bookend vortices at 2-3 km above ground level (AGL) on the north and south flanks of the bowing segment, respectively. Additionally, the system had developed a well-defined, elevated rear-inflow jet in between the two bookend vortices (Fig. 83b; Weisman, 1992).

Weisman (1993) found the RIJ to be focused and strengthened by the presence of the bookend vortices, which helps to maintain the system longevity. Early in

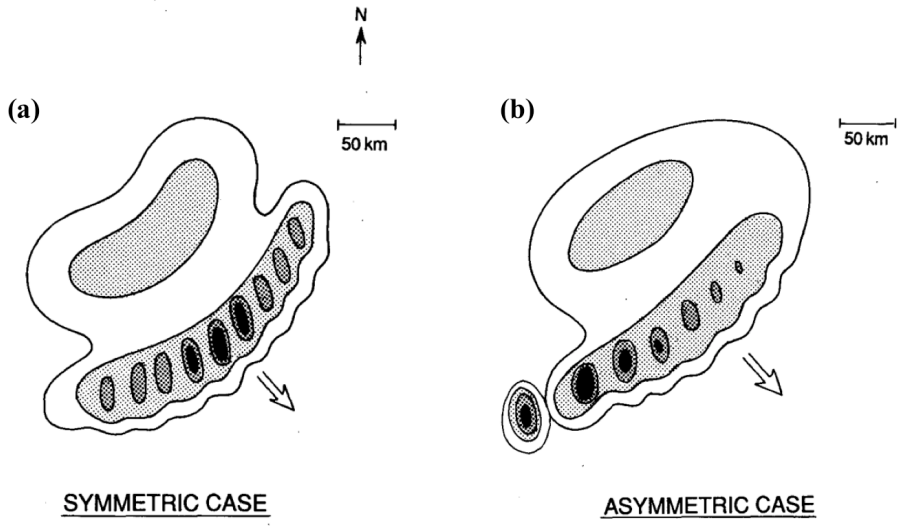

Figure 7: Depiction of (a) symmetric and (b) asymmetric leading-line, trailing-stratiform MCS archetype (from Figs. 7,8 of Houze et al. (1990)).

the lifetime of the system, the bookend vortices were hypothesized to owe their existence to vertical tilting of environmental shear vorticity as these vortex lines ascend over the surface cold pool and are subsequently tilted downward by the downdrafts near the ends of the line. The horizontal dimensions of these vortices were found to range from 10-30 km. However, the study could not confirm the exact source of the vorticity generation that becomes tilted into the vertical during the later portions of the system's lifetime. Regardless, Weisman found that these vortices were a natural consequence of the convective system having finite lateral dimensions, which was supported by the subsequent findings of Skamarock et al. (1994).

Davis and Weisman (1994), Trier et al. (1997), and Weisman and Davis (1998) further examined bookend vortices and found that the main source of vorticity for the bookend vortex formation was from the vertical tilting of baroclinically-generated vorticity along the outflow boundary as air ascended over the cold pool (Fig. 8). For strong systems characterized by strong low-level vertical wind shear,

these vortices were found near the leading edge of the system. The opposing circulations associated with the bookend vortices can also enhance and focus the RIJ circulation between them, further strengthening the system. For stronger environmental wind shear that is supportive of supercell development, embedded stronger convective cells with rotating updraft-downdraft couplets were found. These supercellular structures were favored near the ends of the lines where interference from other cells was minimized, but their existence was also possible at locations along the line. Smaller vortices associated with these cells can promote the formation of smaller-scale bowing segments with their own line-end vortices. In contrast, for environments characterized by weaker shear which is conducive to a more upshear-tilted system (Rotunno et al., 1988), the bookend vortices vortices were found farther behind the leading edge.

Other studies (e.g., Wheatley et al., 2006; Wakimoto et al., 2006) have noted the presence of smaller-scale, cyclonic-only mesovortices in single- and dual-Doppler radar observations. Some studies hypothesize that these cyclonic vortices form at the intersection of the convective system and a mesoscale boundary (e.g., Pryzbylinski et al., 2000; Schmocker et al., 2000), while others attribute the formation of the vortices and possible non-supercell tornadogenesis to system or environmental heterogeneities such as horizontal shearing instability (Miles and Howard, 1964) along the gust front (e.g., Carbone, 1982; Hobbs and Persson, 1982; Lee and Wilhelmson, 1997; Wheatley and Trapp, 2008). Wheatley and Trapp (2008) later found that circulations forming along convergence zones can be strengthened to tornadic intensity by localized vertical stretching from an updraft. Other proposed mechanisms for tornado production in QLCSs include tilting of locally-induced frictional rotors, possibly attributable to terrain inhomogeneities (Schenkman et al., 2012) and interactions of the QLCS with other surface boundaries (Pryzbylinski et al., 2000).

Another recent study by Atkins and St. Laurent (2009) used idealized simulations to examine the genesis of mesovortex formation, finding multiple types of mesovortices. Early in their simulations, bookend vortices of opposite signs developed owing to upward-tilting of baroclinically-generated vorticity along the outflow boundary, as described by Weisman and Davis (1998). These vortices were observed behind the gust front. Additionally, cyclonic-only mesovortices formed as downdraft parcels acquired horizontal vorticity as they encountered the

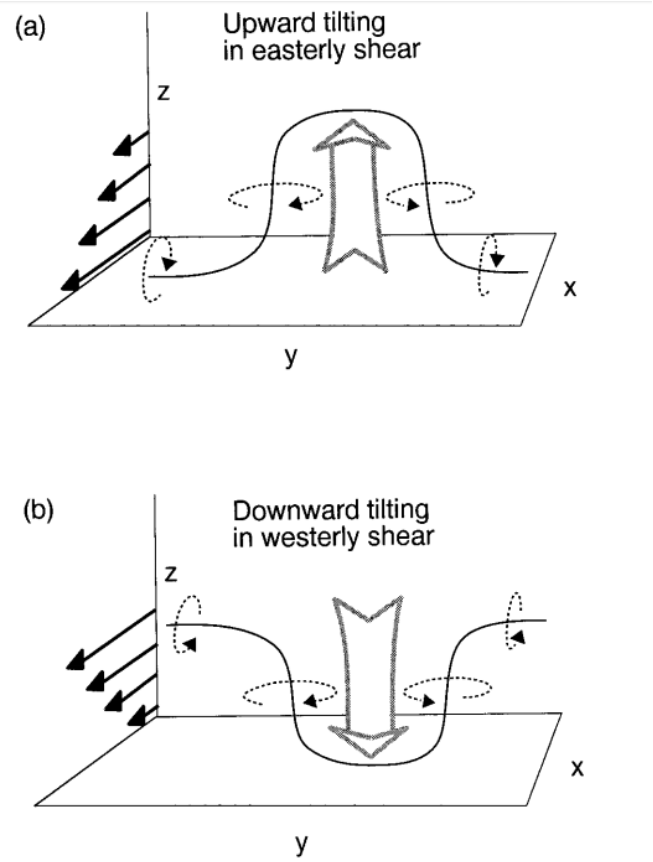

Figure 8: Depiction of vertical vorticity generation through vortex tilting. In easterly shear along the cold pool-updraft interface (a), ascent tilts vortex lines upward, resulting in cyclonic rotation to the north and anticyclonic rotation to the south. For westerly shear (b), a downdraft produces the same vertical vorticity pattern as in (a) (from Fig. 5 of Weisman and Davis (1998)).

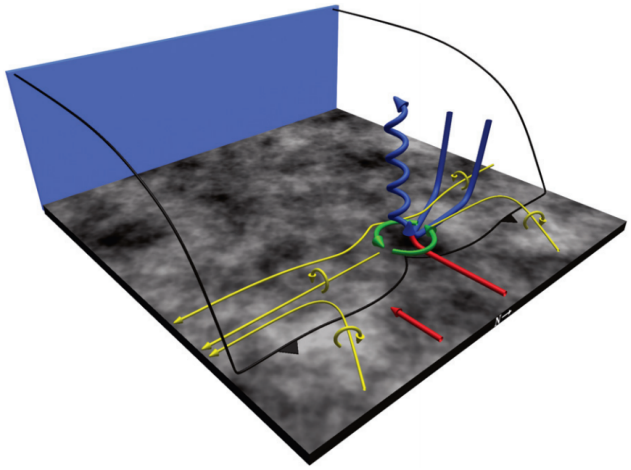

Figure 9: Conceptual schematic of the generation of a cyclonic-only mesovortex along the gust front. Depicted are vortex lines (gold), inflow and updraft (red), downdraft (blue), gust front (black), and mesovortex circulation (green) (from Fig. 15 of Atkins and St. Laurent (2009)).

solenoidal circulation across the gust front; this vorticity was subsequently tilted and stretched upward by the updraft. Parcels inside the mesovortex were found to have two separate origins: from the high θ_e inflow air and the lower θ_e downdraft air. Thus, the existence of buoyancy in the downdraft air is important for these parcels to rise into the circulation, indicating that microphysical processes (i.e., evaporation, melting, etc.) may be important in their formation. Additionally, the formation mechanisms of these cyclonic-only vortices were found to be similar to that of low-level supercell mesocyclones (e.g., Rotunno and Klemp, 1985; Davies-Jones and Brooks, 1993). Atkins and St. Laurent also concluded shearing instability was unlikely to have played a role in generating the cyclonic-only mesovortices in this particular case.

In summary, there are several complexities involved in the evolution and structure of MCSs, especially QLCSs. The system presented in this study was characterized by a QLCS structure early in its lifecycle, with embedded mesoscale

features such as bow echoes and mesovortices. These features resulted in the generation of a nocturnal tornado and the reorganization of the system. Therefore, these smaller-scale, embedded circulations are important for understanding the evolution of these convective systems.

Chapter 2

Observational Overview

The synoptic environment in which this convection formed will be discussed in section 2.1. The evolution of the system from radar and Mesonet observations will be discussed in section 2.2. Additionally, this convective system and its attendant hazards were poorly forecast by operational forecasters and numerical model guidance, which will be discussed further in section 2.3.

Figure 10: The leading edge of the convection as it moved into Norman, Oklahoma, from the perspective of the University of Oklahoma campus. The convection appears to be relatively high based, and the leading edge is laminar which is characteristic of stable ascent. Photograph taken by Derek Stratman.

2.1 Synoptic Environment

The description of this case begins with a presentation of the synoptic conditions. Previous studies have found that elevated, warm season convection is commonly observed on the poleward side of a stationary front in the presence of elevated convergence of high θ_e air from a nocturnal LLJ (e.g., Maddox, 1980; Colman, 1990a,b; Trier and Parsons, 1993; Moore et al., 2003). The system presented in this study, while occurring after the traditional warm season (i.e., April - September), also formed to the north of a synoptic-scale stationary front, which was characterized by a strong moisture gradient across central Oklahoma[1] (Fig. 11). Additionally, the analysis that follows in this section will show that a nocturnal LLJ formed after sunset, which helped to contribute to the formation of this convection.

At 0000 UTC on 6 October 2014, a synoptic-scale, mid- and upper-level trough was located over the eastern portion of the United States, which resulted in northwesterly flow over the Great Plains (Fig. 12)[2]. A weak midlevel disturbance had traversed the ridge over the western U.S. before progressing southeastward over the Great Plains (Fig. 12b). Such disturbances often condition the environment for convection via ascent and destabilization through cold air advection aloft. Moreover, these disturbances can also support the formation of a LLJ (Uccellini and Johnson, 1979; Uccellini, 1980). Weak 700-hPa westerly flow existed over the higher terrain in Colorado and New Mexico (Fig. 13a), which advected midlevel warm, dry air over the Great Plains and resulted in steep midlevel lapse rates (Fig. 14)[3]. Dry midlevel air has been found to be important for diabatic evaporative cooling and cold pool formation within convective systems (e.g., Johns and

[1]Between the Chandler and Lake Marshall Mesonet sites, the dewpoint gradient was approximately $\frac{12K}{100km}$ at 0200 UTC.

[2]Figures obtained online at `http://www.spc.noaa.gov/exper/archive/events/`

[3]For more information on the SPC Mesoanalysis, refer to `http://www.spc.noaa.gov/exper/mesoanalysis/`

Doswell III, 1992). At the surface and 850 hPa, a closed low pressure system was located in the Texas panhandle, and low-level southerly flow was present over the region, which supported low-level moisture advection off the Gulf of Mexico (Fig. 11).

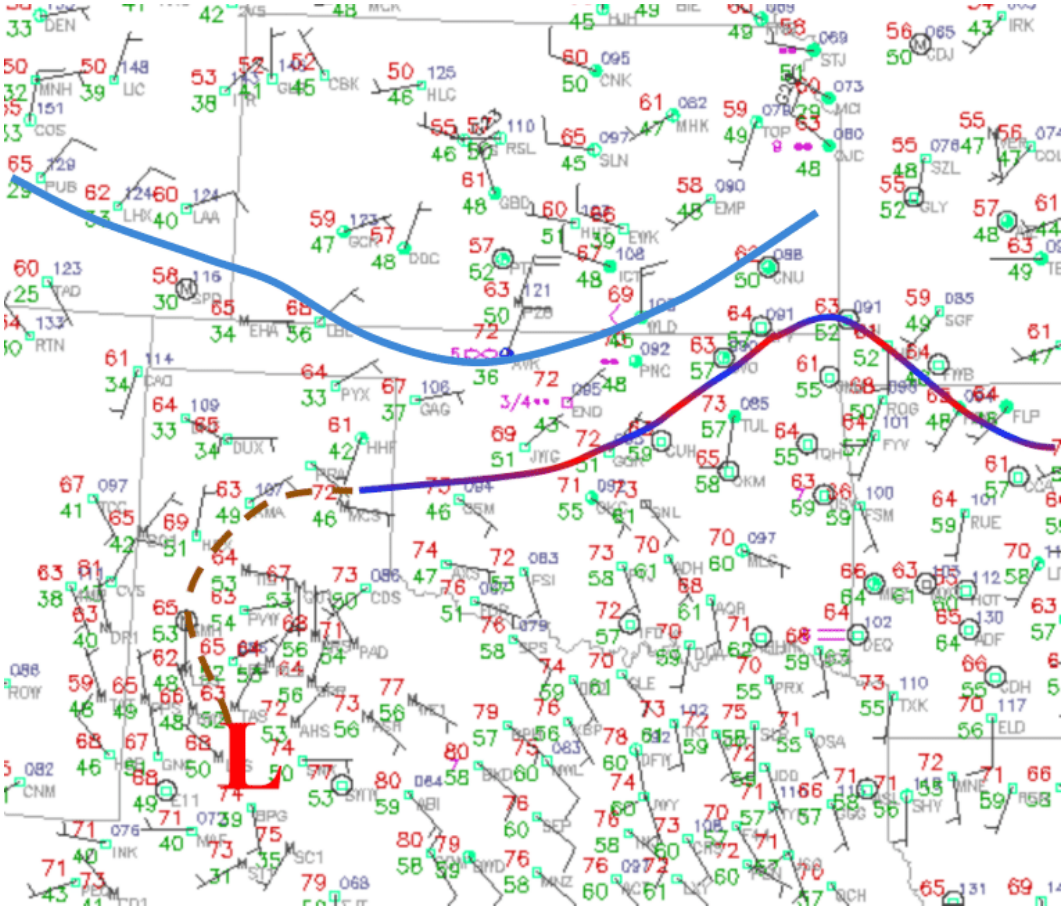

Figure 11: Surface data displayed with traditional ASOS stations at 0200 UTC on 6 October 2014. The alternating red-blue line is the approximate position of the surface quasi-stationary front, and the dashed brown line is the approximate position of the surface trough. The blue line represents the southeastward-moving weak cold front, as determined by its radar fine line. The position of the low pressure center is indicated by the red L. The boundary positions were determined subjectively.

In addition to the synoptic stationary front located throughout central Oklahoma, a weak cold front and associated stratiform precipitation was moving

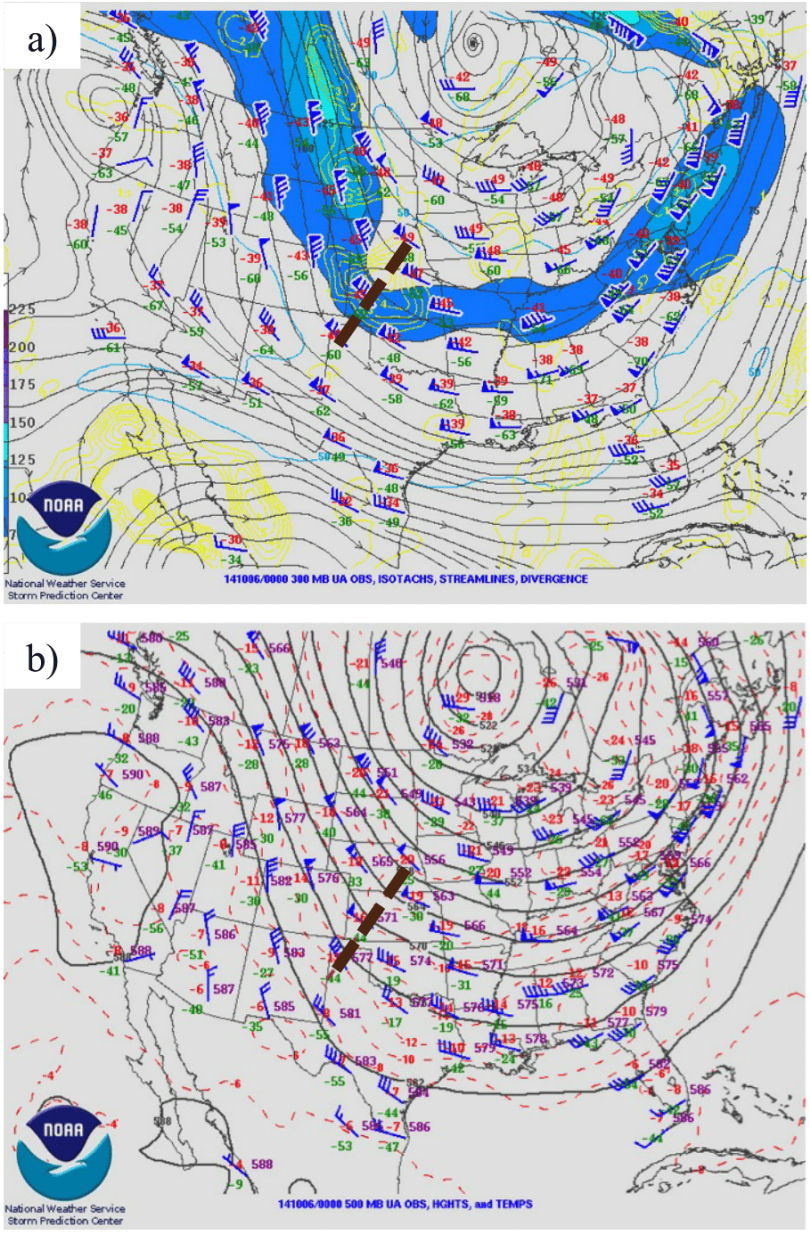

Figure 12: The observational (a) 300-hPa and (b) 500-hPa analyses valid at 0000 UTC on 6 October 2014. The brown dashed line denotes the approximate location of the disturbance that was associated with convective development. Figure was obtained from the Storm Prediction Center Event Archive.

southeastward with the progression of the midlevel disturbance (Fig. 11). This

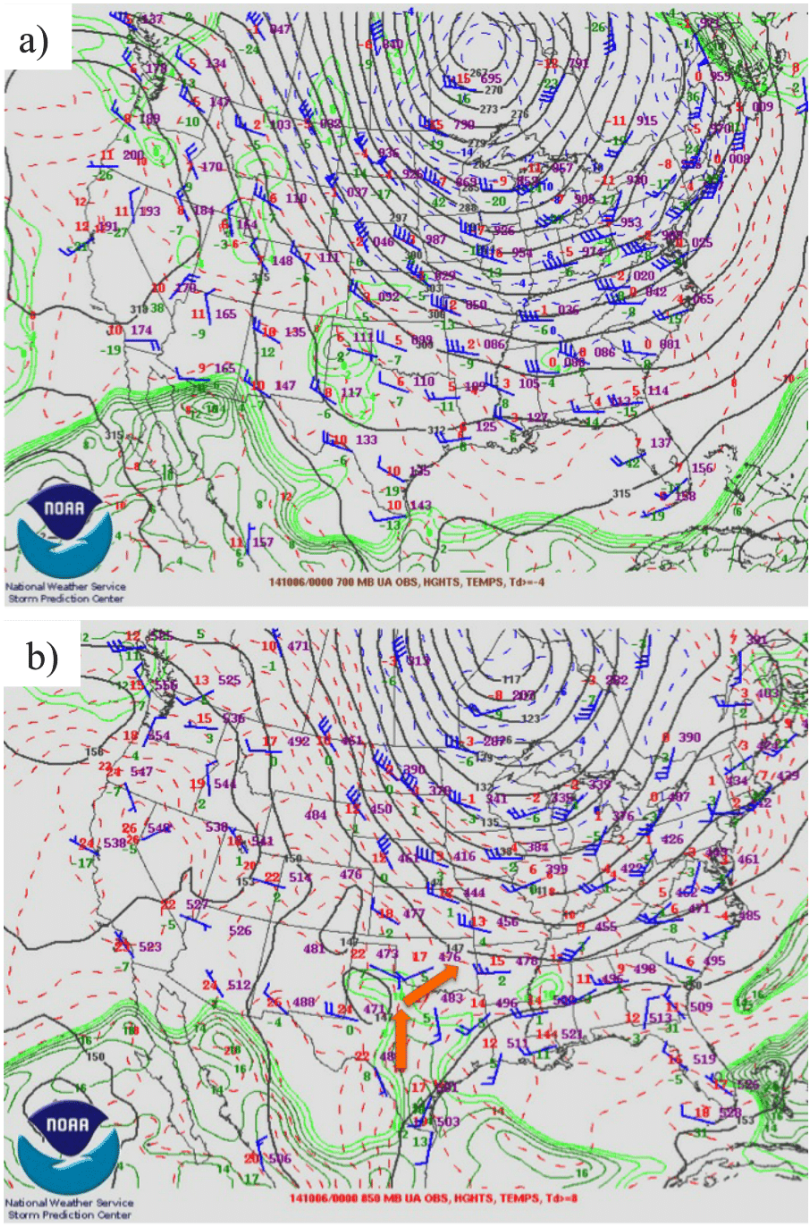

Figure 13: The observational (a) 700-hPa and (b) 850-hPa analyses valid at 0000 UTC on 6 October 2014. The orange arrows in (b) denote the orientation of the LLJ at this level. Figure was obtained from the Storm Prediction Center Event Archive.

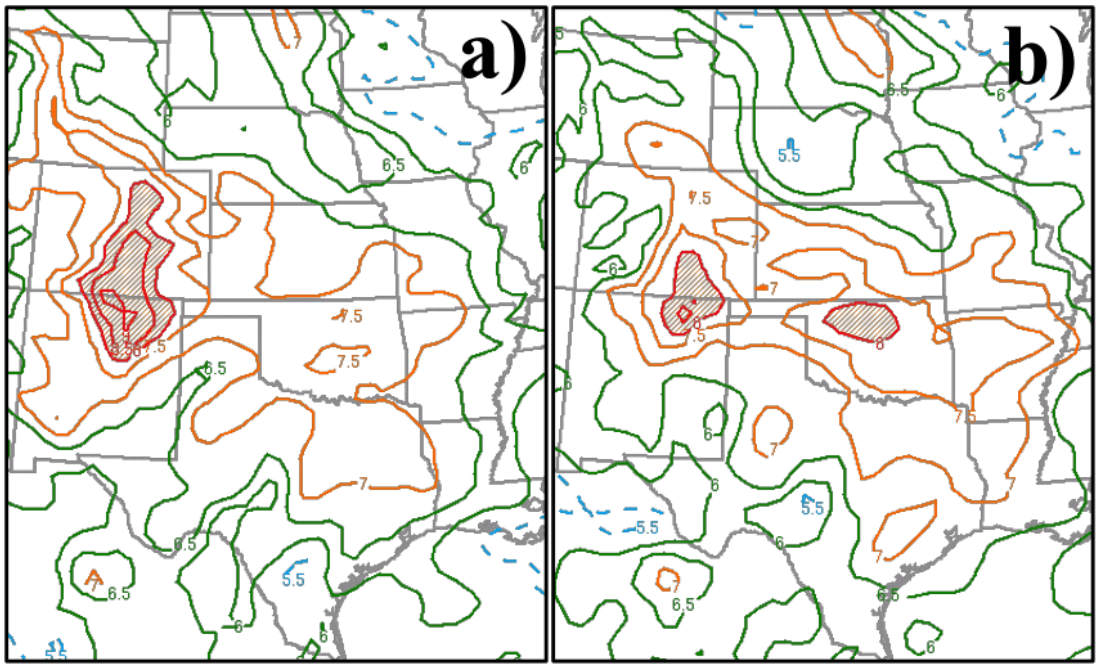

Figure 14: SPC Mesoanalysis depiction of midlevel (700-500 hPa) lapse rates for (a) 0000 UTC and (b) 0300 UTC on 6 October 2014. Between 0000 and 0300 UTC, the average lapse rate over this layer increased to greater than 8 K km^{-1}, providing a more conducive environment to convective initiation in north central Oklahoma. Figure was obtained from the Storm Prediction Center Event Archive.

weak cold front provided forcing for convective initiation throughout central Oklahoma, which will be discussed in section 2.2. The 0000 UTC upper-air sounding at Lamont, Oklahoma, which was located on the dry side of the stationary front, observed a dry environment with no surface-based CAPE[4] just two hours prior to initiation.

The 0000 UTC Norman, Oklahoma, sounding approximately 170 kilometers to the south in the higher θ_e air, depicted a more favorable, but still marginally unstable environment with surface-based CAPE and CIN[5] values of 432.9 J kg^{-1}

[4]CAPE and CIN values were calculated using absolute temperature.

[5]CIN is defined as a negative quantity representing the amount of energy needed to raise an air parcel to its level of free convection. The values listed here should be interpreted as such but

and 214 J kg^{-1}, respectively (Fig. 15b). The soundings were nearly identical above approximately 800 hPa, but the lowest 1.5 km of the Norman sounding was characterized by a layer of higher mixing ratios and a veering wind profile. Therefore, a relatively sharp gradient in low-level moisture and instability existed over central Oklahoma owing to the position of the stationary front, which was not well-represented by the conventional[6] synoptic network.

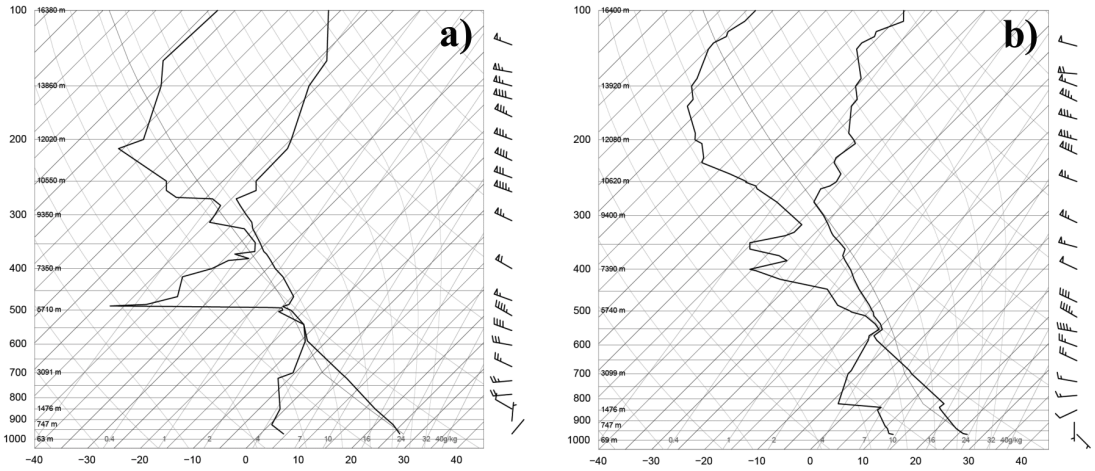

Figure 15: The observed upper air soundings at 0000 UTC on 6 October 2014 for (a) Lamont, Oklahoma, and (b) Norman, Oklahoma. Lamont was located to the north of the quasi-stationary front, and Norman was located to the south. Figures were obtained from the University of Wyoming Upper Air archive.

Once convection had developed, the environmental shear profiles were favorable for convective organization. The observed 0000 UTC Norman rawinsonde suggested that the convective environment was characterized by a 0-6 km bulk wind difference of 35-40 knots[7] (18-21 m s^{-1}), which was manifest in a unidirectional shear profile (Fig. 16). It is worth noting that the hodograph utilized data

are designated as positive in this study to be consistent with the modeling results presented in later sections.

[6]Lamont, Oklahoma, is not a traditional upper-air observing site.

[7]1 knot = 0.51 m s^{-1}

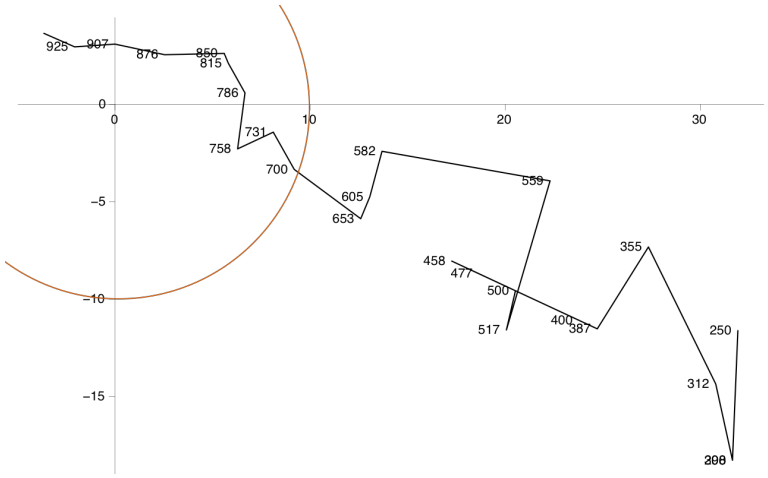

Figure 16: The observed hodograph at 0000 UTC on 6 October 2014 for Norman, Oklahoma. The zonal wind component is shown on the x axis (m s^{-1}), and the meridional wind component is shown on the y axis (m s^{-1}). The orange circle indicates wind speeds of 10 m s^{-1}. Figure was obtained from the University of Wyoming Upper Air archive.

obtained prior to the onset of the LLJ, so low-level shear would likely be enhanced over time owing to this phenomenon.

In summary, the environment observed in this case was similar to those commonly observed with elevated, nocturnal convective systems (e.g., Maddox, 1980; Colman, 1990a; Moore et al., 2003). More specifically, the presence of a midlevel disturbance and synoptic stationary front, in tandem with moisture transport and convergence from a nocturnal LLJ, have commonly been associated with favorable environments for MCS formation.

2.2 Evolution of Observed System

The observed convection initiated in two distinct clusters of cells which were associated with two separate radar fine lines (Fig. 17)[8]. The easternmost cluster developed closer to the quasi-stationary front ahead of a leading fine line (cluster and fine line positions denoted in Fig. 17), and the westernmost cluster developed on the dry side of the quasi-stationary front ahead of a primary fine line (Fig. 18). Both clusters became more invigorated with time as they moved into moist air south of the surface front (Figs. 18d-f), suggesting that the system intensity increased as they moved into a more-unstable air mass. This convection was likely initially elevated and relatively shallow, feeding from moisture ahead of the midlevel disturbance (Fig. 19g). Infrared (IR) satellite observations support the shallow nature of this convection as cloud top temperatures were relatively warm early in the lifetime of these convective clusters (Fig. 19a).

Despite initiating near each other and appearing to be part of one broken line, the two clusters remained mostly separated from each other until approximately 0500 UTC (Fig. 20b). Near this time, the westernmost supercell[9] from the eastern cluster was overtaken by the western cluster, resulting in a single broken line, which collectively moved toward the southeast (Figs. 20a,b). At approximately 0530 UTC, the eastern cluster of cells merged together, and this portion of the system began to accelerate, forming a bowing segment (Fig. 20d). A circulation associated with this bowing segment resulted in the formation of an EF-1 tornado at 0601 UTC (0001 LST; will be discussed in section 2.2.2). This bowing

[8]Radar data herein were obtained using the operational S-band (10-cm wavelength) Weather Surveillance Radar-1988 Doppler (WSR-88D; Crum and Alberty, 1993) network and were visualized using National Oceanic and Atmospheric Administration's (NOAA) Weather and Climate Toolkit, the Oklahoma Climatological Survey's WeatherScope program, and the MMM Image Archive.

[9]The westernmost supercell is denoted by the yellow arrow in Fig. 20.

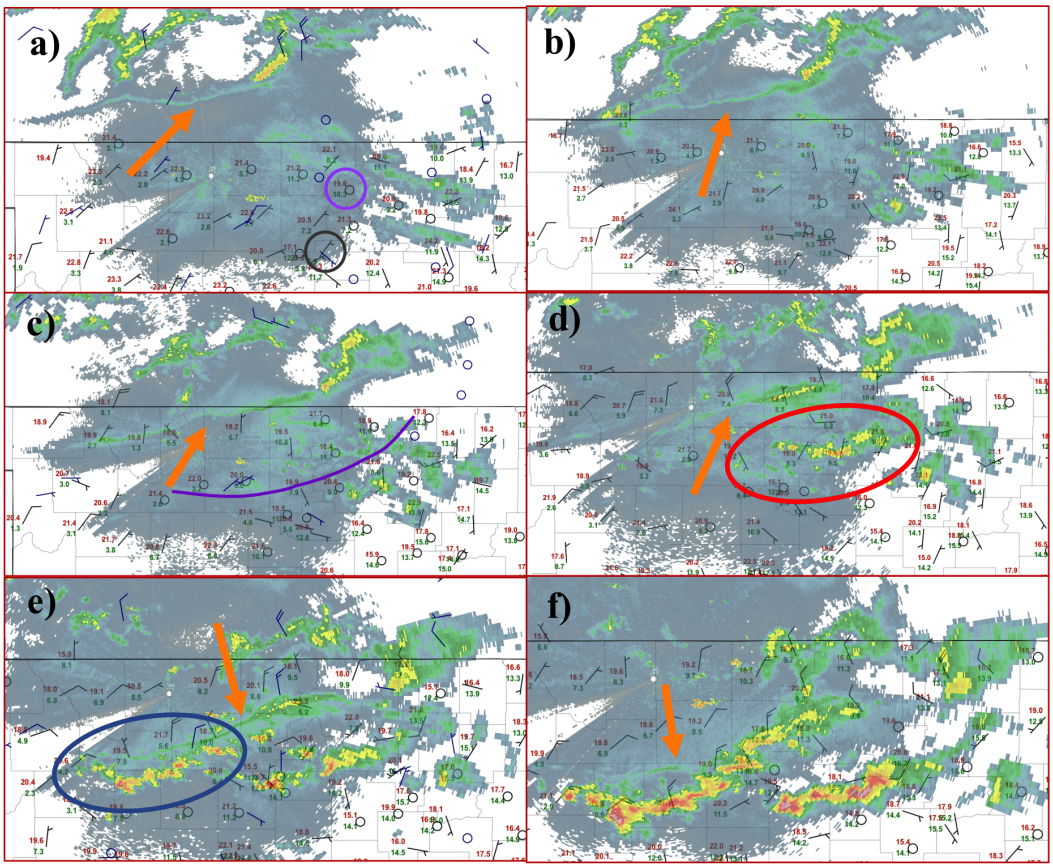

Figure 17: WeatherScope visualization of radar reflectivity (0.5° scan from Vance Air Force Base (KVNX), Oklahoma) overlaid with surface observations for (a) 0100 UTC, (b) 0130 UTC, (c) 0200 UTC, (d) 0230 UTC, (e) 0300 UTC, and (f) 0330 UTC. Oklahoma Mesonet surface data (1.5-m temperature (red; °C), 1.5-m dewpoint temperature (green; °C), and 10-m winds (black; full barb = 10 knots, half barb = 5 knot, 1 knot = 0.51 m s^{-1}) are supplemented by ASOS 10-m winds (blue; knots) at the top of the hour (i.e., in (a), (e), and (i)). The orange arrows denote the position of the primary fine line. The violet line in (f) represents the position of the leading fine line. The large red (d) and blue (e) ovals represent the easternmost and westernmost clusters, respectively. The violet and gray circles in (a) denote the Burbank and Stillwater Oklahoma Mesonet sites, respectively.

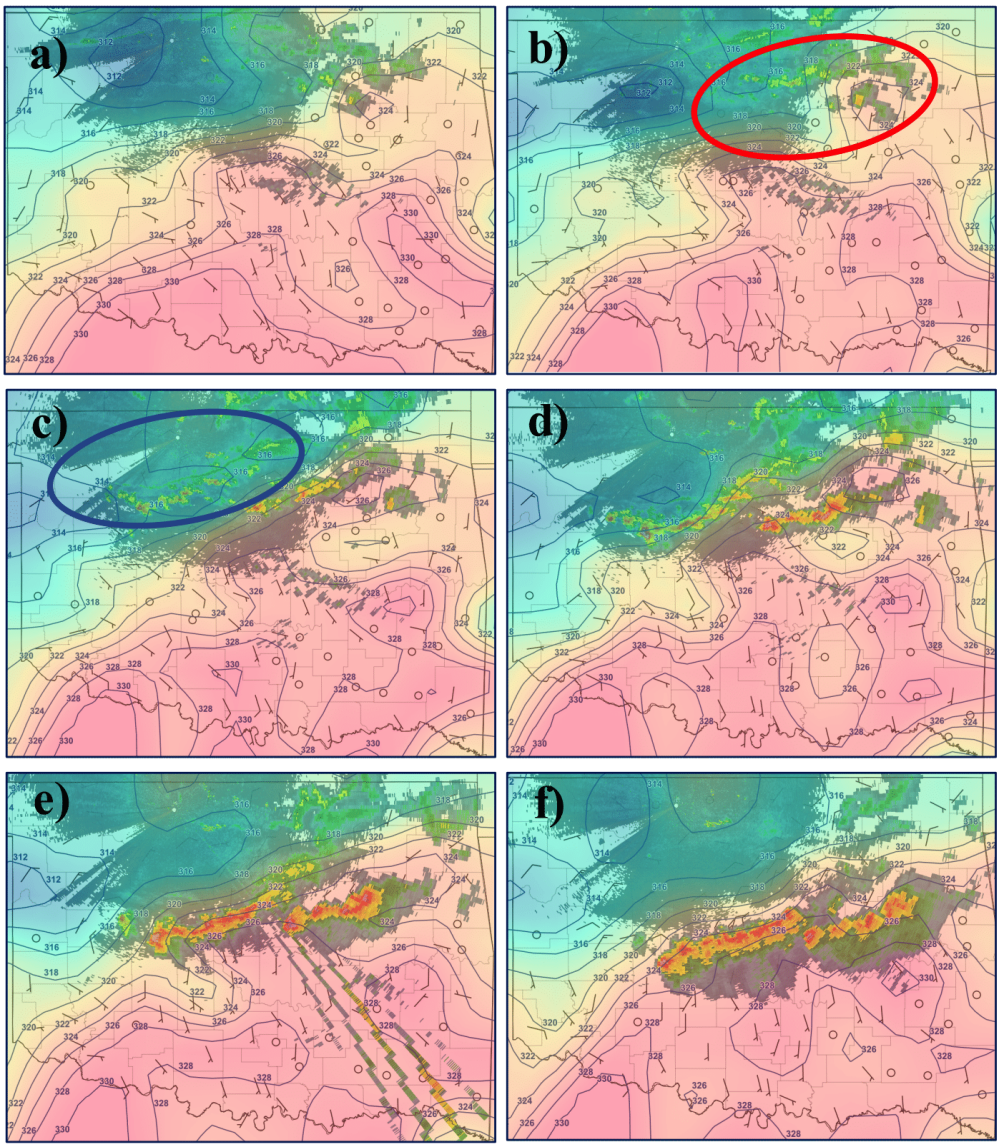

Figure 18: WeatherScope visualization of radar reflectivity (0.5° scan from Vance Air Force Base (KVNX), Oklahoma) overlaid with surface θ_e (shaded with contours every 2 K) for (a) 0200 UTC, (b) 0230 UTC, (c) 0300 UTC, (d) 0330 UTC, (e) 0400 UTC, and (f) 0430 UTC. Oklahoma Mesonet wind observations are the same as in Fig. 17. The red (b) and blue (c) ovals represent the westernmost and easternmost clusters, respectively.

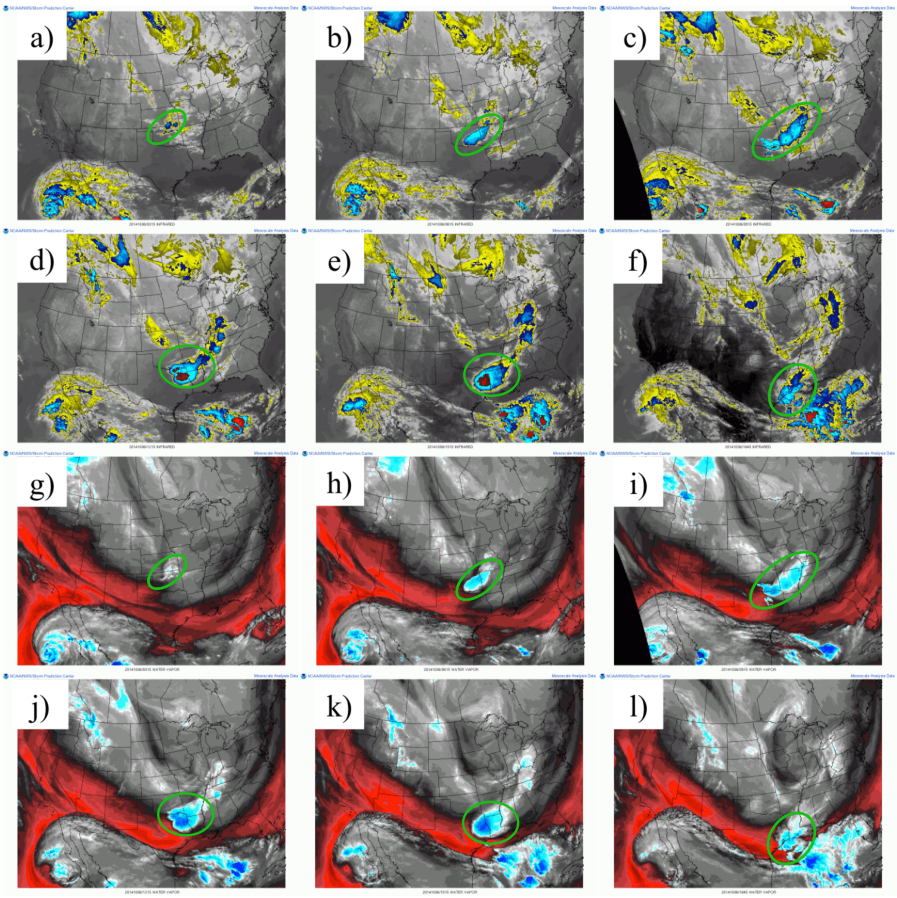

Figure 19: IR satellite imagery (top two rows) observations taken at (a) 0315 UTC, (b) 0615 UTC, (c) 0915 UTC, (d) 1215 UTC, (e) 1515 UTC, (f) 1845 UTC. The green ovals encompass the system of interest. White colors indicate warm cloud top temperatures representing low clouds which transition to yellow, blue, and red as cloud top temperatures get colder with height. The coldest cloud tops are indicated by bright red colors, representing the strongest convective regions. Water vapor satellite imagery (bottom two rows) observations taken at (g) 0315 UTC, (h) 0615 UTC, (i) 0915 UTC, (j) 1215 UTC, (k) 1515 UTC, (l) 1845 UTC. Blue colors indicate high column water vapor content (i.e., moist air), and red colors indicate low column water vapor content (i.e., dry air). Images were not available for 1815 UTC.

segment accelerated toward the east owing to the descending RIJ and downward momentum transport, whereas the rest of the ongoing convection continued to move southeastward (Figs. 20f-i).

As the system continued to progress southeastward near 0700 UTC, back-building convection began to develop along the far western flank of the broken line into central Oklahoma (Fig. 21a; e.g., Schumacher and Johnson, 2005; Peters and Schumacher, 2015). These back-building cells and the western portion of the broken line continued toward the southeast, breaking away from the rest of the convection which continued eastward with the progression of the midlevel disturbance. Therefore, the original broken line had split into two segments, one

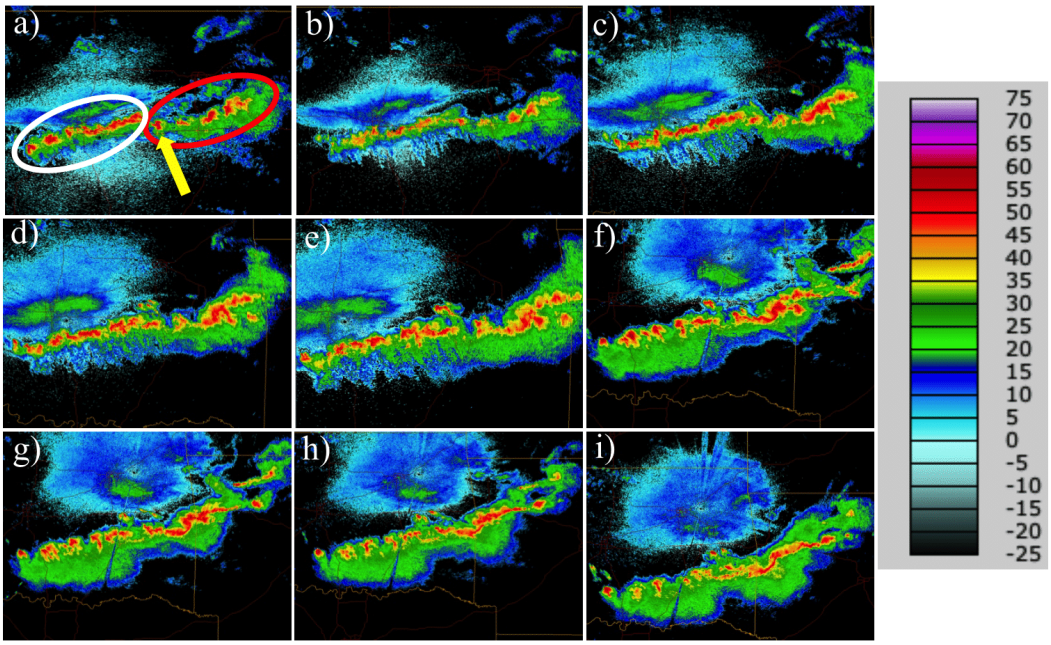

Figure 20: Radar reflectivity factor (dBZ) from Twin Lakes, Oklahoma (KTLX), for (a) 0444 UTC, (b) 0501 UTC, (c) 0517 UTC, (d) 0533 UTC, (e) 0544 UTC, and from Tulsa, Oklahoma (KINX), for (f) 0559 UTC, (g) 0614 UTC, (h) 0628 UTC, and (i) 0648 UTC. The westernmost and easternmost clusters are denoted by the white and red ovals in (a), respectively. The westernmost supercell of the eastern cluster in shown by the yellow arrow.

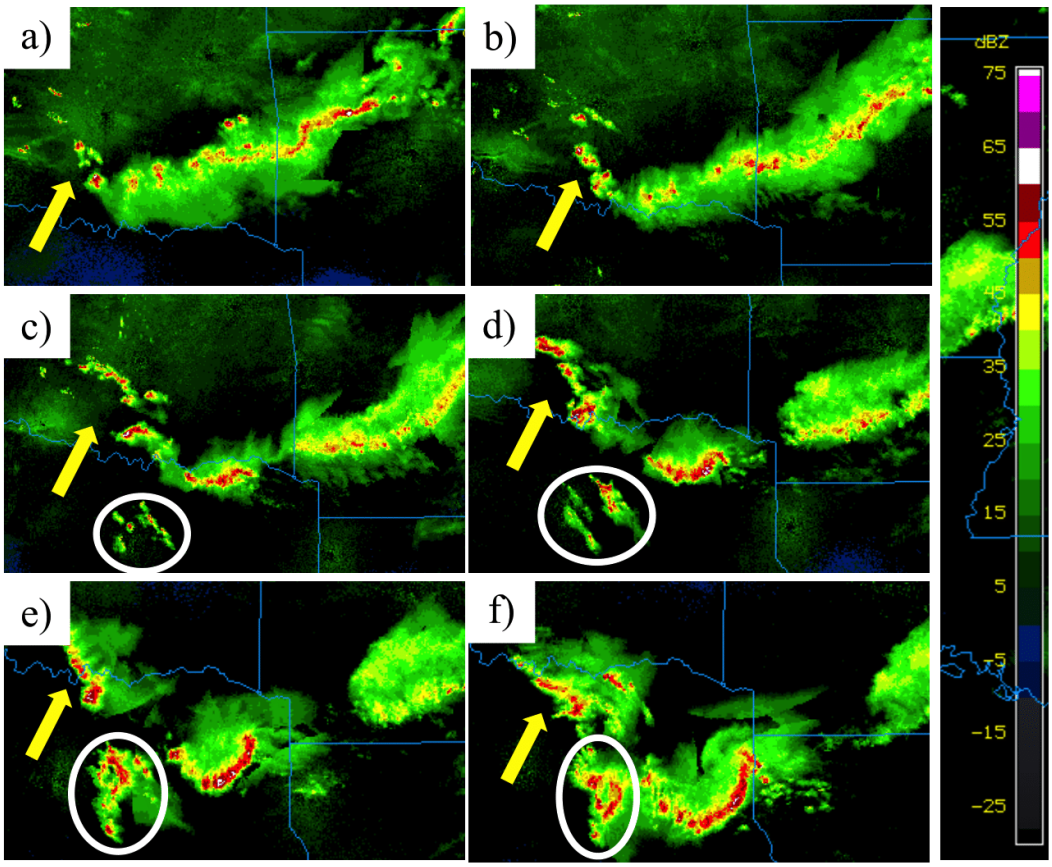

Figure 21: MMM Image Archive radar reflectivity composite (dBZ) for (a) 0655 UTC, (b) 0755 UTC, (c) 0855 UTC, (d) 0955 UTC, (e) 1055 UTC, and (f) 1155 UTC. The yellow arrows point toward the back-building convection, and the white circles denote the secondary cluster of convection in central Texas that merges with the primary MCS.

of which remained linked to the motion of the synoptic forcing, while the other moved southward.

The western line split weakened by 0800 UTC (Fig. 21b), which corresponded to a void in Storm Reports (will be discussed in section 2.3). Between 0800 and 0900 UTC, this weak portion of the system began to reorganize into a leading-line, trailing-stratiform MCS (e.g., Houze et al., 1989), accelerating south-southeastward (Figs. 21c). Water vapor imagery shows that the system began interacting with

the drier midlevel air by 0915 UTC (Fig. 19i), which was attributable to subsidence to the rear of the southeastward-moving midlevel disturbance. The presence of this dry midlevel air in proximity the convective system likely helped to enhance evaporative cooling and convective downdrafts (e.g., Johns and Doswell III, 1992), aiding in the system reorganization and acceleration. By 1000 UTC, the MCS had developed a well-defined trailing stratiform region, and the back-building cells had maintained themselves in clusters moving toward the southeast. Additionally, a cluster of convective cells had begun to form near 0730 UTC in central Texas, which moved eastward and eventually merged with the western flank of the MCS by 1200 UTC (Fig. 21f). This cluster had embedded rotating cells which produced severe hail (not shown), and these cells eventually grew upscale into bowing segment with the appearance of a bookend vortex along its northern flank in the radar composite (Figs. 21e,f). The merging of this convective cluster and the primary convective system resulted in a large, bowing MCS.

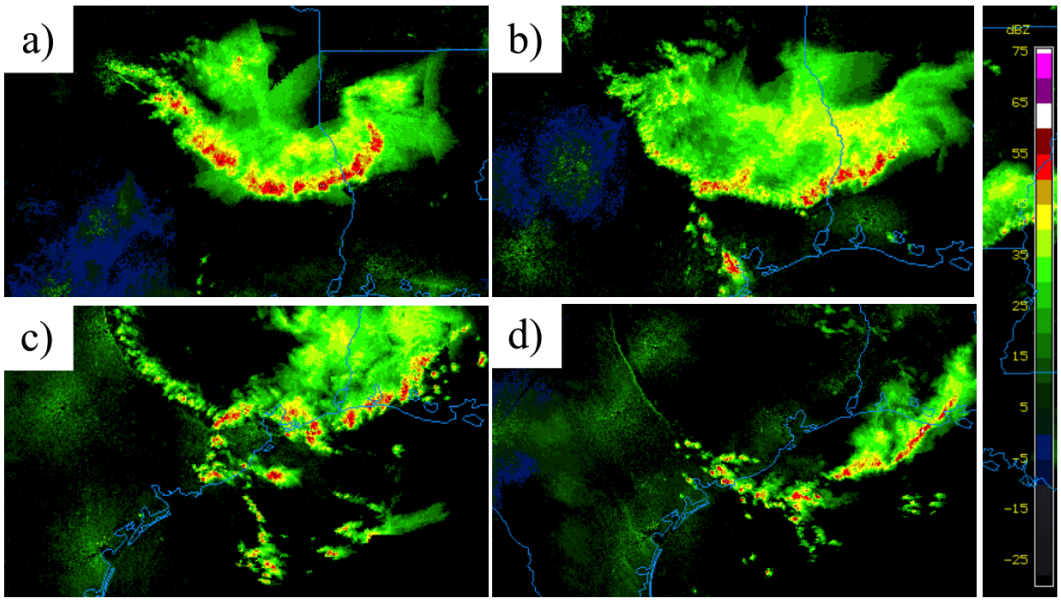

Figure 22: MMM Image Archive radar reflectivity composite (dBZ) for (a) 1355 UTC, (b) 1555 UTC, (c) 1755 UTC, and (d) 1955 UTC.

After 1000 UTC, the primary system began to transition into an asymmetric MCS (Houze et al., 1990), and a portion of the system began accelerating toward the southeast (Figs. 21d-f). This led to the development of a more north-south oriented line and resulted in the formation of a bookend vortex, which eventually grew upscale into a larger-scale MCV along the northeastern flank of the system (Fig. 21f). The former back-building cell clusters weakened and merged with the trailing stratiform region over time. Meanwhile, continual cell development occurred along the western flank of the large MCS throughout the morning, which was an environment characterized by ~1200 J kg^{-1} of surface-based CAPE and <100 J kg^{-1} of SBCIN (per 1200 UTC Dallas sounding; not shown). Based on the cloud top temperatures (Figs. 19c-e), which decreased throughout the duration of the system, the coldest temperatures existed between 1100 and 1500 UTC, suggesting that the updrafts had strengthened prior to sunrise.

After sunrise (i.e., at approximately 1220 UTC for Dallas, Texas), the system horizontally expanded, and by late morning (i.e., after 1400 UTC), the system cold pool was quickly moving away from the convection, especially toward the southwest (Fig. 22a). As a result, the system began weakening first along this flank and progressively more so toward the east with time. By 1600 UTC, the system was mostly characterized by the residual stratiform region with some weak embedded convective elements (Figs. 22b). Despite this, one fatality was reported from a downed tree in the Houston metropolitan area at approximately 1645 UTC. Additionally during this time, strong convection moved inland off the Gulf of Mexico and collided with the MCS, perhaps contributing to these severe winds. The MCS continued to move offshore until approximately 2100 UTC, when it had primarily left the range of the coastal radars (Fig. 22c).

2.2.1 Boundaries and the Initiation of Convection

Details about the boundaries responsible for the convective initiation are discussed in this section. At 0100 UTC, the primary fine line was located in south central Kansas, and winds in north central Oklahoma were light and variable (Fig. 17a). As the primary fine line passed over Oklahoma Mesonet sites at approximately 0200 UTC, the observations immediately following its passage were characterized by a wind shift to northerly or northwesterly with an increase in wind speeds of 15-20 knots (8-10 m s^{-1}). Additionally, a wind shift to northwesterly preceded the passage of the primary fine line at several stations (Fig. 17c). Several sites in north central Oklahoma observed surface warming coincident the passage of this boundary, warranting further investigation into its identity.

Fortunately, this primary fine line passed over the collection of remote sensing instrumentation at the Department of Energy's ARM Central Facility located in Lamont, Oklahoma (Stokes and Schwartz, 1994). The most useful observations were collected by a Raman lidar on-site, which measures the water vapor mixing ratio in the lower to middle atmosphere (e.g., Turner et al., 2016). Lidar measurements over a 24 h period are depicted in Fig. 23, providing insight into the diurnal cycle of PBL moisture concentrations. The daytime growth of the PBL can be inferred by the increasing depth of higher mixing ratios after 1600 UTC. After 0000 UTC, the low-level moisture concentrations begin to increase, indicating the stabilization of the boundary layer and cessation of deep (~2.5-3 km) turbulent mixing.

At approximately 0230 UTC, the primary fine line passed over the Raman lidar. Although data were missing during this period, a substantial increase in low-level mixing ratios (~2 g kg^{-1}) had occurred by 0300 UTC (Fig. 23). By 0400 UTC, moistening was apparent in the lowest ~0.5-1 km, which was likely attributed to both the stabilization of the PBL and moisture advection behind the

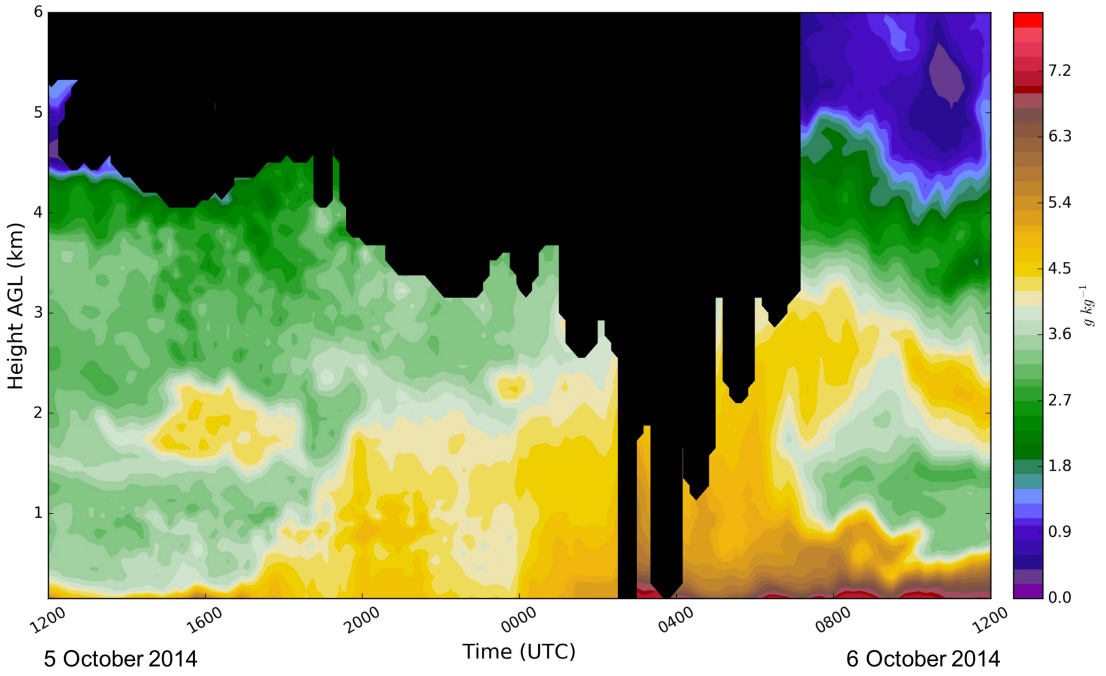

Figure 23: Time series of water vapor concentrations with height from a Raman lidar located at the Department of Energy ARM research Central Facility in Lamont, Oklahoma. Water vapor mixing ratio (g kg^{-1}) is shaded, with warm colors indicating higher concentrations. Black areas are regions of missing data owing to cloud cover contamination. The times are listed on the x-axis, beginning at 1200 UTC on 5 October 2014 (left) and ending at 1200 UTC on 6 October 2014 (right). Figure courtesy of Dylan Reif.

primary fine line. As a result of this low-level moistening, the profile in the lowest ~2 km near the area of initiation had likely become more conducive to convective development as one would infer from the low CAPE measured by the 0000 UTC Lamont sounding. The Raman lidar data (Fig. 23) also indicated the presence of clouds and precipitation associated with this moistening.

In addition to the moistening and wind shift observed with the primary fine line, a surface wind shift was also observed with the passage of the leading fine

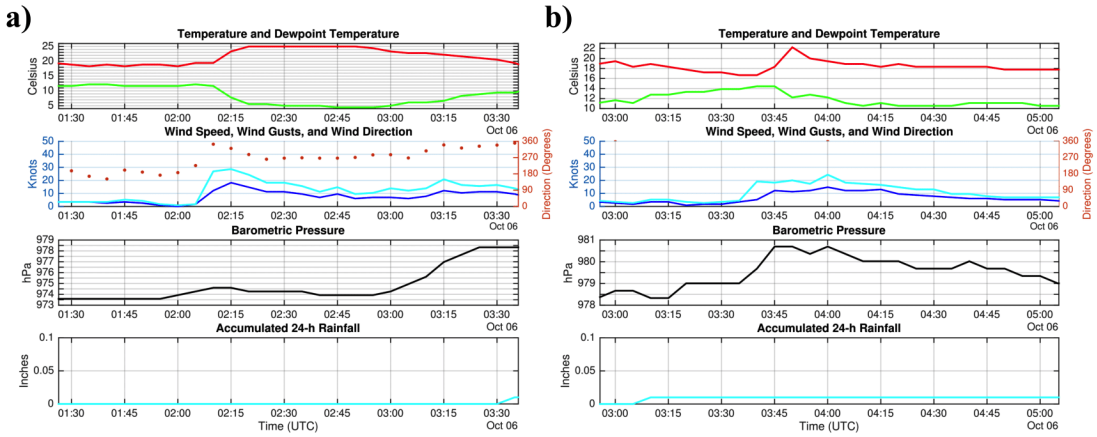

Figure 24: Meteograms using 5-min Oklahoma Mesonet observations from 6 October 2014 valid for (a) 0130 UTC - 0330 UTC at Burbank, Oklahoma, and (b) 0300 UTC - 0500 UTC at Stillwater, Oklahoma. The individual meteogram panels are: (top) temperature (red; °C) and dewpoint temperature (green; °C); (second from top) wind speed (blue; knots, 1 knot = 0.51 m s^{-1}), wind gusts (cyan; knots), and wind direction (orange; degrees); (second from bottom) altimeter pressure (black; hPa); (bottom) accumulated 24-h rainfall (cyan; inches). Mesonet locations are denoted on Fig. 17a. Note the differences in value ranges between the different panels.

line (Fig. 17). Meteograms were plotted using 5-min Oklahoma Mesonet[10] for two sites (Burbank and Stillwater; locations depicted in Fig. 17) that observed the passage of both boundaries in order to better understand the characteristics of each fine line (Fig. 24). With the passage of the leading fine line, the Mesonet site at Burbank, Oklahoma, observed a sudden wind shift and increase in speeds from nearly calm to 30 knots (15 m s^{-1}), which was coincident with a subtle pressure

[10]Data were obtained from the Oklahoma Climatological Survey. The obtained fields include altimeter pressure, 1.5-m air temperature, 1.5-m dewpoint temperature, 1.5-m relative humidity, 10-m wind direction, 10-m wind speed, 10-m maximum wind gust, accumulated precipitation, and incoming solar radiation.

rise of approximately 1.5 hPa. Significant warming and drying occurred simultaneously with this wind shift. Approximately 1 h after the passage of the leading fine line, the primary fine line passed over this site, which was characterized by a steep increase in pressure and subtle cooling (Fig. 24a). Similar characteristics were observed for the leading fine line passage at the Stillwater site (Fig. 24b). However, the passage of the primary fine line resulted in a more prominent signature at Stillwater, which consisted of a sharp increase in pressure and temperature coincident with drying. While the wind speeds increased with the passage of the primary fine line at both sites, the response in the winds was less pronounced at Stillwater.

The tendencies observed at the Mesonet locations were similar between both the passages of the leading and primary fine lines, with the effects of the primary fine line being more pronounced. The pressure rise and slight surface warming[11] were consistent with recent observations of bores over this region (Haghi et al., 2017). However, other explanations are possible for the identity of these boundaries, and the observed pressure tendency after the passage of the primary fine line has been commonly observed with passages of both cold fronts and bores (e.g., Koch et al., 1991; Marsham et al., 2011; Trier et al., 2011; Bluestein et al., 2017). For example, Nallapareddy et al. (2011) documented nocturnal warming events associated with cold frontal passages using the Oklahoma Mesonet and attributed these warming events to downward mixing of warmer air from above the stable layer by gusty winds. They found that nocturnal warming events are commonly observed in Oklahoma, with over 91% of examined cold fronts producing a warming event at one or more Mesonet stations during a 6-year period.

[11]The warming frequently associated with the passage of bores is attributed to the downward mixing of potentially warmer air from above the stable boundary layer.

Because a near-surface inversion had developed by the time the boundaries moved through the region, we cannot determine from solely the surface observations and water vapor profiles whether or not the surface signatures observed were primarily attributed to the cold frontal passage or to a bore induced from the intrusion of the cold front into the stable layer. This determination is complicated by the variety of possible bore structures, such as the incorporation of density current air into a bore (White and Helfrich, 2012). However, two subsequent fine lines, which have distinct surface signatures, are not expected to be associated with one cold front. Therefore, one possibility is that the former weak cold front, in tandem with weak precipitation echoes in a dry environment, may have triggered the formation of one or more bore responses, resulting in a lifting of the stable layer and destabilization of the environment. This finding was at least plausible for the existence of the leading fine line, which was associated with more subtle pressure response and existed ahead of the primary fine line. However, the identity of the primary fine line was more ambiguous based on the available data. Regardless of the identity of these boundaries, their role in the stable, nocturnal environment was important for the initiation of initially-elevated convection in north central Oklahoma, which has been observed in previous studies (e.g., Locatelli et al., 2002; Wilson and Roberts, 2006).

2.2.2 Nocturnal Tornado

Based on the 0000 UTC hodograph from the Norman sounding (Fig. 16), which was characterized by a fairly unidirectional shear vector with height, upscale development of convection into a linear mode was anticipated owing to cell-to-cell interactions and new cell development along the downshear flank of the cold pool (e.g., Thompson et al., 2012). Further, sufficient deep-layer shear of ~35-40 knots

(18-20 m s^{-1}) would support possible embedded rotating updrafts and supercellular structures in the more discrete cells. Therefore, the evolution of the convective system early in its lifetime was supported by a shear profile favoring a QLCS-type convective mode.

An EF-1 tornado formed at approximately 0601 UTC (0001 LST) from an intensifying vortex along the northern flank of a bowing segment characterized by a strong RIJ[12] (Figs. 25,26). The presence of a tornado requires that near-surface air be drawn into the storm and for surface vorticity (generated baroclinically in supercells and some mesovortices or by horizontal shearing instability in many mesovortex tornadoes; Lee and Wilhelmson, 1997) to be stretched and amplified (e.g., Davies-Jones et al., 2001; Trapp and Weisman, 2003). Supercells in the presence of a stable boundary layer have been shown by previous studies to ingest parcels from the near-surface layer if CAPE for this layer exists owing to the enhancement of the updrafts by the dynamically-induced upward-directed perturbation pressure gradient force (Nowotarski et al., 2011; Billings and Parker, 2012). Billings and Parker (2012) have found that forced ascent ahead of a surface cold pool is often sufficient to lift low-level stable air, resulting in partially surface-based squall lines.

The reflectivity of this portion of the system was characterized by supercell-like features, including a sickle-shape and apparent hook echo (Figs. 25,26). However, previous studies have found that mesovortex tornadoes in QLCSs are often associated with supercell-line features, such as hook-echo-like appendages (e.g., Trapp, 2013). Additionally, the radial velocity field within the period leading up to tornadogenesis indicated that the parent circulation was transient (lasting <1 h) and was strongest at low levels, lacking a well-defined midlevel mesoscyclone[13]

[12]Midlevel inbound radial velocities (not shown) on KSRX were folded throughout much of the RIJ. The Nyquist velocity was approximately 50 knots (26 m s^{-1}) in this region.

[13]Mesocyclone criteria were adopted from Trapp et al. (2005).

(Figs. 25-27). Additionally, the intensification of the vortex occurred as the RIJ strengthened and descended behind the leading edge of the convection, forming a rear-inflow notch and bow echo (Figs. 25,26; Przybylinski, 1995). Therefore, while the environment was suitable for supercell formation and supercellular structures

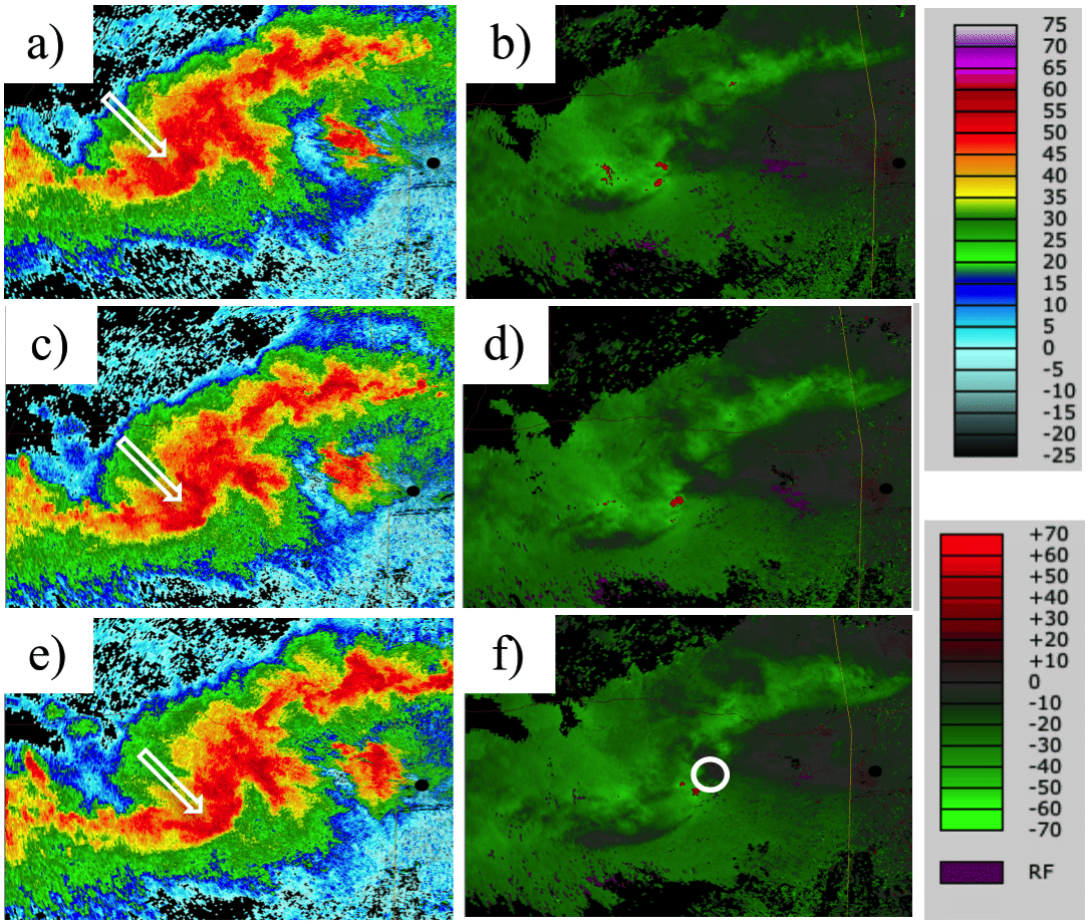

Figure 25: Radar reflectivity factor (dBZ) and radial velocity (knots; 1 knot = 0.51 m s^{-1}) of the tornadic portion of the system from Ft. Smith, Arkansas (KSRX) for (a),(b) 0542 UTC, (c),(d) 0547 UTC, and (e),(f) 0552 UTC. Velocities exceeding the Nyquist velocity are folded accordingly. The radar location is the black filled circle. The approximate location of the low-level rotation is depicted by the white circle. The white arrow represents the approximate orientation of the descending RIJ within the rear-inflow notch.

did exist in the more discrete cells, this tornado was likely generated by a low-level cyclonic mesovortex, which formed along the northern flank of the bowing segment.

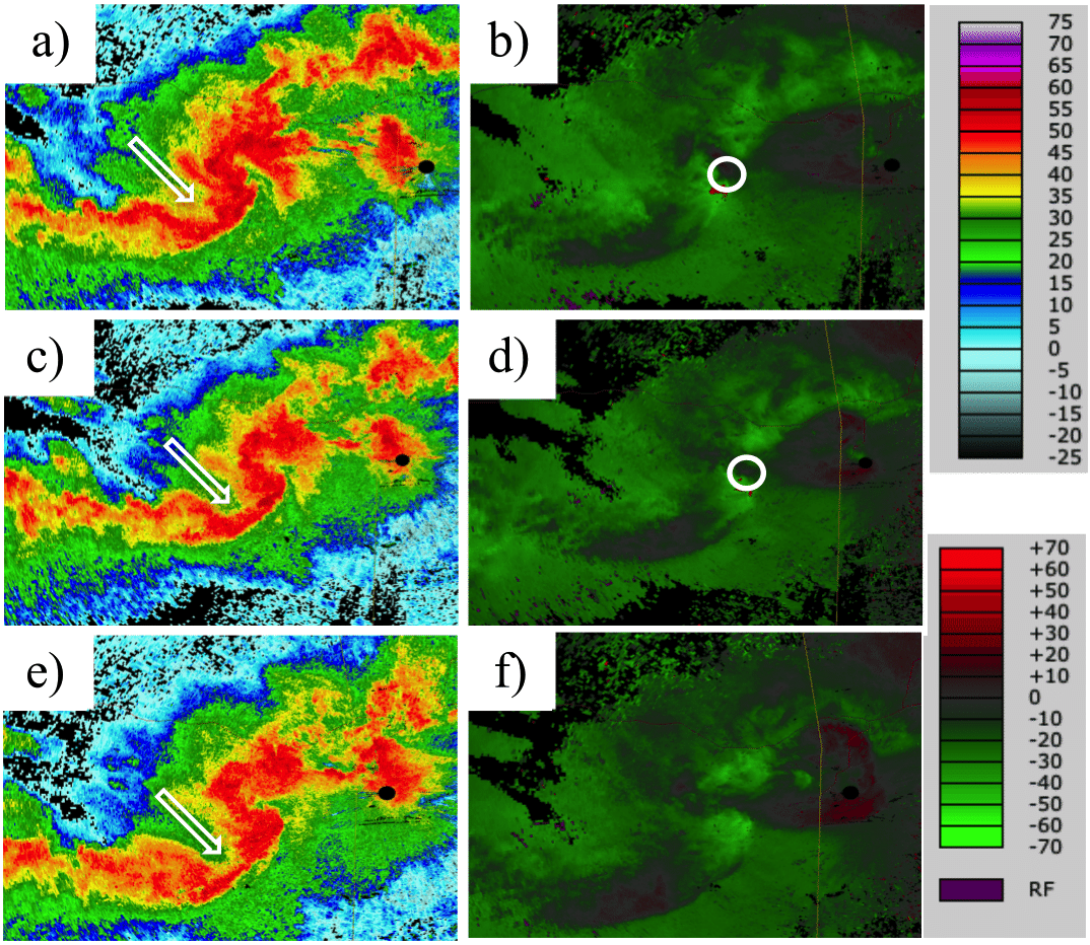

Figure 26: Same as in Fig. 25, but for (a),(b) 0558 UTC, (c),(d) 0603 UTC, and (e),(f) 0609 UTC, respectively. The tornado, rated EF-1, occurred at approximately 0601 UTC.

Because this tornado occurred in Oklahoma, 5-min observations from the Oklahoma Mesonet could be utilized to examine to inflow environment in proximity to the tornado. Four sites were examined, the locations of which are depicted in Fig.

27: Wister[14], Wilburton, Stigler, and Sallisaw, Oklahoma. Prior to the arrival of the convective system, the winds were calm and the surface dewpoint depression was minimal (Fig. 28). These observations are consistent with the presence of a stable near-surface inversion, which developed after sunset owing to radiative

[14]This Mesonet site was located 30 km to the south of the tornado and was thus the most representative of the inflow environment.

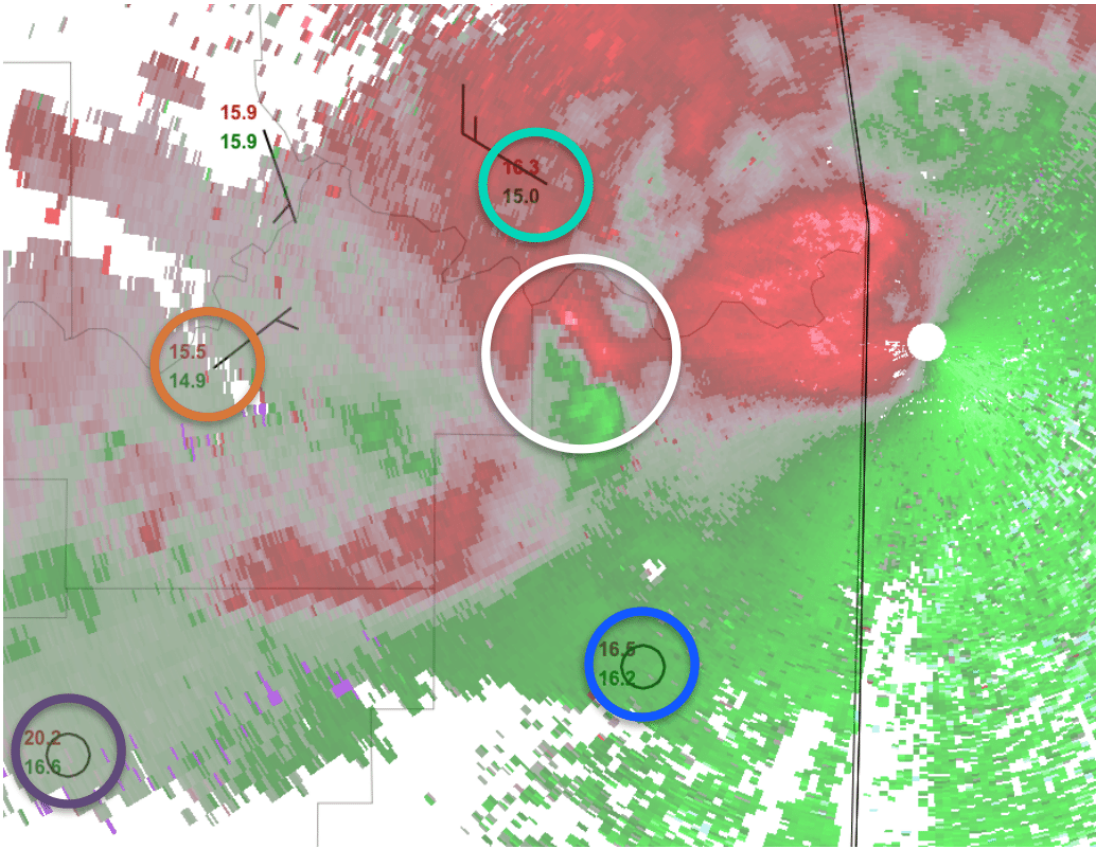

Figure 27: Storm-relative velocity from Ft. Smith, Arkansas (KSRX) at 0600 UTC (0000 LST). Green values are inbound velocities, and red values are outbound velocities. The solid white circle indicates the location of the radar, and the outlined white circle indicates the region of rotation corresponding to the brief EF-1 tornado near Spiro, OK. The blue, violet, orange, and cyan outlined circles correspond to the Wister, Wilburton, Stigler, and Sallisaw Oklahoma Mesonet sites, respectively.

cooling (Fig. 29). As the convection approached Wister, the winds increased from nearly calm to gusting to approximately 35 knots (18 m s^{-1}). This increase was coincident with a considerable rise in temperature and pressure over a 10-min interval. After the onset of precipitation, the temperature began to decrease, coincident with the passage of a surface outflow boundary.

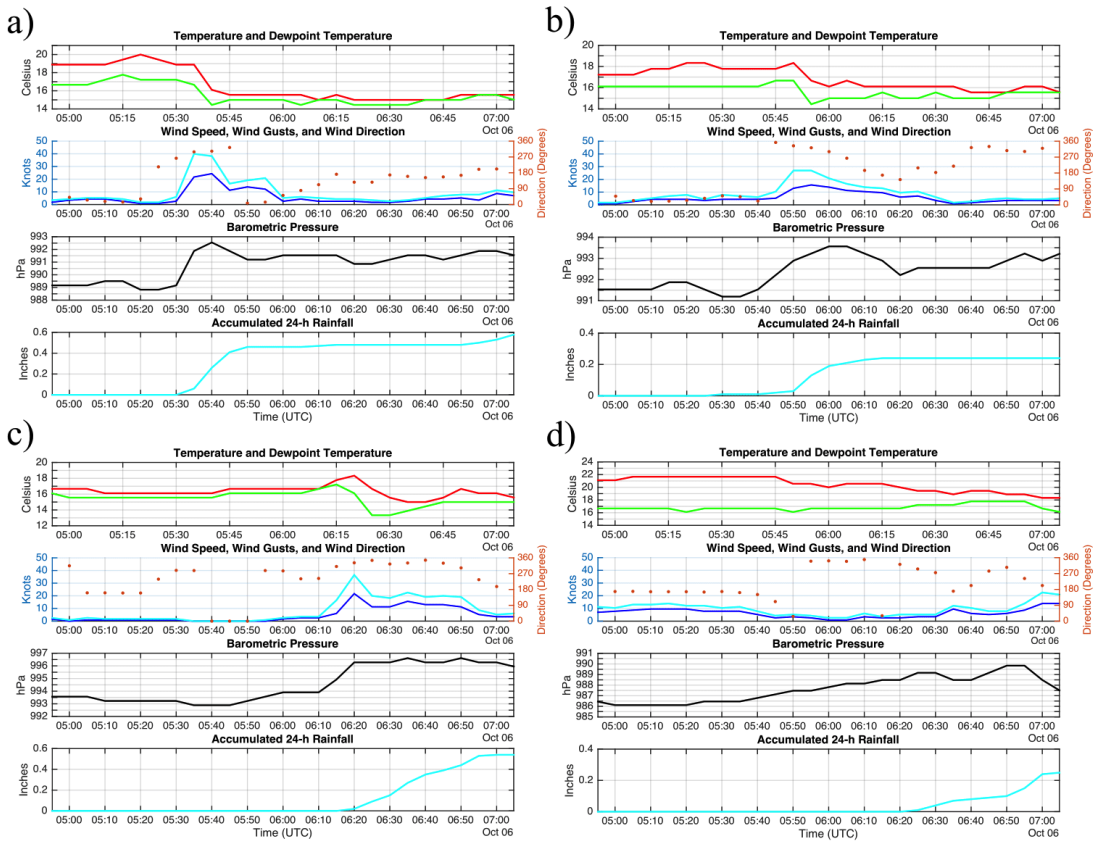

Figure 28: Meteograms using 5-min Oklahoma Mesonet observations from 0500 UTC - 0700 UTC on 6 October 2014 valid for sites in proximity to the observed tornado at 0601 UTC. The sites included are (a) Stigler, Oklahoma, (b) Sallisaw, Oklahoma, (c) Wister, Oklahoma, and (d) Wilburton, Oklahoma. The individual meteogram panels are the same as in Fig. 24. Note the differences in value ranges between the different panels.

Similar trends in the surface fields were observed at Stigler and Sallisaw, which were characterized by sharp increases in pressure and wind gusts coincident with steady or rising in temperature (Fig. 28). All three sites had nearly calm winds prior to the passage of this feature, which is favorable for the development for a nocturnal inversion. The observations taken at Wilburton were the least representative of the environment near the tornado, and a weaker portion of the convection had moved over this site. Therefore, these sharp responses in the surface fields were absent at this site, with and a gradual increase in pressure was observed. The temperature and pressure tendencies observed at Wister, Stigler,

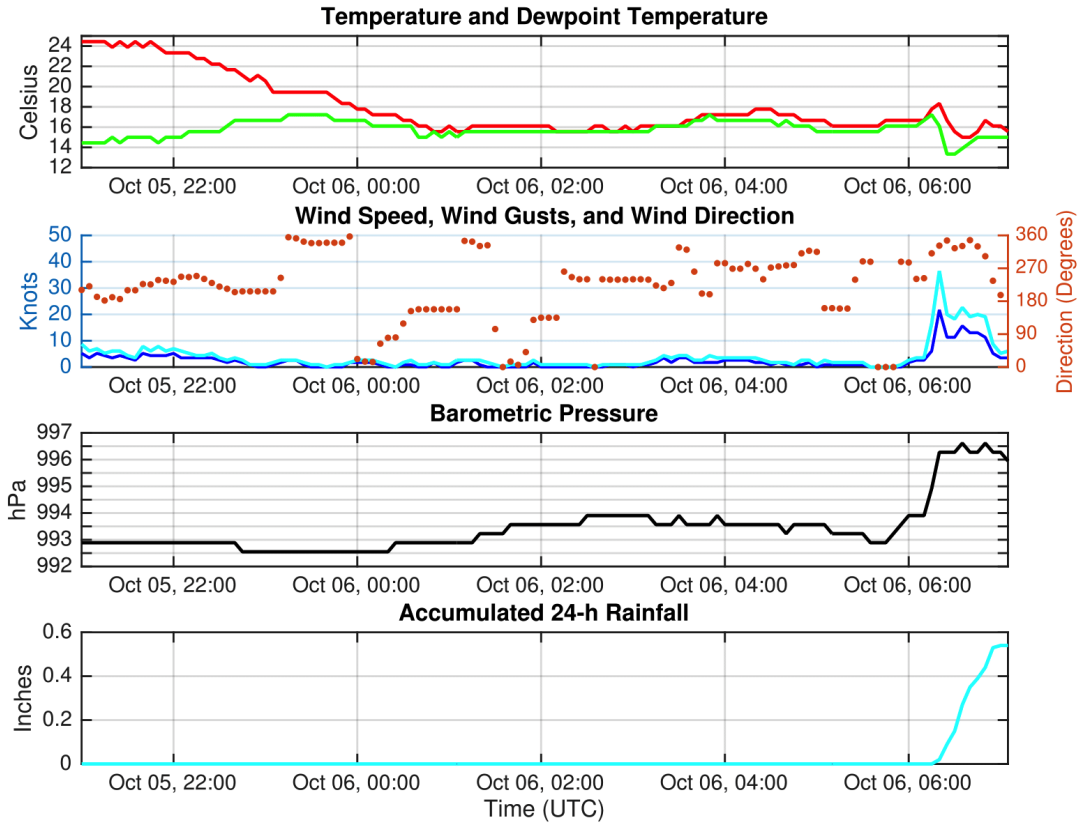

Figure 29: Meteogram showing the radiative cooling of the surface after sunset for the Wister Oklahoma Mesonet site. The individual meteogram panels are the same as in Fig. 24.

and Sallisaw were similar to those commonly associated with the passage of bores (e.g., Bluestein and Snyder, 2015; Haghi et al., 2017).

Based on these trends in the surface observations, we suspect that the existence of convection and a strong descending RIJ in a stable environment may have triggered of a bore response. This bore, which preceded the passage of the outflow boundary ~10-20 min, had resulted in turbulent mixing, which acted to increase the surface temperature and destabilize the low levels (e.g., Koch et al., 1991). While no observations were taken in close proximity to the tornado, perhaps the existence of this bore in an otherwise stable environment had resulted in a more favorable environment for the ingestion of surface parcels by diminishing the effects of this stable layer, enhancing the potential for vortex stretching and tornadogenesis. While we cannot confirm this based on a lack of observations, this is a process that should warrant investigation, especially in the presence of three-dimensional features such as bow echoes and mesovortices. To our knowledge, no studies have examined the role that bore-induced mixing has on providing a more favorable environment for nocturnal tornadogenesis.

2.3 Operational Forecasts and Storm Reports

One primary motivation for examining this convective system is that operational forecasts for this event by the NOAA's Storm Prediction Center (SPC) were somewhat poor. While the SPC anticipated the formation of convection, they failed to accurately predict the both the timing and location and also the severity of this convective event. These poor forecasts were likely in great part attributed to the poor handling of this event by numerical model guidance. Additionally, the difficulty in acquiring a representative WRF simulation using initial conditions from the North American Mesoscale (NAM), Global Forecast System (GFS), and Rapid Refresh (RAP) models for this case study would support this argument, and the

model initial conditions did not seem to accurately depict the observations over the area of interest. The longevity of the poorly-forecast convective system had unanticipated impacts from Oklahoma to the Gulf Coast and thus supports why better forecasts of long-lived events that persist into the following afternoon are needed.

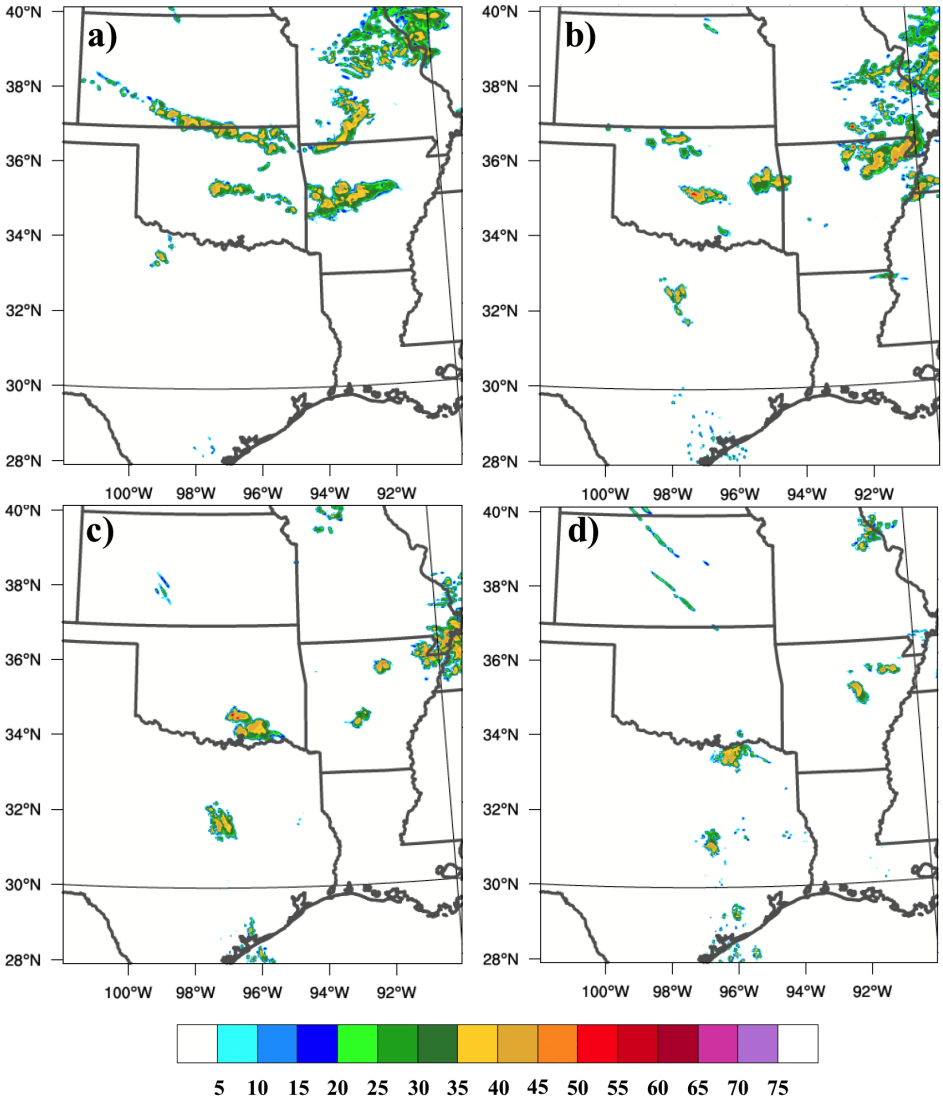

Figure 30: 13-km High-Resolution Rapid Refresh model simulated reflectivity (dBZ) valid at (a) 0600 UTC, (b) 0900 UTC, (c) 1200 UTC, and (d) 1500 UTC on 6 October 2014 for the 0000 UTC 6 October 2014 initialization.

In order to gauge how well the operational model guidance handled this event, the High-Resolution Rapid Refresh (HRRR) operational model forecasts valid every 3 h on 6 October 2014 were examined for the 0000 UTC initialization cycle. The HRRR model has a horizontal grid spacing of 3 km. The HRRR predictions and radar observations are presented for comparison in Figs. 30 and 31, respectively. The HRRR model does have convection initiating in central Oklahoma by 0300 UTC (not shown), but there are no indications of upscale growth into a long-lived convective system, as inferred from the forecasts valid at 0600, 0900, 1200, and 1500 UTC (Fig. 30). Furthermore, the lateral extent of this convection is much less than in the observations as the observed system had begun to reorganize into a well-defined MCS by 0900 UTC (Fig. 31). Thus, while the HRRR model does have convective initiation in approximately the correct location, the upscale growth and sustenance of the system are absent in the model guidance, resulting in the lack of a long-lived MCS in the model. This finding was actually contrary to the results of Pinto et al. (2015), which found that the HRRR model tended to overestimate convective initiation episodes thus MCS activity over the Great Plains during both day and night during 2012 and 2013.

While the HRRR successfully initiated convection in central Oklahoma, this convective-allowing guidance tool is only available to forecasters a few hours in advance. Therefore, longer range model guidance is utilized by forecasters which utilizes a coarser grid spacing with the employment of convective parameterization. However, meteorologists can infer favorable patterns for convection through the examination of larger-scale features farther in advance of the convective event. As a result, the possibility of convection in the southern Great Plains was noted in the Convective Outlooks[15] for several days in advance of the system. The SPC forecasters mentioned that a signal for convection, which was attributed to the

[15] All SPC Outlooks were found online at `http://www.spc.noaa.gov/exper/archive/event.php?date=20141005`

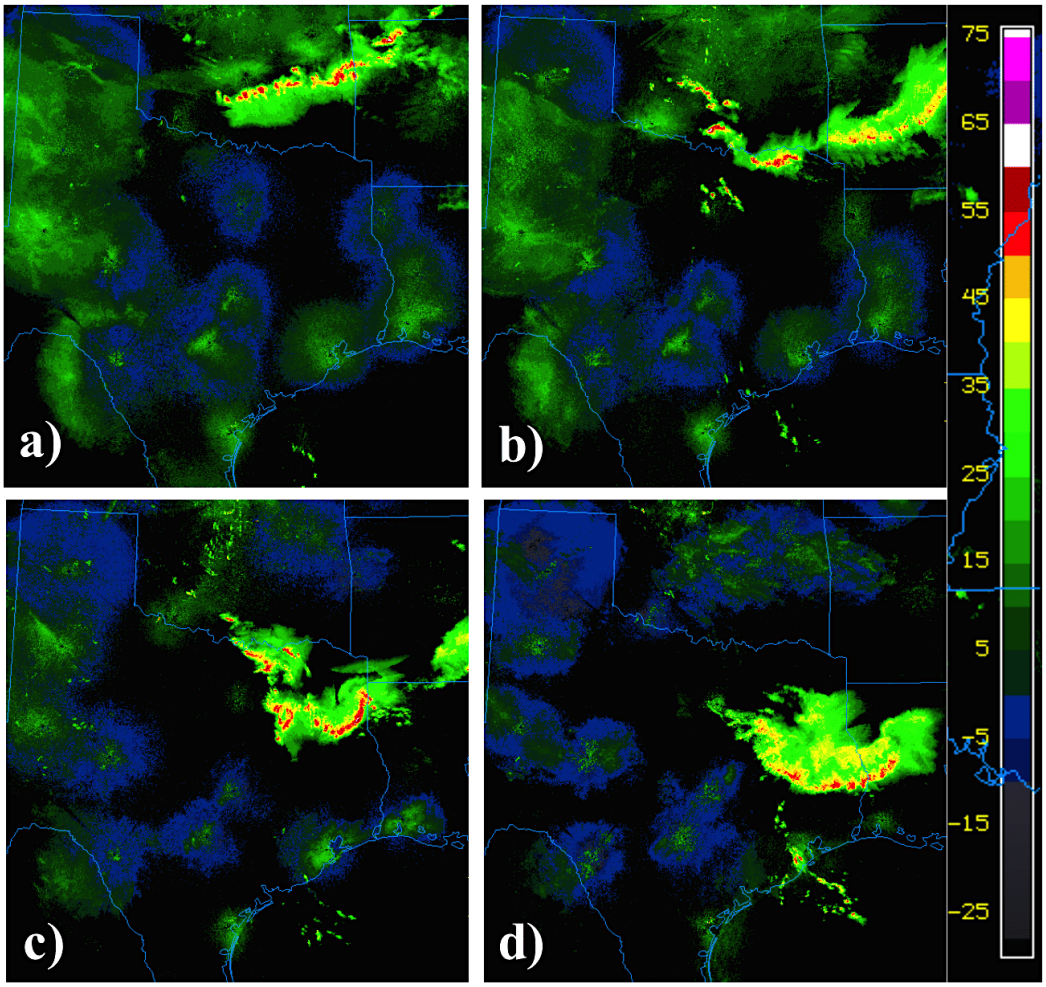

Figure 31: Composite radar reflectivity (dBZ) valid at (a) 0600 UTC, (b) 0900 UTC, (c) 1200 UTC, and (d) 1500 UTC on 6 October 2014, which corresponds with the HRRR forecasts times shown in Fig. 30.

progression of an midlevel disturbance southward over the Great Plains, existed in the coarser numerical guidance at least as far out as 4 days. Based on the environmental setup, the forecaster anticipated a focused area of elevated thunderstorms would develop with an accompanying potential for hail. However, the Day 3 Convective Outlook mentioned a less than 5% probability for severe thunderstorms within 25 miles of a location (not shown).

Closer to the event when higher resolution guidance was available, the Day 1 Outlooks began to detail the situation a bit further, upgrading the outlook to a general thunderstorm with a "SEE TEXT" accompanied by a 5% hail outlook over north central Texas into southwestern Arkansas by 0600 UTC (Figs. 33d,e). The tornado and wind threat probabilities were below the 2% and 5% thresholds, respectively (not shown). By 1300 UTC, the Convective Outlook noted that "model solutions are inconsistent on extent of convective coverage... but it appears at least a storm or two will form after midnight along an axis from north central Texas into central Arkansas". The 0100 UTC Day 1 update, issued approximately 1 h before

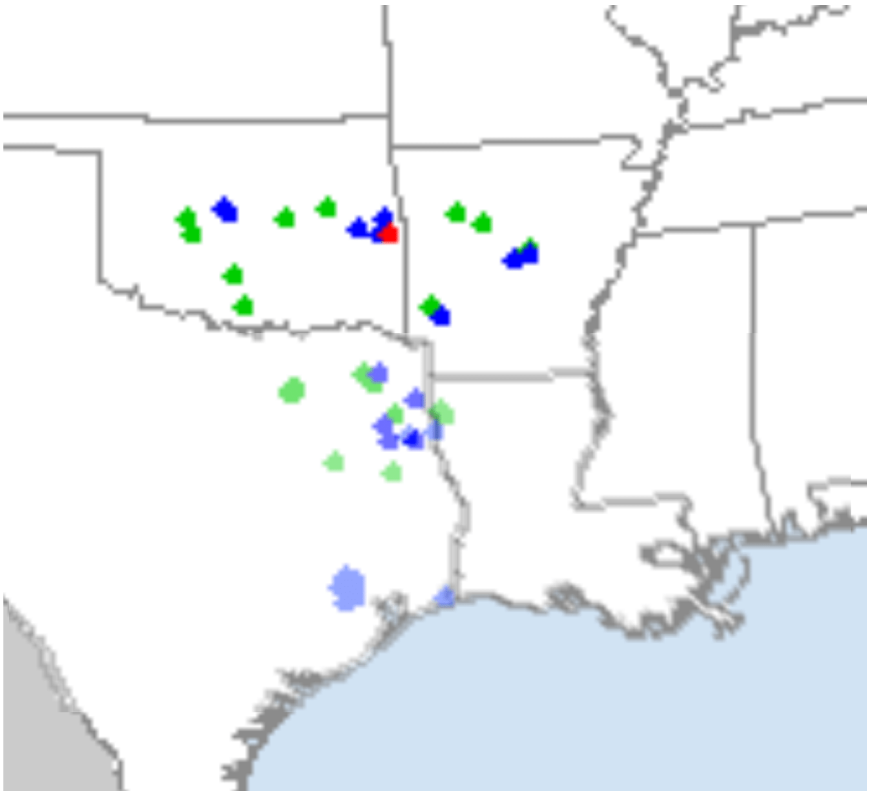

Figure 32: Storm Prediction Center filtered storm reports overlaid from 5 October and 6 October 2014 to encompass the total convective event. Blue circles, green circles, and red circles represent wind, hail, and tornado reports, respectively. Storm reports were obtained from the SPC Event Archive.

convection formed in north central Oklahoma, still noted that convective development was expected after midnight in northern Texas and southern Oklahoma, where a 30 knot (15 m s^{-1}) south-southwesterly LLJ would continue to moisten

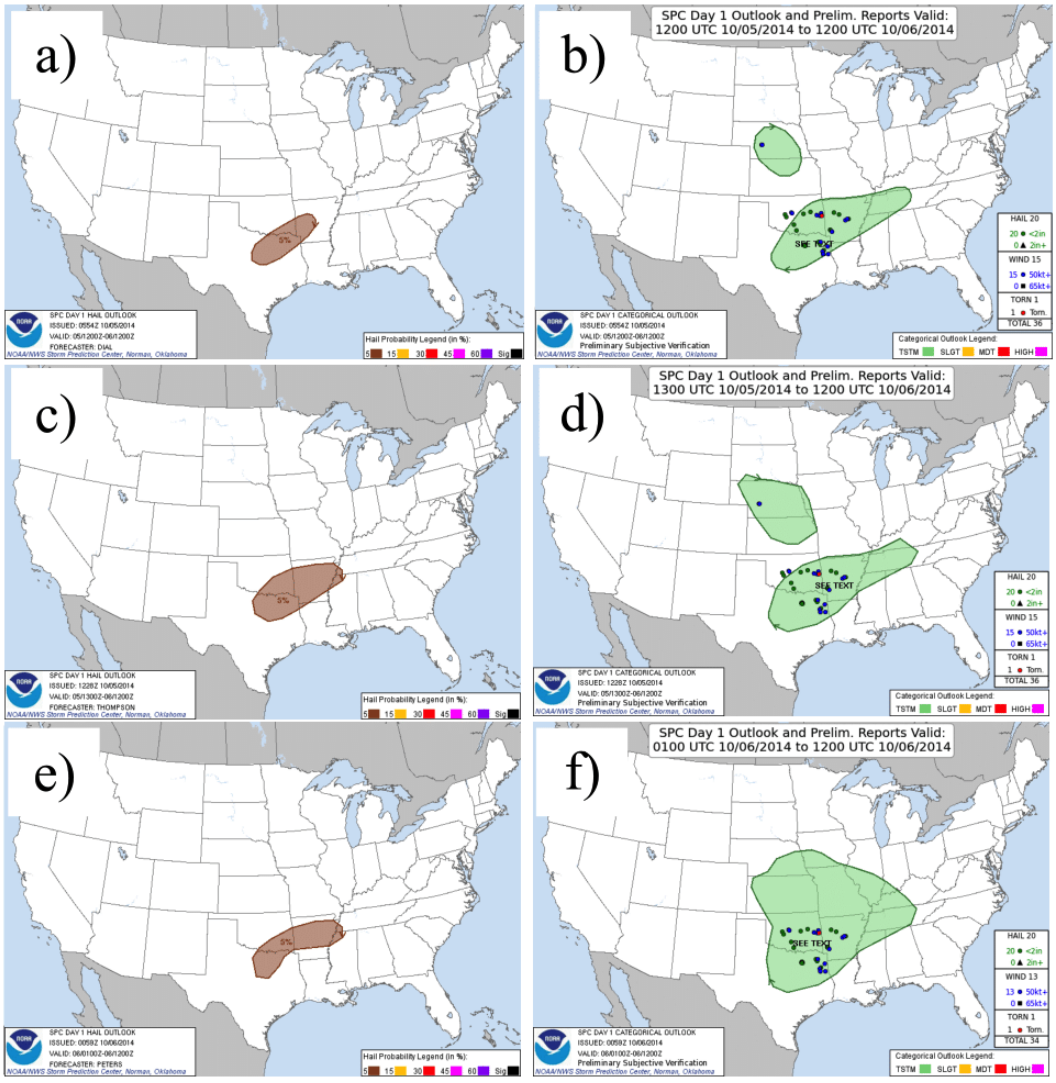

Figure 33: Storm Prediction Center Day 1 Convective Outlooks for the event presented herein. The probability of severe hail within 25 miles of a point (left) and outlook verification (right) are presented for 0600 UTC in (a) and (b), respectively. The same as above is presented for 1300 UTC in (c) and (d) and for 0100 UTC in (e) and (f). Convective Outlooks were obtained from the SPC Event Archive.

the low levels. Therefore, based on the Convective Outlooks issued as little as 1 h in advance of the convective development, forecasters had anticipated the timing of initiation to occur 3 h after observed, and the location of the convection was displaced by a couple hundred kilometers.

Despite the low probability of severe convection, (i.e., between 0355 UTC and 1725 UTC), 21 wind reports, 21 hail reports, and 1 tornado report[16] occurred throughout the duration of the convective system[17] (Fig. 32). The tornado formed briefly in eastern Oklahoma at approximately 0601 UTC and was rated an EF-1 on the Enhanced Fujita Scale (McDonald and Mehta, 2006) after destroying chicken coops and uprooting several trees. Several hours later, one fatality was recorded in the northern Houston, Texas, suburbs owing to severe winds. A void in storm reports existed in southeastern Oklahoma, which could have been attributed to the time of day that the system moved through this region (i.e., 0700 - 0900 UTC, or 0100 - 0300 LST) or the apparent weakening and reorganization of convection during this time period (see section 2.2).

[16]All severe reports utilized were filtered by the National Weather Service. Wind reports are characterized by winds in excess of 50 knots (26 m s^{-1}), and hail reports are characterized by hail 1" or greater in diameter

[17]Storm reports were found online at `http://www.spc.noaa.gov/climo/reports/141005_rpts.html`

Chapter 3

WRF Simulations

Numerical simulations were utilized for this study in order to address the goals of better understanding the longevity of the system and how the MCS structure evolved as it transitioned between elevated and surface-based. This chapter describes the WRF model configurations utilized in the simulations and an overview of the evolution of the simulated convection.

3.1 Model Specifications

The WRF-ARW model (Skamarock et al., 2008) version 3.6.1 was utilized in this study. The WRF-ARW model core uses fully compressible, nonhydrostatic Euler equations (Skamarock et al., 2008). Second- and third-order Runge-Kutta schemes are used for forward time integration with the utilization of a smaller time step for acoustic and gravity-wave modes. The horizontal grid is based on a Lambert conformal mapping system with Arakawa-C grid staggering for nested domains (Fig. 34). The vertical coordinate used in the WRF-ARW model is a terrain-following, hydrostatic-pressure vertical coordinate, η, which is defined as:

$$\eta = \frac{p_h - p_{ht}}{p_{hs} - p_{ht}} \tag{3.1}$$

where p_h is defined as the hydrostatic pressure component, p_{ht} is the hydrostatic pressure at the model top, and p_{hs} is the hydrostatic pressure at the surface. Values of η vary from 1 at the surface to 0 at the model top (Fig. 35). The vertical grid spacing can be stretched nonlinearly such that vertical resolution is higher near the surface and decreases with height. Additionally, either one-way nesting (feedback off) or two-way nesting (feedback on) can be used in WRF-ARW for nested domains. Details of the nesting can be found in Skamarock et al. (2008).

For this study, hourly RAP model analyses, which were updated with real-time assimilation cycles, were used for the initial (ICs) and lateral boundary conditions (BCs). Further details on the assimilation products will be provided in section 3.1.2.

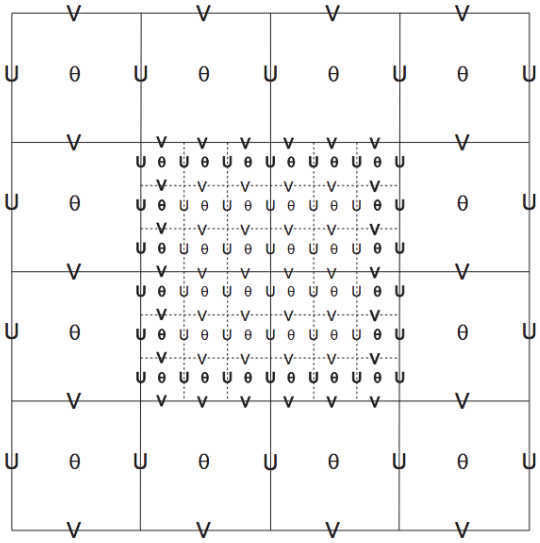

Figure 34: WRF-ARW Arakawa-C grid staggering for a portion of a parent domain and an embedded nest domain with a 3:1 grid size ratio, which was used in our simulations. A 3:1 grid ratio was used in the simulations presented herein (figure taken from Fig. 7.3 of Skamarock et al. (2008)).

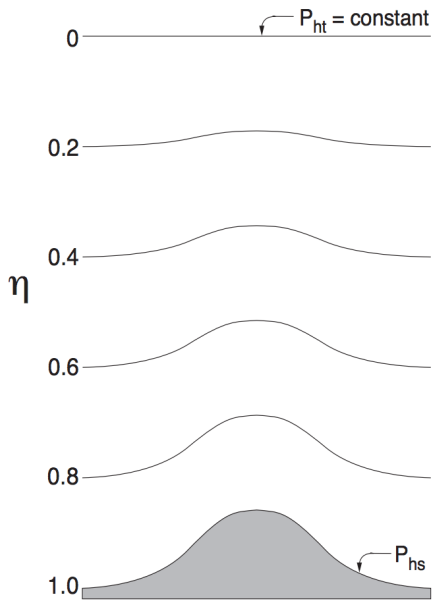

Figure 35: Depiction of terrain-following η coordinate used in the WRF-ARW model. An eta value of 1 represents the lowest model level (i.e., the surface) which decreases to 0 at the defined model top. The effects of the terrain on the eta levels diminish with height (figure taken from Fig. 2.1 of Skamarock et al. (2008)).

3.1.1 Grid Configurations

Convection is permitted in WRF-ARW non-hydrostatic simulations, and the convective parameterization was not utilized on the higher-resolution model grids in this study. However, while convective processes are permitted at these grid spacings, the convection may not be fully resolved. Weisman et al. (1997) examined the sensitivity of a simulated surface-based squall line to the horizontal grid spacing. Their study found that one should be able to simulate a squall line with qualitatively similar results at both 4-km and 1-km horizontal grid spacings. Similar results were obtained by Clark and Coauthors (2012), who found that simulations run with a 1-km horizontal grid spacing do not result in more accurate convective evolutions than those using a 4-km horizontal grid spacing.

In a subsequent study, Bryan et al. (2003) investigated the Weisman et al. (1997) results by using a cloud resolving model with horizontal grid spacing ranging from 125 m to 1 km. These simulations showed that much of the convective structure that is resolved with a grid spacing of O(100 m) cannot be properly resolved at 1 km. In the past, a 1-km grid spacing had been used as a proxy for the "ground-truth". However, the conclusions from Bryan et al. were that higher-resolution simulations should be used as the "ground truth", if possible. However, they concluded that simulations at this coarser grid spacing (i.e., 1-km) can still provide valuable information about the system structure.

Grid Configurations	Small_1km	Expanded_Small	Expanded_Large
3-km grid dimensions	364x434 grid points	420x530 grid points	700x700 grid points
1-km grid dimensions	691x1045 grid points	901x1111 grid points	901x1111 grid points

Table 3.1: The number of grid boxes per nested domain for the three grid configurations. The Expanded_Small configuration was used for the analysis of the convective system.

Given the limited computational and file storage resources available for this study, a 3:1 grid staggering ratio was employed with a 3-km horizontal grid spacing outer domain (run with a 3 s time step) and an inner 1-km nest (run with a 1 s time step). Previous studies such as Wyngaard (2004) have discussed how a 1-km horizontal grid spacing lies within terra incognita for boundary layer processes in which the dominant length scale of the flow is of similar magnitude to the horizontal grid spacing of the model. In this numerical gray zone, the model parameterizes turbulent eddies, but also directly resolves the largest eddies. The situation is particularly problematic during the daytime boundary layer. However, as the boundary layer stabilizes owing to radiative cooling, the dominant length scale of the flow decreases from O(1-2 km) to less than O(100 m) owing to the cessation of

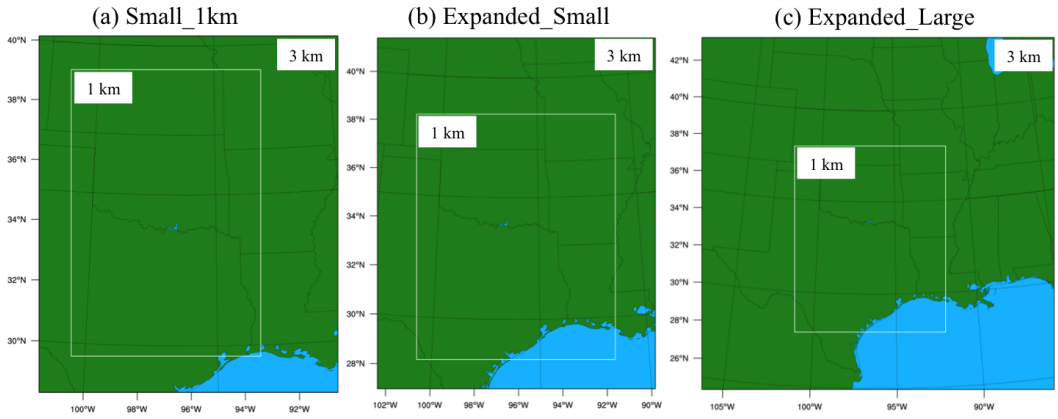

Figure 36: The three grid configurations used for WRF-ARW simulations are shown: (a) Small_1km, (b) Expanded_Small, and (c) Expanded_Large. The analysis of the system dynamics and evolution was completed using simulations run with the Expanded_Small configuration.

deep, convective eddies (Stull, 1988). Therefore, this terra incognita effect is more important during the later hours of the numerical simulation when the boundary layer begins to destabilize, but is of lesser importance during the nocturnal hours of the simulation (Zhou et al., 2014). While noting this shortcoming, insight into the processes responsible for convective maintenance may be gained using simulations of this grid scale (e.g., Clark and Coauthors, 2012; VandenBerg et al., 2014).

Three grid configurations are presented to show the sensitivity of the simulations to the both grid locations and horizontal grid spacing. The results on the system structure and dynamics presented herein utilized the Expanded_Small grid configuration (Fig. 36b). Sensitivity analyses are also presented with output from the Small_1km (Fig. 36a) and Expanded_Large (Fig. 36c) configurations, which will be discussed further in the Appendix. All domains employed the 3:1 grid staggering with an inner 1-km nest. The size of each of the nests varies based on the configuration used, the details of which are presented in Table 3.1. The inner

1-km nests for the Expanded_Small and Expanded_Large configurations have the same dimensions, but the 3-km outer domains differ in size.

3.1.2 Initial Conditions and Physics Options

In order to initialize the model for this study, 13-km RAP Version 2 hourly analyses (Benjamin and Coauthors, 2016) which contained atmospheric and soil data were obtained from the NCAR archive. The RAP model provides hourly-initialized forecasts into which observations, such as those from satellite, radar, surface, and upper air soundings, are assimilated using a Gridpoint Statistical Interpolation analysis system (Benjamin and Coauthors, 2016). The RAP model covers the domain of North America from the surface to a model top of 10 hPa. The simulations were initialized with RAP data from 2100 UTC on 5 October and run with hourly-updated atmospheric BCs for 23 h until 2000 UTC on 6 October. Other hourly initialization times (e.g., the 2000 UTC 5 October analysis) were explored, but the 2100 UTC initialization resulted in the most realistic convective evolution. Given that the goals of this study are to investigate the dynamics of an observed system, the 2100 UTC simulation was utilized in this study. Since the observed convective system initiated between 0200 and 0300 UTC on 6 October, the 2100 UTC initialization provided approximately 5-6 h of model spin up time.

In addition to initializing the model at different times with the RAP products, ICs were also obtained from the 12-km NAM and 0.5° GFS. However, simulations with these ICs were unsuccessful in simulating a long-lived convective system. Upon further inspection, the 0000 UTC NAM analyses were characterized by surface temperatures as great as 3-5° Celsius colder than the 0000 UTC RAP analyses (compare Figs. 37b,c), which made a significant difference in how conducive the environment was to convective development. Additionally, the GFS ICs had a much coarser grid spacing such that fine-scale inhomogeneities, which are often

responsible for convective development, were smoothed, resulting in the lack of a long-lived convective system in these simulations (Fig. 37a). Moreover, central Oklahoma was characterized by a large region of relatively colder surface temperatures in the GFS ICs, which may have been attributed to the parameterized convection in the parent model. Similar smaller-scale inhomogeneities were seen in the 0000 UTC RAP ICs, which may have been attributed to the same phenomenon (Fig. 37c).

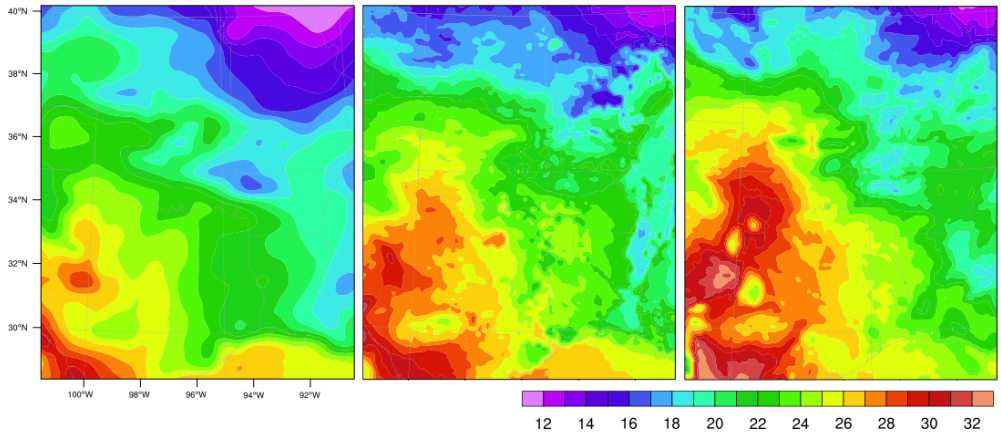

Figure 37: Parameterized 2-m temperatures (°C) for the 0000 UTC 6 October 2014 initial conditions from (a) the 0.5° GFS, (b) the 12-km NAM, and (c) the 13-km RAP models. The 2100 UTC RAP analysis was used as the ICs for the simulations presented herein, but NAM and GFS analyses are only output in 6-h intervals and thus are not available to compare with the 2100 UTC RAP ICs.

Several model physics parameterizations were utilized in order to obtain a long-lived convective system in the WRF-ARW simulations (Table 3.2). Dudhia (Dudhia, 1989) shortwave and Rapid Radiative Transfer Model (RRTM; Mlawer et al., 1997) longwave radiation schemes were used in the analysis presented. Other recent studies which simulated nocturnal MCSs using the WRF model have utilized these radiation schemes (e.g., Trier et al., 2011; Peters and Schumacher, 2015; Lawson

Shortwave Radiation	Longwave Radiation	Planetary Boundary Layer	Microphysics
Dudhia	**RRTM**	**MYNN Level 2.5**	**Morrison**
RRTMG	RRTMG	MYJ	WDM6
New Goddard	New Goddard	YSU	Thompson
		ACM2	NSSL 1 Moment
		QNSE	NSSL 2 Moment
			Lin
			WSM6

Table 3.2: Different WRF parameterization schemes for the shortwave radiation, longwave radiation, planetary boundary layer, and microphysics were used in early simulations. The schemes listed in red are used in the analysis presented herein.

and Gallus Jr, 2016). From subjective inspection, the variation in the radiation parameterization schemes seemed to provide little change to the system evolution.

Because the simulations were run on grids of convective-permitting dimensions (i.e., 3 and 1 km), no cumulus parameterization was employed. However, turbulent eddies of all scales are not able to be directly resolved at these grid spacings (e.g., Wyngaard, 2004), so turbulence is parameterized and represented in the PBL physics schemes. Greater model sensitivity was found when varying the PBL parameterization scheme than with varying the radiation scheme. Since the convective system initiated and persisted throughout the night, the utilization of a local PBL scheme seemed to be critical for capturing the effects of a stable boundary layer as the Yonsei University (YSU; Hong et al., 2006) non-local[1] scheme performed poorly (not shown). This result is consistent with previous studies (e.g., Shin and Hong, 2011) that have concluded that local schemes better capture the nocturnal boundary layer structure. The two schemes which produced the most realistic convective evolutions were the Mellor-Yamada-Janjíc (MYJ; Janjic, 1994) and Mellor-Yamada-Nakanishi-Niino Level 2.5 (MYNN; Nakanishi and

[1]For an overview of differences between the local and non-local parameterization schemes described in this section, refer to Coniglio et al. (2012).

Niino, 2006) local schemes. Noting the goal of obtaining a realistic simulation that matched observations, we chose to use the MYNN PBL scheme with the Eta Similarity (Janjic, 1996) surface layer scheme for the analysis because the simulated convection better matched the observations than with MYJ (not shown). While these conclusions were subjective and based upon the location, areal extent, and horizontal structure of simulated model reflectivity, previous studies such as Coniglio et al. (2013) have examined the PBL parameterizations in WRF have found that MYNN performs better than MYJ.

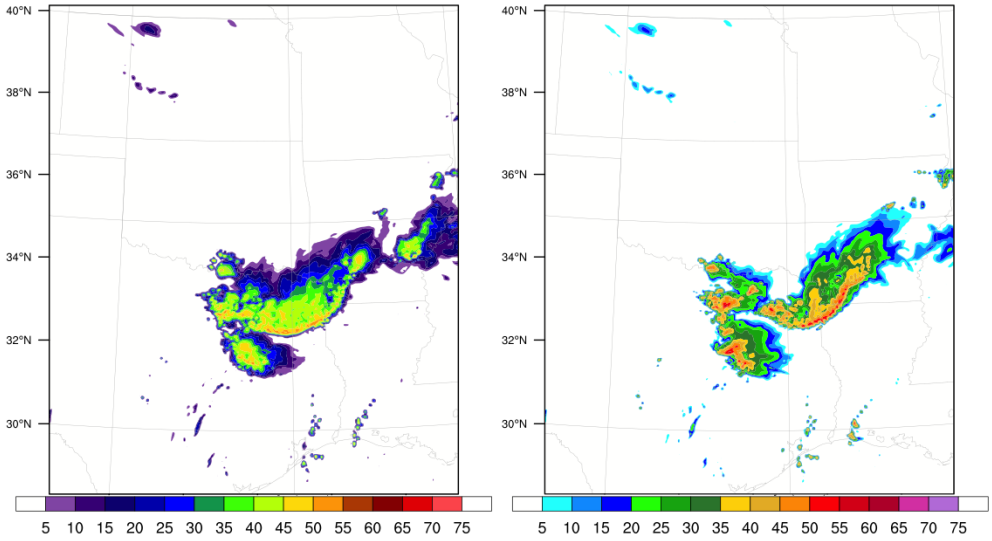

Figure 38: Simulated column-maximum radar reflectivity (dBZ) valid at 1200 UTC for 3-km horizontal grid spacing using the MYNN PBL parameterization scheme and the Morrison microphysics parameterization scheme with (a) hail option turned off and (b) hail option turned on. Despite the use of different color scales and the 3-km grid spacing, the benefit of the utilization of the hail option can be inferred by noting the more distinct convective cores in (b). It should be noted that the 3-km outer domain of the Small_1km horizontal grid configuration was used in this particular simulation.

Utilization of a double moment microphysics scheme was necessary to capture a realistic-looking MCS owing to their complex microphysical structure (e.g., Smith et al., 2009; Bryan and Morrison, 2012), which is largely responsible for their internal circulations (e.g., Houze et al., 1989; Houze, 2004). The two schemes that performed the best were the WRF Double-Moment 6-class (WDM6; Lim and Hong, 2010) and Morrison (Morrison et al., 2009) double-moment, 6-class schemes (not shown). Both schemes were run with the hail parameterization turned on and off. The ability for both WDM6 and Morrison microphysics schemes to parameterize hail instead of graupel resulted in more defined cellular cores (Fig. 38). Moreover, because numerous severe hail reports occurred with this system, the simulations were run with the utilization of the hail parameterization in the Morrison scheme. Like with the PBL schemes, this decision was made subjectively by examining which scheme resulted in a long-lived MCS that best matched the observations.

The majority of test simulations using the different ICs and physics paramterizations were run using the Small_1km grid configuration. However, the inner 1-km nest was not large enough to encompass the entire evolution of the convective system. Therefore, the best schemes were subjectively determined using this grid and were then applied to the larger Expanded_Small and Expanded_Large grid configurations. All three of these grid configurations resulted in significantly different storm evolutions, which is discussed in the Appendix. As a result, the subjectively-determined best ICs and physics paramterizations may not have been the best for these other grid configurations. Despite this, the parameters used for the simulation resulted in a long-lived MCS that had a similar evolution that resembled the observed system, especially in its later stages. Therefore, we are confident that the physics schemes selected (i.e., RRTM shortwave, RRTM longwave, MYNN, Eta Similarity, and Morrison) were adequate in representing the convective system and its environment.

3.2 Overview of the Simulated Convection

This section discusses how well the simulated convection resembles the observed system. A comparison between the simulated (Fig. 39) and observed radar reflectivity (Fig. 40) was undertaken to determine how well the simulation captured the evolution of the observed MCS. These fields were compared every 3 h between 0000 UTC and 1800 UTC on 6 October 2014. Just 3 h after the model initialization time, a cluster of simulated convective cells had formed in central Oklahoma (Fig. 39a). By 0300 UTC, this cluster had grown upscale and was moving southeastward into eastern Oklahoma and central Arkansas (Fig. 39b). This first convective system had weakened by 0600 UTC and was absent by 0900 UTC in the simulation (Fig. 39c,d). However, this initial convective system did not exist in the observations. As previously discussed, the observed convection instead began initiating in two separate, but adjacent clusters after 0200 UTC (Fig. 40b). By 0600 UTC, one quasi-linear system, spanning from northwestern Arkansas to south central Oklahoma, was observed (Fig. 40c).

In order to determine why these non-observed, early convective cells initiated in the model, upper air soundings from the model near the location of convective initiation were plotted for 2100 and 2200 UTC. The environmental characteristics can be estimated by examining the closest observed sounding taken at 0000 UTC in Lamont, Oklahoma (Fig. 15a) and at 0000 UTC in Norman, Oklahoma (Fig. 15b). Both the 2100 and 2200 UTC model soundings were characterized by a well-mixed boundary layer and were convectively unstable (Fig. 41). The surface-based CAPE for the 2100 UTC sounding was 830 J kg^{-1} with only 4 J kg^{-1} of CIN. Therefore, the initial conditions were characterized by surface parcels with high CAPE values and minimal, if any, CIN. The observed profiles were less favorable for the formation of deep convection, as stated earlier. As a result, an "erroneous" surface-based convective system was initiated in the model which was not observed.

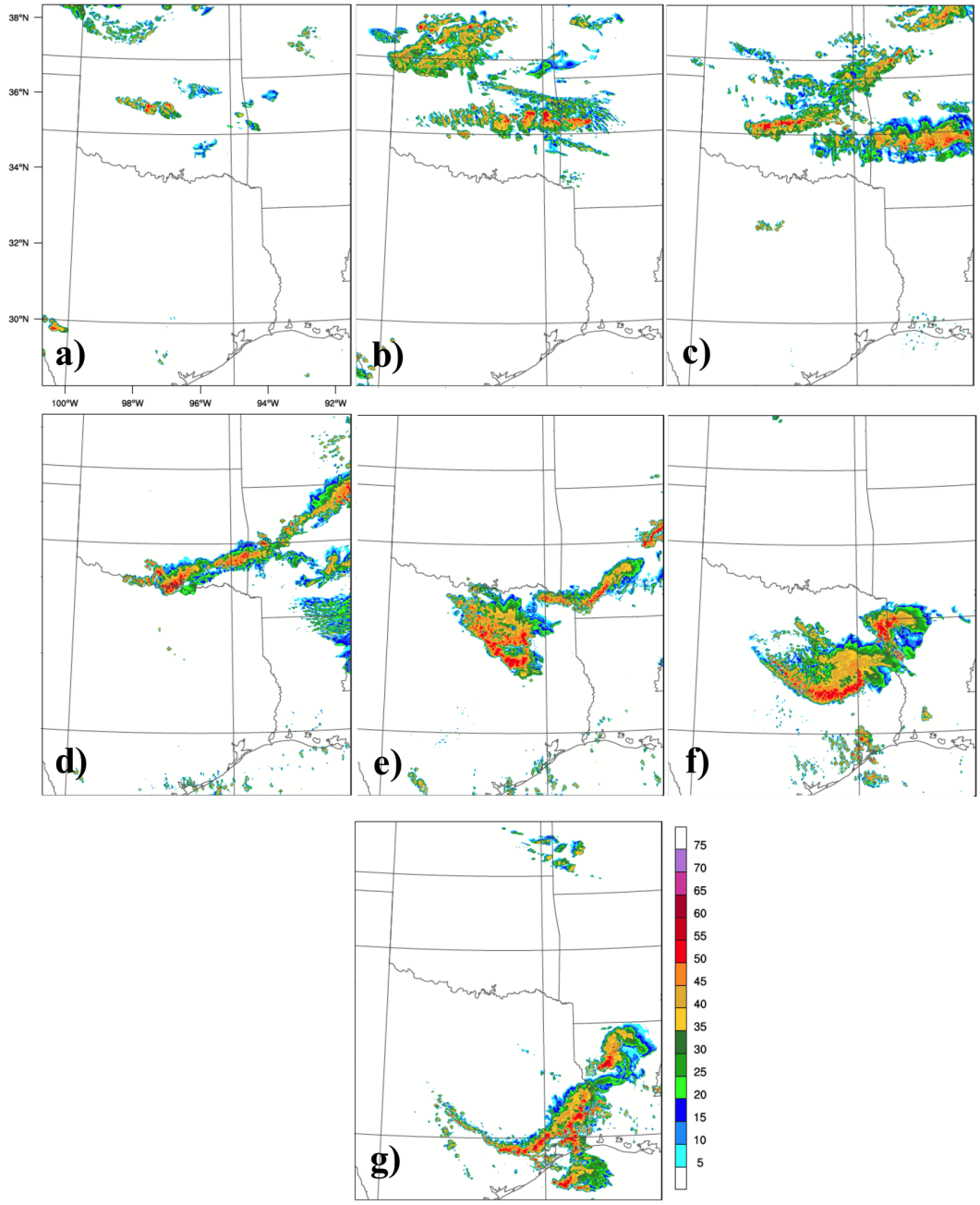

Figure 39: Simulated radar reflectivity factor (dBZ; lowest model level) from the 1-km nest of the Expanded_Small grid configuration valid for (a) 0000 UTC, (b) 0300 UTC, (c) 0600 UTC, (d) 0900 UTC, (e) 1200 UTC, (f) 1500 UTC, and (g) 1800 UTC on 6 October 2014.

The convective cells corresponding to the observed system of interest began initiating after 0300 UTC (2100 LST) in the model (Fig. 39b), which was 1-3 h later than the initiation of the observed system (Fig. 40b), and had organized into a broken line by 0600 UTC (Fig. 39c). The strongest convection was located in central Oklahoma, but weak reflectivity echoes extended northeastward owing to

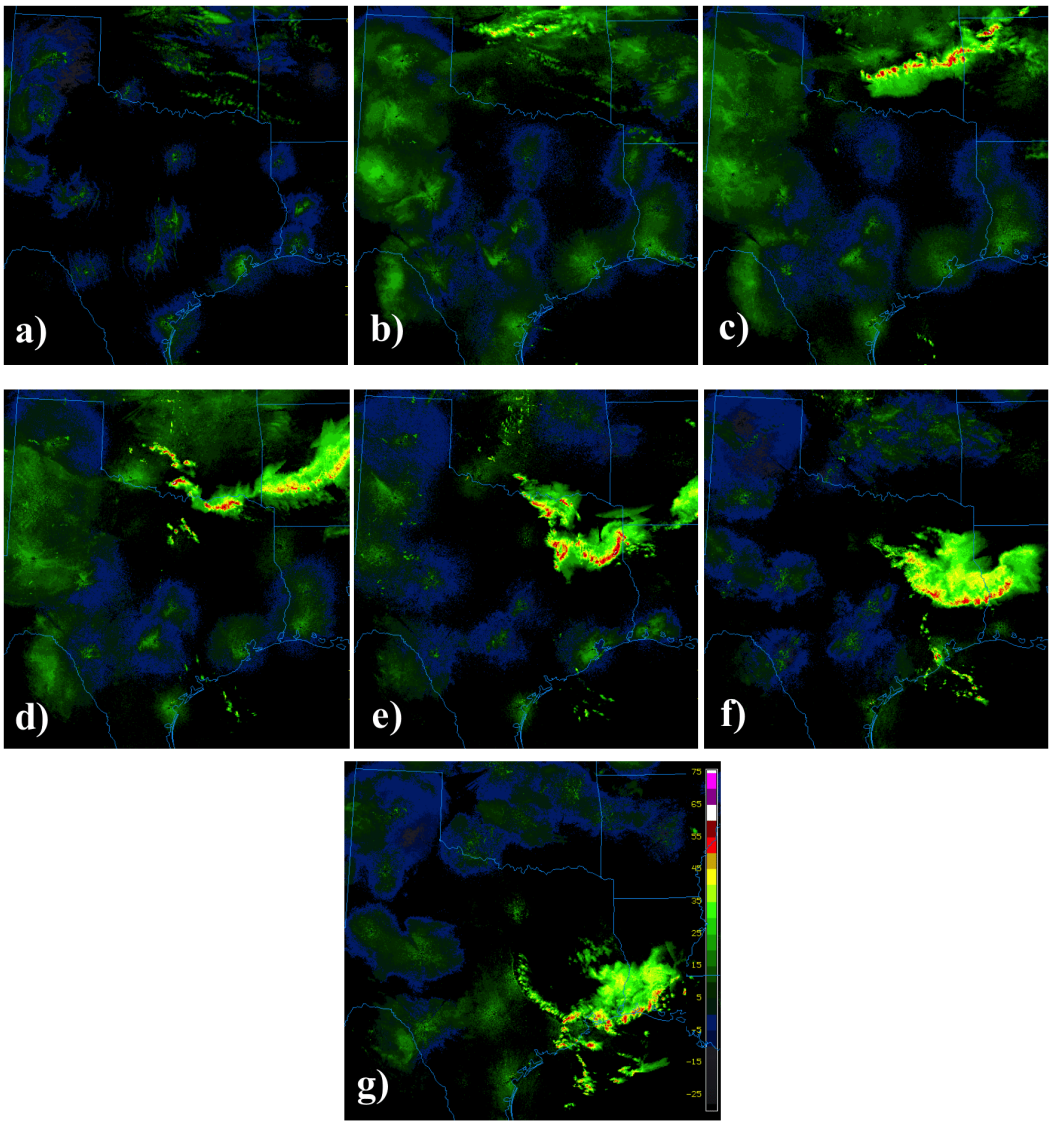

Figure 40: Observed composite radar reflectivity factor (dBZ) valid for (a) 0000 UTC, (b) 0300 UTC, (c) 0600 UTC, (d) 0900 UTC, (e) 1200 UTC, (f) 1500 UTC, and (g) 1800 UTC on 6 October 2014.

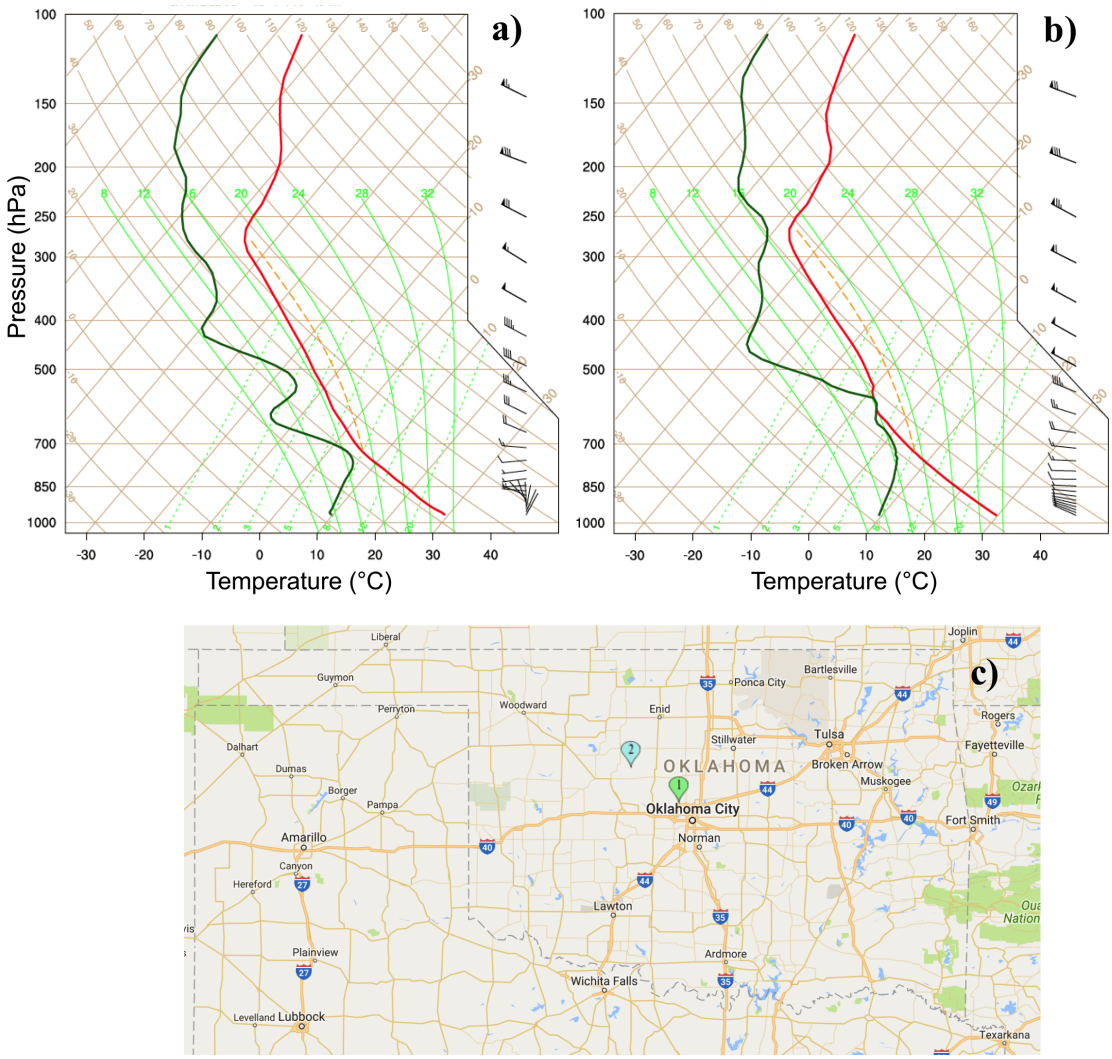

Figure 41: Model output soundings (traditional Skew-T / Log-p diagrams) from the initiation_north inflow point of the initial cluster of convection for (a) 2100 UTC and (b) 2200 UTC on 5 October 2014. The temperature (red) curve and dewpoint temperature (green) curve are displayed. Wind barbs are displayed in knots (1 knot = 0.51 m s^{-1}). The dashed orange parcel trace represents the surface-based parcel. The location of these soundings (initiation_north) is displayed in (c) by the cyan pin, and the initiation_south point is depicted in (c) by the green pin (map obtained from Google).

new development along the surface cold front. The location of the strongest cells in the simulations was similar the observed location of convection by this time, but the line of mature cells extended farther east in the observations.

However, by 0900 UTC, the location of organized convection in the model (Fig. 39d) compared favorably with the observations (Fig. 40d), which were characterized by the reorganization and strengthening of the western cluster of convection near the Oklahoma-Texas border. A weaker line of convection extended northeastward along the cold front, but this convection was separate from the cluster along in southern Oklahoma. Back-building cells (e.g., Schumacher and Johnson, 2005) had developed throughout southern and central Oklahoma, and the secondary cluster of cells was developing farther south, as described in section 2.2 (Fig. 40d). These back-building cells were less developed in the simulations, but new cell initiation was beginning to occur behind the system in the model (Fig. 39d). Overall, despite the model initialization and first few hours of the simulation differing substantially from the observations, the simulations and observations reveal a similar location and lateral extent of convection by 0900 UTC.

By 1200 UTC, both the observations and simulation show that the western cluster of convection had reorganized into a leading-line, trailing-stratiform MCS (Fig. 40e). However, as at earlier times, the convection was displaced to the west in the simulation (Fig. 39e), which was again likely attributed to the effects of the prior convective system on the environment. Additionally, the secondary cluster of convection that had begun to develop at 0900 UTC in central Texas had matured by 1200 UTC, but its westward displacement resulted in a different evolution than the observations (Fig. 40e). More specifically, this secondary cluster intersected the leading line of the MCS and merged with the eastern flank of the system. Additionally, back-building convective development was suppressed in

the simulations compared to the observations at this time, which had clusters of convection extending northwestward from the main MCS (Fig. 39e).

At 1500 UTC, both the observed (Fig. 40f) and simulated (Fig. 39f) MCS had a mature leading-line, trailing stratiform structure. The MCS remained displaced to the west in the simulations and was also slightly farther to the north. Additionally, the simulated MCS had a slightly more asymmetric structure than in the observed system, perhaps consistent with the differing evolutions of the secondary convective cluster in central Texas. The convective portion of the MCS was strongest on its eastern and southern flanks and appeared more disorganized and weaker toward the west and northwest in both the observations and simulations. Additionally, surface-based convection moving inland from over the Gulf of Mexico was present in both the observations and simulations at this time.

By 1800 UTC, both the observed MCS and the simulated system had weakened and disorganized. The western portion of the system weakened first, and the eastern half of the MCS was still characterized by a leading convective line. The convective portions of the system remained more intact in the simulations than in the observations by 1800 UTC. The observed system was also located farther to the south than the simulated system and had already begun moving off the Louisiana and Texas Gulf Coast. Additionally, surface-based convection moving inland off the Gulf of Mexico had begun interacting with the remnants of the MCS in both the observations and simulations.

In summary, despite initializing the model at 2100 UTC and running the simulation for 23 h, the simulated reflectivty field matched the observations relatively well, especially in the later hours of the simulations. A significant difference was that the erroneous initial convective system in the model likely impacted the location and extent of the system of interest, but the presence of this convection did

not inhibit the simulation from eventually producing a realistic convective evolution. This agreement is surprising as previous studies (e.g., Davis et al., 2003) have shown that deterministic numerical weather prediction forecasts struggle to accurately represent the diurnal cycle of convection, especially nocturnal convective systems. Further, mesoscale predictability in convection-allowing simulations of systems of this scale diminishes after just a few hours, and previous studies (e.g., Surcel et al., 2015) have found that obtaining accuracy in such a long-duration simulation (i.e., 23 h) is difficult. As the simulated reflectivity evolution aligns relatively well with the observations, insight into the convective evolution may be gained from examining the model output. However, the impacts from the erroneous convection on the early hours of the simulation are certainly not negligible and will be considered when making conclusions about the convective maintenance and its inflow environment during these hours.

Chapter 4

System Longevity and Role of Environmental Characteristics

The observed convective system persisted for more than 18 hours and traversed from central Oklahoma to the Gulf Coast. This chapter is focused on understanding the factors that allowed the convection to be sustained throughout the lifetime of the system, which spanned over much of the diurnal cycle. In order to provide a framework for this discussion, this chapter begins with a brief overview of how the convective structure evolved throughout the lifecycle of the MCS.

4.1 Evolution of the Convective System

Shallow reflectivity echoes associated with midlevel clouds moved into north central Oklahoma at approximately 0300 UTC (2100 LST; Fig. 42a), but high reflectivity (i.e., greater than 50 dBZ) associated with deep convection was not present in the simulation until 0500 UTC (not shown). These midlevel clouds were associated with the progression of the midlevel shortwave into the region, and an associated

deep baroclinic zone[12], which can be seen in cross sections of vertical velocity (Fig. 42d) and virtual potential temperature (Fig. 43a), provided strong low-level ascent of ~5 m s^{-1}. This area of ascent was confined to the lowest 5 km and was not associated with a deep convective updraft at this time. Additionally, elevated updrafts within the precipitation region were located ~15-20 km behind the leading baroclinic zone, suggesting that weak convective updrafts within the greater stratiform precipitation region locally enhanced precipitation, resulting in stronger convective downdrafts and higher reflectivity (Fig. 39b).

The ascent coincident with the leading edge of the baroclinic zone was also evident at 0400 UTC (Figs. 42e,43b), but this boundary was unable to trigger deep convection until around 0500 UTC. By 0500 UTC, this deep convection had developed and moved approximately 50 km ahead of the initiating boundary (Figs. 42f,43c). An elevated downdraft was located approximately 20 km behind the deep convective updraft, which would promote elevated convergence, allowing the system to sustain itself and regenerate new updrafts as it moved away from the surface boundary. Moreover, the convection had moved atop the residual outflow from the first erroneous convective system in the model by this time, and the elevated cold pool produced by the ongoing convection was much smaller than the cold air mass behind the initiating baroclinic zone.

It is important to note that early in the lifetime of the system, its evolution was impacted by the first convective system in the model, which was not observed. The observed convective system, based upon Oklahoma Mesonet observations, had surface signatures associated with a surface cold pool as it moved throughout central Oklahoma - 2-3 hours after its initiation as an elevated system. However,

[1]All cross sections through the convective system have the inflow point at 0 km (corresponding to the green circles on the cross section paths diagrams), and the system motion is from the right side toward the left side of the figures.

[2]The baroclinic zone was located at ~20 km in Fig. 42d.

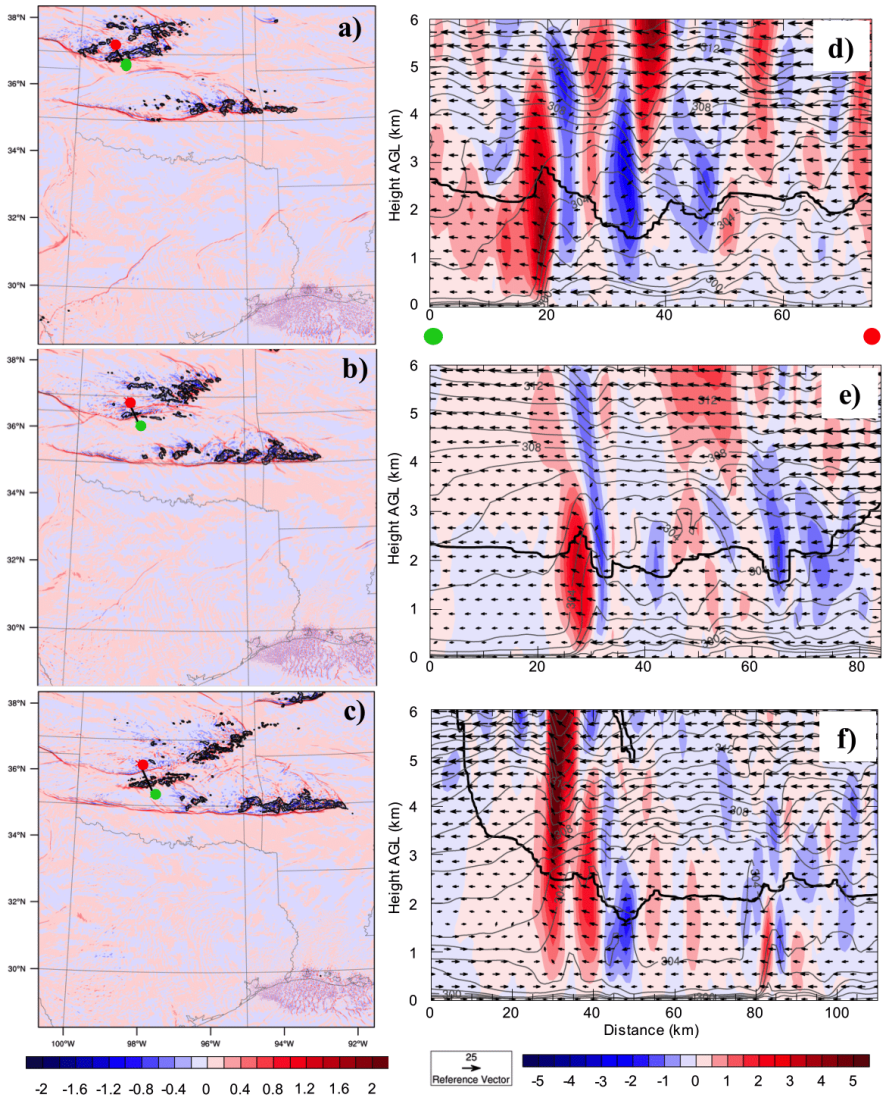

Figure 42: Plan view of 1-km vertical velocity (shaded; m s^{-1}), reflectivity (every 20 dBZ), and cross section paths (from the green to red circles where green corresponds to 0 km on the x-axis) for (a) 0300 UTC, (b) 0400 UTC, and (c) 0500 UTC. 0-6 km AGL vertical cross sections of vertical motion (shaded; m s^{-1}), wind vectors (m s^{-1}; reference vector 25 m s^{-1}), and cloud boundary (thick black line) for the paths designated in (a),(b),(c) for (d) 0300 UTC, (e) 0400 UTC, and (f) 0500 UTC on 6 October 2014, respectively. Note that the vertical motion scales differ between the plan view and cross section plots.

the observations indicated that this cold pool was preceded by a period of warming and an increase in pressure, which may be suggestive of a bore response (e.g., Trier et al., 2011; Marsham et al., 2011). Moreover, the convective system in the simulations initiated approximately 2-3 h after the observed system, which would allow the simulated boundary layer more time to stabilize owing to radiative cooling (in tandem with effects from the erroneous convective outflow), resulting in greater difficulty for convectively-produced downdrafts to penetrate to the surface. As a result, a convectively-generated surface cold pool may have taken longer to develop in the simulations than in the observed system.

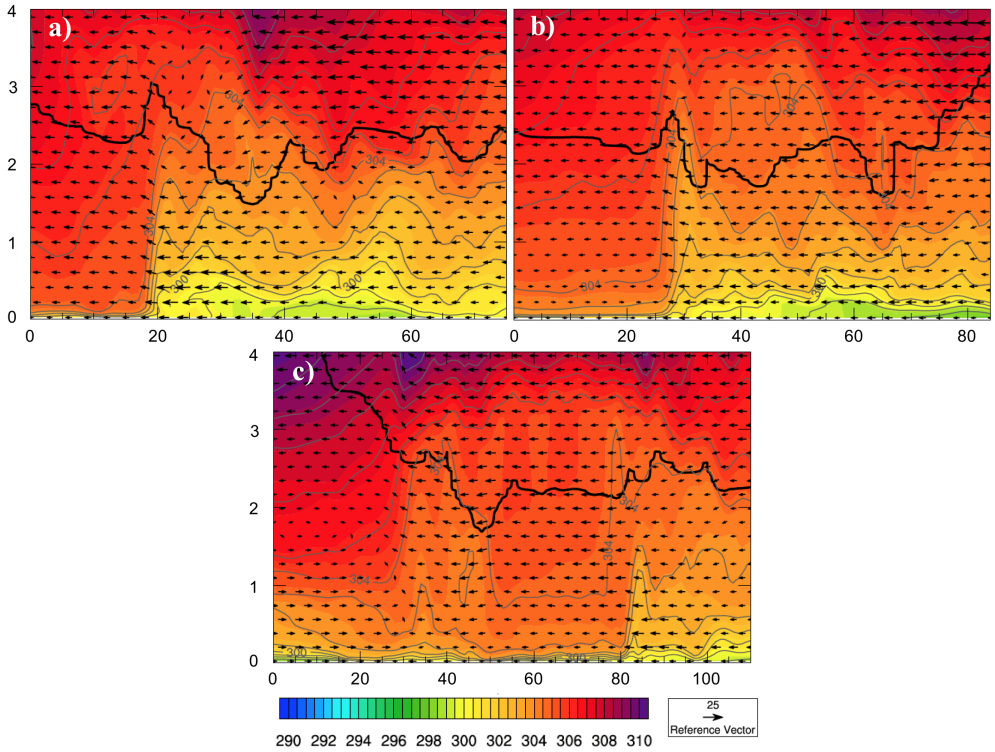

Figure 43: Vertical cross sections of virtual potential temperature (shaded; K), potential temperature (contours; K), ground-relative wind vectors (m s^{-1}; reference vector 25 m s^{-1}), and cloud boundary (thick black line) for (a) 0300 UTC, (b) 0400 UTC, and (c) 0500 UTC on 6 October 2014, respectively. Cross section paths are the same as in Fig. 42.

After deep convection had formed, the system intensified and moved toward the south, as shown in the horizontal reflectivity fields (Fig. 44) and in the corresponding vertical cross sections through the convective system. At 0600 UTC, shortly after convective updrafts had formed and moved away from the initiating

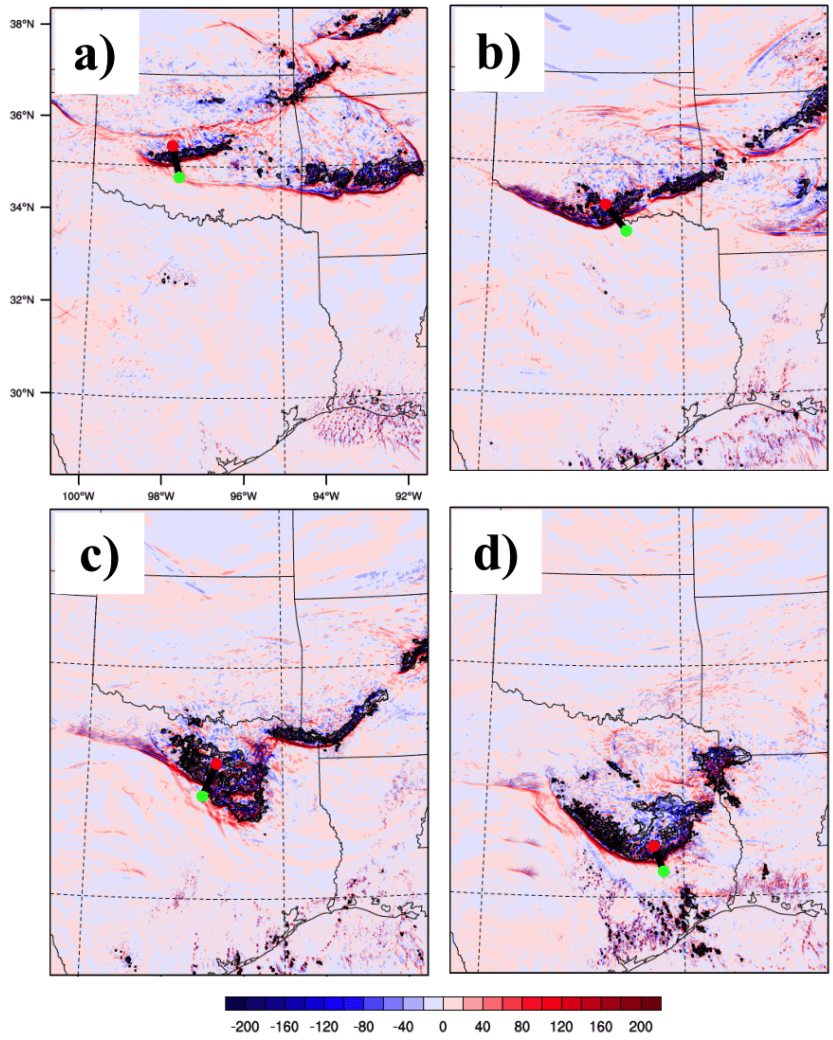

Figure 44: Vertical velocity at 1 km (shaded; cm s^{-1}), radar reflectivity contours (every 10 dBZ), and zoomed in cross section paths (from the green to red circles) for (a) 0600 UTC, (b) 0900 UTC, (c) 1200 UTC, and (d) 1500 UTC. The cross sections through the convection were expanded along these paths, where 0 km corresponds to the inflow environment.

boundary, the system was characterized by a downshear tilt and the lack of a stratiform region or distinct surface cold pool (Figs. 45a,46a). The lowest ~2 km beneath cloud base were dry (RH <70%), and RH values were relatively higher beneath the convective downdrafts (Fig. 47a), suggesting that evaporation of precipitation was likely occurring (Fig. 46a). In contrast to the deep cold air mass behind the initiating boundary, the system appeared to be maintained by ascent from a gravity wave or bore-like disturbance within near-surface stable layer early in its lifetime (Fig. 48a).

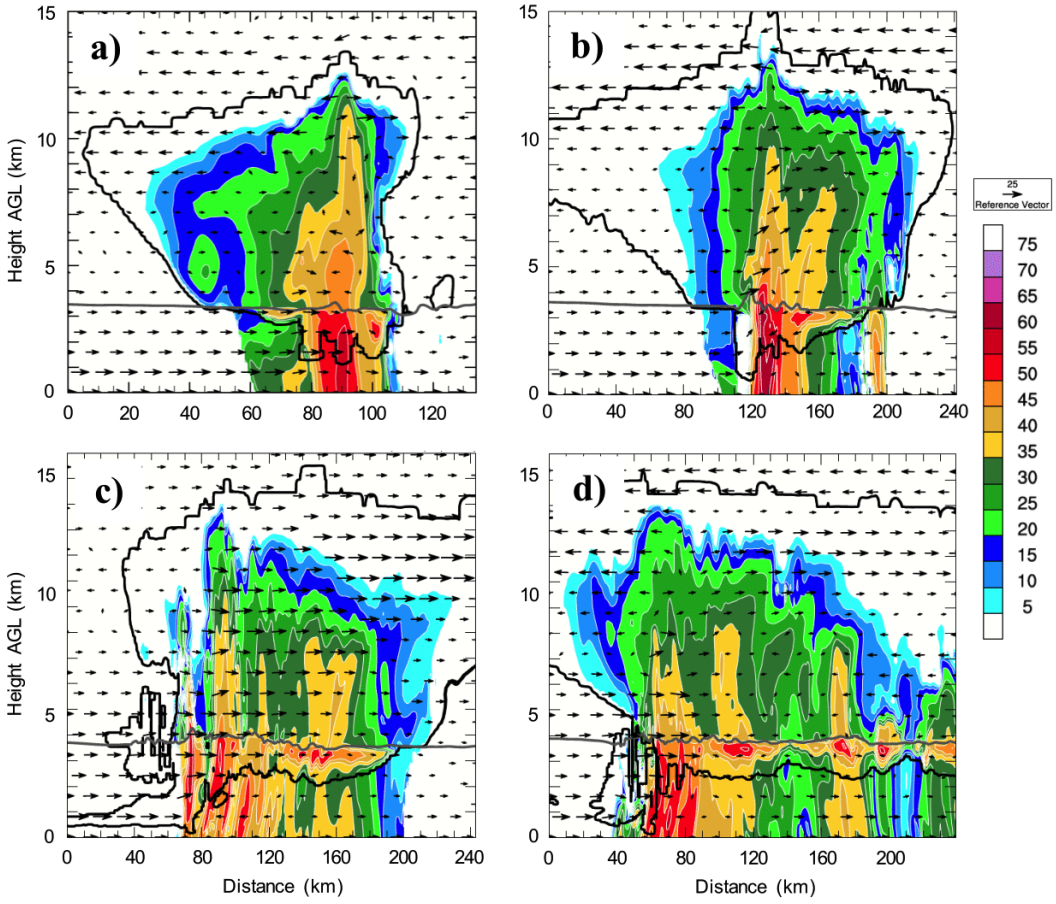

Figure 45: Vertical cross sections of simulated radar reflectivity (shaded; dBZ), system-relative wind vectors (m s^{-1}), melting line (thick gray line), and cloud boundary (thick black line) for (a) 0600 UTC, (b) 0900 UTC, (c) 1200 UTC, and (d) 1500 UTC. The cross section paths are expanded on those depicted in Fig. 44.

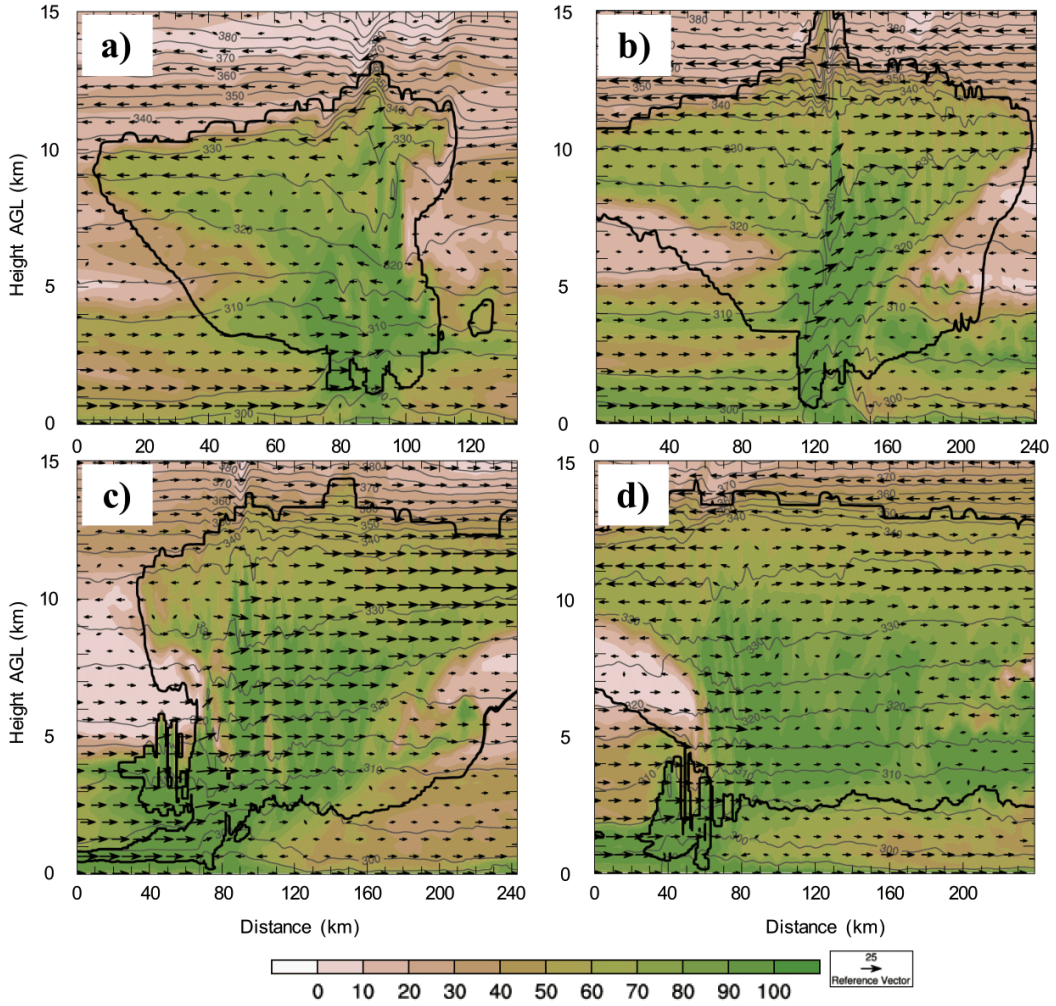

Figure 46: Vertical cross sections of relative humidity (shaded; %), system-relative wind vectors (m s^{-1}), and cloud boundary (thick black line) for (a) 0600 UTC, (b) 0900 UTC, (c) 1200 UTC, and (d) 1500 UTC. The cross section paths are expanded on those depicted in Fig. 44.

Between 0600 and 1000 UTC, the convection had developed a surface cold pool and had transitioned from being previously downshear-tilted to upshear-tilted (Fig. 49). The system cold pool was preceded by a bore at 0800 UTC (Fig. 50d), which lifted ambient air prior to its ingestion into a convective updraft above the system outflow boundary (Fig. 50a). This convective updraft was located ~20 km behind the leading wave (Fig. 49a), suggesting that the bore lifting helped to destabilize

the environment, but was not sufficient to lift parcels to their LFCs. However, by 0900 UTC, this preceding bore was absent owing to the acceleration of the cold pool during the previous hour, and deep ascent (3-4 km) was associated with the outflow boundary. Therefore, while wave dynamics were critical to the system's

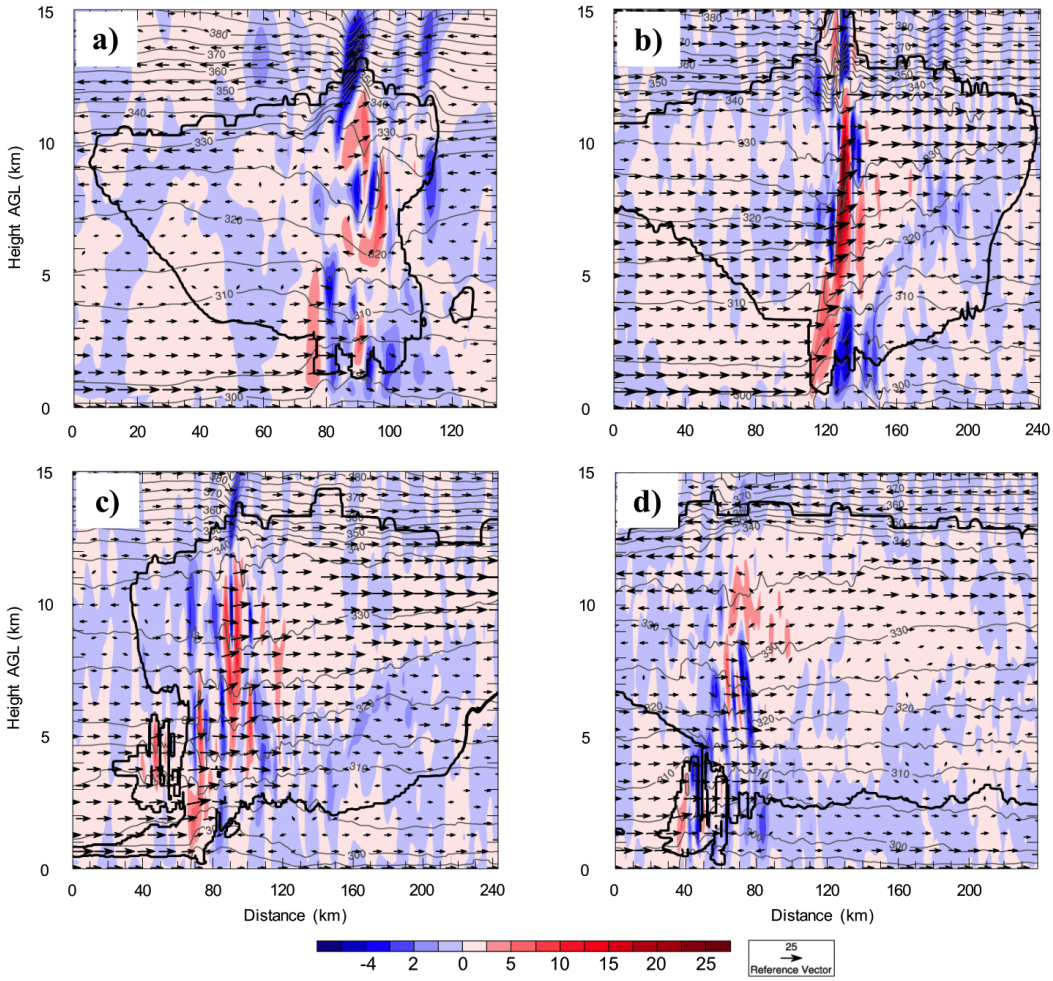

Figure 47: Vertical cross sections of vertical velocity (shaded; m s^{-1}), system-relative wind vectors (m s^{-1}), and cloud boundary (thick black line) for (a) 0600 UTC, (b) 0900 UTC, (c) 1200 UTC, and (d) 1500 UTC. The cross section paths are expanded on those depicted in Fig. 44. Note the difference in contour intervals between the positive and negative vertical velocities.

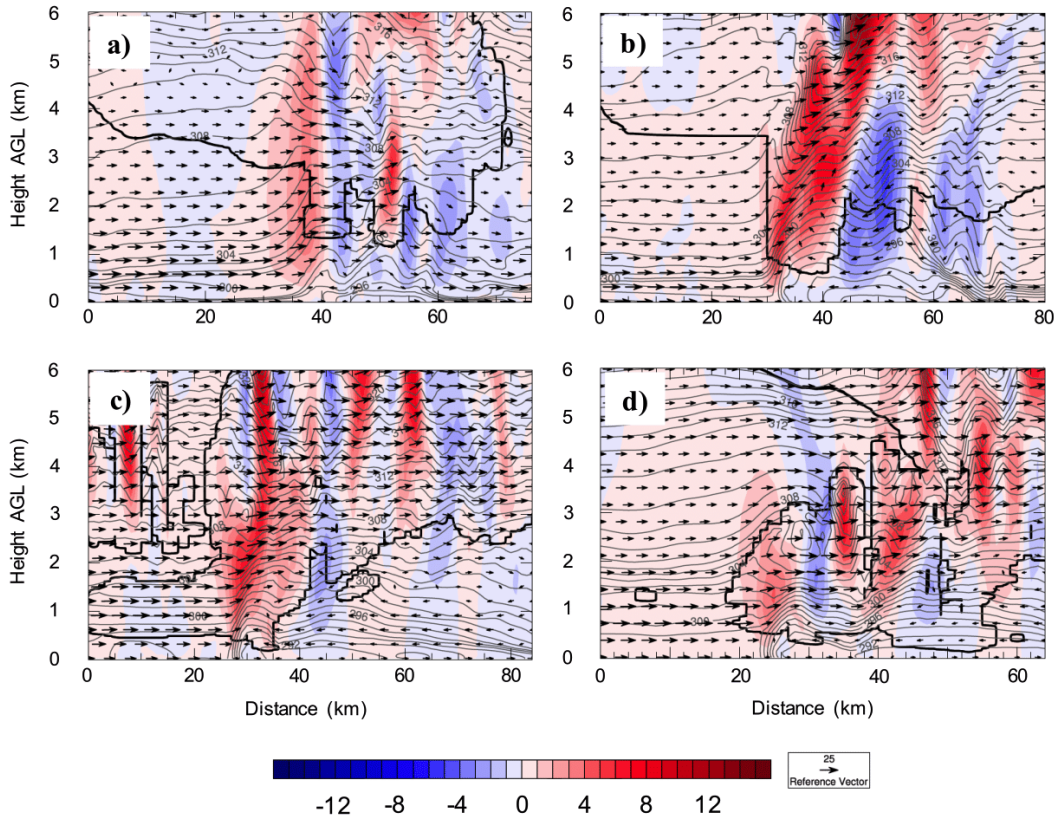

Figure 48: 0-6 km AGL cross sections of vertical motion (shaded; m s^{-1}), system-relative wind vectors (m s^{-1}), potential temperature contours (gray; K), and cloud boundary (thick black line) for (a) 0600 UTC, (b) 0900 UTC, (c) 1200 UTC, and (d) 1500 UTC. The cross section paths are depicted in Fig. 44 with the green circle representing 0 km.

maintenance early in its lifetime, these effects were less important as the cold pool further developed.

As a result of this deepening and accelerating cold pool, the convection had developed into a bowing segment by 1000 UTC. The development of this bowing segment corresponded to the transition to an upshear-tilted system, with a front-to-rear mesoscale updraft located above a RIJ and mesoscale downdraft by this time. This change is structure during this period allowed the system to transition into a well-defined leading-line, trailing-stratiform MCS by 1200 UTC (Fig. 45c). This

transition in structure was examined in a vorticity balance framework (Rotunno et al., 1988; Weisman, 1992, 1993) and will be discussed later in this chapter.

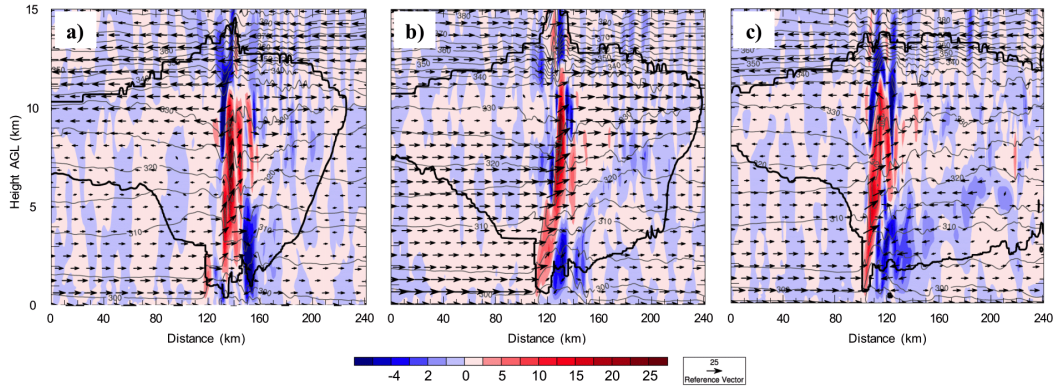

Figure 49: Vertical cross sections of vertical motion (shaded; m s^{-1}), system-relative wind vectors (m s^{-1}), potential temperature contours (gray; K), and cloud boundary (thick black line) for (d) 0800 UTC, (e) 0900 UTC, and (f) 1000 UTC. The cross section paths are expanded on those depicted in Fig. 44.

The primary convective portion of the system[3] resembled a surface-based MCS, with a low cloud base and well-defined surface cold pool, which lacked a preceding wave response (Fig. 48c). While the outflow boundary provided sufficient lift to maintain the system (Fig. 48c), inflow parcels tilted substantially rearward with height and contributed to a well-defined mesoscale updraft (Fig. 47c). Moreover, the updraft strength had diminished somewhat since 0900 UTC, which was consistent with the prominent upshear tilt of the updraft by this time. Parker (2010) found that sloped updrafts tend to be more negatively impacted by downward-directed pressure perturbation accelerations owing to their greater horizontal extent[4], especially in the presence of a surface cold pool. Because CAPE was more

[3]Cross sections at 1200 UTC were taken through the southwestern flank owing to the interaction between the primary MCS and a secondary convective cluster in Texas.

[4]These contributions, along with entrainment, are neglected from traditional parcel theory and thus CAPE calculations.

than sufficient for convective sustenance (will be discussed in section 4.3), this increased downward-directed pressure perturbation may have contributed to weakening convective updrafts at this time. Additionally, while convective downdrafts were weaker than previous hours, a well-defined mesoscale downdraft region with an accompanying RIJ still existed in the convective system, helping to maintain this upshear tilt (Fig. 47c).

By 1500 UTC, the cold pool had begun to move away from the convection (Fig. 66d), and the leading updraft induced by the convective outflow boundary was

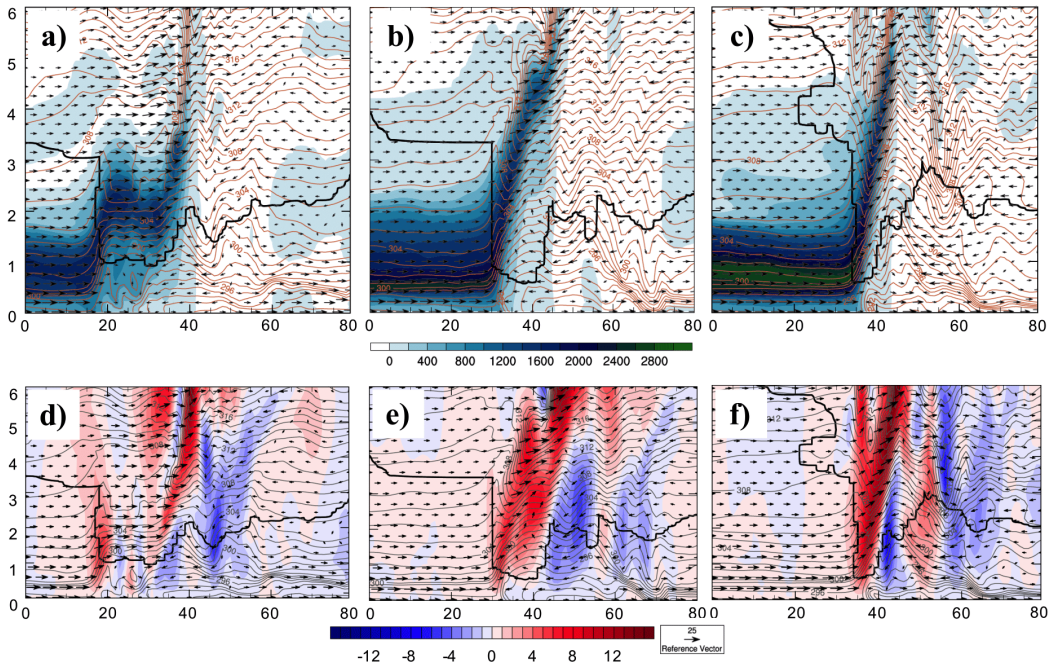

Figure 50: Vertical cross sections of (top) CAPE (shaded; J kg^{-1}), system-relative wind vectors (m s^{-1}), potential temperature contours (orange; K), and cloud boundary (thick black line) for (a) 0800 UTC, (b) 0900 UTC, and (c) 1000 UTC, and (bottom) vertical motion (shaded; m s^{-1}), system-relative wind vectors (m s^{-1}), potential temperature contours (gray; K), and cloud boundary (thick black line) for (d) 0800 UTC, (e) 0900 UTC, and (f) 1000 UTC. The cross section paths are depicted in Fig. 44 with the green circle representing 0 km.

only ~3 m s^{-1}. The strongest convective updraft was located 15-20 km behind the outflow boundary (Fig. 48d), suggesting that convective maintenance owing to the surface cold pool had considerably diminished, and the MCS began to weaken. At this time, the system had developed a well-defined stratiform region (Fig. 45d), but lacked a distinct RIJ-induced mesoscale downdraft (Fig. 47d). After 1800 UTC, the system further weakened and became disorganized, but discrete clusters of convection proceeded to move toward the Gulf Coast (Fig. 39g). The stratiform region had diminished in lateral extent by this time, which was consistent with the observations (Fig. 40g). However, several wind reports occurred with the observed system during this time, which were possibly attributed to either the vast region of surface outflow that moved into the region or more localized convective downdrafts in the clusters of convection.

In summary, the system exhibited a relatively complicated lifecycle. Early in the lifetime of the system, weak convection was associated with a deep baroclinic zone and associated cold air mass. After deep convection had formed, the system moved rapidly away from the baroclinic zone, likely in association with the generation of a wave response. This hypothesis will be discussed later in subsequent sections. Over time, the system developed a strong surface cold pool and eventually appeared to be surface-based. Therefore, the system was able to transition from being elevated and bore-driven to surface-based and cold-pool-driven prior to the low-level destabilization after sunrise. However, the system weakened over time as the outflow boundary became displaced from the convection and the system had acquired a substantial upshear tilt. While the convection had lost much of its organization by the time it reached southeastern Texas, the system still produced severe wind reports, one of which resulted in a fatality. Therefore, in contrast to most nocturnal MCSs, which decay near sunrise (Hane et al., 2008), this system,

was able to persist throughout much of the diurnal cycle despite encountering a destabilizing boundary layer and moving through a changing environment.

4.2 Characteristics of the Low-Level Jet

This section discusses the evolution of the LLJ in this simulation and how it contributes to the evolution of the convective system. Additionally, the simulated LLJ is compared to previous theoretical and observational studies of LLJs.

The horizontal wind field at 400 m AGL (Fig. 51) suggests that strong southerly flow associated with the LLJ interacted with the convective system from its initiation until at least 1200 UTC. In order to examine the variations in LLJ structure and strength with time, vertical profiles of the horizontal wind field were taken at a fixed location in central Texas (depicted by the orange circle in Fig. 52) (Figs. 53,54). These profiles were taken in an area of strongly sloping terrain, which has been thought to play a role in LLJ formation and structure (Holton, 1967; Shapiro et al., 2016). West-east vertical cross sections through this point were also utilized to evaluate variations along the sloping terrain (Fig. 55).

Although the dynamics of the LLJ were not the focus of this study, several inferences concerning the LLJ evolution at this location can be drawn. For example, prior to sunset, the low-level wind profile was characterized by southeasterly, upslope flow, which was consistent with the findings of previous studies (Holton, 1967; Shapiro et al., 2016). This behavior of the low-level flow during the afternoon was consistent with the response to daytime heating over higher terrain in the west, which generally results in an upslope component. Aspects of the low-level flow, such as the initial enhancement in the easterly low-level winds after sunset, was consistent with the onset of the inertial oscillation (Blackadar, 1957; Shapiro et al., 2016). The low-level winds eventually veered with time to having a downslope westerly component, which has been attributed to both enhanced radiative

cooling effects on the higher terrain to the west after the onset of nocturnal cooling and to the inertial oscillation (Blackadar, 1957; Holton, 1967; Shapiro et al., 2016).

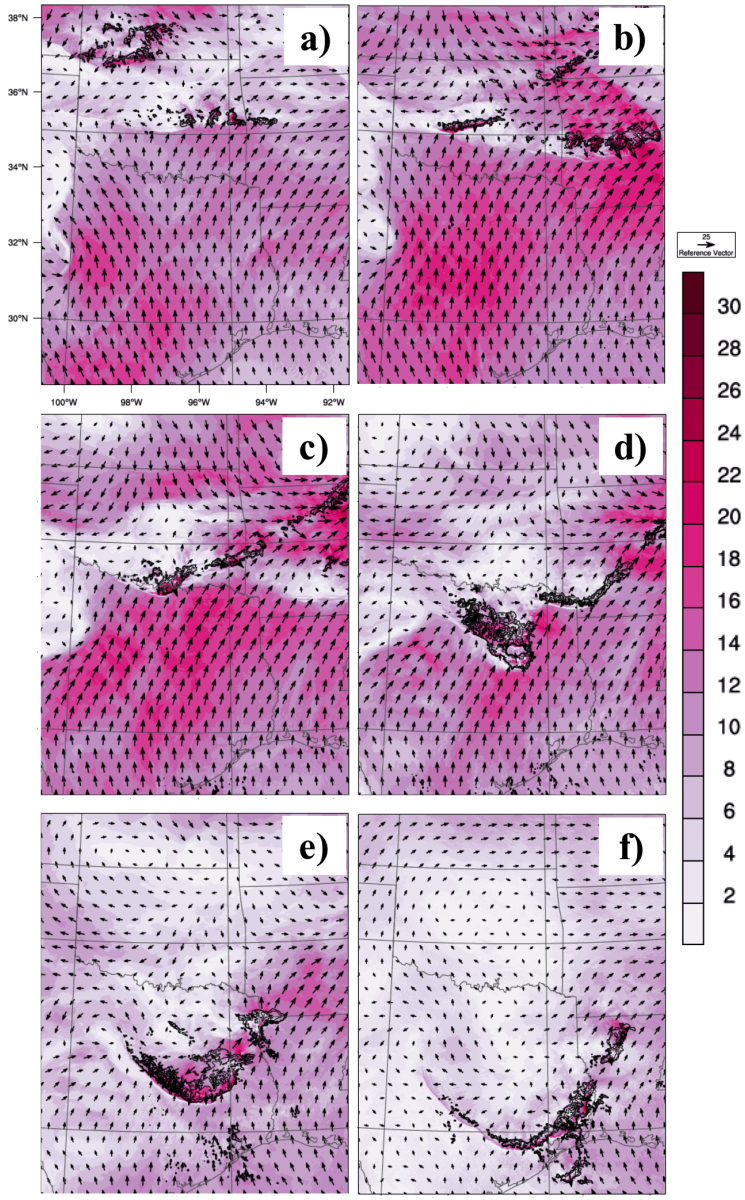

Figure 51: Horizontal wind (vector; reference vector 25 m s^{-1}), wind speed (shaded; m s^{-1}), and reflectivity contours (every 20 dBZ) at 400 m AGL for (a) 0300 UTC, (b) 0600 UTC, (c) 0900 UTC, (d) 1200 UTC, (e) 1500 UTC, and (f) 1800 UTC on 6 October 2014.

Additionally, influences from the synoptic-scale environment were important owing to the northeastward progression of the surface low with time, which likely resulted in enhancing the westerly wind component in the simulation.

The wind maximum at this location was initially located near the top of a stable nocturnal boundary layer (Fig. 53). However, over time, the low-level stable layer eroded along the sloping terrain, resulting in nearly uniform profiles of θ and mixing ratio with height (Figs. 53,54). This turbulent mixing beneath the maximum winds was also manifest in higher turbulent kinetic energy (TKE) values along the sloping terrain at 0600 and 0900 UTC (Figs. 55h,i). As a result of the onset of this LLJ-induced turbulence, the height of the wind maximum shifted upward between 0300 UTC and 0600 UTC (Figs. 53,55,56) and the thermodynamic

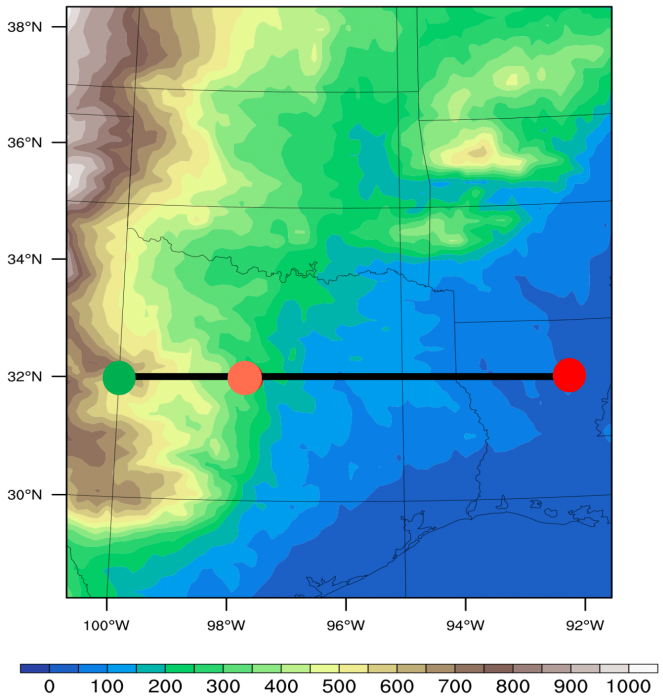

Figure 52: Terrain height above mean sea level (shaded; m). The black line represents the cross section path for the plots in this section. The green and red circles represent the start (0 km) and end points, respectively. The orange filled circle represents the location of the LLJ profiles in Figs. 53,54.

structure of the nocturnal boundary layer exhibited nearly-neutral stability (Figs. 53), which was consistent with the findings of previous observational studies (e.g., Klein et al., 2016). In addition to the thermal evolution at low-levels, the vertical wind profile aided in modifying the θ profile and stability above ~500 m. More specifically, persistent westerly flow acted to advect higher θ air eastward off the higher terrain. This westerly flow resulted in the development of a prominent capping inversion over time (Fig. 55). The evolving vertical structure in the LLJ profile had implications for the development and evolution of the instability fields, which will be discussed in the next section.

We have a few hypotheses for the existence of low-level mixing beneath the LLJ, which has been associated with mechanically-generated turbulence from strong LLJs (e.g., Blackadar, 1957; Banta et al., 2003, 2006; Klein et al., 2016). One likely contribution is from the initial enhancement of easterly upslope flow at ~125

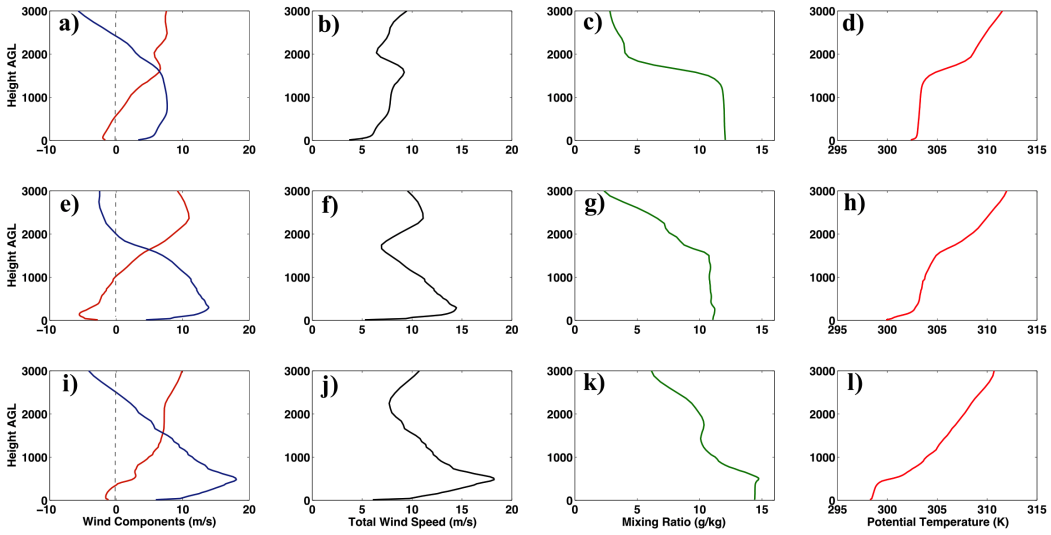

Figure 53: Vertical profiles of (a),(e),(i) zonal (orange) and meridional (blue) wind components (m s^{-1}), (b),(f),(j) horizontal wind speed (m s^{-1}), (c),(g),(k) water vapor mixing ratio (g kg^{-1}), and (d),(h),(l) potential temperature (K) for (top) 0000 UTC, (middle) 0300 UTC, and (bottom) 0600 UTC.

m AGL, which provided an elevated source of adiabatic cooling, acting to decrease the low-level stability. Effects from this enhanced cooling aloft aiding in the onset of turbulence seem to be plausible owing to the corresponding depths of the low-level easterly flow and nearly well-mixed θ at 0600 UTC (Fig. 53i,l). Moreover, after 0900 UTC when the easterly flow component was absent from the profile, the stable nocturnal PBL redeveloped prior to the onset of solar heating (Fig. 54d,h).

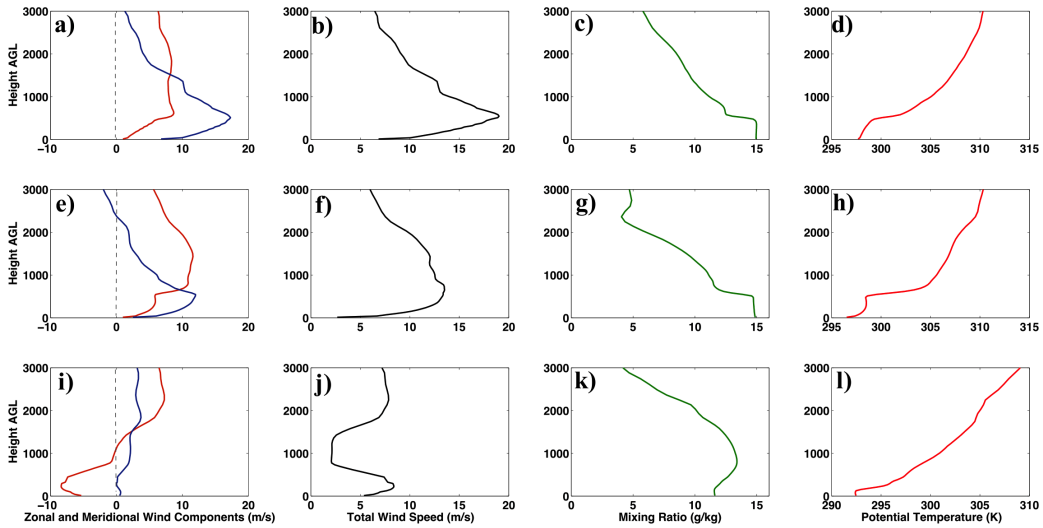

Figure 54: Same as in Fig. 53, but for (top) 0900 UTC, (middle) 1200 UTC, and (bottom) 1500 UTC. Note the different axis limits on the potential temperature panels. This location had been impacted by convection by 1500 UTC.

The LLJ in this simulation resulted in substantial moisture advection over time, with water vapor mixing ratio values increasing dramatically from approximately 11 g kg^{-1} to nearly 15 g kg^{-1} below the level of maximum winds (Figs. 53,54,55). One consequence of moisture advection by a LLJ that has not received significant attention in the literature is the distinct enhancement in the downwelling long-wave radiation emitted by water vapor and possible cloud cover (Fig. 57). The enhancement of downwelling radiation along the LLJ axis reduced the cooling rate relative to the drier air mass farther east, which can be inferred by less prominent

radiation contributions away from the LLJ axis. While the rate of cooling was less than that farther east where a nocturnal inversion developed, the lowest ~500 m still progressively cooled throughout the night along the LLJ axis. However, the stability of this layer was much less than farther east, resulting in a lower

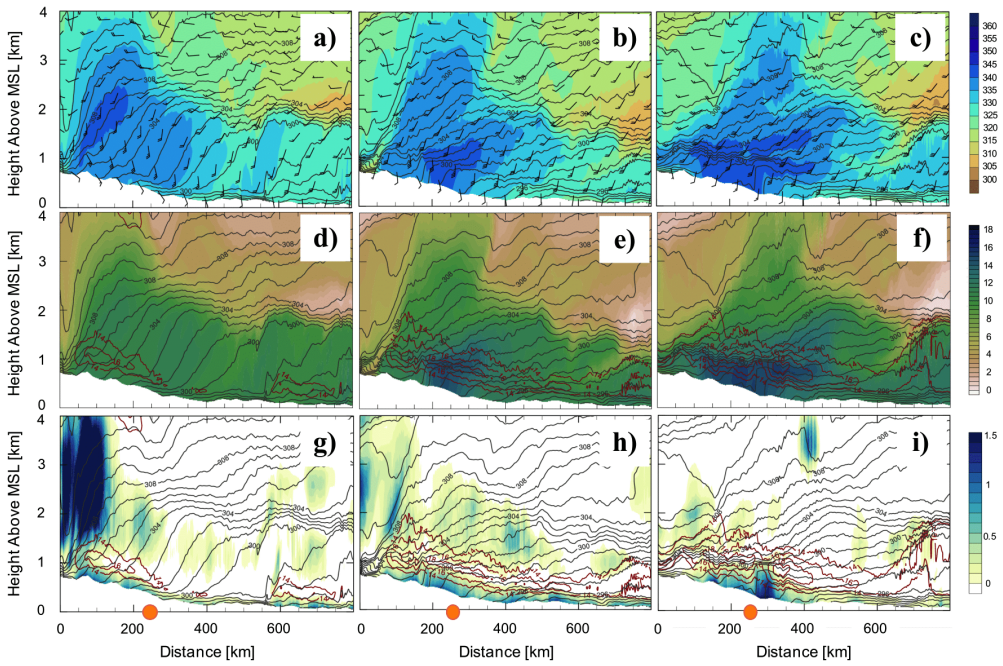

Figure 55: West-east vertical cross sections of (top) θ_e (shaded; K), theta (black contours; K), and wind barbs (knots; 1 knot = 0.51 m s^{-1}) for (a) 0300 UTC, (b) 0600 UTC, and (c) 0900 UTC, (middle) water vapor mixing ratio (shaded; g kg^{-1}), theta (gray contours; K), and horizontal wind speed (red contours; every 2 m s^{-1} starting at 14 m s^{-1}) for (d) 0300 UTC, (e) 0600 UTC, and (f) 0900 UTC, and (bottom) turbulent kinetic energy (shaded; m^2 s^{-2}), theta (gray contours; K), and horizontal wind speed (red contours; every 2 m s^{-1} starting at 14 m s^{-1}) for (g) 0300 UTC, (h) 0600 UTC, and (i) 0900 UTC on 6 October 2014. Cross section path depicted in Fig. 52 where 0 km corresponds to the green filled circle. The orange circles depict the location of the point profiles depicted in Figs. 53,54, and 56.

Richardson number and increased likelihood of mechanically-generated turbulence by a strengthening LLJ (e.g., Klein et al., 2016).

In addition to the temporal trends observed at the selected location, spatial variability in the low-level stability existed along the terrain slope existed (Fig. 55). While the low-level stable layer had eroded beneath the maximum winds along the sloping terrain, this effect was absent farther east, and a well-developed nocturnal boundary layer continued to develop throughout the night. After sunset, a deep residual boundary layer was present over the higher terrain to the west (Fig. 55). Persistent westerly flow from the synoptic environment and inertial oscillation advected this warm aloft eastward, contributing to the formation of the capping inversion in Figs. 53,54,55. However, effects of this advection were less apparent farther east, limiting the capping in this region.

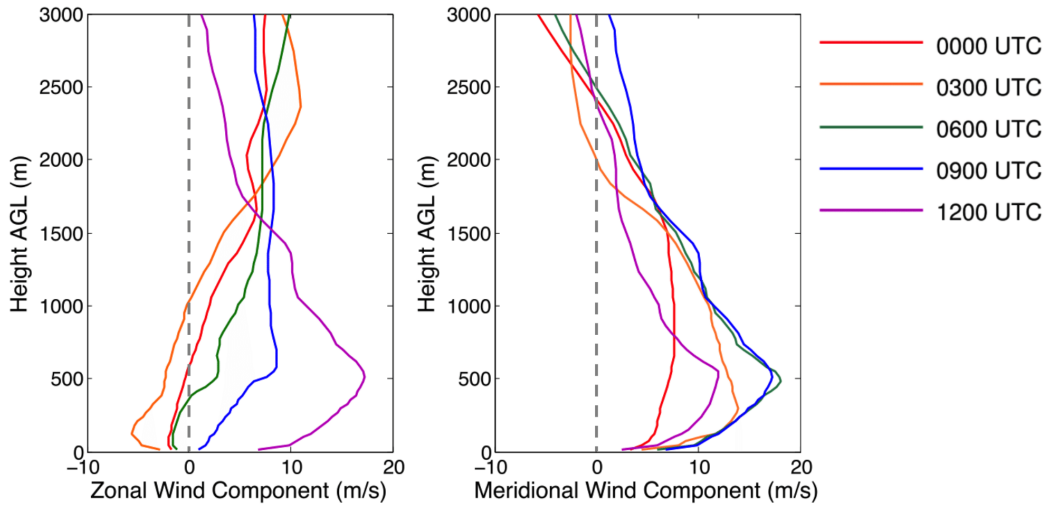

Figure 56: Time-evolution of zonal (left) and meridional (right) wind components (m s^{-1}) in the lowest 3 km for (red) 0000 UTC, (orange) 0300 UTC, (green) 0600 UTC, (blue) 0900 UTC, and (violet) 1200 UTC. 1500 UTC is not included owing to contamination by convection. Location is the same as in Figs. 53,54.

Initially, moist, high θ_e air existed solely aloft, which corresponded to poleward moisture advection by the LLJ. However, as the LLJ veered with time, this moist air was advected farther east above the stable layer. Additionally, along the sloping terrain where the greatest moisture advection was occurring, this moisture

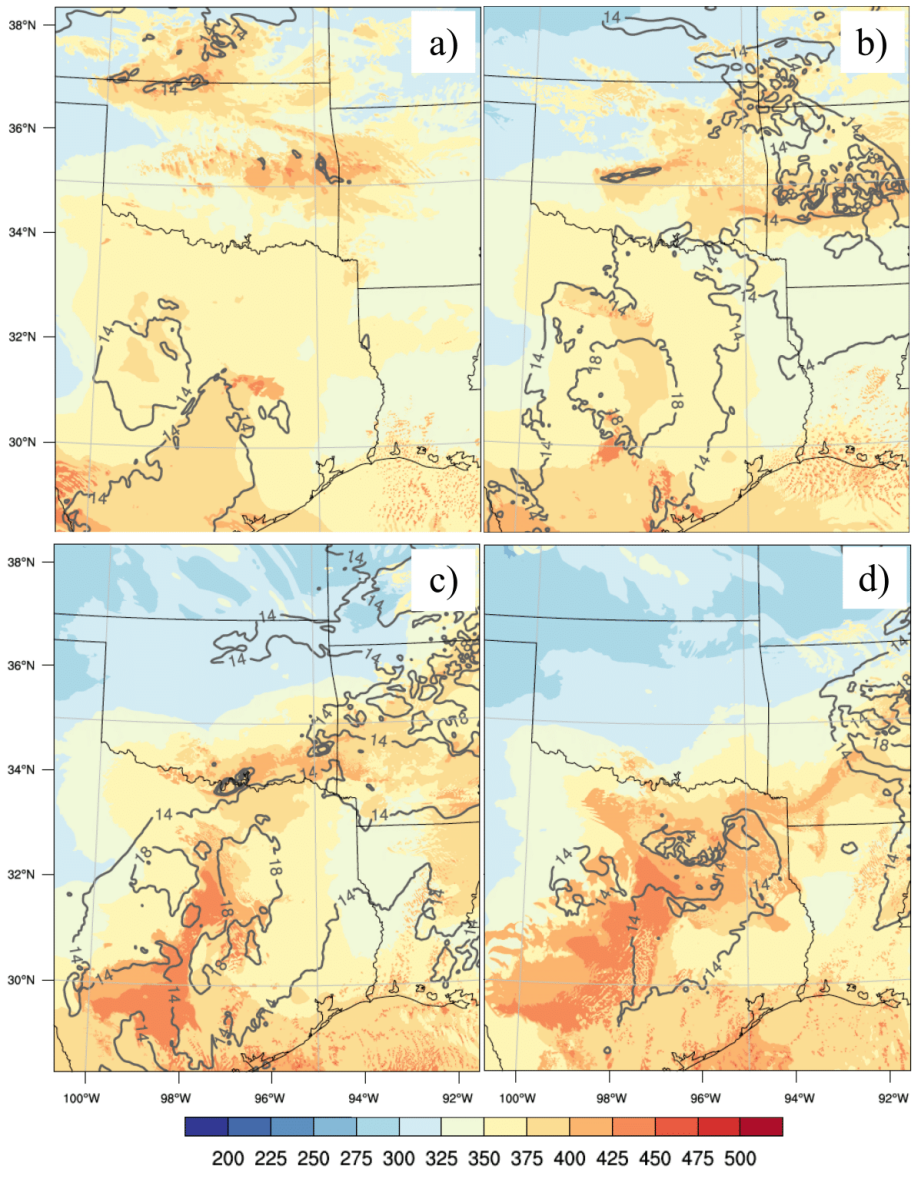

Figure 57: Downwelling longwave radiation at the surface (shaded; W m^{-2}) and 500-m horizontal wind speed (contour; m s^{-1}) for (a) 0300 UTC, (b) 0600 UTC, (c) 0900 UTC, and (d) 1200 UTC.

extended downward to the surface, resulting in the layer of nearly uniform mixing ratios and θ_e (Figs. 53,54,55). This dramatic increase in surface moisture (from ~11 to ~15 g kg^{-1}) and θ_e was likely the outcome of two concurrent processes related to the turbulence beneath the LLJ. One likely contribution was that moisture advected poleward by the LLJ was enhanced at low levels through downward turbulent mixing of air beneath the maximum winds of the LLJ. Additionally, turbulent mixing also resulted in the downward mixing of horizontal momentum such that the near-surface wind speeds were not negligible, allowing surface winds to advect moist, high θ_e air in the region of sloping terrain. Farther east, where the stable layer strengthened over time and little mixing occurred at low levels, these temporal trends were absent, and the moist, high θ_e air existed aloft throughout the nighttime.

4.3 Evolution of the Convective Instability

Several past studies have examined favorable environments for nocturnal convective systems over the Great Plains. These studies (e.g., Moore et al., 2003) have found that surface-based CAPE diminishes over time in the nocturnal environment owing to radiative cooling of the boundary layer. The analysis in the previous section revealed how the LLJ resulted in dramatic moisture advection, which acted to modify the radiation budget to slow nocturnal cooling beneath the jet axis. The vertical profiles along the sloping terrain displayed strong evidence for vertical mixing, which would modify the CAPE and CIN within the lower atmosphere. Additionally, CAPE and CIN would be impacted by the eastward advection of a deep, residual boundary layer, which formed atop the higher terrain. This section discusses the evolution of the CAPE and CIN fields throughout the night and how this evolution played a role in maintaining the convective system.

Although surface-based CAPE typically diminishes over time in nocturnal convective environments owing to radiative cooling, a relatively narrow corridor (~200-300 km wide) of high surface-based CAPE had progressed northward along the sloping terrain throughout the night (Fig. 58). This corridor corresponded to high surface mixing ratio values (>13 g kg^{-1}; Fig. 59) and strong surface winds, and its evolution reflected the expected veering of the LLJ with time. However,

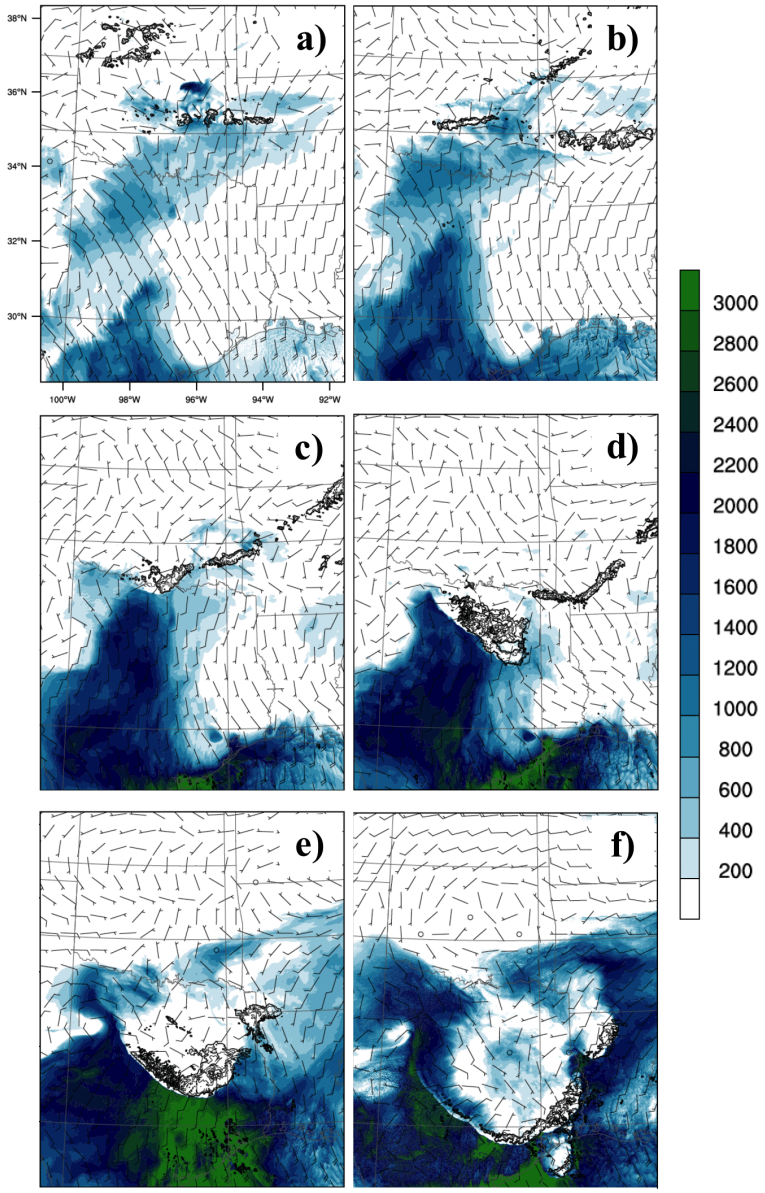

Figure 58: Same as in Fig. 59, but for surface-based CAPE (shaded; J kg^{-1}).

this corridor of high surface-based instability corresponded to substantial inhibition (~150-350 J kg^{-1}; Fig. 60), which would act to suppress the development of convective updrafts in this region. This capping was attributed to the eastward

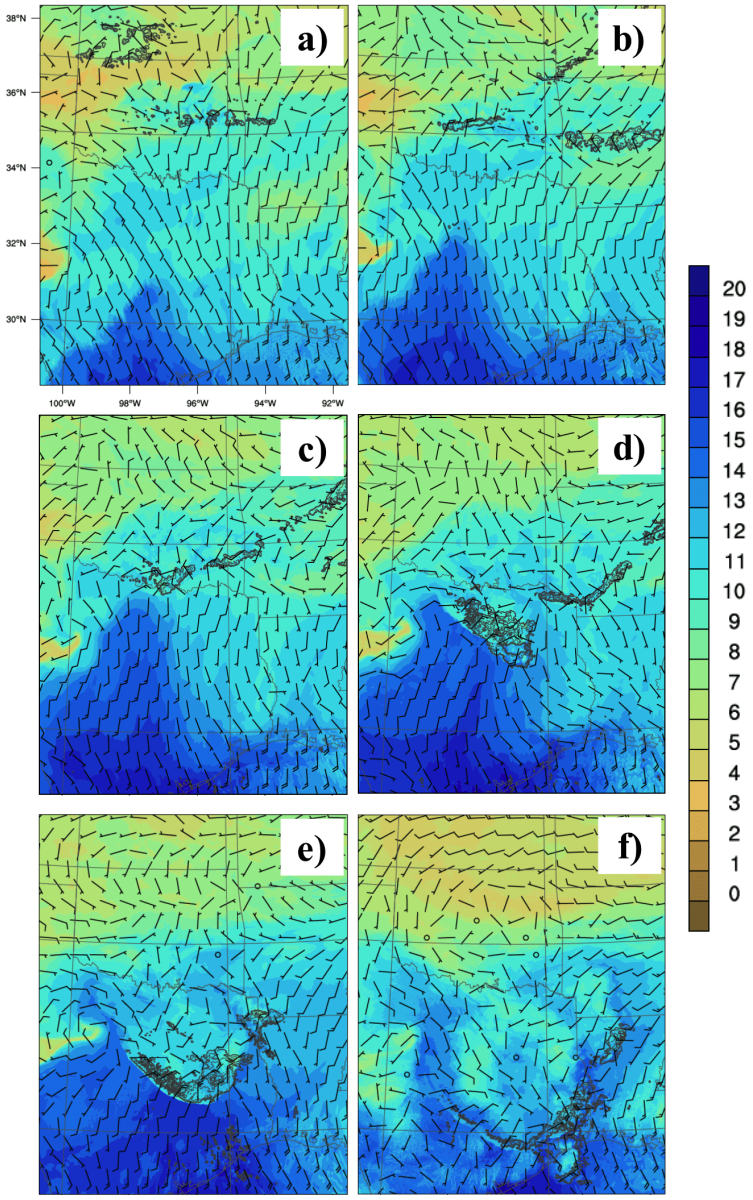

Figure 59: Surface mixing ratio (shaded; g kg^{-1}), wind barbs (knots; 1 knot = 0.51 m s^{-1}), and reflectivity contours (every 20 dBZ) for (a) 0300 UTC, (b) 0600 UTC, (c) 0900 UTC, (d) 1200 UTC, (e) 1500 UTC, and (f) 1800 UTC on 6 October 2014.

advection of the residual well-mixed boundary layer from westerly flow associated with a veering LLJ, as described in section 4.2.

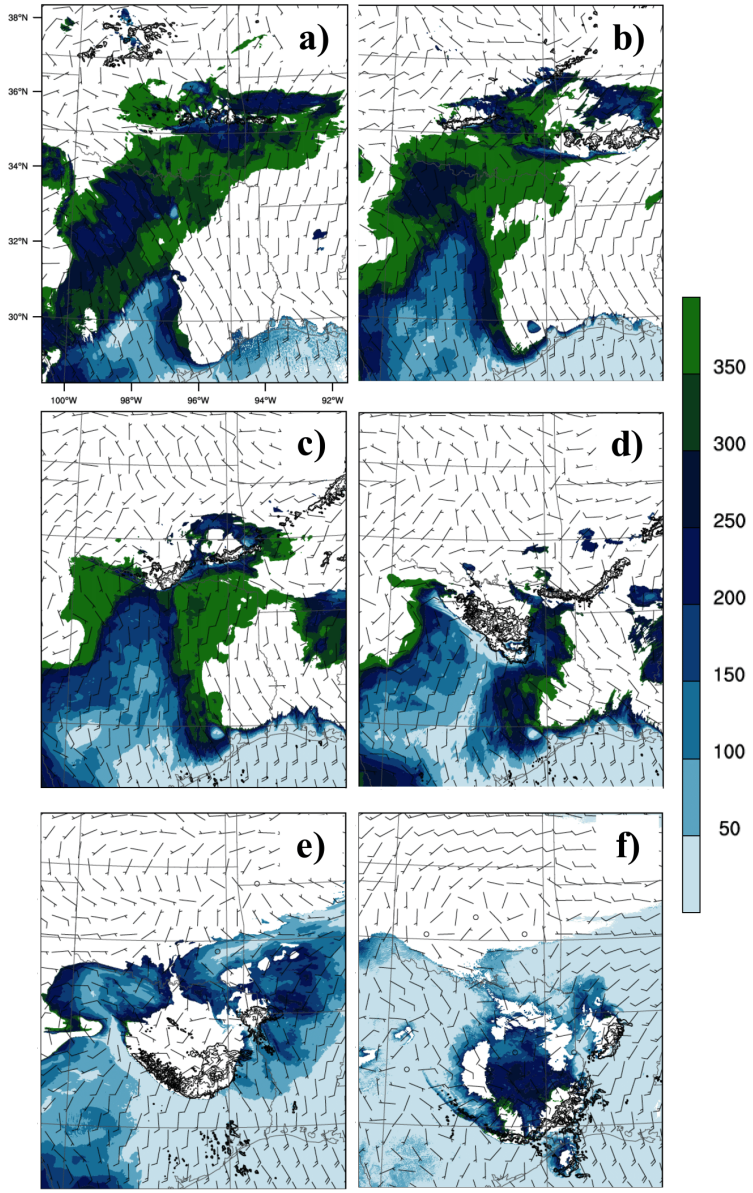

Figure 60: Same as in Fig. 59, but for surface-based CIN (shaded; J kg^{-1}).

The evolution of the vertical profiles of CAPE and CIN along the sloping terrain is depicted in Fig. 61. The horizontal and vertical distribution in CAPE is highly resemblant of the water vapor mixing ratio profiles described in the previous section, suggesting that moisture advected by a veering LLJ dominated the

development and evolution of this instability. Moreover, the strengthening of the capping inversion is evident in the potential temperature cross sections and soundings from the location described in the previous section (Fig. 62). This capping inversion limited the decrease in low-level CIN (Fig. 61d-f) over time despite that CAPE dramatically increased (Fig. 61a-c) owing to increasing moisture, preventing this instability from being realized. Therefore, effects from the LLJ acted to modulate both the CAPE and CIN profiles in the environment.

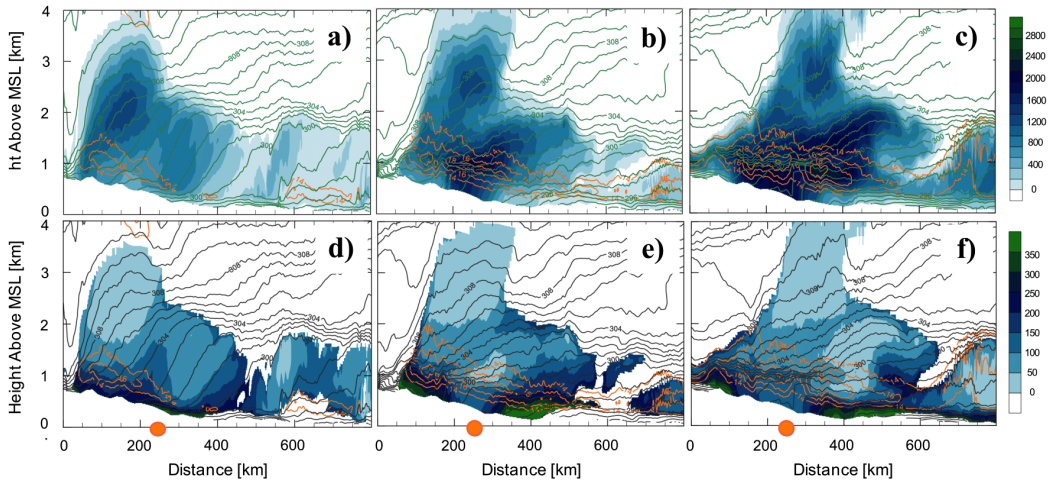

Figure 61: Same as in Fig. 55, but for (top) CAPE (shaded; J kg^{-1}), theta (green contours; K), and horizontal wind speed (orange contours; every 2 m s^{-1} starting at 14 m s^{-1}) for (a) 0300 UTC, (b) 0600 UTC, (c) 0900 UTC, and (bottom) CIN (shaded; J kg^{-1}), theta (gray contours; K), and horizontal wind speed (orange contours; every 2 m s^{-1} starting at 14 m s^{-1}) for (g) 0300 UTC, (h) 0600 UTC, (i) 0900 UTC. Cross section path depicted in Fig. 52 where 0 km corresponds to the green filled circle. The orange circles represent the location of the point profiles depicted in Figs. 53,54, and 56.

The development of this capping inversion was mostly confined to the area of considerably sloped terrain, and these effects were muted farther east. In this eastern region, elevated CAPE >2000 J kg^{-1} corresponded to less (<50-100 J kg^{-1})

inhibition (Fig. 61). However, a stable PBL existed in this region, and surface winds were weaker, which limited surface moisture advection for the development

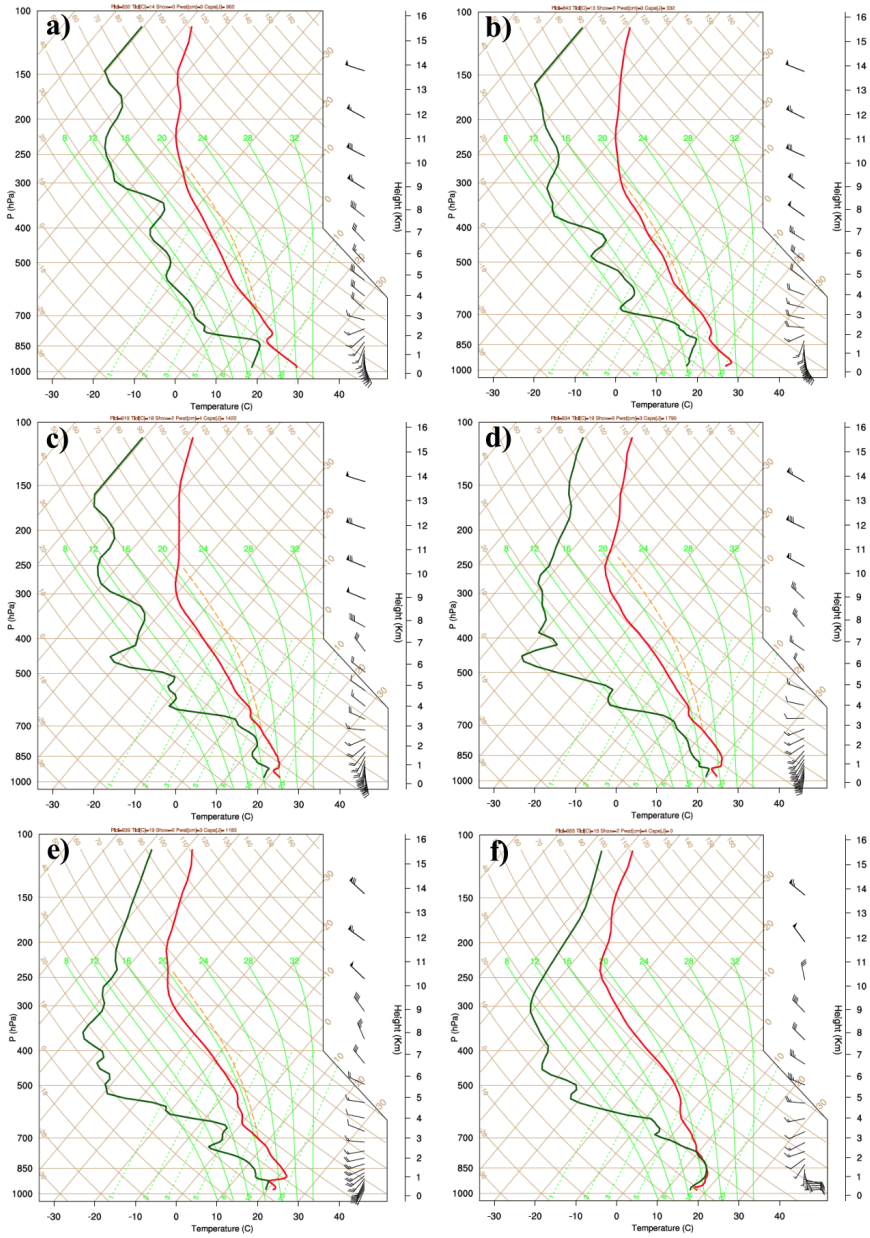

Figure 62: Model output soundings (traditional Skew-T / Log-p diagrams) at the same location as in Figs. 53,54 for (a) 0000 UTC, (b) 0300 UTC, (c) 0600 UTC, (d) 0900 UTC, (e) 1200 UTC, and (f) 1500 UTC on 6 October 2014. Height listed is in km above MSL. Wind barbs are depicted in knots (1 knot = 0.51 m s^{-1}).

of high surface-based CAPE (Fig. 61). As a result, the environment within this region remained favorable for elevated convection until the low-level winds had veered to having a more southwesterly component, resulting in an increase in surface moisture and CAPE (Figs. 58d,59d).

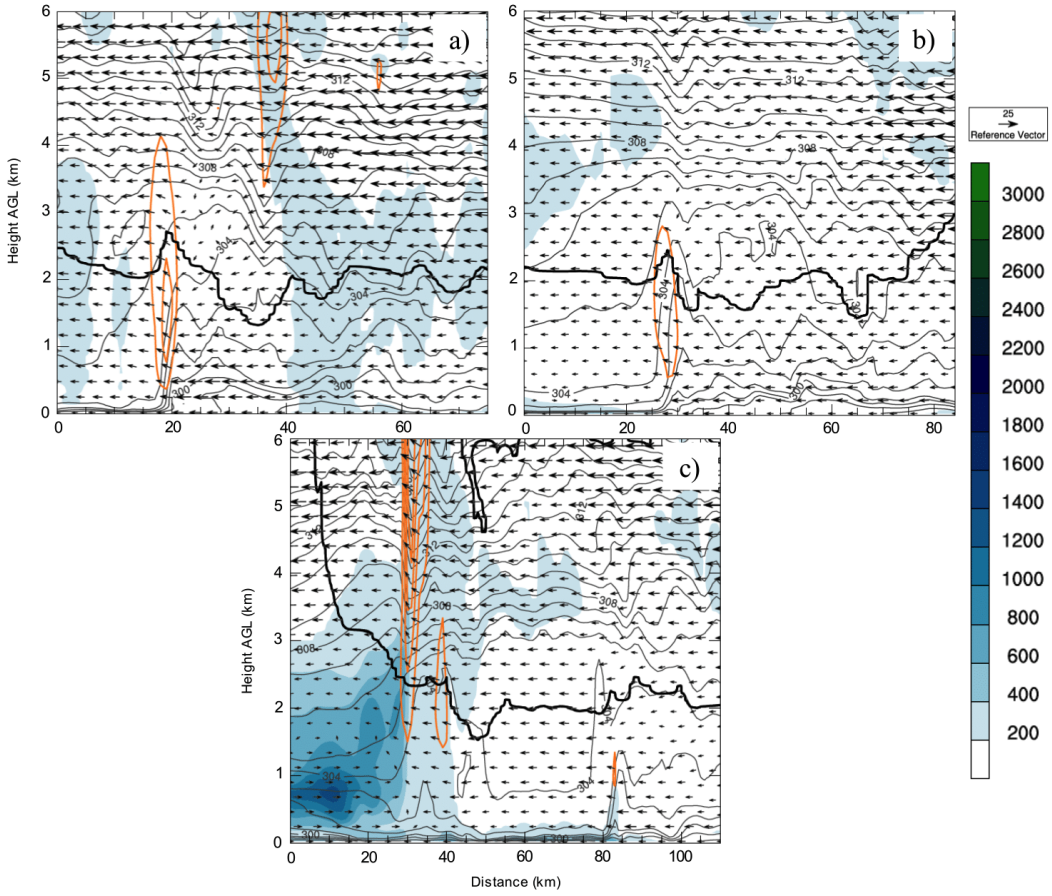

Figure 63: Vertical cross sections (0-6 km AGL) of CAPE (shaded; J kg^{-1}), wind vectors (m s^{-1}; reference vector 25 m s^{-1}), potential temperature (K), and vertical velocity (orange line; every 2 m s^{-1}) for (d) 0300 UTC, (e) 0400 UTC, and (f) 0500 UTC on 6 October 2014. Cross section paths are the same as in Fig. 42.

Despite the high spatiotemporal variability in surface moisture and instability, the evolution of the convective system indicates that the system moved southward into an increasingly unstable environment over time (Figs. 58,59). Surface-based CAPE was nearly absent near the location of convective initiation at both 0300

UTC and 0600 UTC (Figs. 58a,b). Moreover, cross sections through the baroclinic zone indicate that CAPE was absent at all levels ahead of the initiating boundary until approximately 0500 UTC, at which time deep convective updrafts began to form (Fig. 63). This deep convection was located in proximity to elevated CAPE values of approximately 800-1200 J kg^{-1} (Fig. 63c). Additionally, CIN values of less than 50 J kg^{-1} existed from ~1-2.5 km AGL (Fig. 64), suggesting that these convective updrafts were most likely to be rooted in this layer. This finding was

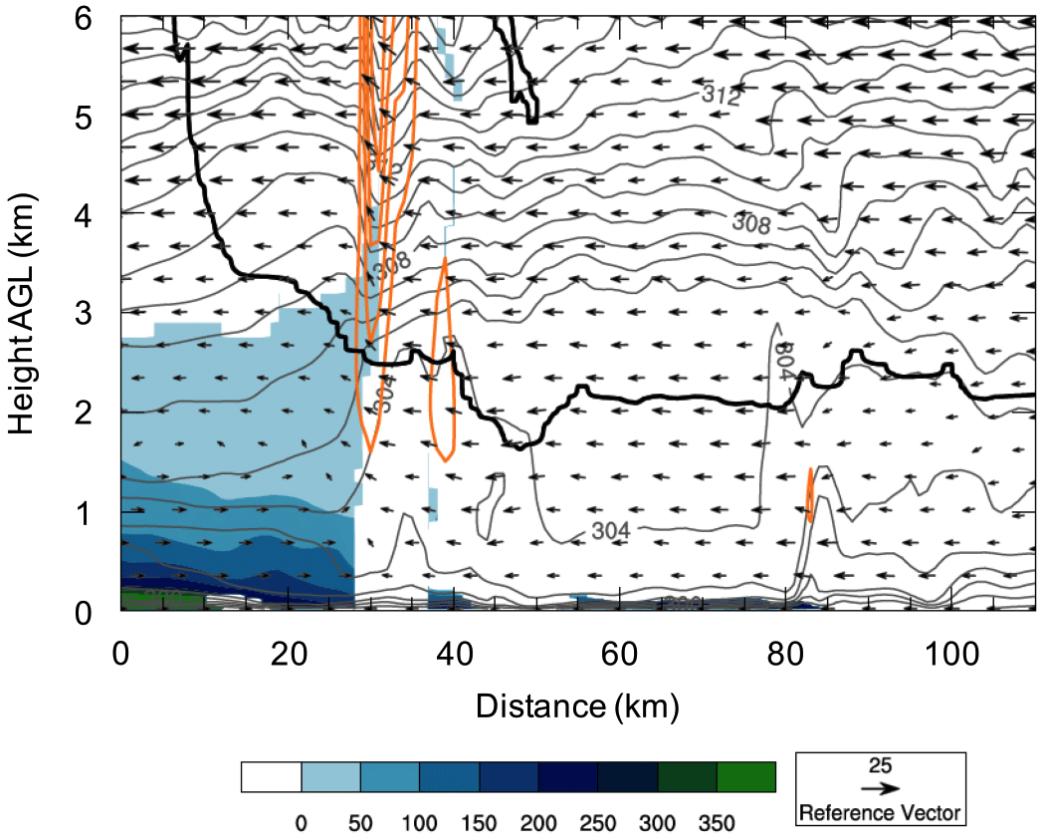

Figure 64: 0-6 km vertical cross section of CIN (shaded; J kg^{-1}), ground-relative wind vectors (m s^{-1}; reference vector 25 m s^{-1}), potential temperature (K), vertical velocity (orange line; every 2 m s^{-1}), and cloud boundary (thick black line) at 0500 UTC. Cross section path is the same as in Fig. 42.

consistent with the observations, which suggested that the convective system was highly elevated and relatively shallow at initiation.

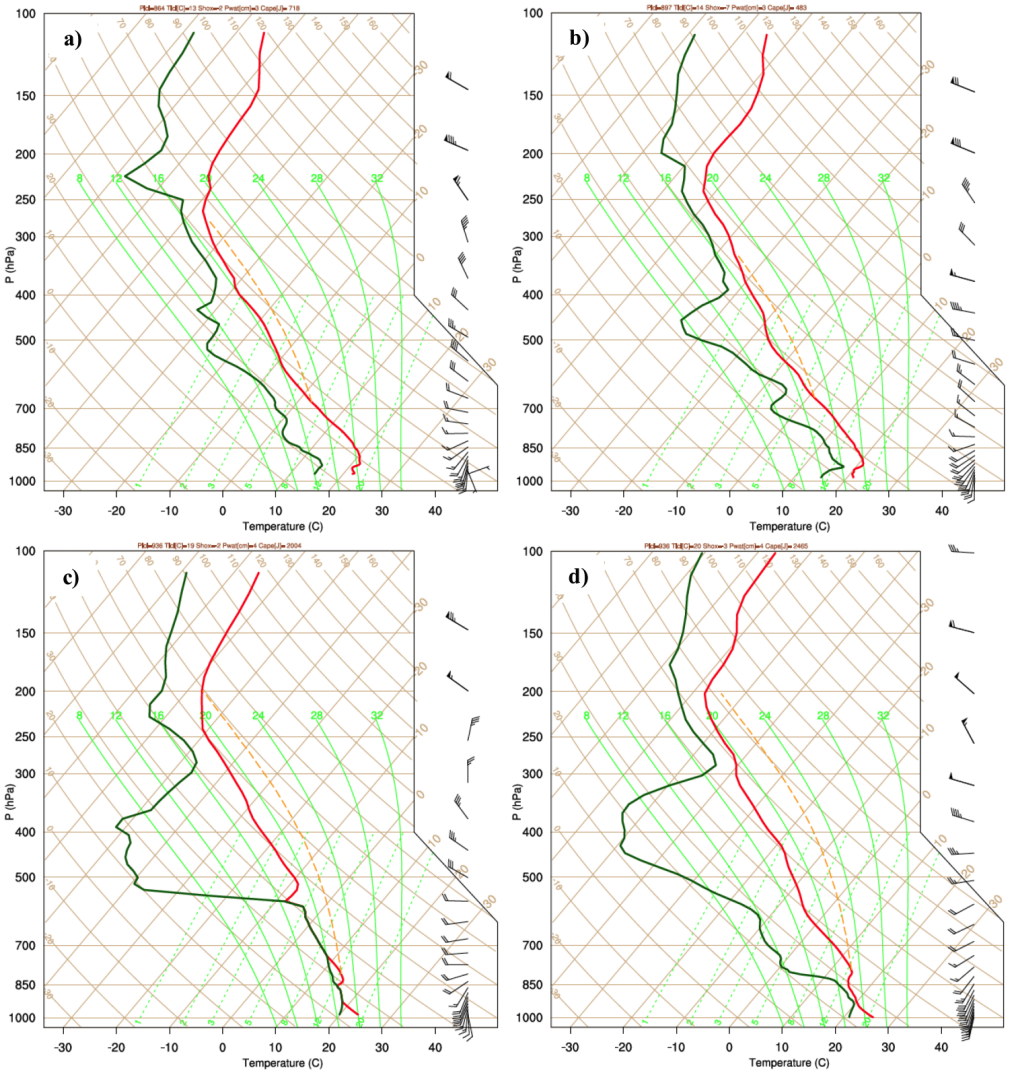

Figure 65: Model output soundings (traditional Skew-T / Log-p diagrams) at the inflow point location (0 km in Fig. 48)) for (a) 0600 UTC, (b) 0900 UTC, (c) 1200 UTC, and (d) 1500 UTC on 6 October 2014. Height listed is in km above MSL.

Despite the lack of surface-based CAPE near initiation, convective inflow became more unstable over time. Inflow soundings (Fig. 65) and vertical cross sections through the convective line (Figs. 66,67) provide insight into the evolution of instability in the inflow region. At 0600 UTC when surface-based CAPE

was nearly absent ahead of the line, the convective system was maintained by a bore, which was supported by the presence of a stable boundary layer topped by a deep layer of lesser stability (Fig. 65a). At this time, the system was fed by a layer of elevated CAPE in excess of 2000 J kg^{-1}, which gradually ascended prior to being lifted ~1 km over the bore (Fig. 66a). Moreover, along the isentropes,

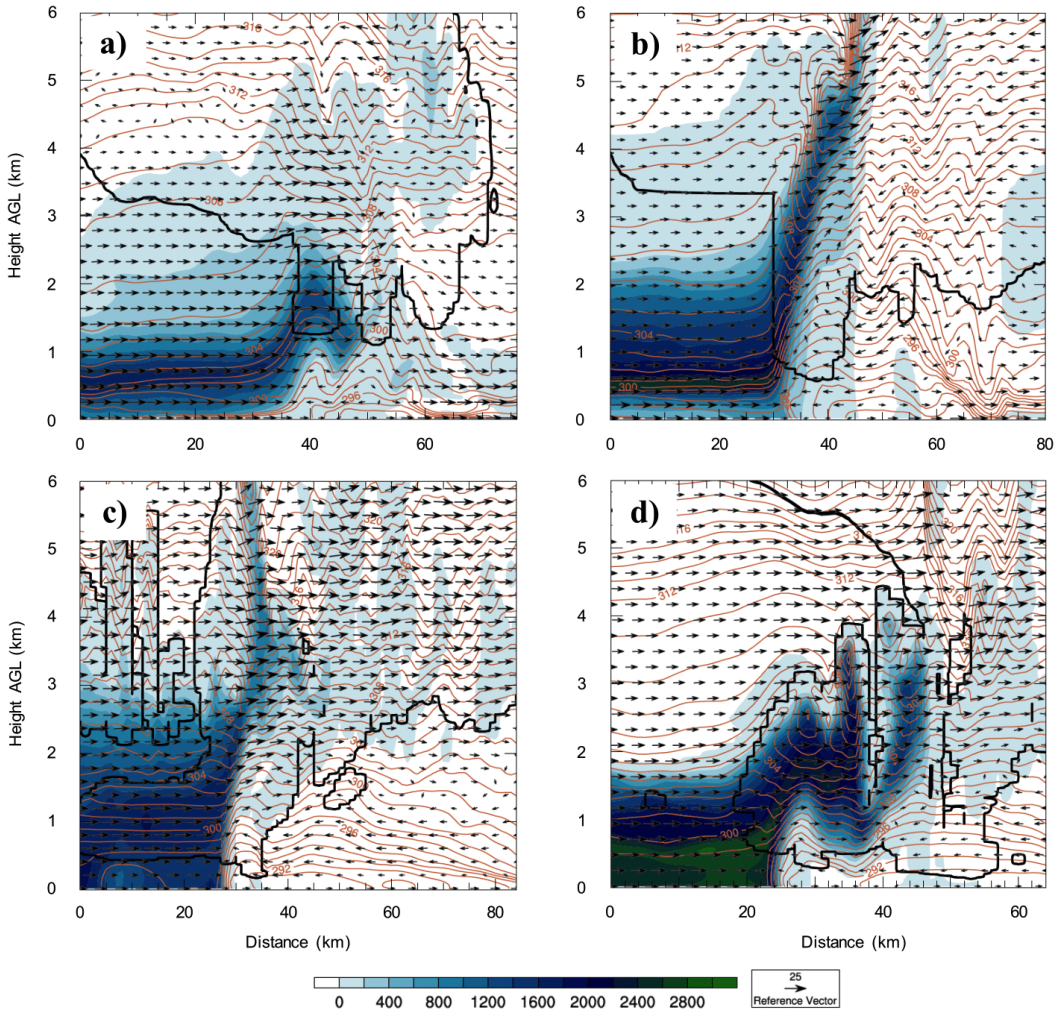

Figure 66: Vertical cross sections of CAPE (shaded; J kg^{-1}), system-relative wind vectors (m s^{-1}), potential temperature contours (orange; K), and cloud boundary (thick black line) for (a) 0600 UTC, (b) 0900 UTC, (c) 1200 UTC, and (d) 1500 UTC. The cross section paths are depicted in Fig. 44 with the green circle representing 0 km.

CIN decreased dramatically as this inflowing air was lifted by the bore, suggesting that the bore helped to destabilize the environment (Fig. 67a).

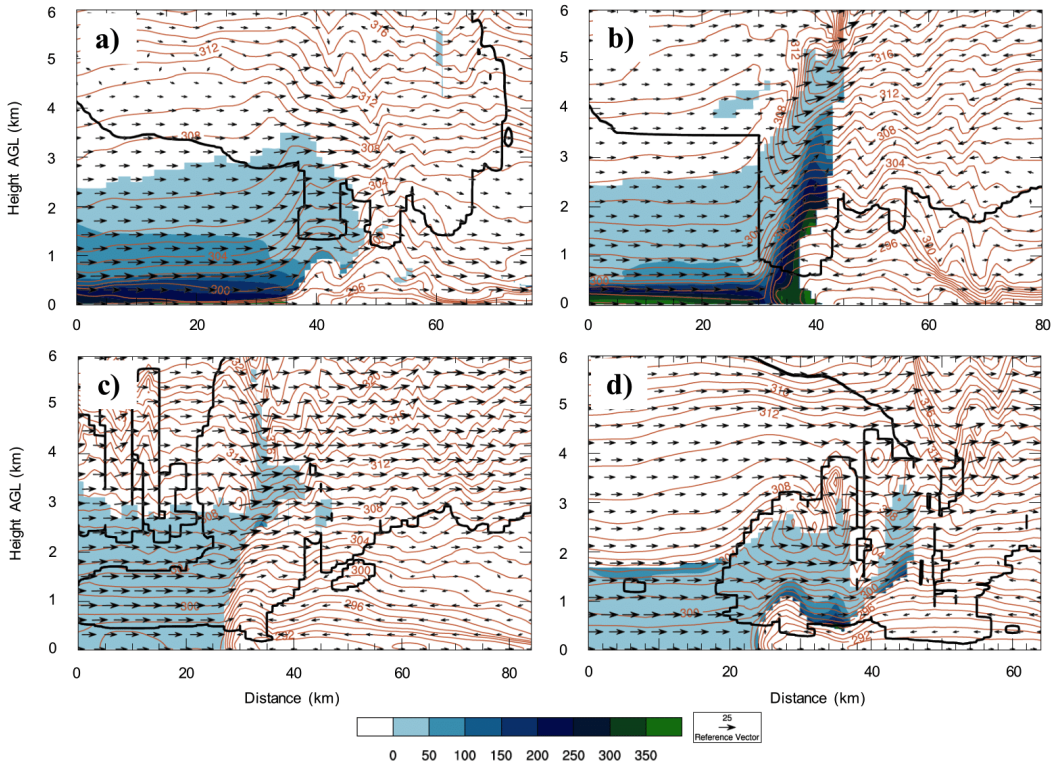

Figure 67: Vertical cross sections of CIN (shaded; J kg^{-1}), system-relative wind vectors (m s^{-1}), potential temperature contours (orange; K), and cloud boundary (thick black line) for (a) 0600 UTC, (b) 0900 UTC, (c) 1200 UTC, and (d) 1500 UTC. The cross section paths are depicted in Fig. 44 with the green circle representing 0 km.

By 0900 UTC, the low-level profile remained stable, but the the system had become maintained by a deep, surface cold pool. Moreover, the system had moved farther south into an environment with instability over a deeper layer (Fig. 66b), which likely contributed to strengthening the convection and the cold pool by this time. While surface-based CAPE had increased in proximity to the convective line since 0600 UTC (Fig. 66b), substantial inhibition greater than 350 J kg^{-1} (Fig. 67b) limited the potential for these parcels to be ingested into buoyant updrafts.

Deep cold pool lifting (~3-4 km) may have been sufficient to lift these stable surface parcels to their LFCs (Fig. 65b), but the system likely remained primarily elevated at this time.

The system remained within an environment characterized by primarily elevated CAPE until approximately 1200 UTC (Fig. 66). By this time, substantial surface-based CAPE (>1400 J kg^{-1}; Fig. 66c) existed adjacent to the cold pool forcing, and an inflow sounding confirmed that the boundary layer was well-mixed (Fig. 65c). Minimal capping (<50 J kg^{-1}) existed for these near-surface parcels (Figs. 67c), suggesting that the convection was able to transition from being elevated prior to sunrise.

Although the boundary layer began to destabilize owing to the onset of solar heating and turbulence which led to the cessation of the LLJ, moisture advected northward by the LLJ remained, allowing the environment to possess substantial instability during the daytime. As a result, the environment remained favorable for strong surface-based convection by 1500 UTC owing to minimally-capped (Figs. 65d,67d), low-level CAPE values exceeding 2800 J kg^{-1} (Fig. 66d) near the cold pool forcing. The presence of this instability allowed for the development of a widespread leading-line, trailing-stratiform MCS by this time. Therefore, the strengthening and persistence of the convective system during the morning suggested that it was able to transition from elevated to surface-based and continue as solar heating commenced and the LLJ broke down.

Gale et al. (2002) found that MCSs often have a tendency to dissipate after becoming separated from the contributions from the LLJ. However, the long-lived MCS herein continued to interact with the LLJ and did not exhibit this dissipation tendency during the morning. Additionally, despite that the LLJ weakened with the onset of solar insolation, contributions to the environmental instability from moisture advection existed after its cessation, allowing the MCS to persist in a

convectively unstable environment after sunrise. While the evolution of instability over time is atypical of what has been documented in previous studies of nocturnal convective environments, the convection exhibited an evolution typical of nocturnal systems until sunrise. After this time, the system was able to persist in a high-CAPE air mass for several hours despite that nocturnal convective systems typically dissipate after the onset of solar heating (Hane et al., 2003).

4.4 Characteristics of the Environmental Shear

The observed convective system was characterized by bowing segments and bookend vortices, one of which was associated with a nocturnal tornado. Additionally, the observed convection also contained supercellular structures in the more discrete convective cells. Because these phenomena are associated with strong vertical wind shear (e.g., Weisman, 1993; Thompson et al., 2007), the evolution of the environmental shear and its relationship to the simulated convective system is discussed in this section.

In addition to the strength of favorable environmental shear for severe convection, the orientation of the deep-layer (i.e., 0-6 km) shear vector relative to the initiating boundary (e.g., Bluestein and Weisman, 2000; Dial et al., 2010) and hodograph shape also play a role in determining storm mode. In this context, straight hodographs (environments with a unidirectional shear vector with height) tend to favor eventual upscale development owing to cell-cell interactions between left and right splitting storms (e.g., Weisman and Klemp, 1984) and the promotion of new cell development along the cold pool (e.g., Rotunno et al., 1988). The 0000 UTC environmental hodograph shape, as was discussed in section 2.1, was characterized by a mostly unidirectional shear profile in mid and upper levels. The low-level winds, especially during the nighttime, exhibited cyclonic curvature owing to a veering wind profile associated with the LLJ, as discussed in section 4.2.

This curvature may support rotating updrafts through the ingestion of streamwise vorticity (Davies-Jones, 1984).

The 0-6 km bulk shear magnitude is a standard tool that has been utilized in operational forecasting to discriminate between different modes of storm structure and evolution (e.g., Thompson et al., 2007). More specifically, shear in excess of 20 m s^{-1} (40 knots) over this layer has been shown to support of supercell rotation, while values in excess of 10 m s^{-1} (20 knots) have been shown to support gust front regeneration in multicell environments (e.g., Weisman and Klemp, 1982).

The 0-6 km bulk shear was in excess of 20 m s^{-1} (40 knots) throughout the northern portion of the domain for the entire duration of the simulation (Fig. 68). This area of stronger shear was coincident with the midlevel jet maxima, and shear values decreased toward the south away from the midlevel forcing. The existence of the strongest deep-layer shear to the north is supportive of the observations, which had embedded rotating updrafts and discrete supercells prior to upscale development into an organized MCS (discussed previously in section 4.1).

By 0900 UTC, the primary MCS was restrengthening into a bowing segment in south central Oklahoma (Fig. 68c). Near this strengthening convection, the shear was northwesterly and oriented orthogonal to the strongest portion of the line with values of ~45 knots (23 m s^{-1}). Previous studies such as Corfidi (2003) have found that MCSs tend move in the downshear direction, so the fact that the convection strengthened and accelerated toward the southeast around 0900 UTC is unsurprising from a forecasting perspective.

As the storm moved toward lower latitudes, the shear values generally decreased. Toward the south, the shear values were dominated by the stronger surface winds[5] accompanying the LLJ as upper-level winds were light (~20 knots or 10

[5]The surface winds used in the bulk shear calculation were from the lowest model level which was approximately 14 m AGL.

m s^{-1}) in this region. However, the utilization of the lowest model level likely resulted in an underestimation of the low-level shear values compared to using winds at the nose of the LLJ, so some caution should be taken when examining the shear in the region impacted by the LLJ. Additionally, these effective shear quantities are of greater utility for elevated convective environments since the effective shear only incorporate layers with positive CAPE (Thompson et al., 2007).

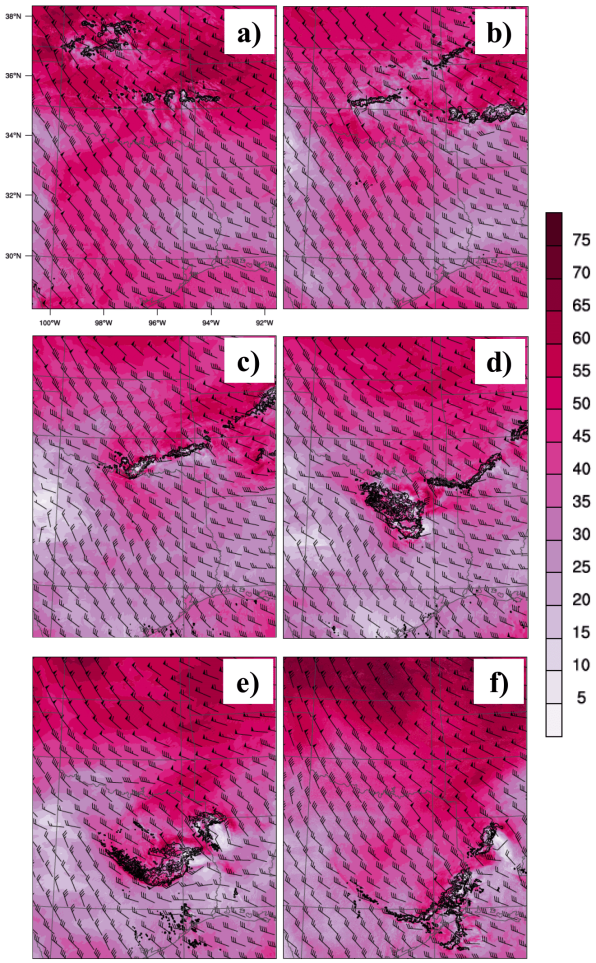

Figure 68: Bulk wind difference (knots; 1 knot = 0.51 m s^{-1}) between 0-6 km AGL (vectors; magnitude shaded) for (a) 0300 UTC, (b) 0600 UTC, (c) 0900 UTC, (d) 1200 UTC, (e) 1500 UTC, and (f) 1800 UTC on 6 October 2014.

By 1200 UTC, the primary convective system had organized and was located in northern Texas. The 0-6 km shear vector orientation near this system continued to be oriented approximately orthogonal to the strongest portion of the convection (Fig. 68d). By this time, environmental shear was decreasing throughout the region, which was likely attributed to both the weakening of the LLJ and the progression of the jet max to the east of the region. By 1500 UTC, the environmental shear over the 0-6 km depth had further decreased to 20-30 knots (10-15 m s^{-1}) owing to the cessation of the LLJ (Fig. 68e).

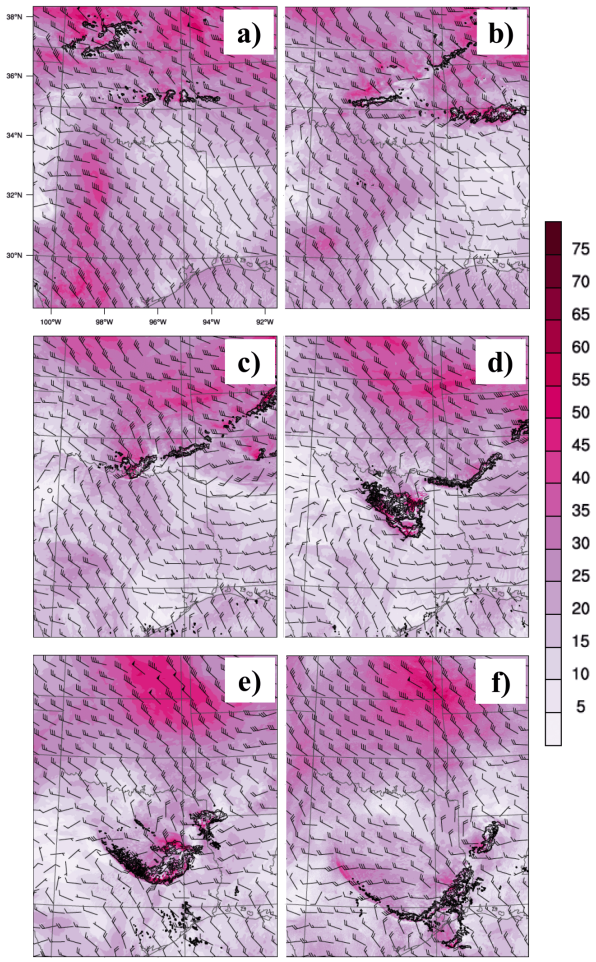

Figure 69: Same as in Fig. 68, but for the 0-3 km AGL layer.

The bulk wind shear over the lowest 3 km was also examined in order to evaluate the potential for the environment to support bow echoes. Previous studies (e.g., Weisman and Trapp, 2003) have found that environments with shear values of 30-40 knots (15-21 m s^{-1}) over the lowest 2-5 km were favorable for the development of strong bow echoes. Furthermore, the aforementioned study found that shear in excess of 40 knots (21 m s^{-1}) over the lowest 2.5 km was favorable for the development of mesovortices. Throughout the duration of the simulation, the 0-3 km bulk shear values in the inflow region of the convection system remained less than the 30-knot (15 m s^{-1}) threshold (Fig. 69). At 0900 UTC when a strong bowing segment existed in the simulation, 0-3 km shear values in the inflow region were ~20-25 knots (10-13 m s^{-1}). While the bulk shear values in the lowest 3 km layer are below the threshold found by Weisman and Trapp (2003) for strong bow echoes, the magnitude of the vertical shear calculated from the height of maximum LLJ winds (~200 m AGL) to a height of 3-5 km exceeded the 30-knot (15 m s^{-1}) threshold in the vicinity of the bowing segment, with values of 31-33 knots (16-17 m s^{-1}).

In summary, deep layer shear was supportive for organized MCS development throughout the evolution of the system. Simulated deep shear values were greater in the northern portion of the domain, which likely contributed to the formation of discrete supercells and a QLCS early in the system's lifetime. As the system moved southward away from the strongest midlevel forcing and into an environment characterized by a nocturnal LLJ, the system reorganized from a multicell cluster to a well-defined leading-line, trailing-stratiform MCS. Although the formation of a bowing segment preceded this reorganization, 0-3 km shear values in the inflow environment were below the thresholds found by previous studies (e.g., Weisman and Trapp, 2003). However, as previously mentioned, the application of these shear calculations may have been less useful in this study owing to the elevated nature

of the convection and presence of a LLJ. Therefore, the effective shear ahead of the bowing segment was computed from the height of maximum LLJ winds to 3-5 km AGL with more favorable agreement with past studies.

Chapter 5

Application of Theories to Convective Evolution and Longevity

This chapter discusses the applications of convective maintenance theories and wave theories to the evolution of the convective system in our simulation. Early in the lifetime of the simulated system, convectively-generated bores appeared to be critical for convective maintenance, which has been documented in previous studies of nocturnal convection (e.g., Wilson and Roberts, 2006; Parker, 2008; Blake et al., 2017). Therefore, section 5.1 attempts to quantify this bore hypothesis by discussing the conduciveness of the nocturnal environment to generating bores and whether or not these bores could be sustained (Rottman and Simpson, 1989; Koch et al., 1991). Since the system moved into a convectively-unstable environment and the cold pool became the dominant forcing for regeneration, convective maintenance theories, such as RKW theory (Rotunno et al., 1988) and its expansion by Weisman (Weisman, 1992), were applied to our simulation. These convective maintenance theories have also been examined in previous studies (e.g., Gale et al., 2002) to evaluate the characteristics of convection near dissipation, but these applications have not proven fruitful. Additionally, Gale et al. (2002) examined the magnitude of system-relative inflow at both the surface and aloft and found that these magnitudes tended to decrease prior to MCS dissipation. The parameters

investigated in Gale et al. (2002) were also examined within the context of our simulation and will be discussed in this chapter.

5.1 Wave Analysis

Early in the lifetime of the simulated system, the convection had the appearance of being wave-driven and moved rapidly away from the baroclinic zone after initiation. Convectively-generated bores have been linked to the initiation and maintenance of nocturnal convection over the Great Plains in previous observational and modeling studies. Specifically, bore disturbances can be generated when a density current (i.e., convectively-generated outflow boundary) intrudes into the stable nocturnal boundary layer layer (e.g., Wilson and Roberts, 2006; Trier et al., 2011; Marsham et al., 2011; Schumacher, 2015; Haghi et al., 2017). Bores are potentially more effective than gravity waves in initiating or maintaining deep convection since the passage of a bore corresponds to a net upward displacement of a layer rather than the oscillations associated with gravity waves.

Parker (2008) and French and Parker (2010) have used idealized, convectively-permitting simulations to explore the potential role of bores in maintaining nocturnal convective systems. These studies found that the formation of a stable boundary layer through imposing low-level cooling can result in the transition from a cold-pool-driven system, which is surface-based, to one that is maintained by a gravity-wave-like bore and fully elevated.

Recently, Haghi et al. (2017) showed that the interaction between convective outflow and the nocturnal, warm season environment over the Great Plains will typically result in the generation of atmospheric bores. Following the analysis outlined in previous applications of hydraulic theory (Rottman and Simpson, 1989; Koch et al., 1991; Haghi et al., 2017), we will determine the characteristics of the flow in proximity to the convection and waves in the simulation. In order to do

this, we first define a two-parameter space of the nondimensional height, which is a ratio of the depth of the density current, d_0, to the depth of the stable boundary layer, h_0, given by:

$$H = \frac{d_0}{h_0} \tag{5.1}$$

and the Froude number, Fr, which is given by:

$$Fr = \frac{U_{inv} - C_{dc}}{\sqrt{g\frac{\Delta\theta}{\bar{\theta_v}}h_0}} \tag{5.2}$$

where U_{inv} is the mean wind component within the stable layer that is orthogonal to the density current, C_{dc} is the speed of the density current, g is the gravitational acceleration, $\Delta\theta$ is the change in potential temperature across the inversion, and $\bar{\theta_v}$ is the mean virtual temperature within the inversion.

For the analysis presented in this section, the density current depth was estimated by subjectively analyzing vertical cross sections of virtual potential temperature and winds through the leading edge. More details on this estimation are discussed in Appendix A. Additionally, the density current speed was estimated by calculating the distance traveled between two locations over a 1 h period and then computing the average speed. Thus, these values are estimates and are certainly prone to error. The inversion depth was defined as the lowest layer in the ambient environment characterized by $\frac{\partial\theta}{\partial z}$>5 K km^{-1}, similar to that proposed by Haghi et al. (2017). Such a layer is characterized by a thermal profile with a lapse rate less than moist adiabatic such that it is stable for both moist and dry ascent. The mean wind component and mean virtual temperature were calculated within this layer.

Applying these parameters to the flow in which a density current (or other barrier, such as a mountain) exists yields four possible flow regimes: supercritical, partially blocked, completely blocked, and subcritical. A bore can develop if the

flow is either partially or completely blocked. According to Haghi et al. (2017), the nocturnal convective environment over the Great Plains may frequently lie in the partially blocked regime.

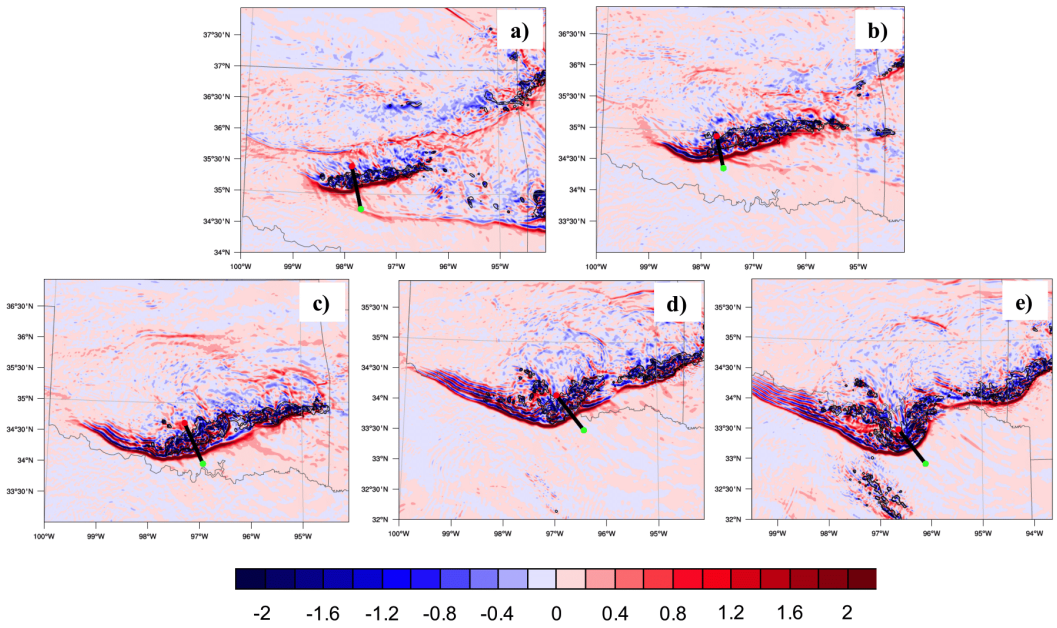

Figure 70: Vertical velocity at 1 km AGL (shaded; m s^{-1}) radar reflectivity (contour; every 20 dBZ), and cross section paths (from the green to red circles) for the (a) 0600 UTC surge, (b) 0700 UTC surge, (c) 0800 UTC surge, (d) 0900 UTC surge, and (e) 1000 UTC surge locations.

In both the simulation and observations, a bore-like response preceded the convective system and was presumptively responsible for lifting elevated parcels to their LFCs. This was apparent early in the lifetime of the simulated system before the strongest portion of the convection (hereafter "surge" region) became maintained by a surface cold pool (Fig. 70). Additionally, after the primary convective region became cold-pool-driven, a well-defined amplitude-ordered wave train was located farther west (hereafter "SW" region), which persisted until nearly sunrise (Figs. 71,72). While much of this region was characterized by high CIN (discussed further in section 4.3), the western portion of the convection was influenced by this

bore. Thus, determining the ability for the environment to generate a bore and for this bore to maintain its strength and propagate for long duration is important for understanding the evolution of this convective system.

In order to gauge the ability for the environment to trigger a bore, a comparison of the nondimensional parameters, H and Fr, was utilized in proximity to the initiating baroclinic zone in this simulation. Additionally, the parameters were compared at 0600 UTC shortly after the convection had intensified as a wave-driven system. A depiction of the possible flow regimes is shown in Fig. 73. Overlaid on the diagram of blocking regimes are the approximate values for the environment at 0500 and 0600 UTC. The flow regime at 0400 UTC was not displayed owing to its values exceeding the range of the diagram. The values for all times and orientations are listed in Table 5.1.

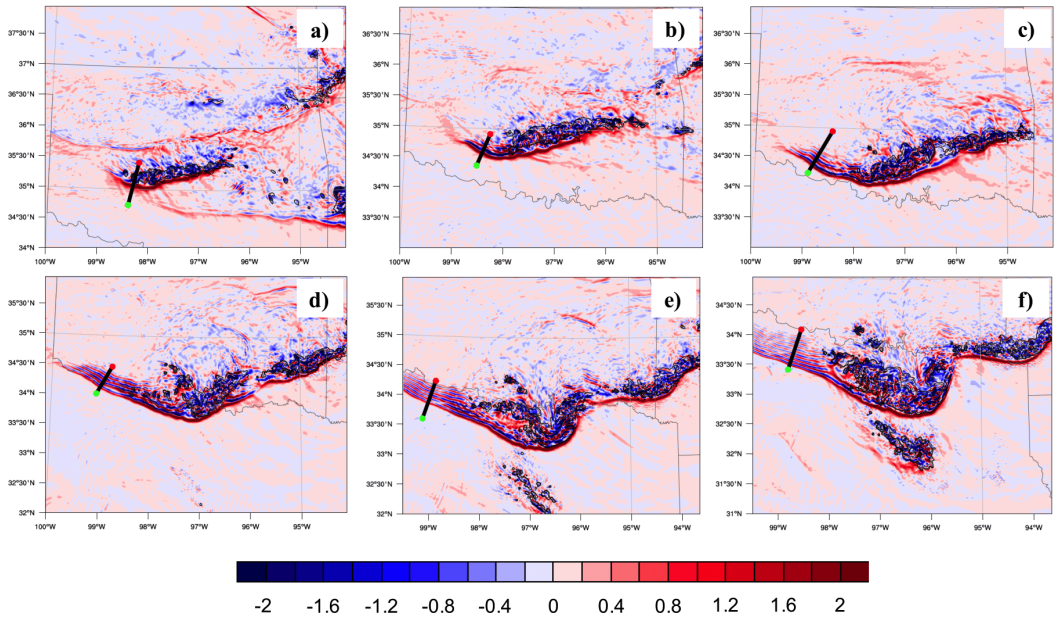

Figure 71: Vertical velocity at 1 km AGL (shaded; m s^{-1}) radar reflectivity (contour; every 20 dBZ), and cross section paths (from the green to red circles) for the (a) 0600 UTC SW, (b) 0700 UTC SW, (c) 0800 UTC SW, (d) 0900 UTC SW, (e) 1000 UTC SW, and (f) 1100 UTC SW locations.

Near the initiation location at 0400 and 0500 UTC (hereafter "init" region), the flow regime was characterized by either complete or partial blocking, both of which are favorable for the generation of a bore (Fig. 73, Table 5.1). This blocking occurred as the cold air mass associated with the initiating baroclinic zone moved into an environment characterized by a shallow nocturnal boundary layer. By 0500 UTC, the inversion depth within the ambient air had increased owing to the presence of the cold pool from the first convective system. By this time, deep convection had moved away from the baroclinic zone. The environmental flow regime was less favorable for the generation of a bore by 0600 UTC, but because the system had already become maintained by a wave response by this time, the blocking analyses from this time were less relevant than at 0400 and 0500 UTC.

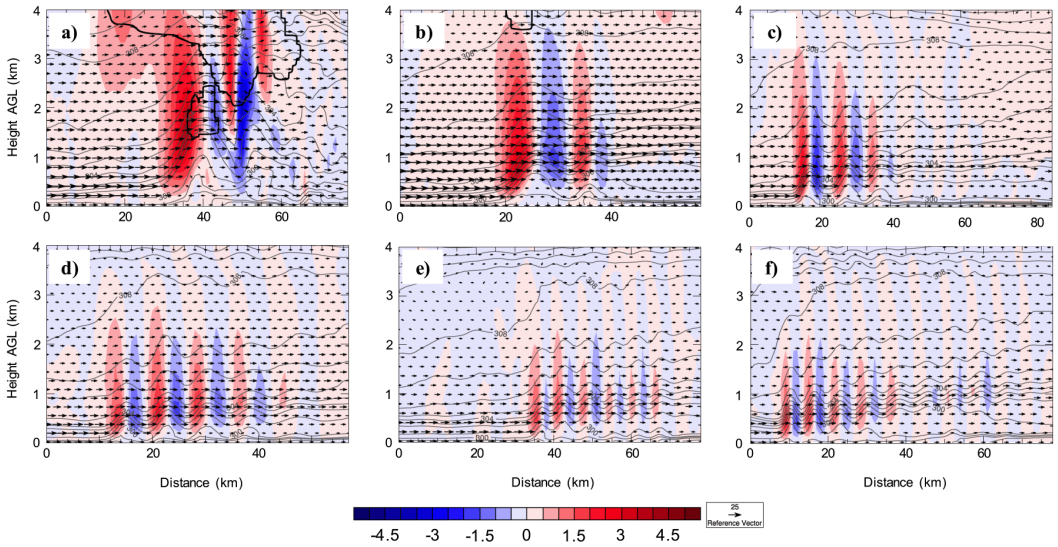

Figure 72: Vertical cross sections of vertical velocity (shaded; m s^{-1}), potential temperature (contours; K), system-relative winds (vectors; m s^{-1}) for the (a) 0600 UTC SW, (b) 0700 UTC SW, (c) 0800 UTC SW, (d) 0900 UTC SW, (e) 1000 UTC SW, and (f) 1100 UTC SW locations. The inflow locations are depicted by the green circles in Fig. 71.

A supercritical flow regime was found within the southwestern portion of the system (i.e., 0600 UTC SW) based on the H and Fr values. However, the waves in this region were generated prior to this time. An examination of the potential temperature displacements in proximity to the simulated wave in this portion of the system would suggest that this wave disturbance may have had characteristics of solitary waves in that isentropes were not permanently displaced upward after

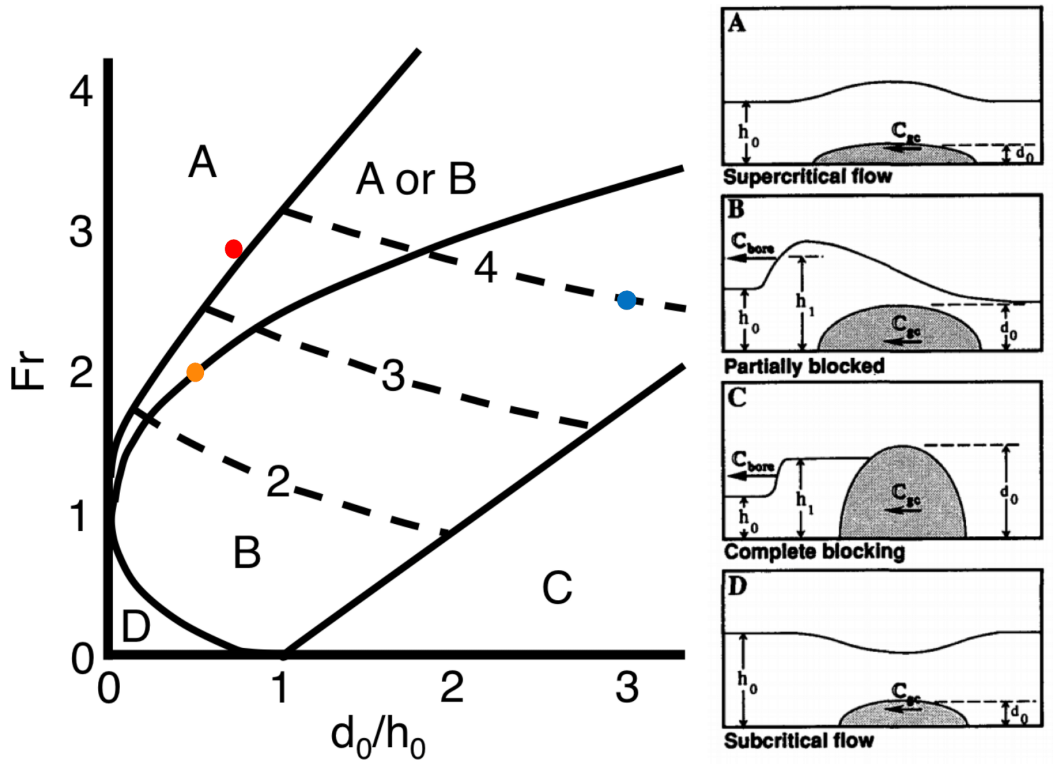

Figure 73: Blocking regimes by Froude number (y-axis) and nondimensional height (x-axis) for (blue) 0500 UTC init, (red) 0600 UTC SW, (orange) 0600 UTC surge locations. The flow regime for 0400 UTC init is not shown because the values are located off of the diagram. The solid lines separate the various flow regimes, and the dashed lines represent the bore strength. On the right are schematics of possible outcomes from these combinations, with (A) representing supercritical flow, (B) representing partially blocked flow, (C) representing completely blocked flow, and (D) representing subcritical flow. Adapted from Koch et al. (1991).

their passages (Fig. 72; Knupp, 2006; Toms et al., 2017). However, given that bores can evolve into solitary waves, we will refer to this disturbance as a bore for simplicity. Over time, a well-defined amplitude-ordered wave train developed in this region owing to the dispersive nature of these waves (Figs. 71,72).

The next step in the analysis is to determine whether the environment is able to sustain a long-lived bore. Dynamically this outcome can occur if the energy associated with a gravity wave packet or bore is retained within a wave duct (i.e., the wave is trapped). If wave trapping is incomplete, the bore will vertically propagate, causing a reduction in the wave energy and thus longevity (e.g., Scorer, 1949; Lindzen and Tung, 1976; Crook, 1988). Crook (1988) identified three conditions by which waves are trapped, which commonly occur within the nocturnal environment: (i) a level aloft at which winds are approximately the same as the motion of the bore (i.e., a critical layer), (ii) a secondary inversion found above the low-level stable boundary layer, and (iii) a jet which opposes the bore motion which

	04 INIT	05 INIT	06 SW	06 SURGE
Inversion Depth	112 m	267 m	391 m	722 m
Density Current Depth	1000 m	800 m	300 m	400 m
Nondimensional Height	8.9	3.0	0.8	0.6
Froude Number	3.3	2.5	2.9	2.0
Density Current Speed	12.2	12.2	12.8	15.1

Table 5.1: Parameter values used in the computation of the Froude number and nondimensional height for the 0400 UTC init, 0500 UTC init, 0600 UTC SW, and 0600 UTC surge environments. These values were computed at the inflow points for the paths given in Figs. 42b,c, 71a, and 70a, respectively.

is characterized by substantial curvature. The third scenario would be anticipated in the proximity of a nocturnal LLJ, which is relatively shallow and characterized by strong winds - yielding large curvature effects.

More recently, Haghi et al. (2017) showed that the curvature effects are generally responsible for defining the wave duct in the nocturnal warm season over the Great Plains. The environment in this case would favor waves propagating in a direction opposite to the LLJ. For a long-lived bore in the presence of a LLJ, such as the one in the simulation, we would anticipate that the environment was supportive of wave trapping, allowing this wave train to continue to propagate for several hours after generation.

In order to determine if favorable conditions for wave trapping were present in the environment, the vertical profile of the Scorer parameter, l^2, (Scorer, 1949) was examined. Favorable values of Scorer parameter satisfy the Taylor-Goldstein equation, and solutions for wave trapping exist when a layer characterized by a positive square of vertical wavenumber, m, is located beneath a layer characterized by a negative value of m^2. The wave duct is thus the layer characterized by a positive m^2, which occurs when Scorer parameter is greater than the square of the horizontal wavenumber, k, or if l^2 is positive and k^2 is negligible. The equation for m^2 is given by:

$$m^2 = \frac{N^2}{(U - C_b)^2} - \frac{\frac{\partial^2 U}{\partial z^2}}{(U - C_b)} - k^2 \tag{5.3}$$

where N^2 is the square of the Brunt-Väisälä frequency, given by $N^2 = \frac{g}{\theta_v}\frac{\partial \theta_v}{\partial z}$, C_b is the bore speed, U is the wind component orthogonal to the bore, k is the horizontal wavenumber, given by $k = \frac{2\pi}{L}$ where L is the horizontal wavelength, and $\frac{\partial^2 U}{\partial z^2}$ represents the curvature in the environmental wind profile. The first two terms on the right side of the equation are the stability and curvature terms in the Scorer parameter, respectively.

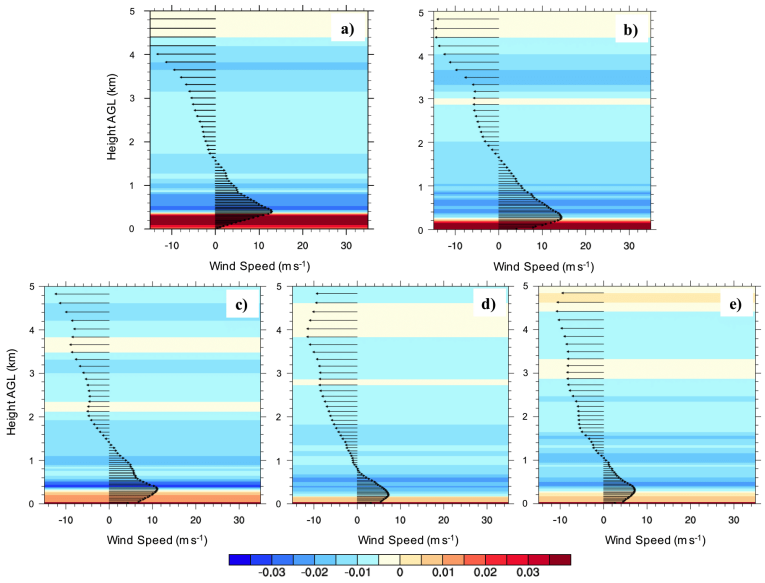

Figure 74: Vertical profiles of line-normal winds (vectors; m s^{-1}) and line-normal vertical wind shear (shaded; s^{-1}) for the inflow locations (a) 0600 UTC surge, (b) 0700 UTC surge, (c) 0800 UTC surge, (d) 0900 UTC surge, and (e) 1000 UTC surge locations. The inflow locations are depicted by the green circles in Fig. 70.

In the Scorer parameter computation, C_b was estimated by tracking the distance that the bore moved over 1 h and computing the mean speed. An examination of the line-normal wind profile (Fig. 74) after the bore was generated (0600 to 1000 UTC) in the region of the strongest convection suggests that strong low-level curvature effects from the LLJ initially existed (Fig. 74a), raising the possibility of a wave duct at 0600 UTC. Therefore, the environment supported that the bore previously generated by the intrusion of the baroclinic zone into a nocturnal stable layer was able to continue. However, the curvature diminished with time in this region as the convection acquired an increasingly parallel orientation to the LLJ, suggesting that the system could not be maintained by a bore after 0800 UTC (Figs. 74c-e). As previously mentioned, the convection continued in this region as a cold-pool-driven system after this time. In a physical sense, the deterioration of

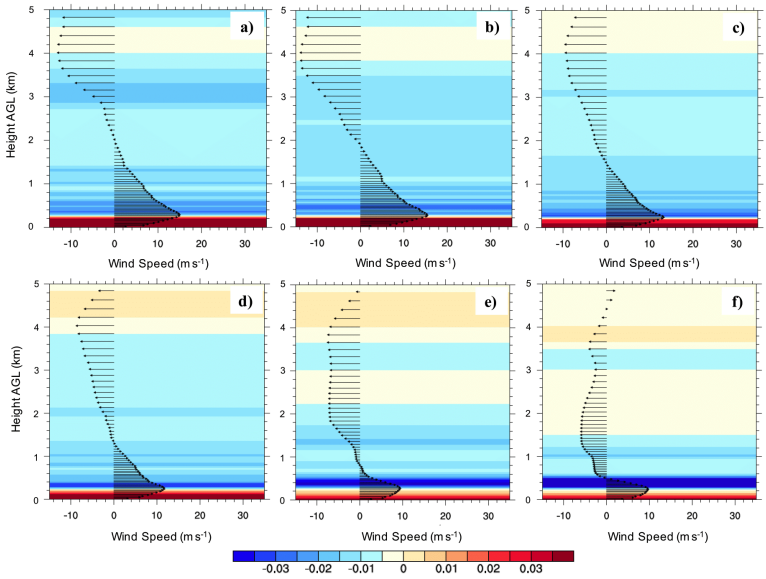

Figure 75: Vertical profiles of line-normal winds (vectors; m s^{-1}) and line-normal vertical wind shear (shaded; s^{-1}) for the inflow locations at (a) 0600 UTC SW, (b) 0700 UTC SW, (c) 0800 UTC SW, (d) 0900 UTC SW, (e) 1000 UTC SW, and (f) 1100 UTC SW locations. The inflow locations are depicted by the green circles in Fig. 71.

the wave duct and the creation of conditions more favorable for cold-pool-driven convection are linked. This link will be discussed further in the following sections.

However, a long-lived wave train had formed along the western flank of the system which helped to sustain elevated convection. In this region, a strong LLJ was oriented nearly parallel to the direction of propagation, yielding strong low-level curvature supportive of wave trapping (Fig. 75). This LLJ was weaker at 1000 and 1100 UTC, during the period that the wave amplitude began to diminish. The vertical profile of the Scorer parameter at 0600 and 0700 UTC indicates that between 500 m and 1 km MSL, the Scorer parameter changed from being positive to negative, the effects of which were attributed to the change in sign of the curvature term (Fig. 76). Therefore, the curvature attributed to the LLJ was the dominant mechanism participating in trapping the wave energy at low levels. As the LLJ

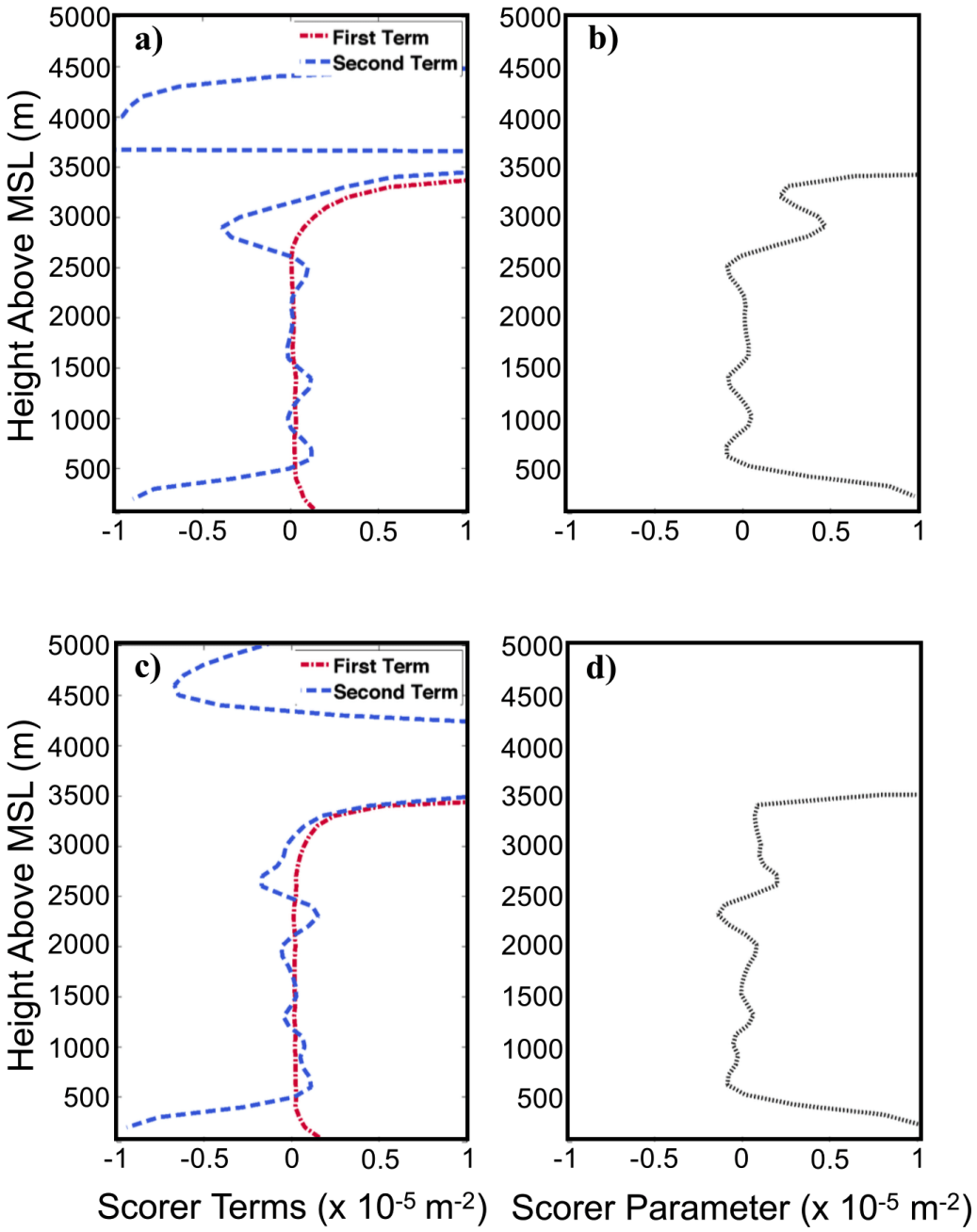

Figure 76: Vertical profiles of the (a),(c) stability term and curvature terms and (b),(d) total Scorer parameter for the western portion of the system at (top) 0600 UTC and 0700 UTC. Figure was made by Kevin Haghi.

diminished in strength over time, less energy was trapped, and the waves weakened as they propagated vertically.

In summary, early during the lifetime of the convection when the system was elevated and bore-driven, the application of hydraulic theory supports that the interaction of the initiating baroclinic zone with the nocturnal environment could generate a bore. Analysis of the environment ahead of the system suggests that a wave duct initially existed owing to strong curvature of the wind profile associated with LLJ. However, as the region of strongest convection accelerated toward the southeast and acquired a more-parallel orientation to the LLJ, the wave duct deteriorated, and the system continued as cold-pool-driven convection. However, farther west, a distinct undular bore existed until nearly sunrise, when destabilization owing to solar heating and the cessation of the LLJ occurred. In this region, the shear effects from the LLJ were more prominent, and a favorable Scorer parameter for wave trapping suggests that the environment could support a long-lived bore.

5.2 RKW Framework

As discussed in section 1.4, a well-established theory about the structure and maintenance of squall lines was developed by Rotunno et al. (1988) (hereafter RKW theory) and extended by numerous studies, including Weisman et al. (1988). Both aforementioned studies utilized a two-dimensional idealized cloud model, which was initialized using a thermodynamic profile typically observed in surface-based squall line environments (Bluestein and Jain, 1985). Thus, one obvious shortcoming of RKW theory is that it only describes surface-based squall lines interacting with a well-mixed boundary layer and is not necessarily directly applicable to elevated convective systems.

In order to explain the internal dynamics and maintenance of these systems, the interaction between the environmental vertical wind shear versus the horizontal buoyancy gradient associated with convectively-generated outflow was explored

within the context of horizontal vorticity. Using a fixed thermodynamic profile to characterize the environment, Rotunno et al. (1988) and Weisman et al. (1988) varied the line-normal environmental wind shear in both magnitude and depth. These studies found that strong low-level line-normal shear promotes the development of a line of ordinary convective cells which exist simultaneously in various stages of their lifecycle. In other words, the system is continually promoting new cell development along its leading edge, and these cells move rearward in a system-relative framework with time. Additionally, they found that strong, deep wind shear at an angle less than perpendicular to the line results in the development of a line of quasi-steady supercells.

The foundation of RKW theory is based upon the fact that flux across the outflow boundary of horizontal vorticity produced by the vertical wind shear of the environmental inflow is, to some degree, balanced by baroclinically-generated vorticity in the system. If the two vorticity contributions are approximately equal, the system is said to be in an "optimal state", with vertically-oriented updrafts along the cold pool. This "optimal state" is defined as:

$$\frac{C}{\Delta u} \approx 1 \tag{5.4}$$

where C is a proxy for the cold pool strength via its buoyancy deficit and depth (i.e., the theoretical propagation speed of a density current; Benjamin, 1968), and Δu is the line-normal bulk wind difference over some layer. The square of C can be defined as:

$$C^2 = 2 \int_0^H (-B)\, dz \tag{5.5}$$

where H is the approximate depth of the cold pool and B is the buoyancy, given by:

$$B = g\left(\frac{\theta'}{\overline{\theta}} + 0.61(q_v - \bar{q_v}) - q_c - q_r\right) \tag{5.6}$$

In equation 5.6, $\overline{\theta}$ is the mean potential temperature, θ' is the perturbation potential temperature, $\overline{q_v}$ is the mean water vapor mixing ratio, and q_v, q_c, and q_r are the perturbation mixing ratios of water vapor, cloud water, and rainwater, respectively. The mean state terms are averaged around an inflow point and are a function of height. The perturbation terms are functions of height and distance along a cross section and are determined relative to the mean inflow state.

In our study, we approximate C from equation 5.5 as:

$$C = \sqrt{-2\bar{B}H} \tag{5.7}$$

where $\overline{B}$ is the average buoyancy over the approximate cold pool depth at a selected location. Additionally, because equation 5.5 was defined in a simple 2-D, inviscid framework which assumes no ambient flow, the computed value of C may not necessarily be an exact representation of the cold pool speed. Also, the computed value of C depends on the depth of the cold pool, which was estimated subjectively in this study and was thus prone to error (more details on this estimate are discussed in Appendix A). Therefore, we also estimated the cold pool speed by tracking the displacement over 1 h periods. Both the computed and estimated values for C were utilized in the RKW comparisons.

In RKW theory, it can be shown that for some value of C, a magnitude of line-normal shear over some depth exists such that new updrafts initiated along the outflow boundary will have an erect orientation - i.e., an "optimal state" exists. Aside from the "optimal state", depending on the magnitudes of C and Δu, the system may alternatively tilt downshear ($\frac{C}{\Delta u} \ll 1$) or upshear over the system-generated cold pool ($\frac{C}{\Delta u} \gg 1$). This point is illustrated in Fig. 77, where the

updraft initiated in Fig. 77c initially had a downshear tilt owing to the ambient environmental wind shear. As a cold pool developed and its vorticity began to balance the environmental shear vorticity, new updraft trajectories along the leading edge of the cold pool were vertically erect (Fig. 77d). As the cold pool strength further increased and its associated baroclinically-generated circulation overwhelmed that of the environmental shear, the system sloped upshear, and new

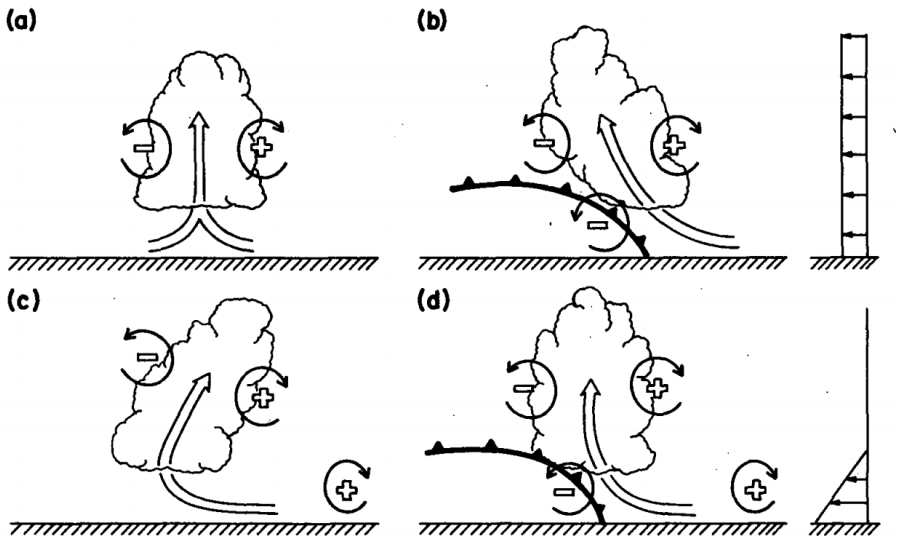

Figure 77: Illustration of how a buoyant updraft can be influenced by ambient wind shear and/or a surface cold pool. Panel (a) represents an initial updraft in the presence of no vertical shear or cold pool, (b) represents an updraft in a no-shear environment in the presence of a cold pool, (c) represents an updraft in an environment with vertical shear but no cold pool, and (d) represents an updraft in an environment with vertical shear and a surface cold pool. In (b), the initial updraft leans rearward over the cold pool owing to a lack of vorticity from the enviromental shear. In (c), an initial updraft leans downshear, but after the development of a cold pool, the vorticity contributions from the shear and the cold pool may balance, resulting in an erect updraft in (d) (from Fig. 18 of Rotunno et al. (1988)).

updrafts were slanted such that their trajectories were no longer vertical (Rotunno et al., 1988; Weisman et al., 1988). The development of an RIJ can also modify this vorticity balance through the "importation" of an additional source of horizontal vorticity (Weisman, 1992), which will be discussed in the section 5.4.

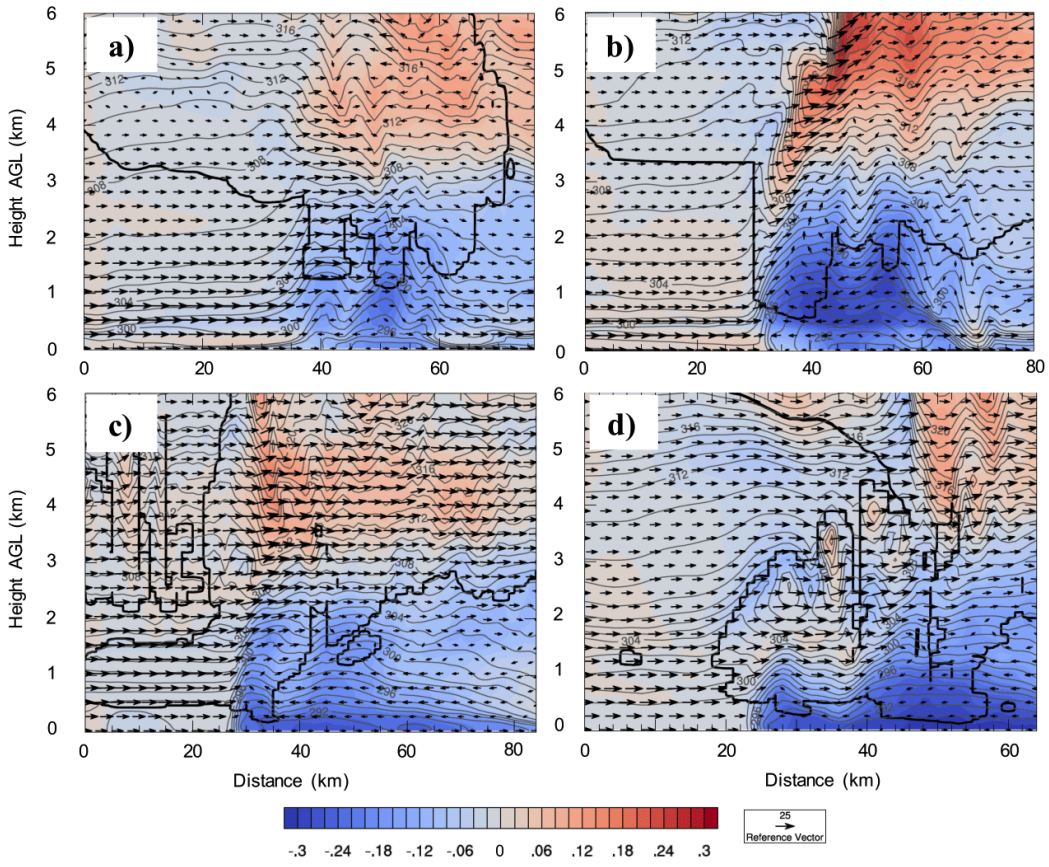

Figure 78: 0-6 km AGL cross sections of buoyancy (shaded; m s^{-2}), system-relative wind vectors (m s^{-1}), potential temperature contours (gray; K), and cloud boundary (thick black line) for (a) 0600 UTC, (b) 0900 UTC, (c) 1200 UTC, and (d) 1500 UTC. The cross section paths are depicted in Fig. 44 with the green circle representing 0 km.

Regarding the "optimal state", Parsons (1992) demonstrated that this regime corresponded to deeper and stronger cold pool lift within a well-mixed environment. Additionally, Parker (2010) showed that buoyant, vertically-oriented updrafts characterized by an "optimal state" realize more of their buoyancy because their attendant downward-directed pressure perturbation accelerations are weaker. Inferences from both studies suggest that both the vertical shear interacting with the convectively-generated cold pool and the slope of the buoyant convection are important in determining updraft intensity.

While RKW theory is often thought to represent favorable conditions for "strong, long-lived squall lines", one should note that it is idealized in nature and does not necessarily represent conditions observed in all MCSs or convective environments. Moreover, its purpose is really to gauge how a density current interacts with environmental shear to produce new updrafts (Bryan and Weisman, 2006). The depth of the relevant vertical shear for this interaction has been the focus of some debate. While the original RKW studies noted that the shear within the cold pool layer is critical for a vorticity balance (Rotunno et al., 1988; Weisman et al., 1988), a later study by Weisman and Rotunno (2004) concluded that shear over a deeper layer (5 km) may be important. Additional studies have generally found that strong squall lines and derechos are typically not characterized by an "optimal state" and that upper-level shear (i.e., above the lowest 2.5-5 km) is also important in their longevity (Stensrud et al., 2005; Coniglio et al., 2012).

Coniglio et al. (2012) suggested that even deeper layers be considered as other prior studies have found that MCS cold pools depths may be substantially larger than those found in the RKW simulations. Additionally, because of their frequently-elevated nature, shear in the lowest levels may not be the most applicable, which was addressed by Coniglio et al. (2012) in their calculation of the effective wind

shear. Blake et al. (2017) argued that deeper shear layers are needed for maintenance of elevated convection since deep lifting of the stable boundary layer provides an additional source of baroclinically-generated vorticity. Since Coniglio et al. (2012) investigated a nocturnal system, the finding of Blake et al. (2017) may support their results. Because the cold pool depth in our simulation was not constant over time, C will be compared with shear over the fixed depths of 2.5, 5, and 8 km[1].

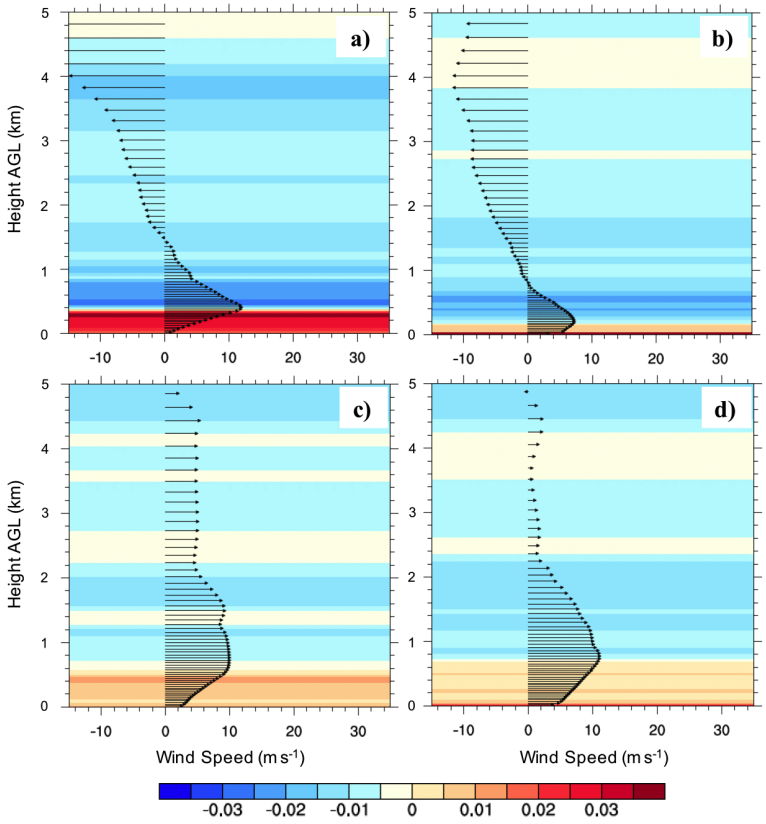

Figure 79: Vertical profiles of line-normal winds (vectors; m s^{-1}) and line-normal vertical wind shear (shaded; s^{-1}) for the inflow points at (a) 0600 UTC, (b) 0900 UTC, (c) 1200 UTC, and (d) 1500 UTC. The inflow locations are depicted by the green circles in Fig. 44.

[1]These shear values were computed by subtracting the line-normal winds at the surface from these heights.

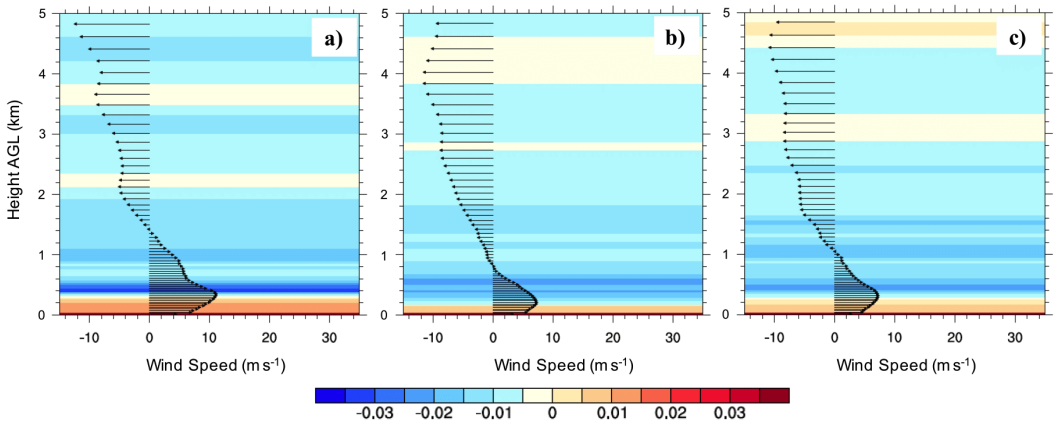

Figure 80: Vertical profiles of line-normal winds (vectors; m s^{-1}) and line-normal vertical wind shear (shaded; s^{-1}) for the inflow points at (a) 0800 UTC, (b) 0900 UTC, and (c) 1000 UTC. The inflow locations are depicted by the green circles in Fig. 44.

In this simulation, low-level shear was unfavorable beneath the jet maximum such that the induced circulation was in the same orientation as that produced by the surface cold pool (Fig. 79). This unfavorable orientation occurred throughout the duration of the simulation (Figs. 79,80) although the magnitude of this shear varied. While the height of the LLJ maximum varied spatially and temporally, the occurrence of this unfavorable low-level shear profile indicates that shear in a layer above the LLJ must be considered in an RKW framework. Moreover, because the LLJ resulted in elevated moisture advection aiding in the development of CAPE for parcels aloft, using an effective shear layer was likely more useful owing to inflow parcels originating farther aloft (Thompson et al., 2007; French and Parker, 2010).

After the dissipation of the LLJ and when the environment supported surface-based convection, the low-level profile remained unfavorable for an RKW balance. However, the low-level shear was likely more critical to the system's maintenance in this later period than earlier in the simulation when the system was wave-driven.

Therefore, the shear beginning at height of maximum LLJ winds was considered prior to 1200 UTC, when the system was primarily elevated. The winds at this maximum were subtracted from the winds at 2.5, 5, and 8 km[2] to provide an effective bulk-shear estimate.

Before comparing the values of C and Δu, it is important to discuss the evolution of the cold pool temperature deficit. As described in the previous section, the system was characterized by a downshear tilt and a developing cold pool between 0600 and 0800 UTC. However, between 0800 UTC and 1000 UTC, the cold pool had accelerated, resulting in the transition to an upshear-tilted system which had a well-defined RIJ. While the most unstable air was still found aloft during this period, the system had become primarily cold-pool-driven. Between 0600 and 0900 UTC, the temperature deficit across the cold pool was similar in magnitude both at the surface and 1 km. This result is in contrast to the findings of Blake et al. (2017), which found a stronger cold pool aloft during the elevated portion of their system. However in our study, the near-surface temperature difference between the cold pool and environment at the surface began to increase after 0900 UTC, but decreased over time at 1 km AGL (Fig. 81), indicating that the effects of the cold pool had begun become more prominent near the ground.

By 1200 UTC, the environment favored a surface-based system that was cold-pool-driven, and no indications of a preceding bore response in proximity to the main convective region were present. The minimum buoyancy was now located near the ground, indicating that the prior stable boundary layer was no longer inhibiting the cold pool from reaching the surface nor was it contributing to stable ascent and cooling aloft (Fig. 78c). Additionally, the mean temperature difference between the cold pool and the environment had increased to nearly 5.5 °C, which

[2]The heights of maximum wind utilized in these calculations ranged from 200 to 400 m AGL, resulting in a slightly shallower shear depth than with the the calculations using the surface parcel.

began to further increase after 1200 UTC owing to the onset of solar heating (Fig. 81). Because the shear in the cold pool layer (lowest ~1 km) was in an

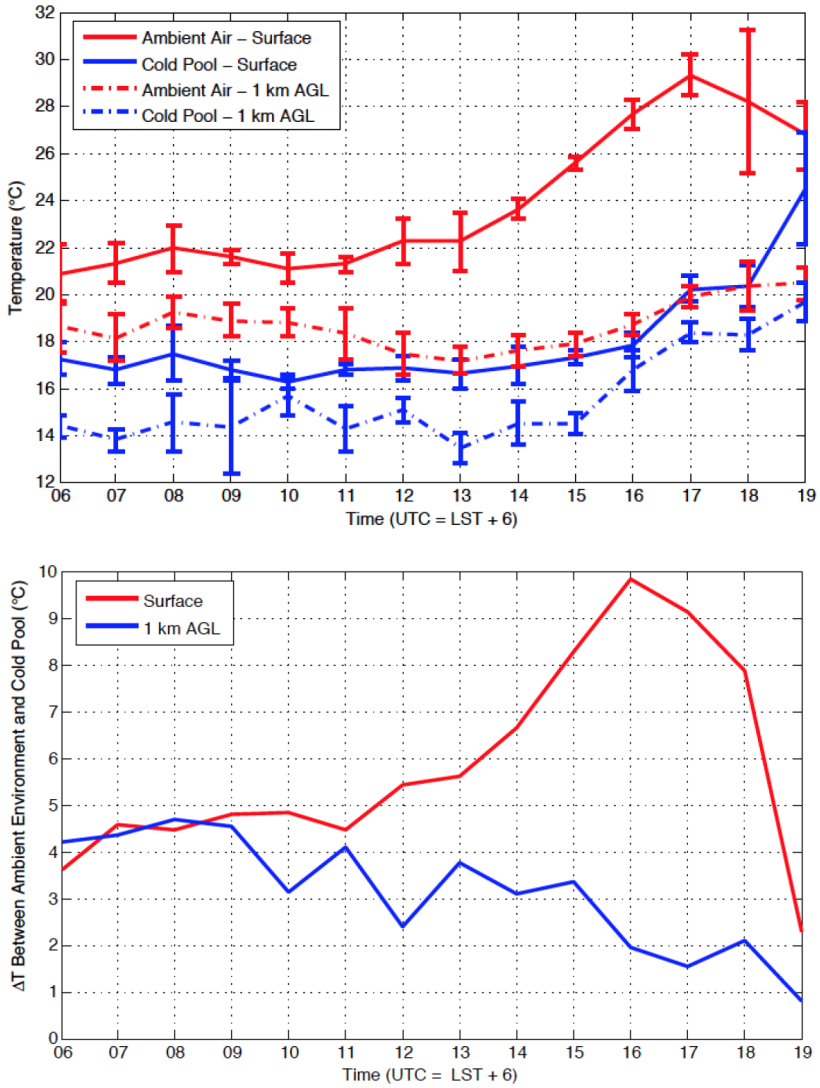

Figure 81: Time evolution of (top) mean ambient environmental temperature (red) and cold pool temperature (blue) for the surface (solid) and 1 km AGL (dashed) and (bottom) the average temperature difference between the ambient environment and cold pool at the surface (red) and 1 km AGL (blue). The error bars in the top panel represent 1 standard deviation from the mean.

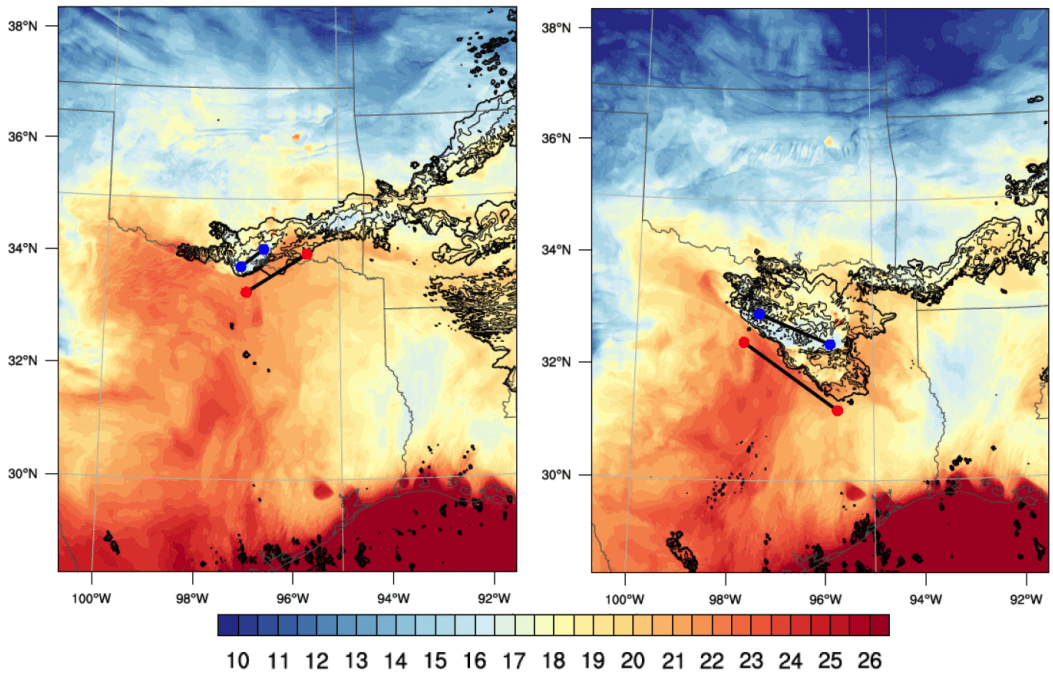

Figure 82: Temperature at the lowest model grid level (°C) and radar reflectivity (contour; every 20 dBZ) for (left) 1200 UTC and (right) 1500 UTC. The path designated by the blue (red) start and end points represent the section along which the mean temperature of the cold pool (environment) were computed. These paths varied by hour and were drawn subjectively.

orientation unfavorable for RKW balance, the hypothesis that the near-surface cold pool circulation, which was strengthening with time, overwhelmed that of the environmental shear seems to be plausible. As a result, newly developed updrafts along the outflow boundary would be expected to tilt rearward with height.

This upshear, rearward tilt was more pronounced by 1500 UTC, and the cold pool had begun to move away from the convective system, causing much of the convective region to weaken after this time. The mean cold pool temperature deficit had increased dramatically since 1200 UTC to more than 8 °C (Fig. 81), and the greatest negative buoyancy was mostly confined to the lowest ~1 km (Fig. 78d). The shear profile over this layer was even more unfavorable for RKW balance

than at 1200 UTC (Fig. 79d), which continued to support the hypothesis that the cold pool circulation had overwhelmed that of the environmental wind shear. The mean cold pool temperature deficit had further increased in magnitude until nearly 10 °C at 1600 UTC, before diminishing with time. These changes in cold pool temperature deficit were likely attributable to both solar insolation of the inflow environment and the weakening of convection, resulting in less evaporative cooling to support a cold pool.

Therefore, by just qualitatively examining the evolution of the shear and cold pool temperature deficit in proximity to the convection, one might suspect that the system behaved in a manner similar to what would be expected from RKW theory. Now we will apply comparisons of C to Δu the evolution of the system to gauge how well these values corresponded with the evolution of the system structure.

TIME/LOCATION	C_{EST}	C_{DC}
06 SURGE	15.1 m s^{-1}	20.6 m s^{-1} (H = 1 km)
08 SURGE	17.2 m s^{-1}	22.0 m s^{-1} (H = 1 km)
09 SURGE	17.6 m s^{-1}	31.0 m s^{-1} (H = 2 km)
10 SURGE	18.1 m s^{-1}	30.0 m s^{-1} (H = 2 km)
12 CONVECTION	11.4 m s^{-1}	20.7 m s^{-1} (H = 1 km)
15 CONVECTION	10.6 m s^{-1}	21.2 m s^{-1} (H = 1 km)

Table 5.2: Estimated density current speed (C_{EST}) and computed density current speed (C_{DC}; H represents the density current depth used in computation) for the cross sections through the convective line at 0600 UTC (surge), 0800 UTC (surge), 0900 UTC (surge), 1000 UTC (surge), 1200 UTC (convection), and 1500 UTC (convection). Cross section paths for 0600, 0900, 1200, and 1500 UTC depicted in Fig. 44.

The values used for the cold pool speed for the analyzed times are listed in Table 5.2. The computed values (C_{DC}) were calculated based upon the subjectively-estimated cold pool depths. The depth values utilized in the calculations are depicted in the rightmost column of Table 5.2. However, the computed values

were substantially greater than the cold pool speeds estimated by examining the displacement over 1 h periods (C_{EST}). Bryan and Rotunno (2008) found that the equation yielding these values, which were derived assuming an incompressible atmosphere and no friction, tended to significantly overestimate density current speeds computed using an anelastic approximation, which is typically a more realistic depiction of the atmosphere than the incompressible assumption.

TIME/LOCATION	$\frac{C_{EST}}{\Delta u_{2.5}}$	$\frac{C_{EST}}{\Delta u_{5}}$	$\frac{C_{EST}}{\Delta u_{8}}$	$\frac{C_{DC}}{\Delta u_{2.5}}$	$\frac{C_{DC}}{\Delta u_{5}}$	$\frac{C_{DC}}{\Delta u_{8}}$
06 SURGE	3.32	1.00	0.60	4.52	1.35	0.82
08 SURGE	1.90	1.01	0.70	2.42	1.28	0.89
09 SURGE	1.50	1.39	0.77	2.64	2.43	1.35
10 SURGE	1.72	1.70	0.64	2.86	2.83	1.06
12 CONVECTION	-	4.39	0.98	-	7.96	1.77
15 CONVECTION	3.56	1.98	0.59	7.13	3.97	1.18

Table 5.3: Ratios of the estimated (C_{EST}) and computed (C_{DC}) density current speeds to the bulk shear from the surface to 2.5, 5, and 8 km AGL. Cross sections are the same as in Table 5.2.

TIME/LOCATION	U_{MAX}	Z_{MAX}	$\frac{C_{EST}}{\Delta u_{eff2.5}}$	$\frac{C_{EST}}{\Delta u_{eff5}}$	$\frac{C_{EST}}{\Delta u_{eff8}}$	$\frac{C_{DC}}{\Delta u_{eff2.5}}$	$\frac{C_{DC}}{\Delta u_{eff5}}$	$\frac{C_{DC}}{\Delta u_{eff8}}$
06 SURGE	13.1 m s^{-1}	400 m	0.99	0.55	0.40	1.35	0.74	0.55
08 SURGE	11.3 m s^{-1}	350 m	1.08	0.72	0.55	1.38	0.92	0.70
09 SURGE	7.3 m s^{-1}	200 m	1.12	1.05	0.65	1.96	1.84	1.14
10 SURGE	7.2 m s^{-1}	320 m	1.20	1.19	0.51	1.99	1.97	0.84

Table 5.4: Ratios of the estimated (C_{EST}) and computed (C_{DC}) density current speeds to the effective bulk-shear from the level of maximum winds (U_{MAX} at Z_{MAX}) to 2.5, 5, and 8 km AGL. Cross sections are the same as (surge) in Table 5.2.

The calculations using the fixed-layer depths beginning at 0 km were not particularly useful in describing the evolution of the system tilt (Table 5.3). Depending on both the cold pool speeds and the shear layers utilized, the ratios ranged from

being much greater than 1 when the system was downshear-tilted (C_{EST} and Δu over 2.5 km) to remaining much less than 1 when the system was upshear-tilted (C_{EST} and Δu over 8 km). Over the fixed-layer depths, the ratio that performed the best used C_{DC} and Δu over 8 km. For both C_{EST} and C_{DC}, the shear over the lowest 2.5 km performed notably poorly, with values far from what would be expected based on the system structure. Therefore, the inclusion of shear over a deeper layer seems to be critical in accurately estimating the system structure based on an RKW framework, as was proposed by previous studies.

However, more favorable results were obtained when using the effective shear comparisons, where the unfavorable shear layer beneath the LLJ was omitted (Table 5.4). The values for the maximum LLJ winds and the height at which they occurred are listed in the columns 2 and 3, respectively. We found the maximum wind within the lowest 2 km in order to be consistent with the comparisons of Gale et al. (2002). Despite that these effective layer computations were only utilized during the elevated portion of the system (i.e., prior to 1200 UTC), the computations using the effective Δu over the lowest ~5 km performed well with both cold pool speeds, with C_{EST} performing slightly better. These both resulted in a ratio <1 when the system was downshear tilted (0600 and 0800 UTC), which transitioned to >1 when the system became upshear tilted (1000 UTC; Tables 5.3,5.4). Additionally, the shear over the lowest 2.5 km performed better when the below-jet shear was omitted.

Therefore, the utilization of an effective shear layer seems to be necessary for applying an RKW framework to an elevated system, which was suggested by previous studies (French and Parker, 2010; Coniglio et al., 2012). Moreover, shear over a depth greater than that proposed by earlier studies (i.e., within the depth of the cold pool, lowest 2.5 km, etc.) seems to be necessary to gauge values that are consistent with the tilt of the observed system. However, these computations

do not directly account for internal circulations such as the RIJ, which Weisman (1992) suggested is important for obtaining a vorticity balance. However, the RIJ often does impact the speed of the cold pool through downward momentum transport (e.g., Mahoney et al., 2009), which may have influenced C_{EST}. The role that the RIJ played in impacting the vorticity will be discussed in section 5.4.

In summary, applying RKW calculations to a nocturnal system is complicated by the low-level stability and presence of a LLJ, which often results in a low-level shear profile unfavorable for a vorticity balance. These considerations were not accounted for by Rotunno et al. (1988), but have been noted by other studies (French and Parker, 2010; Coniglio et al., 2012). In this simulation, accounting for midlevel shear seems to be critical in obtaining ratios of C to Δu that are consistent with the system structure. Moreover, omitting the low-level shear where negative effects from a LLJ are important is also necessary to gauge a realistic estimate of this ratio. However, as the LLJ acts to transport moisture which provides elevated CAPE, omitting this layer seems to be fair as these parcels are likely not the main contributors to deep convective updrafts during the nocturnal period. As the environment becomes increasingly favorable for surface-based convection, the fixed layer calculates provide values consistent with the system tilt. Despite the development of an upshear tilt, the system remained organized for several hours prior to moving off the Gulf Coast.

5.3 System-Relative Inflow

In addition to applying RKW theory to dissipating MCSs, Gale et al. (2002) examined the role that the LLJ played in MCS dissipation and found that systems previously impacted by a LLJ tended to weaken or dissipate after these contributions were removed. However, in this case, the system had actually strengthened

considerably by 0900 UTC, when the system acquired an orientation largely parallel to the LLJ. Additionally, despite the weakening of the LLJ by 1200 and 1500 UTC, the system persisted for several more hours. In an RKW perspective, the removal of the LLJ forcing actually resulted in a "less unfavorable" shear profile in low levels during the nighttime, which may have helped to hinder the strength of the upshear tilt until the boundary layer began to destabilize. However, previous studies (e.g., Stensrud et al., 2005) have found that systems may maintain their intensity despite that the cold pool circulation had overwhelmed the environmental shear.

TIME/LOCATION	C_{EST}	SSRI	Z_{MAX}	ESRI
06 SURGE	15.1 m s^{-1}	15.6 m s^{-1}	400 m	28.2 m s^{-1}
08 SURGE	17.2 m s^{-1}	21.6 m s^{-1}	350 m	28.5 m s^{-1}
09 SURGE	17.6 m s^{-1}	20.9 m s^{-1}	200 m	25.0 m s^{-1}
10 SURGE	18.1 m s^{-1}	20.7 m s^{-1}	320 m	25.3 m s^{-1}
12 CONVECTION	11.4 m s^{-1}	13.9 m s^{-1}	765 m	21.4 m s^{-1}
15 CONVECTION	10.6 m s^{-1}	14.7 m s^{-1}	860 m	21.4 m s^{-1}

Table 5.5: Table of the estimated density current speed (C_{EST}), SSRI, height of LLJ maximum (Z_{MAX}), and ESRI. Cross sections are the same as in Table 5.2.

RKW theory provides insight into how the interaction between the environmental shear and cold pool strength can impact squall line intensity. This theory, however, does not quantify how squall line intensity depends on environmental buoyancy or the speed of the convective system. Therefore, Gale et al. (2002) also examined the role that the system-relative inflow had in predicting MCS dissipation. Their study found that both the surface system-relative inflow (SSRI; defined as the difference in system speed and the line-normal surface wind) and elevated system-relative inflow (ESRI; defined as the difference between the system speed and the line-normal maximum wind in the lowest 2 km) tended to decrease prior to MCS dissipation. These decreases were attributed to the decrease in system

speed (for SSRI) and the cessation or movement away from a LLJ (ESRI). We applied this to our simulation (Table 5.5), and found that both tended to decrease over time as the convective system persisted into the daytime. By 1500 UTC, the simulated system had began to disorganize, and the system had weakened considerably by 1800 UTC. However, both the SSRI and ESRI had increased slightly between 1200 and 1500 UTC despite that the system speed had decreased. Fig. 79d suggests that the ambient winds had increased during this period, resulting in this increase. Therefore, like in Gale et al. (2002), a decrease in the system speed over time was observed with the weakening of the MCS. The decrease in this case may have been attributed to the movement of the cold pool away from the convective line, preventing deep lifting and continual regeneration of new cells.

5.4 Weisman Framework

Several studies have followed up on RKW theory in order to better theoretically explain the structure and internal dynamics of squall lines. One such study by Weisman (1992) examined the role of RIJs in the evolution of MCSs. In his study, the formation of these RIJs was attributed to horizontal buoyancy gradients induced by an upshear-tilted MCS. According to the previous discussions of RKW theory, the upshear tilt would imply a weakened system when $\frac{C}{\Delta u} \gg 1$. Weisman (1992) found that the added contributions to the horizontal vorticity from a RIJ may modulate this vorticity balance and help the system regain an "optimal state". Strong RIJs that remain elevated until reaching the leading edge are commonly observed with bow echoes. In this scenario, a more "optimal state" balance in vorticity exists for updrafts along the leading edge, resulting in a more erect circulation and stronger convection (Fig. 83b). However, if the RIJ descends prior to reaching the leading edge of the system, a vorticity distribution exists such that the leading updraft circulation has a more upshear tilt and is weaker (Fig. 83a).

In his study, Weisman utilized an idealized cloud model which assumed a unidirectional wind shear profile. Weisman varied the magnitude of both the buoyancy (i.e., CAPE) and wind shear, but each individual simulation had horizontally homogeneous initial conditions. As such, Weisman assumed the system to be two-dimensional, and all computations were done using a cross section orthogonal to the convective line. Therefore, one obvious possible shortcoming of this technique is that it does not allow for contributions from three-dimensional structures such as mesovortices. Additionally, the unidirectional shear profile with height is typically not representative of a nocturnal environment in which effects from the LLJ (i.e., shear-induced vorticity, convergence, etc.) are important.

Specifically, Weisman (1992) utilized a two-dimensional horizontal vorticity equation which assumes that the convective system is invariable in the along-line component:

$$\frac{d\eta}{dt} = -\frac{\partial B}{\partial x} \tag{5.8}$$

$$\eta = \frac{\partial u}{\partial z} - \frac{\partial w}{\partial x} \tag{5.9}$$

where η is the component of vorticity normal to the cross section (or parallel to the convective line). In this equation, u is defined as the wind component along the cross section (+x to the right), and w is the vertical wind component.

The primary forcing term in the horizontal vorticity equation is the horizontal buoyancy gradient, where B is given by equation 5.6. The total derivative of η can be expanded as follows:

$$\frac{d\eta}{dt} = \frac{\partial \eta}{\partial t} + u\frac{\partial \eta}{\partial x} + w\frac{\partial \eta}{\partial z} \tag{5.10}$$

Henceforth we will collectively refer to the last two terms in equation 5.10 as the "advection terms".

As mentioned above, equation 5.8 assumes that the only sources of horizontal vorticity generation in this framework are horizontal gradients of buoyancy, which generate a circulation in thermally-direct orientation (i.e., subsidence in the region of lesser buoyancy, and ascent in the region of greater buoyancy). One should note that shear-induced vorticity is inherent in Weisman's simulation, but because the model background is in a steady-state and the environment is horizontally homogeneous, this background vorticity is not changing with time in the ambient

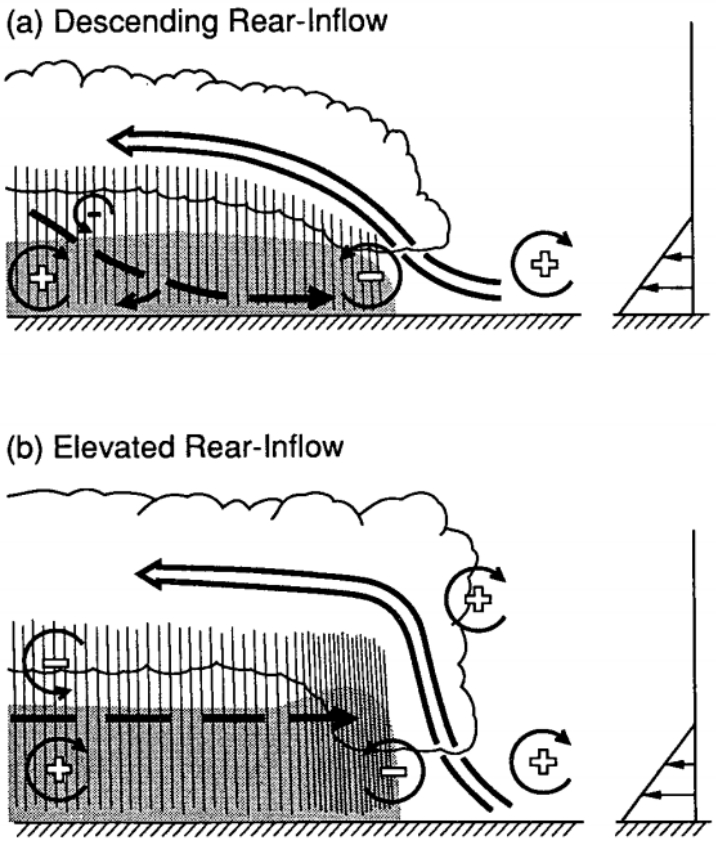

Figure 83: Idealized 2-D depiction of a mature squall line with (a) a descending rear-inflow jet, and (b) an elevated rear-inflow jet. The rear-inflow jet is represented by the dashed arrow. All other features are the same as Fig. 77 (from Fig. 23 of Weisman (1992)).

environment (i.e., the total derivative of vorticity is 0 owing to shear-induced background effects). The flux of horizontal vorticity induced by the vertical wind shear across the outflow boundary (i.e., vorticity advected by the system-relative flow) is in opposition to the baroclinically-generated vorticity within the system. If the system were in an "optimal state", these two contributions would approximately balance, resulting in an upward trajectory for newly developing updrafts along the outflow boundary.

Equation 5.8 can be written to include effects from convergence-induced "stretching", which was neglected in Weisman (1992) owing to their assumption of an incompressible atmosphere and integration over a vertical layer. With the inclusion of this term, equation 5.8 becomes:

$$\frac{d\eta}{dt} = -\eta\left(\frac{\partial u}{\partial x} + \frac{\partial w}{\partial z}\right) - \frac{\partial B}{\partial x} \tag{5.11}$$

This equation was obtained from equation 4 in Weisman (1992). In this form, two-dimensional convergence (or divergence) can act on ambient vorticity induced both baroclinically and by environmental wind shear to modify the magnitude of the vorticity (i.e., "stretch" or "squash" the vorticity). This effect was neglected by Weisman (1992) because of their incompressibility assumption. Henceforth, we will refer to the first term in equation 5.4 as the "total vorticity tendency term", the second as the "stretching term", and the last as the "baroclinic term".

We applied this frame of reference to our system with the inclusion of the stretching term to gauge its importance in contributing to the generation of horizontal vorticity. It is noteworthy that the results of stretching are three-dimensional and that this form of the vorticity equation neglects tilting. Therefore, the application of equation to a three-dimensional system likely provides an incomplete explanation of all possible contributions of vorticity within the system.

By breaking up equation into separate terms, the importance of various effects can be inferred. Owing to the infrequent outputting of our simulations (i.e., every 1 h), the forcing and spatial advection terms were calculated in order to infer the temporal tendencies. Thus, for the local horizontal vorticity, the advection, stretching, and baroclinic terms were all computed using system-relative winds[3].

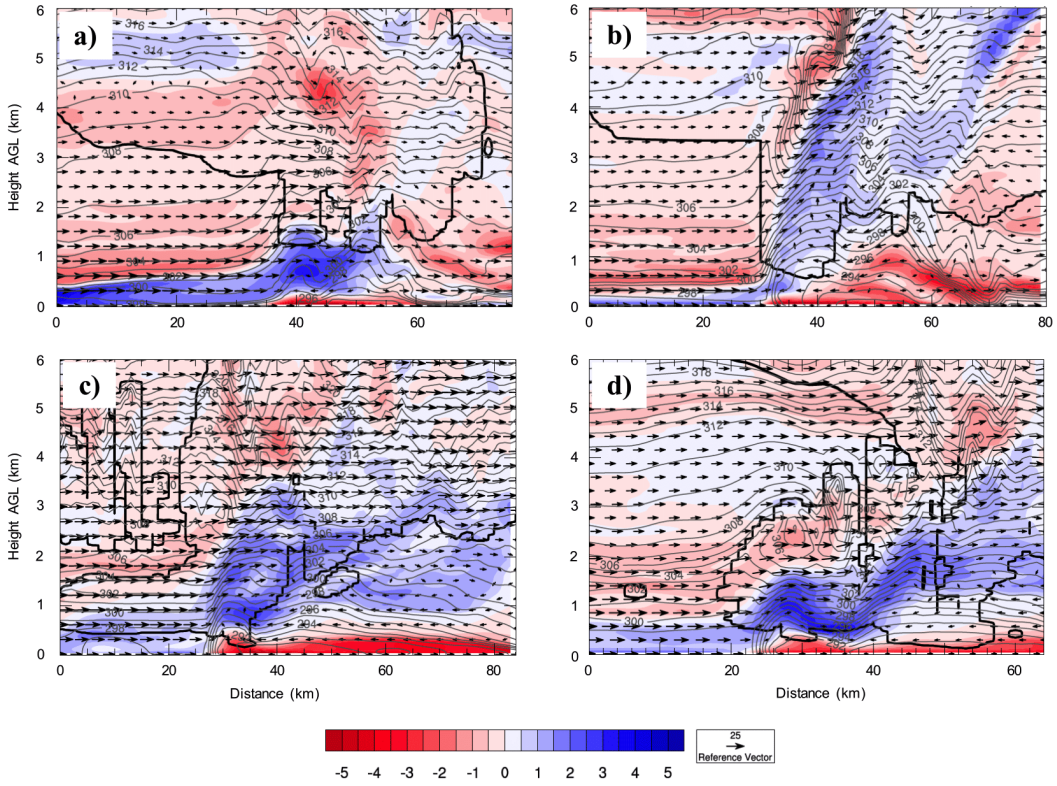

Figure 84: 0-6 km AGL cross sections of cross-section-relative horizontal vorticity (shaded; 10^{-2} s^{-1}), system-relative wind vectors (m s^{-1}), potential temperature contours (gray; K), and cloud boundary (thick black line) for (a) 0600 UTC, (b) 0900 UTC, (c) 1200 UTC, and (d) 1500 UTC. Positive values of vorticity are oriented into the page. The cross section paths are depicted in Fig. 44 with the green circle representing 0 km.

[3]The only term impacted by the system motion is the horizontal advection term.

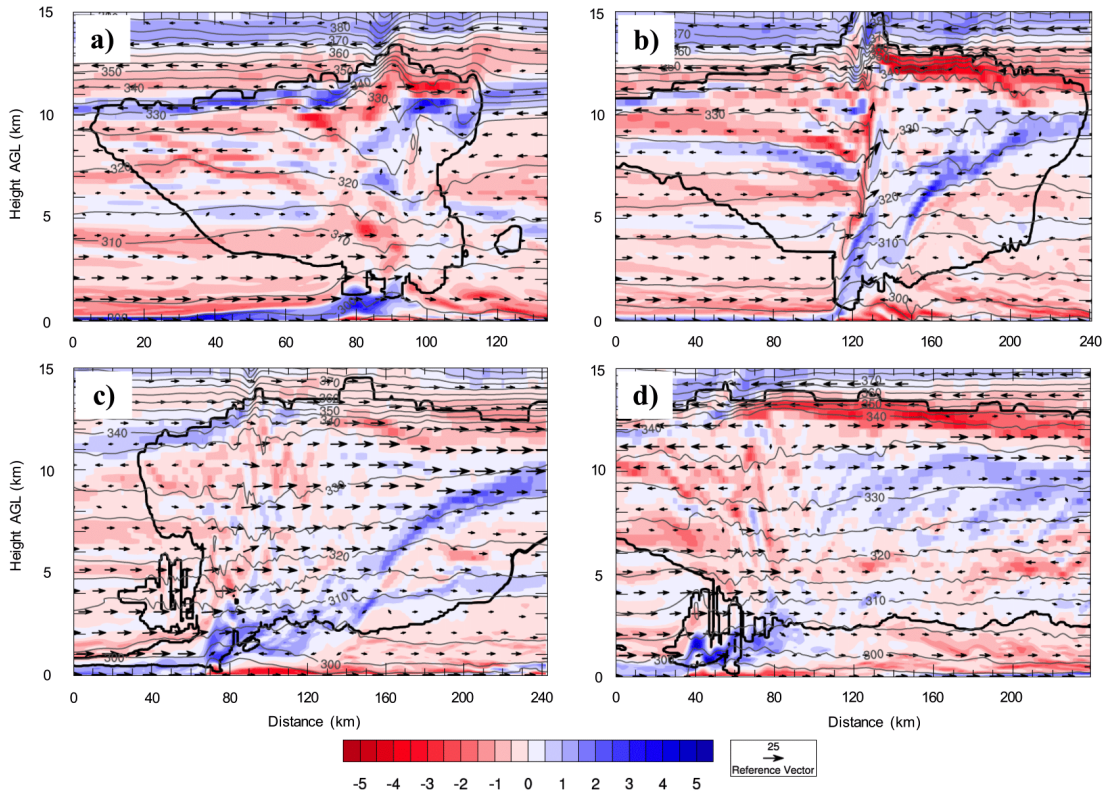

Figure 85: Same as in Fig. 84, but for 0-15 km AGL. The cross section paths are expanded on those depicted in Fig. 44.

An examination of the horizontal vorticity (Figs. 84,85) field is important to gauge the distribution of the ambient fields prior to any external forcing or advection. Throughout the duration of the system, the low-level vorticity orientation beneath the height of the maximum winds associated with the LLJ (positive is defined as pointing into the page) was unfavorable for RKW balance owing to the low-level shear as earlier discussed in section 5.2). However, the magnitude of this low-level vorticity and depth over which it existed decreased over time between 0600 and 0900 UTC (Figs. 84a,b), owing to the LLJ becoming largely parallel to the convective line (Fig. 51c). This decrease in vorticity resulted in "less unfavorable" conditions for RKW balance, which occurred coincident with the onset of unfavorable wave trapping conditions, as described in section 5.1. Therefore, the

evolving low-level shear favored the transition from elevated, bore-driven convection to cold-pool-driven convection.

This layer had deepened by 1200 UTC, but the magnitude of the vorticity had decreased. However, an increase in the line-normal environmental shear at 1500 UTC resulted in an increase in the magnitude of vorticity (Fig. 84d), by which time the system cold pool had begun to move away from the convection and the system was weakening.

In order to expand upon the RKW computations and examine the contributions of vorticity from the internal circulation and the horizontal gradients of buoyancy, the horizontal vorticity tendency equation from Weisman (1992) was applied. If just the forcing terms (baroclinic generation and stretching terms only) are examined, one potentially important finding is that the stretching term, which was neglected by Weisman, was not negligible in the strongest convective regions of the system. Its contributions either acted to supplement the vorticity generated baroclinically by the system or acted in opposition, depending on the system-relative flow. These forcing contributions will be discussed during the period of transition between being a downshear-tilted and an upshear-tilted system (i.e., 0800 - 1000 UTC).

At 0800 UTC, the system was downshear-tilted and preceded by a low-level bore (~15-20 km), but a strengthening cold pool behind this bore was located beneath the primary convective updraft (~30-40 km). The most prominent source of low-level vorticity was baroclinic generation across the bore as the stable layer was lifted upward (Fig. 86d). A contribution from the stretching term existed within this region, but this was of the opposite sign, muting the effects of the baroclinic term (Fig. 86c). A secondary region of baroclinic vorticity generation was located farther behind the bore (~50 km), which was associated with convective downdrafts and the cold pool. Within this region, the low-level contributions to vorticity from

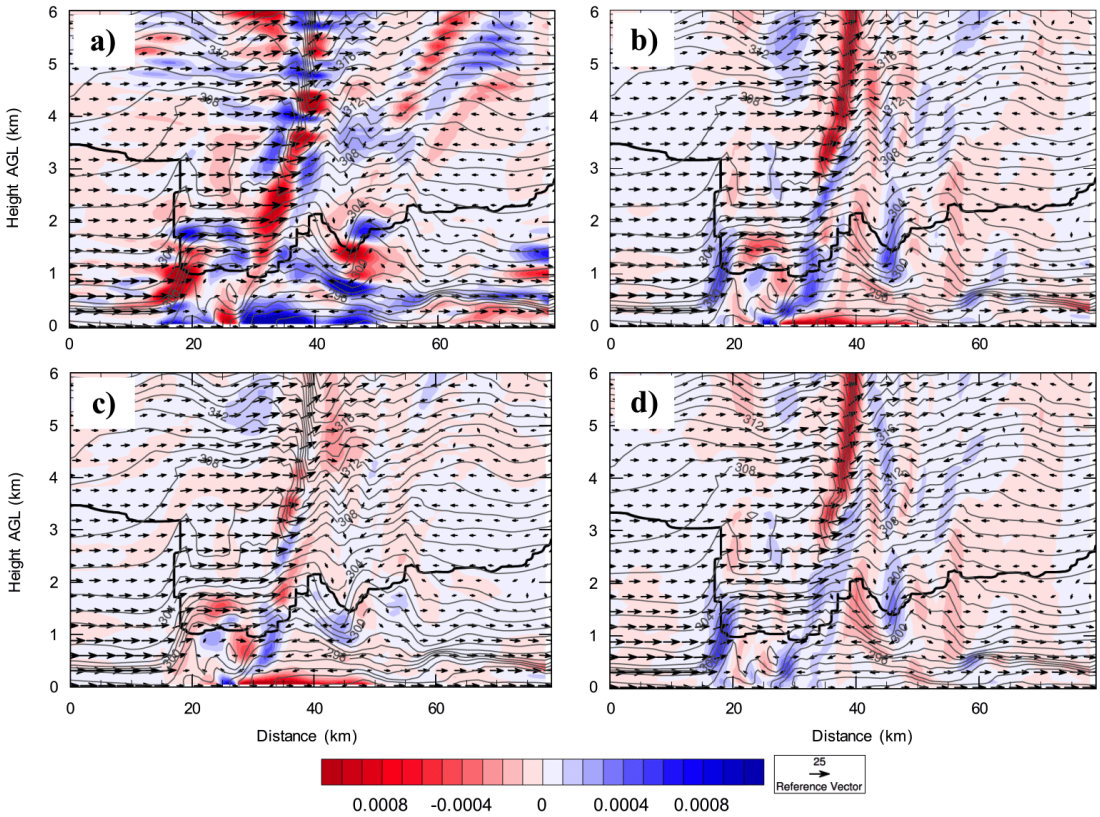

Figure 86: 0-6 km AGL cross sections of system-relative wind vectors (m s^{-1}), potential temperature contours (gray; K), cloud boundary (thick black line), and (a) advection terms (shaded; s^{-2}), (b) total vorticity tendency term (shaded; s^{-2}), (c) stretching term (shaded; s^{-2}), and (d) baroclinic term (shaded; s^{-2}) for 0800 UTC. The cross section path is depicted in Fig. 44a with the green circle representing 0 km.

the stretching term were positive, reinforcing the baroclinic circulation and likely strengthening the cold pool circulation with time (Fig. 86b).

By 0900 UTC, the system had evolved from a downshear-tilted system to an erect system. Moreover, the system cold pool had become collocated with the leading bore and accelerated, and the stretching term had greatest magnitude along the outflow boundary above ~3 km (~40 km; Fig. 87c). The contributions from the stretching term in this region were of the same sign as that from the baroclinic

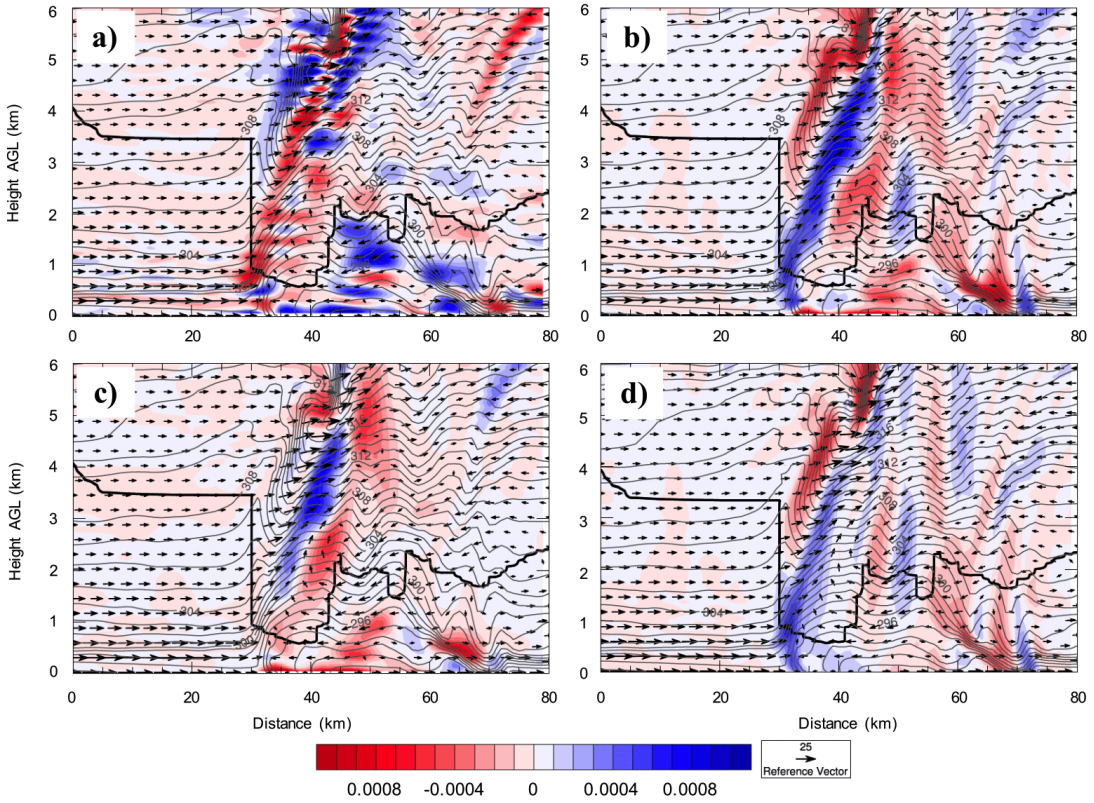

Figure 87: Same as in Fig. 86, but for 0900 UTC. The cross section path is depicted in Fig. 44b with the green circle representing 0 km.

term, which was maximized beneath ~2 km (~30-40 km; Fig. 87d). Moreover, the magnitudes associated with this term exceeded those from just the baroclinic contribution. The additive effects of the terms are shown in Fig. 87b, where the two contributions result in a deep (~5 km) region of positive vorticity generation along the cold pool in the region of strong, forced ascent (~30-40 km). In order for a vorticity balance to occur, this deep layer of vorticity would require a sufficiently deep layer of environmental wind shear, corroborating the findings of section 5.2 that wind shear over a ~5 km or deeper layer was required for representative ratios of $\frac{C}{\Delta u}$.

One explanation for the strongly positive contributions from the stretching term in this region is that horizontal convergence orthogonal to the line was strong, but

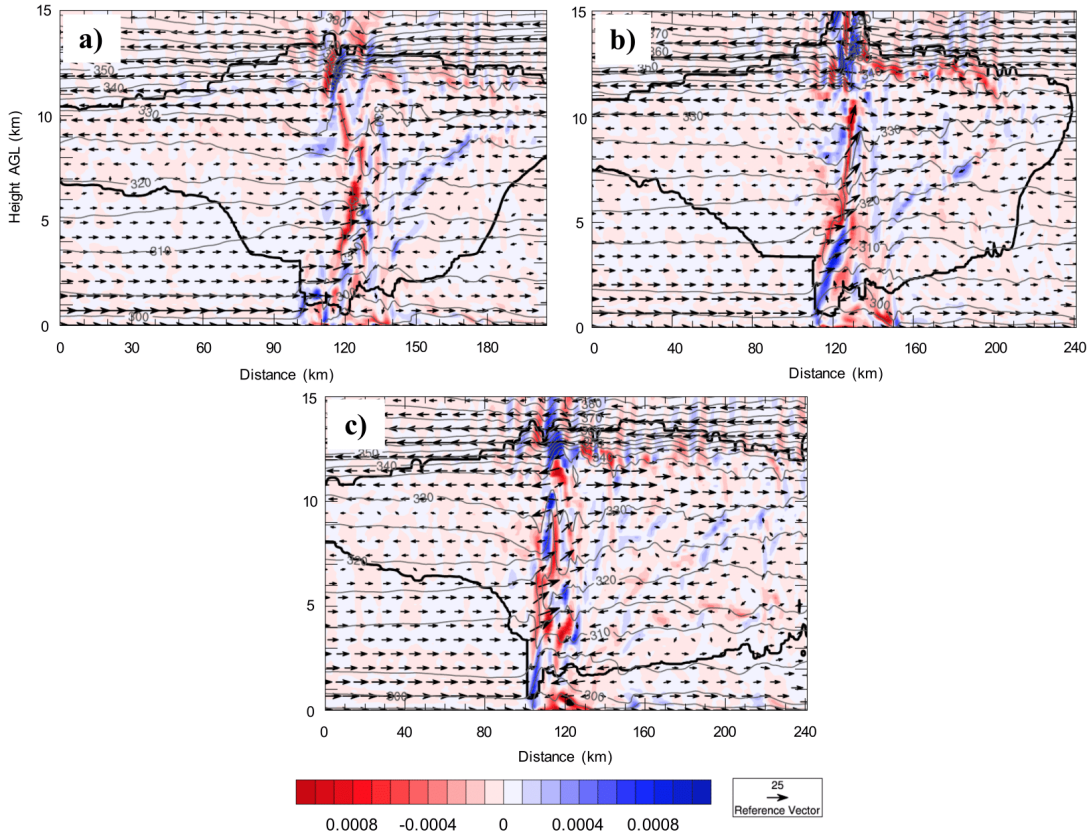

Figure 88: Total vorticity tendency term (shaded; s^{-2}), potential temperature contours (gray; K), cloud boundary (thick black line) for (a) 0800 UTC, (b) 0900 UTC, and (c) 1000 UTC. The cross sections are through the primary convective portion of the system, and the path for (b) is expanded on that depicted in Fig. 44b.

these parcels were primarily stable and had not realized their potential instability, resulting in a large contribution from $\frac{\partial u}{\partial x}$ <0, but minimal contributions from $\frac{\partial w}{\partial z}$ >0. Above 5 km, in the primary updraft region, the contribution from the stretching term was of the opposite sign (~45-55 km), which was likely attributed to the realization of CAPE and thus a change of sign of the vertical derivative to $\frac{\partial w}{\partial z}$ >0.

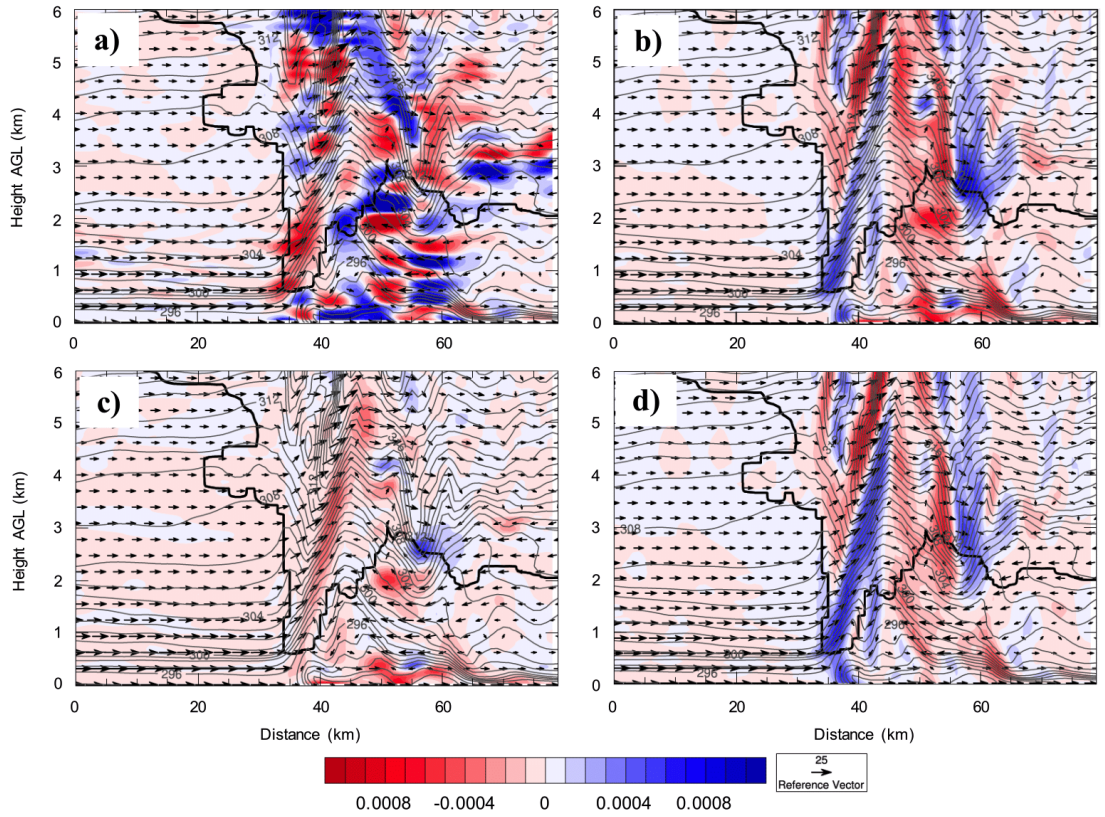

Figure 89: Same as in Fig. 86, but for 1000 UTC. The cross section path is through the bowing segment, with 0 km corresponding to the inflow point (not shown).

In this region, the updraft had a slight upshear tilt over the cold pool, providing vertical and horizontal shear in an orientation such that an additional contribution to positive vorticity existed. While the stretching term would have zero contributions in the absence of already-present vorticity, the enhancements caused by this term could act to reinforce circulations already present within the system. As a result, the cold pool circulation may have been enhanced by stretching and thus more easily overwhelmed the circulation produced by the environmental wind shear, resulting in an accelerating cold pool during this time. This process is one hypothesis for why the system accelerated and transitioned from being downshear-tilted to upshear-tilted between 0800 and 1000 UTC. Additionally, as described in

section 4.3, the enhancement of environmental CAPE during this time would aid in strengthening the cold pool, which would only further enhance this process.

It is worth emphasizing that at 0900 UTC, the magnitude of this stretching enhancement was actually greater than that from the baroclinic generation term alone, providing a strong argument that the negligence of this term yields an incomplete explanation for an "optimal state". However, while the previous discussion only considered contributions along the leading edge, internal circulations farther in the rear of the system (i.e., a RIJ) also played an important role in the vorticity balance (Weisman, 1992, 1993). These contributions could either help to resume an "optimal state" in the presence of a dominant cold pool circulation or further contribute to an upshear-tilted, weaker system (Fig. 83).

The RIJ in the simulation strengthened between 0800 and 1000 UTC, which has previously been attributed to an acceleration into the rear of the circulation by a thermally-induced low pressure (e.g., Houze et al., 1989, or, in this framework, horizontal buoyancy gradients). The RIJ, which was located beneath the ascending front-to-rear mesoscale updraft circulation, induced a region of strong vertical wind shear above it, with lesser magnitude wind shear of the opposite sign beneath the maximum rear-inflow level. Moreover, horizontal convergence was associated with this inflow as it approached the rear of the convective updrafts. Therefore, some enhancement of positive vorticity generation via stretching effects could exist in this portion of the system owing to the internal flow distribution, which was observed in the vertical cross sections (~150-180 km; Fig. 88). This reinforcement of the RIJ circulation by stretching could result in a positive feedback and a strengthening system. This seems to be plausible as the RIJ remained elevated until descending abruptly to the rear of the convective updraft during the strongest portion of the system (Fig. 88b). This observation is consistent with the structure of the elevated

rear-inflow jet in Weisman (1992), which yields a stronger system through a more "optimal state".

By 1000 UTC, the system had evolved from being an erect system at 0900 UTC to an upshear-tilted system with a well-defined mesoscale downdraft owing to the RIJ. The environmental CAPE profile had increased since 0900 UTC, and the primary convective updraft was rooted above a surface cold pool. At 1000 UTC, the contributions from the stretching term (Fig. 89c) were of the opposite sign from that of the baroclinic generation term (Fig. 89d), which extended from the surface to above 5 km (~35-45 km). Therefore, the total vorticity generation contribution was less than from the baroclinic effect alone (Fig. 89b). Moreover, the stretching effect had the greatest contribution between 2 and 4 km, which likely was attributed to the realization of potential instability within the convective updraft; this likely occurred lower than at 0900 UTC since the environmental instability (inhibition) had increased (decreased). The stretching contributions may have helped to mitigate some of the effects from the deepening cold pool in the presence of an unfavorable shear profile (Fig. 80c), preventing the cold pool from surging away from the convective region at this time.

In summary, the evolution of the system can largely be explained by contributions to vorticity in a RKW/Weisman framework, where the baroclinic generation effects in the presence of unfavorable environmental shear profiles resulted in the gradual upshear tilting of the system. Additionally, the inclusion of the stretching term either acted in tandem with or against the baroclinic contributions, likely impacting the evolution of the system. The stretching term had the greatest contributions at 0900 UTC, which may have aided in the strengthening and acceleration of the system. Moreover, its contributions led to a substantially deep layer of positive vorticity tendency, which would require much deeper layer of vertical wind shear to balance than proposed by (Rotunno et al., 1988; Weisman et al., 1988).

The large stretching contributions at 0900 UTC were likely dependent on the stability and orientation inflow over the cold pool, which resulted in cold-pool-driven forced ascent but little realized buoyancy until farther aloft, where the stretching term changed signs. However, the large magnitude of this term, which was even greater than that of the baroclinic term, supports that these effects should not be neglected when applying the horizontal vorticity balance to nocturnal convective systems. Moreover, the role of tilting of vorticity into the horizontal plane, which was neglected in our analysis, should be investigated to provide a complete explanation of the vorticity distribution in three-dimensional convective systems.

Chapter 6

Conclusions, Implications, and Future Work

While previous studies have observed that MCSs often dissipate with the cessation of the LLJ and onset of boundary layer mixing (e.g., Gale et al., 2002), Hane et al. (2008) found that 28% of warm season MCSs over a portion of the southern Great Plains maintain their intensity or strengthen during the morning. Despite this, few previous studies (e.g., Marsham et al., 2011; Trier et al., 2011) have investigated the evolution of long-lived MCSs that transition from being elevated to surface-based. Thus, this study aims to advance to knowledge in this relatively unexplored area by examining a case study of a long-lived MCS that occurred on 6 October 2014. This system initiated in the nocturnal environment on the dry side of a surface stationary front, which was an environment not thought to be supportive of convection. Further investigation suggests that two mesoscale boundaries, which originated from a weak cold front and had surface signatures commonly observed with the bore passages, were responsible for triggering this initially-elevated convection. The MCS, which was poorly forecast by operational convection-allowing models, produced several wind and hail reports and one nocturnal tornado.

Previous studies (e.g., Billings and Parker, 2012) have documented convection that was thought to be elevated but produced a tornado despite the existence of a stable boundary layer. These studies concluded that dynamical forcing induced

by the system is often able to draw in stable, near-surface air, resulting in a partially surface-based system. However, Oklahoma Mesonet sites in proximity to the tornado observed surface signatures often attributed to the passage of bores (e.g., Koch et al., 1991; Marsham et al., 2011). These bore signatures (i.e., increasing winds from calm to gusty which is coincident with substantial warming and a steep rise in pressure) reveal that the stable layer was eroded by turbulent mixing prior to the arrival of the convective system. Therefore, perhaps bore-induced mixing yielded a more favorable environment for tornadogenesis by destabilizing the near-surface layer. However, to our knowledge, this process has never been documented.

The westernmost convection weakened considerably as it moved into southern Oklahoma and northern Texas. However, this portion of the convection subsequently restrengthened, forming a bowing segment and accelerating toward the southeast as a well-defined leading-line, trailing-stratiform MCS. The convective system persisted for approximately 18 h before eventually moving off the Gulf Coast during the early afternoon. Despite that, climatologically, nocturnal MCSs tend to dissipate with the cessation of the LLJ and the destabilization of the boundary layer, this MCS was able to sustain itself throughout the diurnal cycle.

WRF-ARW simulations were utilized in order to examine how the system reorganized and persisted as it moved into a more-unstable environment. Owing to errors in the RAP initial conditions, the WRF model simulated an erroneous first wave of convection that left a residual cold pool over central Oklahoma before dissipating. Afterward, a weak baroclinic boundary moved into the region, which triggered deep convection as this boundary collided with an elevated source of high-CAPE air. This elevated CAPE was attributed to ascent of the LLJ over the residual cold pool from the erroneous system. This mechanism for initiation,

which did not occur in the observations, was similar to that in Marsham et al. (2011), who also documented a long-lived, transitioning system.

The initial convection was elevated and maintained by a bore-like feature for ~2 hours prior to the development of a strong surface cold pool. Between 0800 and 1000 UTC, 3-5 hours after convective initiation in the simulations, a portion of the system developed a strong RIJ and began to surge toward the southeast, forming a cold-pool-driven bowing segment. However, convection farther to the west was still bore-driven and elevated, which was associated with more favorable conditions for wave trapping.

The development of the RIJ and bowing segment were examined in an RKW framework (Rotunno et al., 1988; Weisman, 1992, 1993), which suggested that the nearly-parallel orientation of the LLJ to the convective line helped to suppress vorticity contributions from low-level shear, which were unfavorably oriented for an "optimal state" of RKW balance. Additionally, contributions from the horizontal stretching of vorticity may have helped to enhance this leading cold pool circulation, possibly aiding in the transition from a downshear-tilted to an upshear-tilted MCS. This process is explained in an RKW framework as the result of the cold pool circulation overwhelming that associated with the environmental wind shear (i.e., $\frac{C}{\Delta u} \gg 1$) (Rotunno et al., 1988; Weisman, 1992; Parker, 2008). The superposition of these stretching effects and the baroclinic-generation of vorticity at 0900 UTC support that a sufficiently-deep layer of environmental wind shear must be considered when examining an RKW balance. Contributions from stretching were also observed in the rear of the system, helping to enhance the RIJ circulation and possibly strengthening the system.

As the simulated MCS continued to move toward the south, the environment progressively became more unstable, and the strongest portion of the system became surface-based prior to sunrise. During this time, the system reorganized into

a leading-line, trailing-stratiform MCS. Because the strongest portion of the system was able to evolve into a cold-pool-driven and surface-based system prior to daytime boundary layer mixing, the MCS maintained its strength and persisted into the afternoon. As mixing continued and the cold pool strengthened with respect to the environment, the cold pool accelerated away from the convection, resulting in a greater upshear tilt subsequent weakening (Rotunno et al., 1988; Parker, 2008). However, smaller clusters of convection were present until the end of the simulation at 2000 UTC.

An examination of the environmental CAPE and CIN distribution over time suggests that the LLJ was critical in providing the elevated instability which initially fed the system. Moreover, flow from the LLJ relative to the sloping terrain resulted in an increasing region of surface-based CAPE throughout the night. However, westerly flow aloft resulted in a strengthening capping inversion with time, preventing new convective development within this region. Farther east where terrain effects were minimal, the highest-CAPE air remained elevated throughout most of the night. However, this region had little capping, allowing new cells to be generated as the MCS moved into this area.

This study suggests that a relatively complex sequence of events occurred, allowing the system to be long-lived and persist into the following day. Specifically, the convective system originated due to lift by a large-scale boundary as it interacted with elevated instability from the LLJ. The system was initially maintained by a bore and moved away from the baroclinic boundary. As the environment became less favorable for maintaining this wave disturbance, the system was able to transition to being surface-based in association with a deepening cold pool. Strong moisture advection and mixing beneath the LLJ resulted in a favorable environment for surface-based convection prior to sunrise. Therefore, one could argue

that a relatively unique set of conditions played a role in producing this long-lived system.

The study also provides insight into the challenges of accurately simulating a long-lived convective event that transitioned between being elevated and surface-based. The convection in this case formed in response to lifting over a baroclinic boundary in an environment with low CAPE. The system was initially maintained by a bore and moved ahead of the baroclinic zone. Convective parameterizations in coarser grid models, such as the RAP and NAM, do not account for such processes, and grid spacings of 3-4 km may have difficulty in representing bores, hindering forecasts of these events. Coarse grid models may also have difficulty in representing the narrow corridor of moist air advected by the LLJ. The system subsequently became surface-based and cold-pool-driven, which was associated with the environment becoming increasingly unstable at low levels owing to mixing within the stable boundary layer. The stable boundary layer alone is currently a major challenge for numerical weather prediction, as described in Holtslag and Coauthors (2013). These aforementioned points are likely why the operational numerical models, even just prior to the initiation of this convection, poorly depicted this system evolution. Moreover, the simulated convection in WRF was highly sensitive to horizontal grid spacing, boundary conditions, and parameterization schemes, causing great difficulty in acquiring a realistic simulation. Therefore, we hope that the increased understanding of the processes responsible for the initiation and persistence of this system can be incorporated into efforts to better predict nocturnal convection.

Additional simulations of similar, long-lived convective systems are needed to determine whether or not the evolution of the environment and convection in this study is typical of these persistent systems. Moreover, an examination of convective systems in unique, rapidly-evolving environments that do not exhibit this daytime

persistence would be useful for better understanding the processes controlling system longevity. Future studies should also examine the sensitivity of the convective evolution to grid spacing and physics parameterizations to determine their relative contributions to the simulated system longevity. Additionally, high-resolution observations of these persistent, transitioning systems and their environments are needed to better understand how convection responds to the inhomogeneous and evolving nature of instability and vertical wind shear.

Bibliography

Arritt, R. W., T. D. Rink, M. Segal, D. P. Todey, C. A. Clark, M. J. Mitchell, and K. M. Labas, 1997: The Great Plains low-level jet during the warm season of 1993. *Mon. Wea. Rev.*, **125 (9)**, 2176–2192.

Atkins, N. T. and M. St. Laurent, 2009: Bow echo mesovortices. part II: Their genesis. *Mon. Wea. Rev.*, **137 (5)**, 1514–1532.

Augustine, J. A. and F. Caracena, 1994: Lower-tropospheric precursors to nocturnal MCS development over the central United States. *Wea. Forecasting*, **9 (1)**, 116–135.

Banta, R. M., Y. L. Pichugina, and W. A. Brewer, 2006: Turbulent velocity-variance profiles in the stable boundary layer generated by a nocturnal low-level jet. *J. Atmos. Sci.*, **63 (11)**, 2700–2719.

Banta, R. M., Y. L. Pichugina, and R. K. Newsom, 2003: Relationship between low-level jet properties and turbulence kinetic energy in the nocturnal stable boundary layer. *J. Atmos. Sci.*, **60 (20)**, 2549–2555.

Bartels, D. L. and R. A. Maddox, 1991: Midlevel cyclonic vortices generated by mesoscale convective systems. *Mon. Wea. Rev.*, **119 (1)**, 104–118.

Benjamin, S. G. and Coauthors, 2013: Data assimilation and model updates in the 2013 Rapid Refresh (RAP) and High-Resolution Rapid Refresh (HRRR) analysis and forecast systems.

Benjamin, S. G. and Coauthors, 2016: A North American hourly assimilation and model forecast cycle: The Rapid Refresh. *Mon. Wea. Rev.*, **144 (4)**, 1669–1694.

Benjamin, T. B., 1968: Gravity currents and related phenomena. *Journal of Fluid Mechanics*, **31 (02)**, 209–248.

Billings, J. M. and M. D. Parker, 2012: Evolution and maintenance of the 22-23 June 2003 nocturnal convection during BAMEX. *Wea. Forecasting*, **27**, 279–300.

Blackadar, A. K., 1957: Boundary layer wind maxima and their significance for the growth of nocturnal inversions. *Bull. Amer. Meteor. Soc.*, **38 (5)**, 283–290.

Blake, B., 2015: The structure, evolution, and dynamics of a nocturnal convective system simulated using the WRF-ARW model. M.S. thesis, University of Oklahoma.

Blake, B. T., D. B. Parsons, K. R. Haghi, and S. G. Castleberry, 2017: The Structure, Evolution and Dynamics of a Nocturnal Convective System Simulated Using the WRF-ARW Model. *Mon. Wea. Rev.,* in review.

Bluestein, H. B., 1985: An observational study of a mesoscale area of convection under weak synoptic-scale forcing. *Mon. Wea. Rev.*, **113 (4)**, 520–539.

Bluestein, H. B., 1993: *Synoptic-Dynamic Meteorology in Midlatitudes: Observations and theory of weather systems*. Synoptic-Dynamic Meteorology in Midlatitudes, Oxford University Press, New York, NY, USA, 594 pp.

Bluestein, H. B. and M. H. Jain, 1985: Formation of mesoscale lines of precipitation: Severe squall lines in Oklahoma during the spring. *J. Atmos. Sci.*, **42 (16)**, 1711–1732.

Bluestein, H. B. and J. C. Snyder, 2015: An observational study of the effects of dry air produced in dissipating convective storms on the predictability of severe weather. *Wea. Forecasting*, **30 (1)**, 79–114.

Bluestein, H. B. and M. L. Weisman, 2000: The interaction of numerically simulated supercells initiated along lines. *Mon. Wea. Rev.*, **128 (9)**, 3128–3149.

Bluestein, H. B., Z. B. Wienhoff, D. D. Turner, D. W. Reif, J. C. Snyder, K. J. Thiem, and J. B. Houser, 2017: A comparison of the fine-scale structures of a prefrontal wind-shift line and a strong cold front in the Southern Plains of the U.S. *Mon. Wea. Rev.,* in review.

Bonner, W. D., 1968: Climatology of the low-level jet. *Mon. Wea. Rev.*, **96 (12)**, 833–850.

Bonner, W. D. and J. Paegle, 1970: Diurnal variations in boundary layer winds over the south-central United States in summer. *Mon. Wea. Rev.*, **98 (10)**, 735–744.

Browning, K. A. and T. Harrold, 1969: Air motion and precipitation growth in a wave depression. *Quart. J. Roy. Meteor. Soc.*, **95 (404)**, 288–309.

Bryan, G., D. Ahijevych, C. Davis, S. Trier, and M. Weisman, 2005: Observations of cold pool properties in mesoscale convective systems during BAMEX. *Preprints, 11th Conf. on Mesoscale Processes, Albuquerque, NM, Amer. Meteor. Soc., JP5J*, Vol. 12.

Bryan, G. H. and H. Morrison, 2012: Sensitivity of a simulated squall line to horizontal resolution and parameterization of microphysics. *Mon. Wea. Rev.*, **140 (1)**, 202–225.

Bryan, G. H. and R. Rotunno, 2008: Gravity currents in a deep anelastic atmosphere. *J. Atmos. Sci.*, **65 (2)**, 536–556.

Bryan, G. H. and M. L. Weisman, 2006: Mechanisms for the production of severe surface winds in a simulation of an elevated convective system.

Bryan, G. H., J. C. Wyngaard, and J. M. Fritsch, 2003: Resolution requirements for the simulation of deep moist convection. *Mon. Wea. Rev.*, **131 (10)**, 2394–2416.

Carbone, R. E., 1982: A severe frontal rainband. Part I: Stormwide hydrodynamic structure. *J. Atmos. Sci.*, **39 (2)**, 258–279.

Carbone, R. E. and J. D. Tuttle, 2008: Rainfall occurrence in the U.S. warm season: The diurnal cycle. *J. Climate*, **21 (16)**, 4132–4146.

Clark, A. J. and Coauthors, 2012: An overview of the 2010 hazardous weather testbed experimental forecast program spring experiment. *Bull. Amer. Meteor. Soc.*, **93 (1)**, 55.

Clark, A. J., W. A. Gallus Jr, and T.-C. Chen, 2007: Comparison of the diurnal precipitation cycle in convection-resolving and non-convection-resolving mesoscale models. *Mon. Wea. Rev.*, **135 (10)**, 3456–3473.

Colman, B. R., 1990a: Thunderstorms above frontal surfaces in environments without positive CAPE. Part I: A climatology. *Mon. Wea. Rev.*, **118 (5)**, 1103–1122.

Colman, B. R., 1990b: Thunderstorms above frontal surfaces in environments without positive CAPE. Part II: Organization and instability mechanisms. *Mon. Wea. Rev.*, **118 (5)**, 1123–1144.

Coniglio, M. C., S. F. Corfidi, and J. S. Kain, 2012: Views on applying RKW theory: An illustration using the 8 May 2009 derecho-producing convective system. *Mon. Wea. Rev.*, **140 (3)**, 1023–1043.

Coniglio, M. C., J. Correia Jr, P. T. Marsh, and F. Kong, 2013: Verification of convection-allowing WRF model forecasts of the planetary boundary layer using sounding observations. *Wea. Forecasting*, **28 (3)**, 842–862.

Corfidi, S. F., 2003: Cold pools and MCS propagation: Forecasting the motion of downwind-developing MCSs. *Wea. Forecasting*, **18 (6)**, 997–1017.

Corfidi, S. F., S. J. Corfidi, and D. M. Schultz, 2008: Elevated convection and castellanus: Ambiguities, significance, and questions. *Wea. Forecasting*, **23 (6)**, 1280–1303.

Crook, N. A., 1988: Trapping of low-level internal gravity waves. *J. Atmos. Sci.*, **45 (10)**, 1533–1541.

Crook, N. A., 1996: Sensitivity of moist convection forced by boundary layer processes to low-level thermodynamic fields. *Mon. Wea. Rev.*, **124 (8)**, 1767–1785.

Crum, T. D. and R. L. Alberty, 1993: The WSR-88D and the WSR-88D operational support facility. *Bull. Amer. Meteor. Soc.*, **74 (9)**, 1669–1687.

Curtis, R. and H. Panofsky, 1958: The relation between large-scale vertical motion and weather in summer. *Bull. Amer. Meteor. Soc.*, **39**, 521–531.

Davies-Jones, R., 1984: Streamwise vorticity: The origin of updraft rotation in supercell storms. *J. Atmos. Sci.*, **41 (20)**, 2991–3006.

Davies-Jones, R. and H. Brooks, 1993: Mesocyclogenesis from a theoretical perspective. *The Tornado: Its Structure, Dynamics, Prediction, and Hazards*, 105–114.

Davies-Jones, R., R. J. Trapp, and H. B. Bluestein, 2001: Tornadoes and tornadic storms. *Severe Convective Storms*, Springer, 167–221.

Davis, C. A., K. W. Manning, R. E. Carbone, S. B. Trier, and J. D. Tuttle, 2003: Coherence of warm-season continental rainfall in numerical weather prediction models. *Mon. Wea. Rev.*, **131 (11)**, 2667–2679.

Davis, C. A. and M. L. Weisman, 1994: Balanced dynamics of mesoscale vortices produced in simulated convective systems. *J. Atmos. Sci.*, **51 (14)**, 2005–2030.

Dial, G. L., J. P. Racy, and R. L. Thompson, 2010: Short-term convective mode evolution along synoptic boundaries. *Wea. Forecasting*, **25 (5)**, 1430–1446.

Dudhia, J., 1989: Numerical study of convection observed during the winter monsoon experiment using a mesoscale two-dimensional model. *J. Atmos. Sci.*, **46 (20)**, 3077–3107.

Easterling, D. R. and P. J. Robinson, 1985: The diurnal variation of thunderstorm activity in the United States. *J. Climate Appl. Meteor.*, **24 (10)**, 1048–1058.

Fabry, F., 2006: The spatial variability of moisture in the boundary layer and its effect on convection initiation: Project-long characterization. *Mon. Wea. Rev.*, **134 (1)**, 79–91.

French, A. J. and M. D. Parker, 2010: The response of simulated nocturnal convective systems to a developing low-level jet. *J. Atmos. Sci.*, **67 (10)**, 3384–3408.

Fritsch, J., R. Kane, and C. Chelius, 1986: The contribution of mesoscale convective weather systems to the warm-season precipitation in the United States. *J. Climate Appl. Meteor.*, **25 (10)**, 1333–1345.

Fritsch, J. and R. Maddox, 1981: Convectively driven mesoscale weather systems aloft. Part II: Numerical simulations. *J. Appl. Meteor.*, **20 (1)**, 20–26.

Fujita, T. T., 1978: *Manual of downburst identification for project NIMROD.* University of Chicago.

Gale, J. J., W. A. Gallus Jr, and K. A. Jungbluth, 2002: Toward improved prediction of mesoscale convective system dissipation. *Wea. Forecasting*, **17 (4)**, 856–872.

Haghi, K. R., D. B. Parsons, and A. Shapiro, 2017: Bores observed during IHOP_2002: The relationship of bores to the nocturnal environment. *Mon. Wea. Rev.,* in review.

Halbert, K., W. Blumberg, and P. Marsh, 2015: SHARPpy: Fueling the Python Cult. *Preprints, 5th Symposium on Advances in Modeling and Analysis Using Python, Phoenix AZ.*

Hane, C. E., J. A. Haynes, D. L. Andra Jr, and F. H. Carr, 2008: The evolution of morning convective systems over the U.S. Great Plains during the warm season. Part II: A climatology and the influence of environmental factors. *Mon. Wea. Rev.*, **136 (3)**, 929–944.

Hane, C. E., J. D. Watts, D. L. Andra Jr, J. A. Haynes, E. Berry, R. M. Rabin, and F. H. Carr, 2003: The evolution of morning convective systems over the US Great Plains during the warm season. Part I: The forecast problem. *Wea. Forecasting*, **18 (6)**, 1286–1294.

Heideman, K. F. and J. M. Fritsch, 1988: Forcing mechanisms and other characteristics of significant summertime precipitation. *Wea. Forecasting*, **3 (2)**, 115–130.

Hobbs, P. V. and P. O. G. Persson, 1982: The mesoscale and microscale structure and organization of clouds and precipitation in midlatitude cyclones. Part V: The substructure of narrow cold-frontal rainbands. *J. Atmos. Sci.*, **39 (2)**, 280–295.

Holton, J. R., 1967: The diurnal boundary layer wind oscillation above sloping terrain. *Tellus*, **19 (2)**, 199–205.

Holtslag, A. and Coauthors, 2013: Stable atmospheric boundary layers and diurnal cycles: challenges for weather and climate models. *Bull. Amer. Meteor. Soc.*, **94 (11)**, 1691–1706.

Hong, S.-Y., Y. Noh, and J. Dudhia, 2006: A new vertical diffusion package with an explicit treatment of entrainment processes. *Mon. Wea. Rev.*, **134 (9)**, 2318–2341.

Horgan, K. L., D. M. Schultz, J. E. Hales Jr, S. F. Corfidi, and R. H. Johns, 2007: A five-year climatology of elevated severe convective storms in the United States east of the Rocky Mountains. *Wea. Forecasting*, **22 (5)**, 1031–1044.

Houze, R. A., 2004: Mesoscale convective systems. *Reviews of Geophysics*, **42 (4)**.

Houze, R. A., S. Rutledge, M. Biggerstaff, and B. Smull, 1989: Interpretation of Doppler weather radar displays of midlatitude mesoscale convective systems. *Bull. Amer. Meteor. Soc.*, **70 (6)**, 608–619.

Houze, R. A., B. F. Smull, and P. Dodge, 1990: Mesoscale organization of springtime rainstorms in Oklahoma. *Mon. Wea. Rev.*, **118 (3)**, 613–654.

Janjic, Z., 1996: The surface layer parameterization in the NCEP Eta Model. *World Meteorological Organization-Publications-WMO TD*, 4–16.

Janjic, Z. I., 1994: The step-mountain eta coordinate model: Further developments of the convection, viscous sublayer, and turbulence closure schemes. *Mon. Wea. Rev.*, **122 (5)**, 927–945.

Johns, R. H. and C. A. Doswell III, 1992: Severe local storms forecasting. *Wea. Forecasting*, **7 (4)**, 588–612.

Johnston, E. C., 1981: *Meso-scale vorticity centers induced by meso-scale convective complexes*. University of Wisconsin–Madison.

Kain, J. S., et al., 2013: A feasibility study for probabilistic convection initiation forecasts based on explicit numerical guidance. *Bull. Amer. Meteor. Soc.*, **94 (8)**, 1213–1225.

Kincer, J. B., 1916: Daytime and nightime precipitation and their economic significance. *Mon. Wea. Rev.*, **44 (11)**, 628–633.

Klein, P. M., X.-M. Hu, A. Shapiro, and M. Xue, 2016: Linkages between boundary-layer structure and the development of nocturnal low-level jets in central oklahoma. *Boundary-layer Meteor.*, **158 (3)**, 383–408.

Knievel, J. C. and R. H. Johnson, 2003: A scale-discriminating vorticity budget for a mesoscale vortex in a midlatitude, continental mesoscale convective system. *J. Atmos. Sci.*, **60 (6)**, 781–794.

Knupp, K., 2006: Observational analysis of a gust front to bore to solitary wave transition within an evolving nocturnal boundary layer. *J. Atmos. Sci.*, **63 (8)**, 2016–2035.

Koch, S. E., P. B. Dorian, R. Ferrare, S. Melfi, W. C. Skillman, and D. Whiteman, 1991: Structure of an internal bore and dissipating gravity current as revealed by Raman lidar. *Mon. Wea. Rev.*, **119 (4)**, 857–887.

Lawson, J. and W. A. Gallus Jr, 2016: On Contrasting Ensemble Simulations of Two Great Plains Bow Echoes. *Wea. Forecasting*, **31 (3)**, 787–810.

Lee, B. D. and R. B. Wilhelmson, 1997: The numerical simulation of non-supercell tornadogenesis. Part I: Initiation and evolution of pretornadic misocyclone circulations along a dry outflow boundary. *J. Atmos. Sci.*, **54 (1)**, 32–60.

Lillo, S. P. and D. B. Parsons, 2016: Investigating the dynamics of error growth in ECMWF medium range forecast busts. *Quart. J. Roy. Meteor. Soc.*

Lim, K.-S. S. and S.-Y. Hong, 2010: Development of an effective double-moment cloud microphysics scheme with prognostic cloud condensation nuclei (CCN) for weather and climate models. *Mon. Wea. Rev.*, **138 (5)**, 1587–1612.

Lindzen, R. and K. Tung, 1976: Banded convective activity and ducted gravity waves. *Mon. Wea. Rev.*, **104 (12)**, 1602–1617.

Locatelli, J. D., M. T. Stoelinga, and P. V. Hobbs, 2002: A new look at the super outbreak of tornadoes on 3-4 April 1974. *Mon. Wea. Rev.*, **130 (6)**, 1633–1651.

Maddox, R., D. Perkey, and J. Fritsch, 1981: Evolution of upper tropospheric features during the development of a mesoscale convective complex. *J. Atmos. Sci.*, **38 (8)**, 1664–1674.

Maddox, R. A., 1980: Meoscale convective complexes. *Bull. Amer. Meteor. Soc.*, **61 (11)**, 1374–1387.

Maddox, R. A., 1983: Large-scale meteorological conditions associated with midlatitude, mesoscale convective complexes. *Mon. Wea. Rev.*, **111 (7)**, 1475–1493.

Mahoney, K. M., G. M. Lackmann, and M. D. Parker, 2009: The role of momentum transport in the motion of a quasi-idealized mesoscale convective system. *Mon. Wea. Rev.*, **137 (10)**, 3316–3338.

Markowski, P. and Y. Richardson, 2011: *Mesoscale meteorology in midlatitudes*, Vol. 2. John Wiley & Sons.

Marsham, J. H., S. B. Trier, T. M. Weckwerth, and J. W. Wilson, 2011: Observations of elevated convection initiation leading to a surface-based squall line during 13 June IHOP_2002. *Mon. Wea. Rev.*, **139 (1)**, 247–271.

McDonald, J. R. and K. C. Mehta, 2006: *A recommendation for an Enhanced Fujita scale (EF-Scale)*. Wind Science and Engineering Center, Texas Tech University.

Means, L. L., 1944: The nocturnal maximum occurrence of thunderstorms in the midwestern states. *Dept. of Meteor., Univ. of Chicago Misc. Rep.*, **16**, 36.

Means, L. L., 1952: On thunderstorm forecasting in the central United States. *Mon. Wea. Rev.*, **80 (10)**, 165–189.

Miles, J. W. and L. N. Howard, 1964: Note on a heterogeneous shear flow. *Journal of Fluid Mechanics*, **20 (02)**, 331–336.

Mlawer, E. J., S. J. Taubman, P. D. Brown, M. J. Iacono, and S. A. Clough, 1997: Radiative transfer for inhomogeneous atmospheres: RRTM, a validated correlated-k model for the longwave. *Journal of Geophysical Research: Atmospheres*, **102 (D14)**, 16 663–16 682.

Moore, J. T., F. H. Glass, C. E. Graves, S. M. Rochette, and M. J. Singer, 2003: The environment of warm-season elevated thunderstorms associated with heavy rainfall over the central United States. *Wea. Forecasting*, **18 (5)**, 861–878.

Morrison, H., G. Thompson, and V. Tatarskii, 2009: Impact of cloud microphysics on the development of trailing stratiform precipitation in a simulated squall line: Comparison of one-and two-moment schemes. *Mon. Wea. Rev.*, **137 (3)**, 991–1007.

Nakanishi, M. and H. Niino, 2006: An improved Mellor–Yamada level-3 model: Its numerical stability and application to a regional prediction of advection fog. *Boundary-layer Meteor.*, **119 (2)**, 397–407.

Nallapareddy, A., A. Shapiro, and J. J. Gourley, 2011: A climatology of nocturnal warming events associated with cold-frontal passages in Oklahoma. *J. Appl. Meteor. Climatol.*, **50 (10)**, 2042–2061.

Nowotarski, C. J., P. M. Markowski, and Y. Richardson, 2011: The characteristics of numerically simulated supercell storms situated over statically stable boundary layers. *Mon. Wea. Rev.*, **139 (1)**, 3139–3162.

Parker, M. D., 2008: Response of simulated squall lines to low-level cooling. *J. Atmos. Sci.*, **65 (4)**, 1323–1341.

Parker, M. D., 2010: Relationship between system slope and updraft intensity in squall lines. *Mon. Wea. Rev.*, **138 (9)**, 3572–3578.

Parsons, D. B., 1992: An explanation for intense frontal updrafts and narrow cold-frontal rainbands. *J. Atmos. Sci.*, **49 (19)**, 1810–1825.

Peters, J. M. and R. S. Schumacher, 2015: Mechanisms for organization and echo training in a flash-flood-producing mesoscale convective system. *Mon. Wea. Rev.*, **143 (4)**, 1058–1085.

Pielke, R. A., 2013: *Mesoscale meteorological modeling*, Vol. 98. Academic press.

Pinto, J. O., J. A. Grim, and M. Steiner, 2015: Assessment of the high-resolution rapid refresh model's ability to predict mesoscale convective systems using object-based evaluation. *Wea. Forecasting*, **30 (4)**, 892–913.

Pitchford, K. L. and J. London, 1962: The low-level jet as related to nocturnal thunderstorms over midwest United States. *J. Appl. Meteor.*, **1 (1)**, 43–47.

Pryzbylinski, R., G. Schmocker, and Y. Lin, 2000: A study of storm and vortex morphology during the 'intensifying stage' of severe wind mesoscale convective systems. *Preprints, 20th Conf. on Severe Local Storms, Amer. Meteor. Soc., Orlando, FL*, 173–176.

Przybylinski, R. W., 1995: The bow echo: Observations, numerical simulations, and severe weather detection methods. *Wea. Forecasting*, **10 (2)**, 203–218.

Reif, D., 2015: Investigation of nocturnal convection initiation over the central Great Plains during the warm season. M.S. thesis, University of Oklahoma.

Riley, G. T., M. G. Landin, and L. F. Bosart, 1987: The diurnal variability of precipitation across the central Rockies and adjacent Great Plains. *Mon. Wea. Rev.*, **115 (6)**, 1161–1172.

Rodwell, M. J. and Coauthors, 2013: Characteristics of occasional poor medium-range weather forecasts for Europe. *Bull. Amer. Meteor. Soc.*, **94 (9)**, 1393–1405.

Rottman, J. W. and J. E. Simpson, 1989: The formation of internal bores in the atmosphere: A laboratory model. *Quart. J. Roy. Meteor. Soc.*, **115 (488)**, 941–963.

Rotunno, R. and J. Klemp, 1985: On the rotation and propagation of simulated supercell thunderstorms. *J. Atmos. Sci.*, **42 (3)**, 271–292.

Rotunno, R., J. B. Klemp, and M. L. Weisman, 1988: A theory for strong, long-lived squall lines. *J. Atmos. Sci.*, **45 (3)**, 463–485.

Schenkman, A. D., M. Xue, and A. Shapiro, 2012: Tornadogenesis in a simulated mesovortex within a mesoscale convective system. *J. Atmos. Sci.*, **69 (11)**, 3372–3390.

Schmidt, J. M. and W. R. Cotton, 1990: Interactions between upper and lower tropospheric gravity waves on squall line structure and maintenance. *J. Atmos. Sci.*, **47 (10)**, 1205–1222.

Schmocker, G., R. Przybylinski, and E. Rasmussen, 2000: The severe bow echo event of 14 June 1998 over the mid-Mississippi valley region: A case of vortex development near the intersection of a preexisting boundary and a convective line. *Preprints, 20th Conf. on Severe Local Storms, Orlando, FL, Amer. Meteor. Soc*, 169–172.

Schumacher, R. S., 2015: Sensitivity of precipitation accumulation in elevated convective systems to small changes in low-level moisture. *J. Atmos. Sci.*, **72 (6)**, 2507–2524.

Schumacher, R. S. and R. H. Johnson, 2005: Organization and environmental properties of extreme-rain-producing mesoscale convective systems. *Mon. Wea. Rev.*, **133 (4)**, 961–976.

Scorer, R., 1949: Theory of waves in the lee of mountains. *Quart. J. Roy. Meteor. Soc.*, **75 (323)**, 41–56.

Shapiro, A. and E. Fedorovich, 2009: Nocturnal low-level jet over a shallow slope. *Acta Geophysica*, **57 (4)**, 950–980.

Shapiro, A. and E. Fedorovich, 2010: Analytical description of a nocturnal low-level jet. *Quart. J. Roy. Meteor. Soc.*, **136 (650)**, 1255–1262.

Shapiro, A., E. Fedorovich, and S. Rahimi, 2016: A unified theory for the Great Plains nocturnal low-level jet. *J. Atmos. Sci.*, **73 (8)**, 3037–3057.

Shin, H. H. and S.-Y. Hong, 2011: Intercomparison of planetary boundary-layer parametrizations in the wrf model for a single day from cases-99. *Boundary-layer Meteor.*, **139 (2)**, 261–281.

Skamarock, W., et al., 2008: A description of the Advanced Research WRF Version 3, NCAR technical note, Mesoscale and Microscale Meteorology Division. *National Center for Atmospheric Research, Boulder, Colorado, USA*.

Skamarock, W. C., M. L. Weisman, and J. B. Klemp, 1994: Three-dimensional evolution of simulated long-lived squall lines. *J. Atmos. Sci.*, **51 (17)**, 2563–2584.

Smith, A. M., G. M. McFarquhar, R. M. Rauber, J. A. Grim, M. S. Timlin, B. F. Jewett, and D. P. Jorgensen, 2009: Microphysical and thermodynamic structure and evolution of the trailing stratiform regions of mesoscale convective systems during BAMEX. Part I: Observations. *Mon. Wea. Rev.*, **137 (4)**, 1165–1185.

Smull, B. F. and R. A. Houze, 1985: A midlatitude squall line with a trailing region of stratiform rain: Radar and satellite observations. *Mon. Wea. Rev.*, **113 (1)**, 117–133.

Stensrud, D. J., M. C. Coniglio, R. P. Davies-Jones, and J. S. Evans, 2005: Comments on "A Theory for Strong Long-Lived Squall Lines' Revisited". *J. Atmos. Sci.*, **62 (8)**, 2989–2996.

Stokes, G. M. and S. E. Schwartz, 1994: The Atmospheric Radiation Measurement (ARM) Program: Programmatic background and design of the cloud and radiation test bed. *Bull. Amer. Meteor. Soc.*, **75 (7)**, 1201–1221.

Stull, R., 1988: An introduction to boundary layer meteorology.

Surcel, M., M. Berenguer, and I. Zawadzki, 2010: The diurnal cycle of precipitation from continental radar mosaics and numerical weather prediction models. Part I: Methodology and seasonal comparison. *Mon. Wea. Rev.*, **138 (8)**, 3084–3106.

Surcel, M., I. Zawadzki, and M. Yau, 2015: A study on the scale dependence of the predictability of precipitation patterns. *J. Atmos. Sci.*, **72 (1)**, 216–235.

Thompson, R. L., C. M. Mead, and R. Edwards, 2007: Effective storm-relative helicity and bulk shear in supercell thunderstorm environments. *Wea. Forecasting*, **22 (1)**, 102–115.

Thompson, R. L., B. T. Smith, J. S. Grams, A. R. Dean, and C. Broyles, 2012: Convective modes for significant severe thunderstorms in the contiguous United States. Part II: Supercell and QLCS tornado environments. *Wea. Forecasting*, **27 (5)**, 1136–1154.

Toms, B. A., J. M. Tomaszewski, D. D. Turner, and S. E. Koch, 2017: Analysis of a Gravity Wave Train Using Direct and Remote Sensing Measurement Systems. *Mon. Wea. Rev.,* in review.

Trapp, R. J., 2013: *Mesoscale-convective Processes in the Atmosphere*. Cambridge University Press.

Trapp, R. J., G. J. Stumpf, and K. L. Manross, 2005: A reassessment of the percentage of tornadic mesocyclones. *Wea. Forecasting*, **20 (4)**, 680–687.

Trapp, R. J. and M. L. Weisman, 2003: Low-level mesovortices within squall lines and bow echoes. Part II: Their genesis and implications. *Mon. Wea. Rev.*, **131 (11)**, 2804–2823.

Trier, S. B., J. H. Marsham, C. A. Davis, and D. A. Ahijevych, 2011: Numerical simulations of the postsunrise reorganization of a nocturnal mesoscale convective system during 13 June IHOP_2002. *J. Atmos. Sci.*, **68 (12)**, 2988–3011.

Trier, S. B. and D. B. Parsons, 1993: Evolution of environmental conditions preceding the development of a nocturnal mesoscale convective complex. *Mon. Wea. Rev.*, **121 (4)**, 1078–1098.

Trier, S. B., W. C. Skamarock, and M. A. LeMone, 1997: Structure and evolution of the 22 February 1993 TOGA COARE squall line: Organization mechanisms inferred from numerical simulation. *J. Atmos. Sci.*, **54 (3)**, 386–407.

Tripoli, G. J. and W. R. Cotton, 1989: Numerical study of an observed orogenic mesoscale convective system. Part 1: Simulated genesis and comparison with observations. *Mon. Wea. Rev.*, **117 (2)**, 273–304.

Turner, D., J. Goldsmith, and R. Ferrare, 2016: Development and applications of the ARM Raman lidar. *Meteorological Monographs*, **57**, 18–1.

Tuttle, J. D. and C. A. Davis, 2006: Corridors of warm season precipitation in the central United States. *Mon. Wea. Rev.*, **134 (9)**, 2297–2317.

Uccellini, L. W., 1980: The role of upper tropospheric jet streaks and lee-side cyclogenesis in the development of low level jets in the great plains.

Uccellini, L. W. and D. R. Johnson, 1979: The coupling of upper and lower tropospheric jet streaks and implications for the development of severe convective storms. *Mon. Wea. Rev.*, **107 (6)**, 682–703.

VandenBerg, M. A., M. C. Coniglio, and A. J. Clark, 2014: Comparison of next-day convection-allowing forecasts of storm motion on 1-and 4-km grids. *Wea. Forecasting*, **29 (4)**, 878–893.

Wakimoto, R. M., H. V. Murphey, C. A. Davis, and N. T. Atkins, 2006: High winds generated by bow echoes. Part II: The relationship between the mesovortices and damaging straight-line winds. *Mon. Wea. Rev.*, **134 (10)**, 2813–2829.

Wallace, M., J, 1975: Diurnal variations in precipitation and thunderstorm frequency over the conterminous United States. *Mon. Wea. Rev.*, **103 (5)**, 406–419.

Weisman, M. L., 1992: The role of convectively generated rear-inflow jets in the evolution of long-lived mesoconvective systems. *J. Atmos. Sci.*, **49 (19)**, 1826–1847.

Weisman, M. L., 1993: The genesis of severe, long-lived bow echoes. *J. Atmos. Sci.*, **50 (4)**, 645–670.

Weisman, M. L. and C. A. Davis, 1998: Mechanisms for the generation of mesoscale vortices within quasi-linear convective systems. *J. Atmos. Sci.*, **55 (16)**, 2603–2622.

Weisman, M. L. and J. B. Klemp, 1982: The dependence of numerically simulated convective storms on vertical wind shear and buoyancy. *Mon. Wea. Rev.*, **110 (6)**, 504–520.

Weisman, M. L. and J. B. Klemp, 1984: The structure and classification of numerically simulated convective storms in directionally varying wind shears. *Mon. Wea. Rev.*, **112 (12)**, 2479–2498.

Weisman, M. L., J. B. Klemp, and R. Rotunno, 1988: Structure and evolution of numerically simulated squall lines. *J. Atmos. Sci.*, **45 (14)**, 1990–2013.

Weisman, M. L. and R. Rotunno, 2004: "A theory for strong long-lived squall lines" revisited. *J. Atmos. Sci.*, **61 (4)**, 361–382.

Weisman, M. L., W. C. Skamarock, and J. B. Klemp, 1997: The resolution dependence of explicitly modeled convective systems. *Mon. Wea. Rev.*, **125 (4)**, 527–548.

Weisman, M. L. and R. J. Trapp, 2003: Low-level mesovortices within squall lines and bow echoes. Part I: Overview and dependence on environmental shear. *Mon. Wea. Rev.*, **131 (11)**, 2779–2803.

Wheatley, D. M. and R. J. Trapp, 2008: The effect of mesoscale heterogeneity on the genesis and structure of mesovortices within quasi-linear convective systems. *Mon. Wea. Rev.*, **136 (11)**, 4220–4241.

Wheatley, D. M., R. J. Trapp, and N. T. Atkins, 2006: Radar and damage analysis of severe bow echoes observed during BAMEX. *Mon. Wea. Rev.*, **134 (3)**, 791–806.

White, B. L. and K. R. Helfrich, 2012: A general description of a gravity current front propagating in a two-layer stratified fluid. *Journal of Fluid Mechanics*, **711**, 545–575.

Wilson, J. W. and R. D. Roberts, 2006: Summary of convective storm initiation and evolution during IHOP: Observational and modeling perspective. *Mon. Wea. Rev.*, **134 (1)**, 23–47.

Wolyn, P. G. and T. B. McKee, 1994: The mountain-plains circulation east of a 2-km-high north-south barrier. *Mon. Wea. Rev.*, **122 (7)**, 1490–1508.

Wyngaard, J. C., 2004: Toward numerical modeling in the "Terra Incognita". *J. Atmos. Sci.*, **61 (14)**, 1816–1826.

Zhou, B., J. S. Simon, and F. K. Chow, 2014: The convective boundary layer in the terra incognita. *J. Atmos. Sci.*, **71 (7)**, 2545–2563.

Zipser, E., 1977: Mesoscale and convective-scale downdrafts as distinct components of squall-line structure. *Mon. Wea. Rev.*, **105 (12)**, 1568–1589.

Appendix A

Details on Density Current Depth Estimations

Several methods of estimating the depth of the density current for the Froude number calculations were attempted, but a large range of outcomes led to a subjective estimation of this depth. The attempted methods included the hydraulic, theta, hybrid, inversion, and wind shift computations within the density current and across the outflow boundary. These estimates were utilized during operations in the Plains Elevated Convection at Night (PECAN) field campaign and their details are further described in Blake (2015). A range of depths for each of the methods are listed in Table A.1 for the 0800 UTC surge cross section.

Density Current Depth Estimation Method	Depth
Hydraulic	1679 m
Theta	1318 m
Hybrid	1289 m
Inversion	666 m
Wind Shift	2773 m
Subjective	1000 m

Table A.1: Estimated density current depths for the 0800 UTC surge cross section using the hydraulic, theta, hybrid, inversion, and wind shift methods. The subjective estimation of the depth is additionally listed.

Owing to the range of estimated depths for the density current using the computed methods, the density current depths were manually estimated by examining cross sections of potential temperature, equivalent potential temperature, and ground-relative winds. An example of the cross section utilized for 0800 UTC within the surging portion of the system is depicted in Fig. 90. The depth was

estimated by tracing the vertical displacement over the cold pool of the first virtual potential temperature contour along the outflow boundary. An example of such a displacement is depicted by the thick gray line in Fig. 90. However, the depth over which these contours are displaced varied based on the location within the cold pool, so the location chosen for this estimation was also subjectively chosen through the deepest portion of the density current. Therefore, these estimations were highly subjective and prone to errors. However, we believe that this technique provided more reliable results than the computed methods presented in Blake

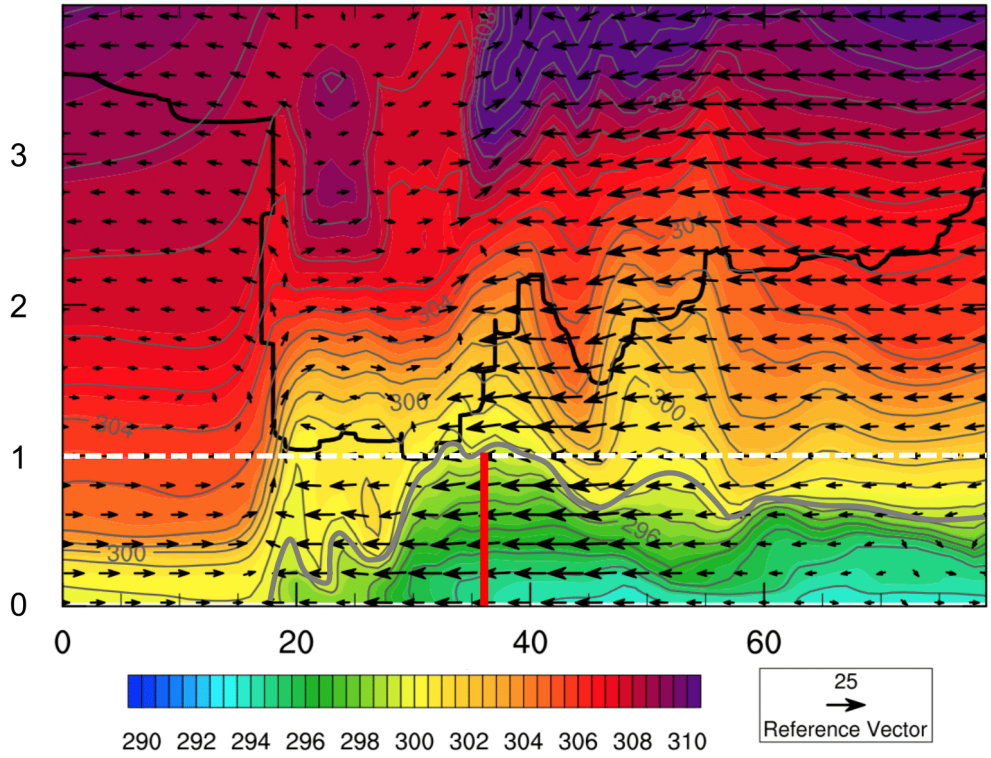

Figure 90: Vertical cross sections of virtual potential temperature (shaded; K), potential temperature (contours; K), ground-relative wind vectors (m s^{-1}; reference vector 25 m s^{-1}), and cloud boundary (thick black line) for 0800 UTC surge. The white dashed line represents 1 km AGL. The thick gray line represents the approximate location of the first environmental θ_v contour of the density current. The solid red line represents the location at which the density current estimates were taken.

(2015) for this simulation. These estimated cold pool depths were also applied to the computations of C in the application of RKW theory.

Appendix B

Model Sensitivity

Several challenges were faced when attempting to obtain a long-lived MCS in the WRF simulations. In addition to the sensitivity to various parameterization schemes, the simulation was highly sensitive to the initial conditions, boundary conditions, and horizontal grid spacing. These results were troubling for those trying to obtain realistic results using deterministic simulations, and the range of solutions suggest that ensemble simulations accounting for these errors may be useful in representing the nocturnal environment (e.g., Lawson and Gallus Jr, 2016) . Some of the challenges faced will be elaborated upon in the following sections.

B.1 Representativeness of Initial Conditions

While the 2100 UTC RAP analysis ICs were subjectively determined to provide the most realistic-looking, long-lived MCS (as previously discussed in section 3.1.2), they were not necessarily well-representative of the atmospheric state at the time of initialization. As previously discussed, WRF outputs an early cluster of surface-based convection that moved through the central portion of the domain and modified the environment. This convection was not observed, but despite this major difference, the model simulated an observed convective system which had an evolution similar to the observed MCS. In order to determine the representativeness of the RAP ICs and if these ICs were responsible for the first erroneous convective

system, the model output at the initial time step (i.e., 2100 UTC) was compared with the Oklahoma Mesonet observations. Since the lowest model level is located several meters above the ground, WRF parameterizes values for 2-m temperature, 2-m dewpoint temperature, and 10-m winds such that these values can be directly compared with conventional surface observations. Additionally, as upper-air observations were not available for 2100 UTC, observed 0000 UTC soundings from Lamont and Norman, Oklahoma, were compared with 0000 UTC WRF vertical profiles from the corresponding grid points.

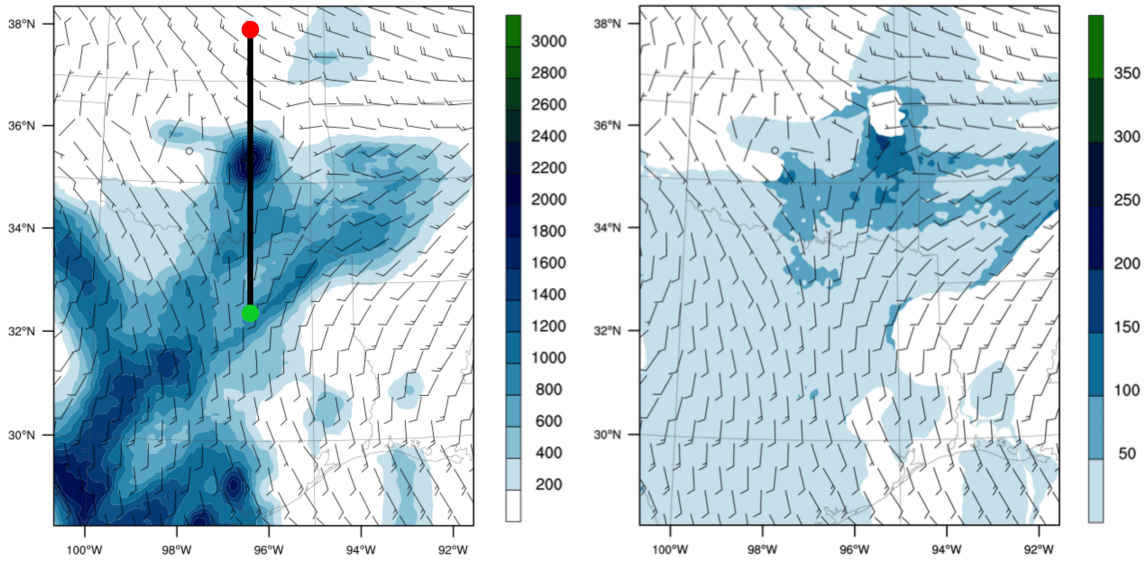

Figure 91: WRF initialization (2100 UTC) surface-based CAPE (shaded; J kg^{-1}; left) and surface-based CIN (shaded; J kg^{-1}; right). Winds (knots; 1 knot = 0.51 m s^{-1}). CIN was only computed in the presence of CAPE. Note the difference in scales between the CAPE and CIN plots. The black line (left) represents the path of the cross section displayed in Fig. 92, where the start point (0 km) corresponds to the green circle.

To investigate why the simulations resulted in an erroneous first wave of convection, 2-m temperature, 2-m dewpoint temperature, CAPE, and CIN were examined at 2100 UTC. Because the 2100 UTC RAP ICs were used for all three grid configurations, the displayed values were the same for each configuration as the fields at the initial time were just the RAP data interpolated to the WRF domain.

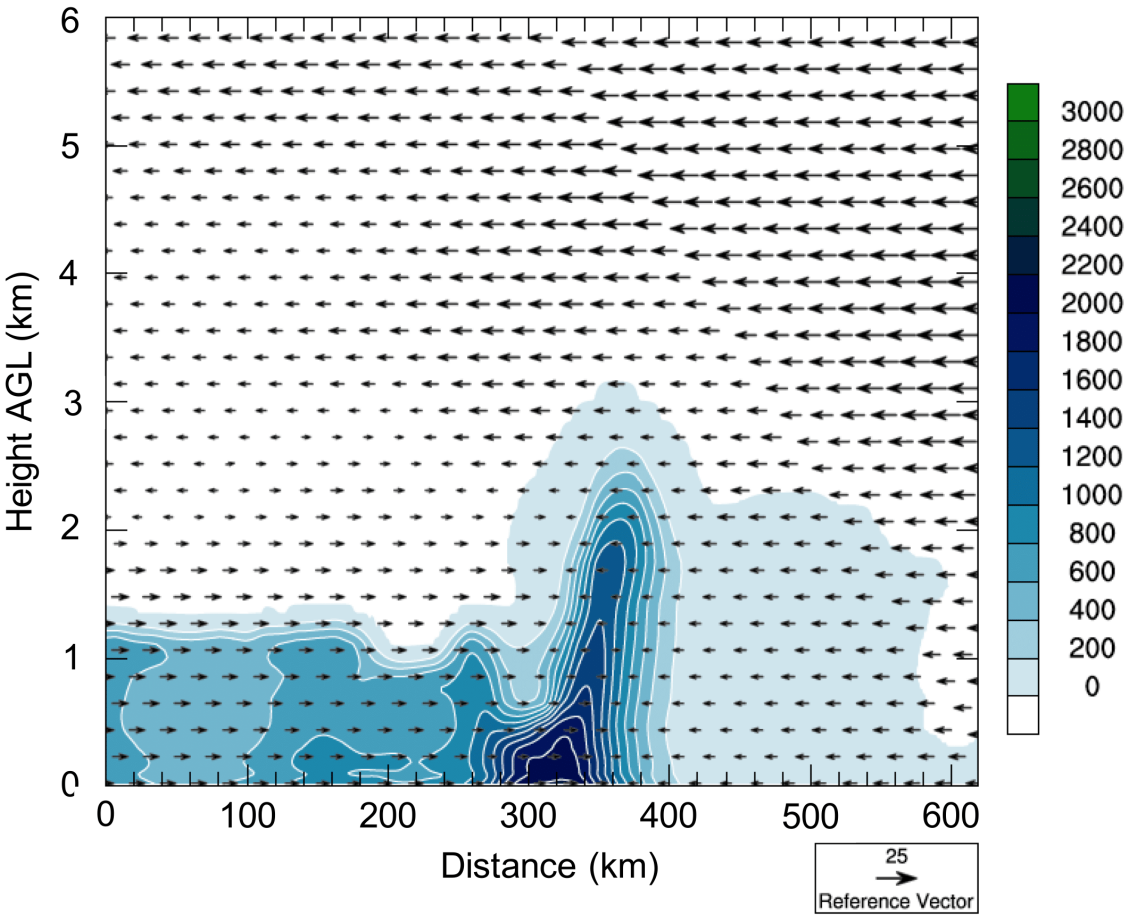

Figure 92: Vertical cross section of CAPE (shaded; J kg^{-1}) and winds (vectors; reference vector 25 m s^{-1}) through the high-CAPE region at 2100 UTC. The cross section path is depicted in Fig. 91.

Therefore, the issues with the ICs was suspected to be responsible for the first wave of convection in all three grid configurations and will be discussed further in section B.2.

The Expanded_Small domain configuration was used for all analyses shown in this section. At 2100 UTC, a local maximum in surface-based CAPE[1] was coincident with low values (<50 J kg^{-1}) of surface-based CIN over central Oklahoma (Fig. 91). This maximum was coincident with a local maximum in 2-m dewpoint

[1]Surface-based CAPE and CIN were computed from the lowest model level; virtual temperature is not accounted for in the computation.

temperature, which was likely responsible for these large CAPE values. Moreover, this high CAPE also had vertical continuity, indicating that it was not simply an error in lowest model level values (Fig. 92).

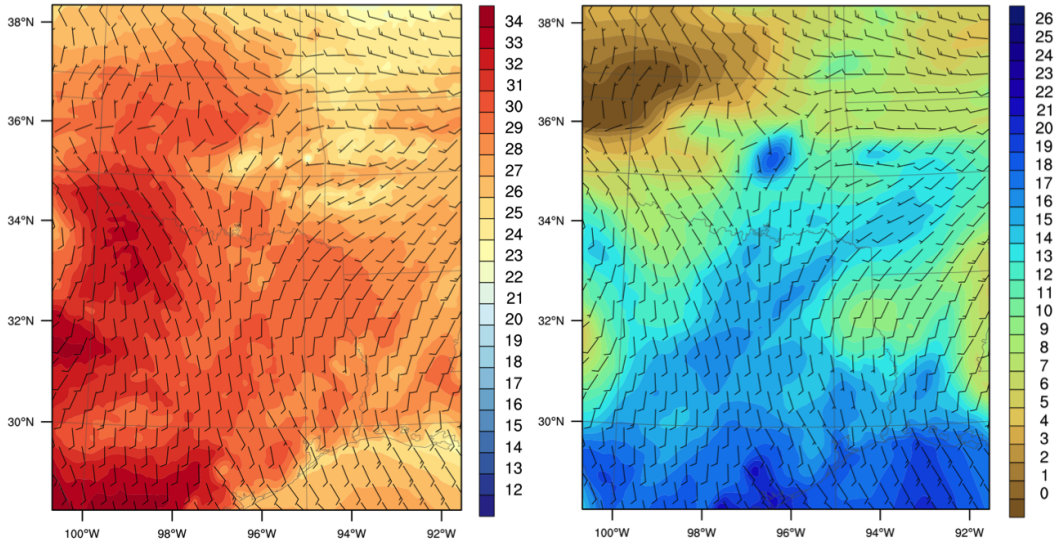

Figure 93: WRF initialization 2100 UTC 2-m temperature (°C; left) and 2-m dewpoint temperature (°C; right). Note the difference in scales between the two panels. Winds (knots) are the same as in Fig. 91.

In order to determine how well the RAP initial surface conditions represented the observed surface conditions, WRF 2-m temperature and 2-m dewpoint temperature were output at the grid point corresponding to each Oklahoma Mesonet site (Fig. 94). These values were then compared with the observed 1.5-m temperature and 1.5-m dewpoint temperature measured by the Mesonet (Fig. 95). At 2100 UTC, the WRF initial conditions had a warm bias throughout most of Oklahoma. The mean temperature error was calculated by subtracting the Mesonet observation from the WRF temperature value at each grid point and averaging the difference. For all Mesonet sites in the state of Oklahoma, the mean 2-m initial condition temperature error was 0.8867 K/°C with a standard deviation of 0.8098 K/°C. Similar results were found for 2-m dewpoint temperature (Fig. 96a), with a mean 2-m initial condition dewpoint temperature error of 0.6633 K/°C and a

standard deviation of 2.2593 K/°C. The variability in the initial condition 2-m dewpoint temperature was much greater than that of the 2-m temperature, and some sites were characterized by an absolute error exceeding 5 °C (Fig. 96a).

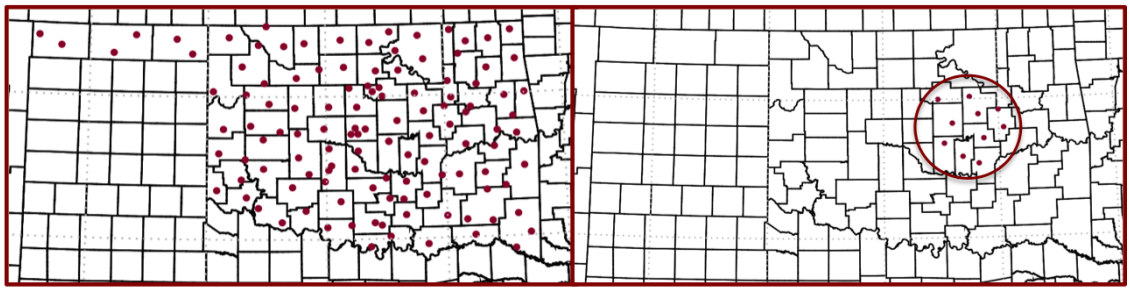

Figure 94: Oklahoma Mesonet sites used in the comparison with the WRF model fields for (left) all sites in Oklahoma and (right) the sites in the vicinity of the high CAPE region. The dark red circle encompasses the sites used for the high CAPE comparison.

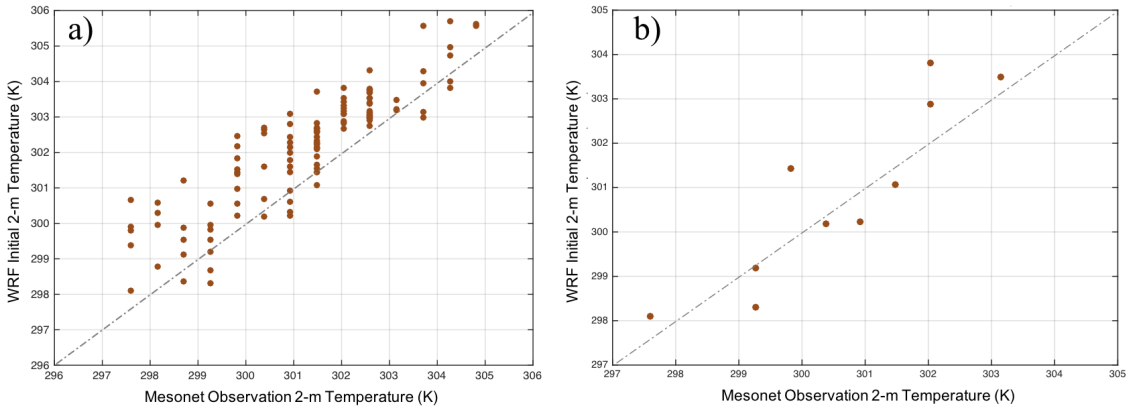

Figure 95: 2100 UTC WRF initial 2-m temperatures (K; y-axis) and Mesonet observed 1.5-m temperatures (K; x-axis) for (a) all Oklahoma Mesonet locations and (b) the Oklahoma Mesonet locations within the region of high CAPE. The dashed gray line indicates where the WRF temperature equals the Mesonet observation. Note that the scales of the x and y axes differ between both panels.

The same comparison was done for 10 Oklahoma Mesonet sites corresponding to the region of high CAPE (Fig. 94b). For the region of high CAPE values, the mean 2-m initial condition temperature error was 0.2762 K/°C with a standard deviation of 0.9262 K/°C (Fig. 95b). The mean absolute temperature error in

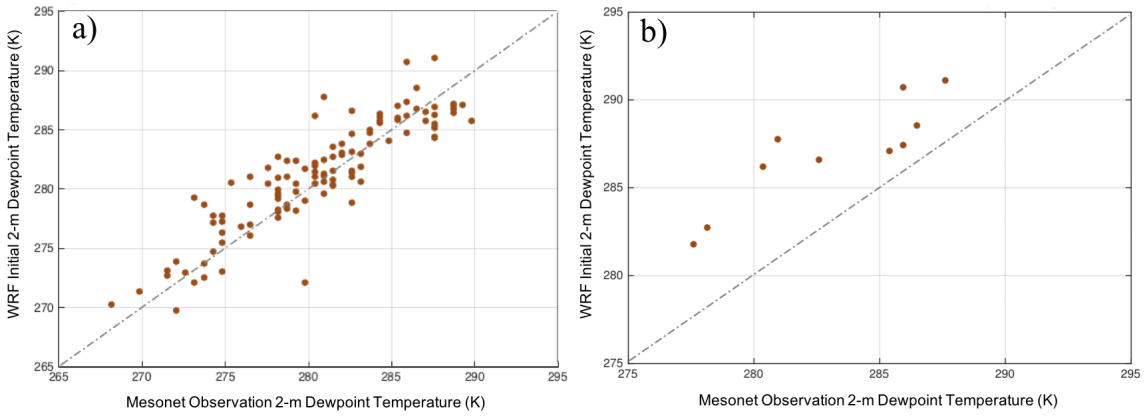

Figure 96: 2100 UTC WRF initial 2-m dewpoint temperatures (K; y-axis) and Mesonet observed 1.5-m dewpoint temperatures (K; x-axis) for (a) all Oklahoma Mesonet locations and (b) the Oklahoma Mesonet locations within the region of high CAPE (maroon dot). The dashed gray line indicates where the WRF dewpoint temperature equals the Mesonet observation. Note that the scales of the x and y axes differ between both panels.

this region was actually smaller than that for all of the Oklahoma Mesonet sites. While the sample size in the high CAPE region was much smaller than the state as a whole, the standard deviation is not much larger. Therefore, it would be inferred that the temperature values in this region were more representative of the observations than in other areas and that temperature errors were likely not primarily responsible for the erroneous high CAPE region. However, the results were much different for the 2-m dewpoint temperature errors in the high CAPE region. All sites within the region of high CAPE had a moist bias (Fig. 96b), and some sites had a 2-m dewpoint temperature error of approximately 5 K/°C. The mean dewpoint temperature error for these sites in the high CAPE region was 3.9059 K/°C with a standard deviation of 1.7651 K/°C.

Therefore, the large moist bias collocated with the region of high CAPE would imply that the CAPE in this region was indeed erroneously large and the result of substantial moisture errors in the RAP. In order to estimate the magnitude of the error, a 2100 UTC model output sounding in the high CAPE region was

modified using the SHARPPy program (Halbert et al., 2015) with the average surface temperature and dewpoint errors from the region of high CAPE. This particular sounding without modification was characterized by a surface-based CAPE value of 2753 J kg^{-1}. After modifying the surface temperature and dewpoint temperature by the mean errors, the surface-based CAPE value was 885 J kg^{-1}, which was nearly 2000 J kg^{-1} less than what was seen in the initial conditions. The results of this were unsurprising as small-scale variations in moisture have a much greater impact on CAPE values than do variations in temperature (e.g., Crook, 1996; Fabry, 2006). Further, CIN increased dramatically, but the actual magnitude was unclear without properly modifying the boundary layer and upper levels of the sounding. However, this increase in CIN was likely more than enough to prevent the spontaneous initiation of convection. Therefore, while the initial condition temperature values in this region matched up fairly well with the observations, the large moisture biases resulted in this erroneous area of high CAPE and low CIN. As a result, an initial surface-based convective system was initiated, which modified the environment, impacting the later convective system (elaborated on further in section 3.2).

Additionally, 0000 UTC Lamont and Norman, Oklahoma, soundings were compared with the vertical WRF profiles at the grid points corresponding to the sounding sites (Fig. 97). The errors in temperature for both sites were mostly confined to within the PBL, with a warm bias in the model. However, the model surface temperatures matched up well with the observed temperatures despite the temperature errors in the PBL. One possible explanation for this discrepancy is that the observed soundings are generally released approximately 1 h before the time for which they are valid (i.e., a 0000 UTC sounding will usually be launched near 2300 UTC; `http://www.nws.noaa.gov/directives/sym/pd01014001curr.pdf`).

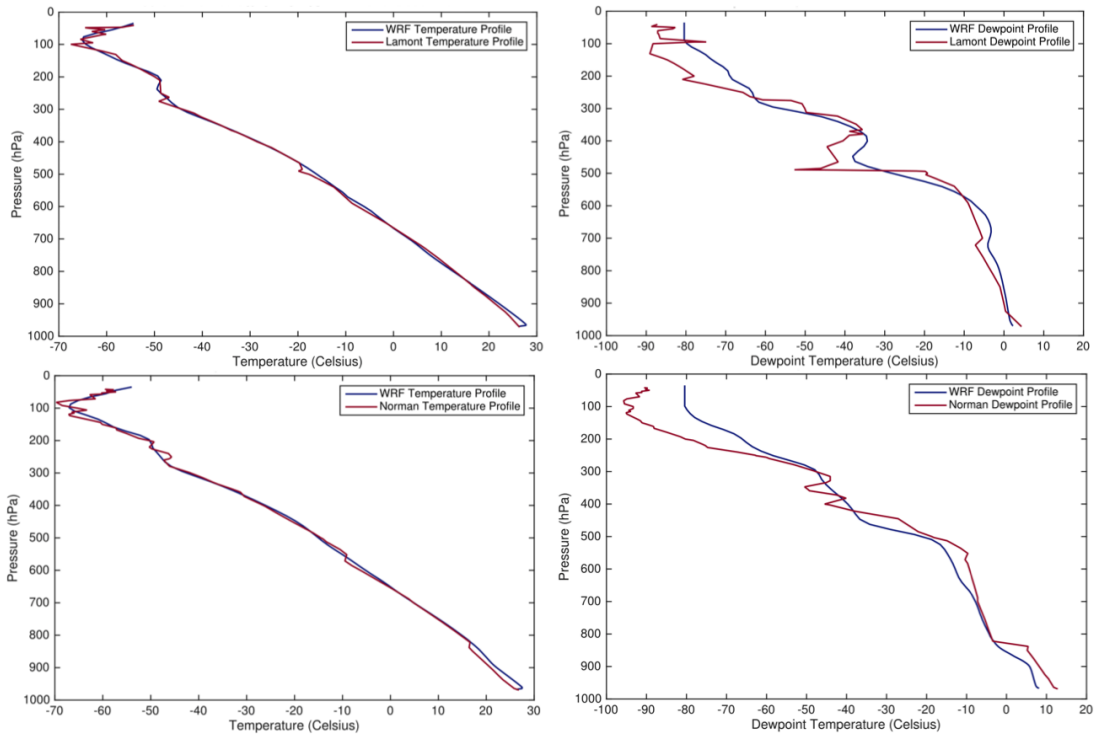

Figure 97: 0000 UTC observed sounding and WRF temperature (°C; left) and dewpoint temperature profiles (°C; right) for Lamont, Oklahoma (top), and Norman, Oklahoma (bottom). The blue line is the WRF profile, and the red line is the observed sounding profile.

Because 0000 UTC was near sunset and the time when the PBL began to stabilize, the 0000 UTC WRF simulations likely captured this boundary layer decoupling while the observed PBL had not begun to cool by 2300 UTC.

The dewpoint temperature profiles for both sounding sites varied much more greatly throughout the atmosphere than do the temperature profiles (Fig. 97). A slight dry bias existed near the surface in the Lamont WRF profile, but a moist bias existed above ~925 hPa. Overall, the dewpoint profile throughout the lowest levels matched better with the observations than in the Norman WRF profile.

Errors also existed throughout both Lamont and Norman 0000 UTC wind profiles, especially in the meridional wind component (Fig. 98). The Lamont WRF profile was characterized by a northerly flow component throughout the depth of

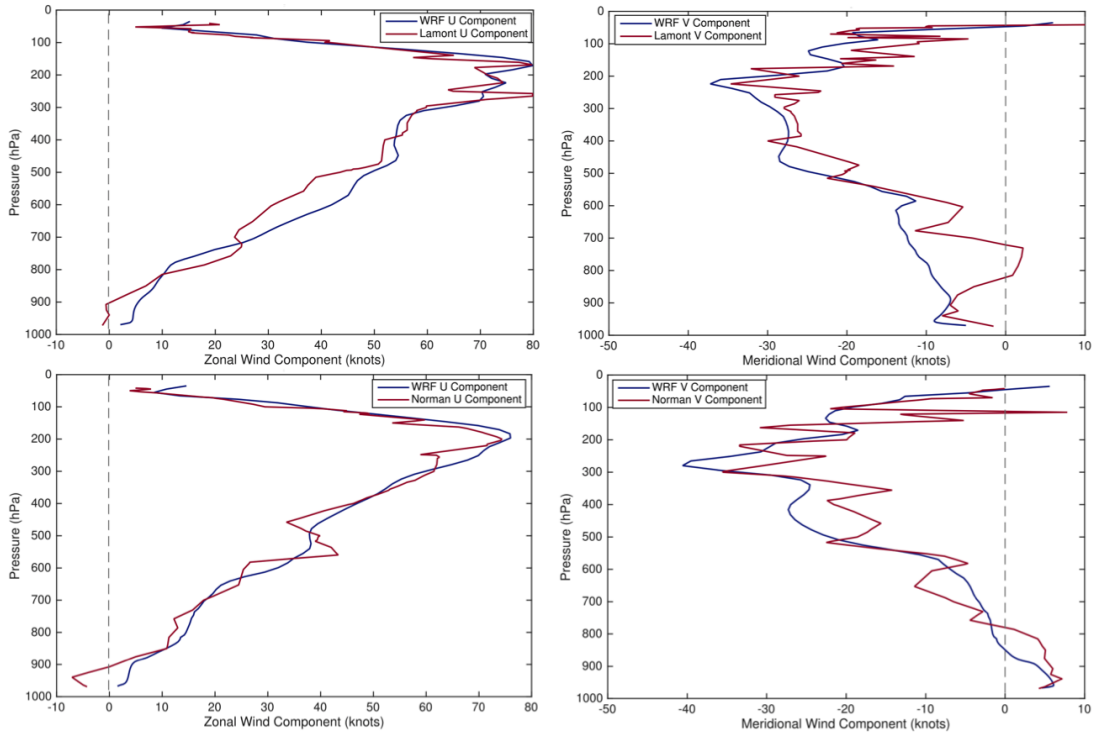

Figure 98: 0000 UTC observed sounding and zonal wind (knots; left) and meridional wind (knots; right) for Lamont, Oklahoma (top), and Norman, Oklahoma (bottom). The blue line is the WRF profile, and the red line is the observed sounding profile. Positive values of zonal and meridional winds are westerly and southerly, respectively.

the troposphere, but the observed sounding had a ~100-hPa deep layer near 700 hPa of west-southwesterly flow. Additionally, wind speed errors were in excess of 10 knots at some levels, and WRF wind profiles were much smoother throughout the depth of the troposphere than the observed wind profiles. Overall, the WRF model did a poor job with representing the meridional wind profile, which may have been attributed to errors in the RAP initial conditions 3 h prior.

Benjamin and Coauthors (2016) evaluated the performance of the different versions of the RAP model and found that the warm season is frequently characterized by a warm, dry bias, and the cold season is frequently characterized by biases in wind and temperature. They attributed the relative humidity (i.e., temperature and moisture) errors during the warm season (April-September) to the frequent

presence of convection, and the cold-season errors in temperature and winds to the increased frequency fronts and synoptic systems. The case presented herein occurred at the beginning of the cold season in the presence of synoptic forcing, which may explain the errors in both RH and winds throughout the RAP and thus WRF profiles.

In summary, WRF struggled with accurately representing the vertical moisture and wind profiles, but performed better with representing the temperature profiles outside of the PBL. The errors in the dewpoint temperature profiles in the low- to mid-troposphere were on the order of 0-5 °C, while wind speed errors were much more significant throughout the entire profile. These errors were likely attributed to the poor representation of the atmosphere throughout central Oklahoma in the RAP initial conditions. Additionally, the large discrepancies in the parameterized surface observations from the Oklahoma Mesonet suggests that there are still shortcomings and challenges faced when using hourly mesoscale data assimilation cycles, such as the one in RAP (Benjamin and Coauthors, 2016).

B.2 Sensitivity to Boundary Conditions

The WRF simulations were also run with the same initialization and physics parameterizations, but on different grid configurations and thus different BCs (Fig. 36). The details of each of the grid dimensions are listed in Table 3.1. As described in section 3.1.1, the various physics parameterization schemes were run using the Small_1km grid configuration. However, this configuration had a smaller lateral extent and as a result, portions of the convection moved out of the domain during the later hours of the simulation (Fig. 99e-g). Therefore, expanding the domain was necessary in order to encompass the entirety of the convective system.

By doing so, problems with obtaining a long-lived MCS in the simulations were encountered. The selected physics paramterizations produced a long-lived MCS that persisted until the end of the model run in the Small_1km grid, but when expanded to the Expanded_Large configuration, the simulations produced convection that dissipated earlier and did not reach the Gulf of Mexico. Additionally, the utilization of the Expanded_Small grid configuration produced a long-lived MCS, but the outcome was different than the simulations from both other aforementioned grid configurations (Fig. 99).

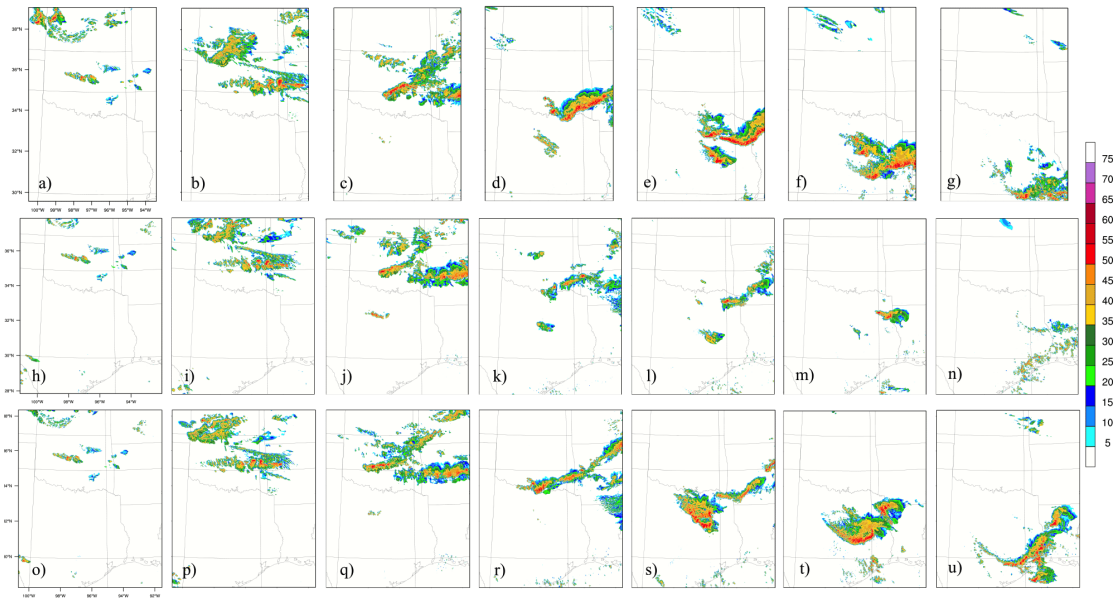

Figure 99: Simulated 10-cm wavelength radar reflectivity factor (dBZ) for the lowest model level of the 1-km inner domains of the Small_1km (top), Expanded_Large (middle), and Expanded_Small (bottom) grid configurations for the hours of (a),(h),(o) 0000 UTC, (b),(i),(p) 0300 UTC, (c),(j),(q) 0600 UTC, (d),(k),(r) 0900 UTC, (e),(l),(s) 1200 UTC, (f),(m),(t) 1500 UTC, and (g),(n),(u) 1800 UTC on 6 October 2014.

One noteworthy similarity between all three grid configurations was that similar convective structures were produced through 0300 UTC. This consistency was

likely attributed to the utilization of the RAP initial conditions which were characterized by a region of high CAPE through central Oklahoma (discussed in Appendix B.1). This resulted in the initiation of erroneous surface-based convection in all three configurations, which moved through Oklahoma before dissipating. The solutions of the three different grid configurations diverge after this time when the main convective system became important. Therefore, the convection resulting in the long-lived MCS was handled differently by all three grid configurations.

By 0600 UTC, all three configurations produced a strong cluster of convective cells in central Oklahoma (Fig. 99c,j,q). However, the orientation of this cluster varied between each configuration, and the strength of the convection was strongest in the Small_1km configuration, where the area of reflectivity values exceeding 50 dBZ was the greatest (Fig. 99c). The inner 1-km grid in this configuration extended farther north than that of the other two configurations, perhaps leading to a better-resolved weak cold front, which initiated this convection. Additionally, the secondary cluster of convection in north central Texas was beginning to initiate by 0600 UTC. However, the strength of this convection appears to be the greatest in the Expanded_Large configuration (Fig. 99j), but its evolution also differs between all three configurations.

By 0900 UTC, the convective system had significantly weakened in the Expanded_Large configuration (Fig. 99k), but the southernmost portions were restrengthening in the other two configurations (Figs. 99d,r). However, the structure of the convection differs between the Small_1km and Expanded_Small configurations, and the system appeared more organized in the Small_1km simulation at this time. Additionally, the convection in north central Texas was nearly absent in the Expanded_Small configuration, but existed in the other two configurations.

At 1200 UTC, the portion of convection that reorganized and strengthened into the long-lived MCS had completely died in the Expanded_Large configuration, and only weak convection remained in northeastern Texas (Fig. 99l). However, the solutions from the other configurations provide completely different evolutions. In the Small_1km configuration, the convection had organized into a strong MCS with a well-defined trailing stratiform region (Fig. 99e). Further, this convection was preceded by the convection in north central Texas, which was characterized by reflectivity values exceeding 50 dBZ. However, the solution from the Expanded_Small configuration resulted in the western portion of the convection strengthening and reorganizing into a long-lived MCS, which deviated toward the south (Fig. 99s). Moreover, the convection in north central Texas had developed and strengthened by this time, merging with the main MCS.

By 1500 UTC, both the Small_1km and Expanded_Small configurations produced long-lived convective systems, with the system appearing more organized in the Expanded_Small configuration. This difference may be attributed to the eastward expansion of this domain into Louisiana while the Small_1km configuration cuts off the easternmost convection. In contrary, the Expanded_Large configuration was characterized by a only small area of convection by this time as the rest had dissipated. It is noteworthy that the inner 1-km domains of both the Expanded_Large and Expanded_Small configurations were in approximately the same locations, yet the two configurations resulted in dramatically different outcomes.

By 1800 UTC, the system had largely moved out of the inner-1 km domain of the Small_1km configuration (Fig. 99g) and had completely dissipated in the Expanded_Large configuration (with the exception of surface-based convection moving northward off the Gulf of Mexico; Fig. 99n). By this time, the convection in

the Expanded_Small configuration had weakened (Fig. 99u) but was resemblant of the observed convective system (discussed in section 3.2).

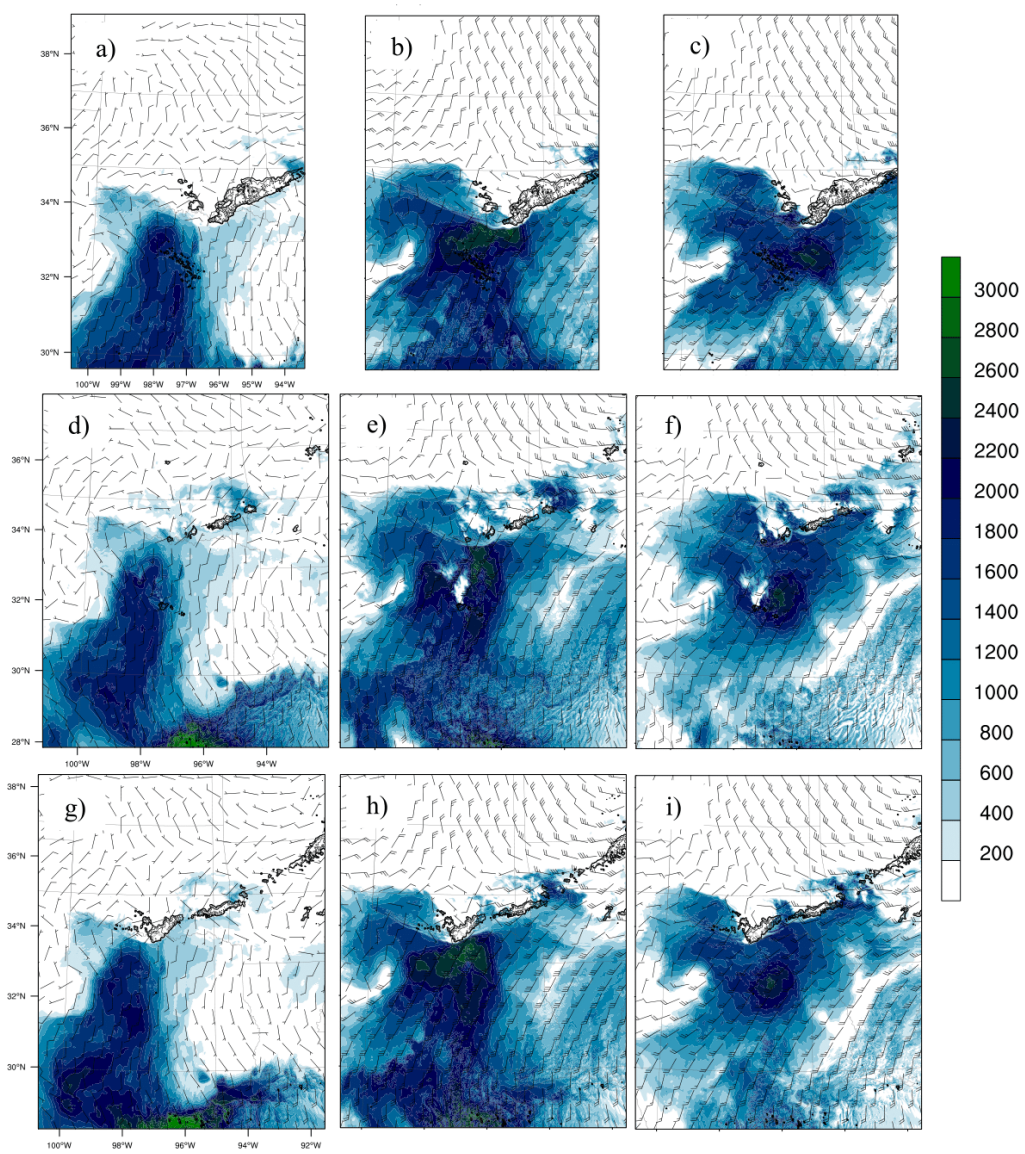

Figure 100: CAPE (shaded; J kg^{-1}), winds (knots; 1 knot = 0.51 m s^{-1}), and radar reflectivity contours (every 20 dBZ) valid at 0900 UTC on 6 October 2014 are depicted for the 1-km inner domains of the Small_1km (top), Expanded_Large (middle), and Expanded_Small (bottom) grid configurations. CAPE was calculated using the absolute temperature of parcels originating at (a),(d),(g) the lowest model level, (b),(e),(h) 500 m AGL, and (c),(f),(i) 1 km AGL.

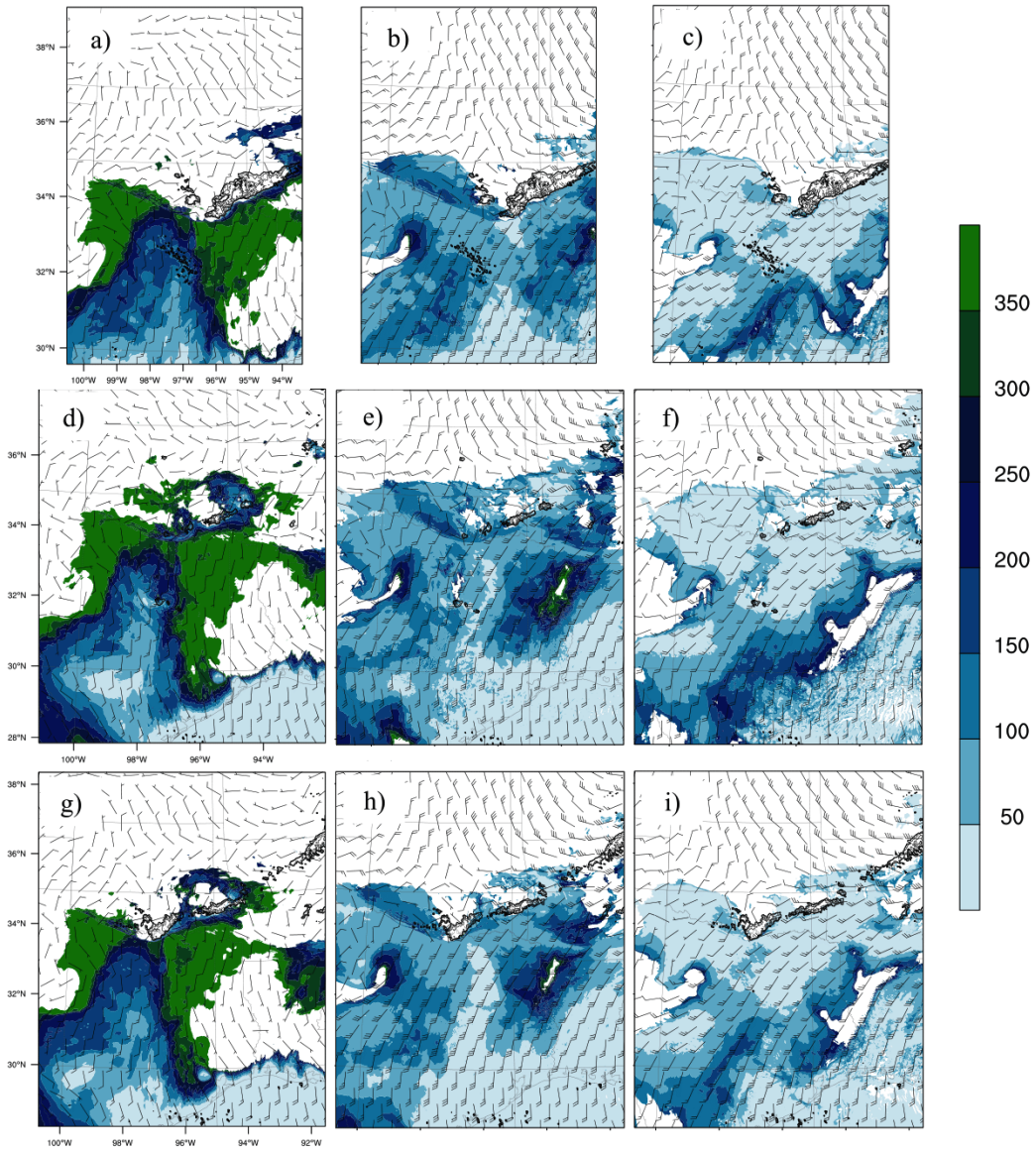

Figure 101: CIN (shaded; J kg^{-1}), winds (knots; 1 knot = 0.51 m s^{-1}), and radar reflectivity contours (every 20 dBZ) valid at 0900 UTC on 6 October 2014 are depicted for the 1-km inner domains of the Small_1km (top), Expanded_Large (middle), and Expanded_Small (bottom) grid configurations. CIN was calculated using the absolute temperature of parcels originating at (a),(d),(g) the lowest model level, (b),(e),(h) 500 m AGL, and (c),(f),(i) 1 km AGL.

One obvious hypothesis for the substantially different convective evolutions would be that the instability fields differed between the three configurations. However, sufficient instability existed in all three configurations throughout the simulation (Figs. 100,101). Therefore, it is unclear from solely examining the instability

fields why the convection was not maintained in the Expanded_Large configuration. However, the outer 3-km domain in the Expanded_Large grid configuration extended much farther west than in the other two configurations, which may have resulted in adverse effects on the ICs and BCs from the complex terrain. However, an investigation into the reasons why convection did not persist in this configuration was beyond the scope of this research and was not investigated further. However, this would be an important topic of future research and illustrates the difficulty and sensitivity faced by NWP when trying to predict a long-lived system several hours in advance.

B.3 Sensitivity to Horizontal Grid Spacing

In addition to the sensitivity of the simulations to lateral BCs using different grid configurations, the evolution of convection differed greatly for the Small_1km configuration depending whether or not information from the inner 1-km grid was written to the 3-km grid. The Small_1km configuration was run with two-way nesting, one-way nesting, and with the outer 3-km domain only (hereafter d01_only; more details on the nesting options are discussed in section 3.1). Differences were found between all three runs, with the most substantial differences in system evolution occurring between the two-way nesting and one-way nesting simulations.

More specifically, a long-lived, organized MCS was not produced by the outer 3-km domains for both the one-way nesting and d01_only simulations (Fig. 102). For the two-way nesting simulation, the simulated reflectivity for the 3-km grid was strongly resemblant to that from the 1-km grid during the later hours of the simulation (e.g., 1600 UTC; Fig. 103). However, this was not the case for the one-way nesting simulation, which produced a long-lived, organized MCS on the inner

1-km domain but weaker, disorganized convection on the outer 3-km domain. Additionally, differences were also apparent when the 3-km grid reflectivity solutions of both one-way and two-way nesting runs were compared with that of d01_only (Fig. 102). While subtle, differences in structure can be seen between the d01_only and the one-way nesting cases, which may be problematic if one chooses to run the outer domain first and then later add an inner nest using the ndown program (refer to Skamarock et al. (2008) for more information).

These differences in structure and evolution were also apparent in the vertical motion field at 1 km AGL during an earlier time in the simulation (e.g., 0900 UTC). At this time when the MCS was organized and strengthening in the Small_1km configuration, several undulations in the 1-km vertical motion suggest that gravity waves or possibly an undular bore were produced by the convection (Fig. 104). These waves were important for the development and maintenance of convection

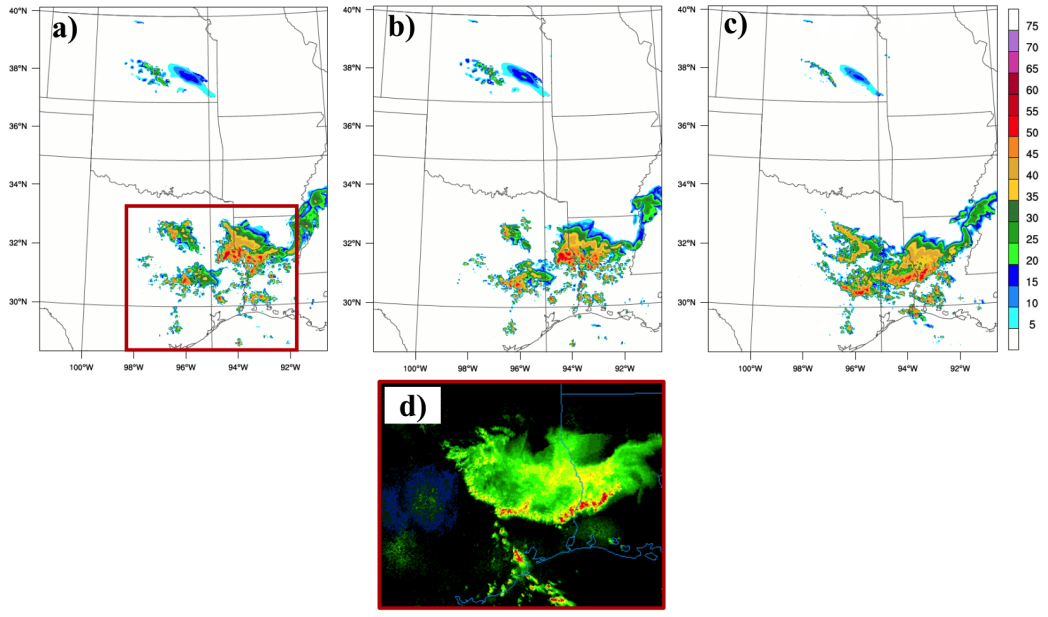

Figure 102: Radar reflectivity (dBZ) valid at 1600 UTC on 6 October 2014 for the Small_1km grid configuration (a) 3-km grid only, (b) 3-km grid with feedback off, and (c) 3-km grid with feedback on. The operational radar reflectivity composite is displayed in (d), where the red outline in (a) represents the approximate position of this composite.

in the Expanded_Small configuration (discussed in chapter 3). The undulations associated with these waves were characterized by a greater amplitude in the two-way nesting case than in either the one-way nesting and d01_only cases. Further, the undulations were more distinct in the two-way nesting case, whereas the other

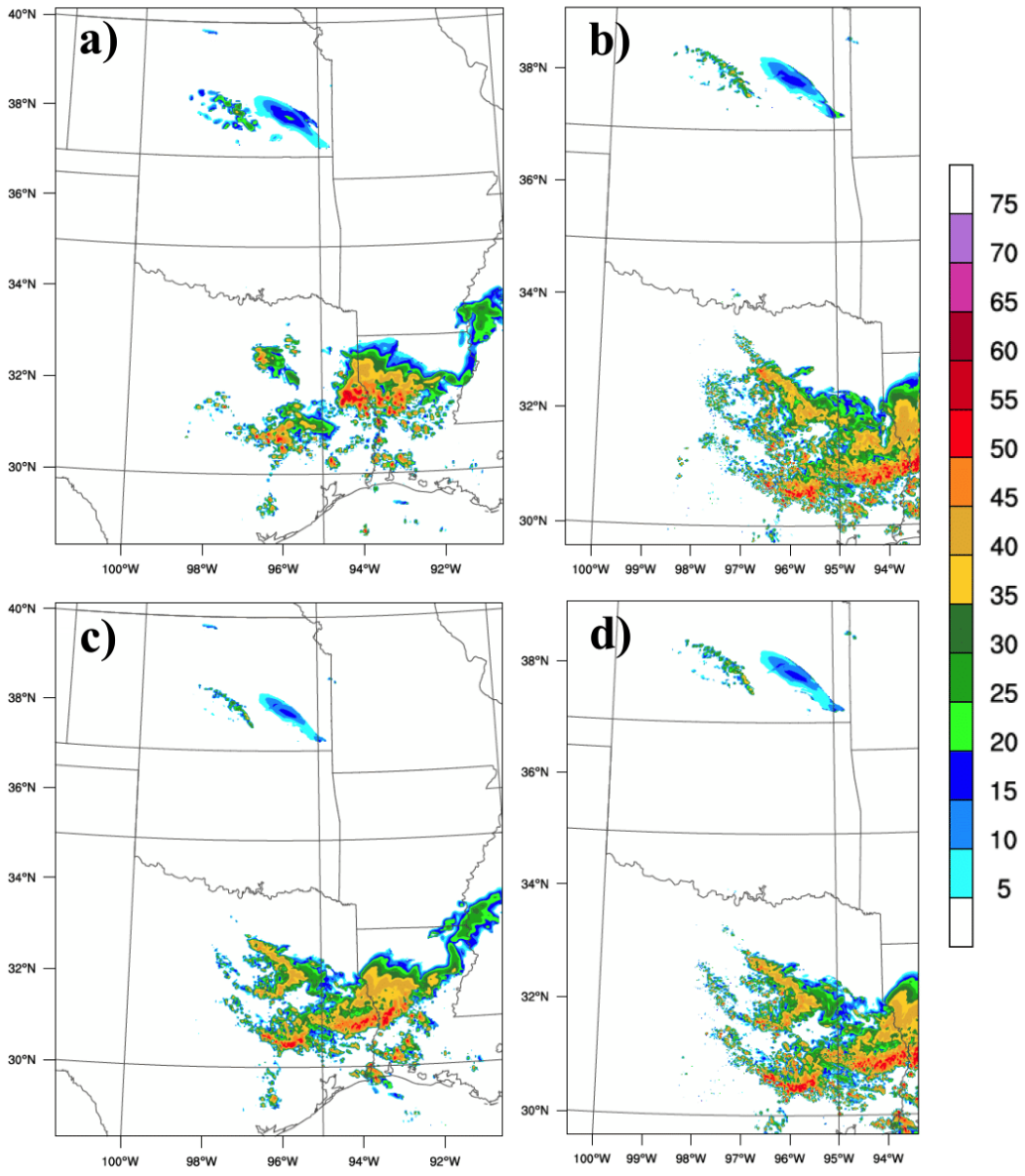

Figure 103: Radar reflectivity (dBZ) valid at 1600 UTC on 6 October 2014 for the Small_1km grid configuration (a) 3-km grid with feedback off, (b) 1-km grid with feedback off, (c) 3-km grid with feedback on, and (d) 1-km grid with feedback on.

two cases show waves with fewer undulations and less distinct subsiding branches. The structures of these waves were not examined thoroughly in the Small_1km configuration, but analysis of these waves on Expanded_Small simulations showed that they were resemblant of an undular bore or soliton characterized by horizontal wavelengths of 10 km or less (discussed further in section 5.1).

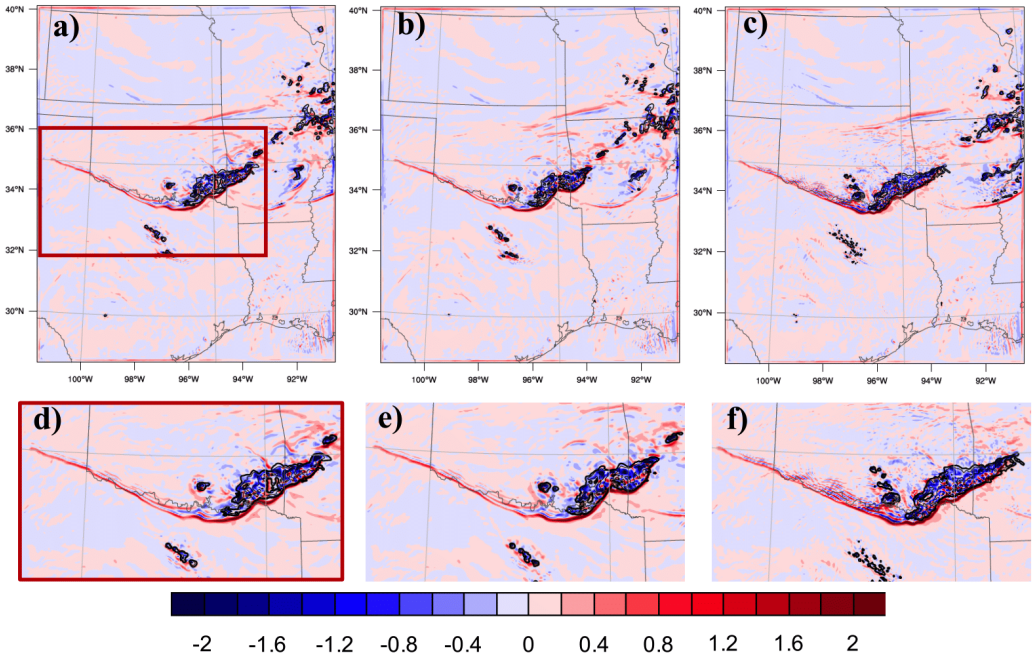

Figure 104: Vertical velocity (m s^{-1}) valid at 0900 UTC on 6 October 2014 for the Small_1km grid configuration (a) 3-km grid only, (b) 3-km grid with feedback off, and (c) 3-km grid with feedback on. A zoomed in depiction is shown in (d),(e),and (f), which correspond with (a),(b), and (c), respectively. The red outline in (a) corresponds with the zoomed in view shown in (d).

If a minimum resolvable wavelength of 4Δx is assumed (Pielke, 2013), the waves in the simulations would need to be at least 12-km in wavelength to be resolvable at a 3-km horizontal grid spacing. Therefore, we hypothesize that because these waves were important for the maintenance of the convective system in the simulations, their failure to be properly resolved at 3 km was likely why the convective system was weaker and disorganized without two-way nesting from the 1-km inner domain. In other words, the significant differences between the convective structures and

evolutions in the absence of two-way nesting suggests that a grid spacing less than 3 km was necessary to properly resolve the convection.

This result is important for several reasons. A previous study by Weisman et al. (1997) used idealized simulations of a squall line to conclude that convection should be simulated qualitatively as well at a 4-km grid spacing as at a 1-km grid spacing. However, these simulations were done on surface-based convection, implying that perhaps this result is not applicable for convection in the presence of a stable boundary layer which may be sustained, at least partially, by gravity waves or bores. Additionally, at present, convection-allowing operational and research models such as the HRRR, National Severe Storms Laboratory WRF, and 4-km NAM are often run at grid scales of 3-4 km (e.g., Benjamin and Coauthors, 2013). Thus, even at convection-permitting grid spacings, these operational models may not be able to property resolve these nocturnal systems, resulting in forecast busts. This maintenance by bores may be one reason why the initiation, evolution, and longevity of nocturnal MCSs are currently poorly forecast by operational models (Kain et al., 2013; Pinto et al., 2015).